# THE CAUSES OF INCREASED HYDROGEN UPTAKE OF ZIRCONIUM BASED FUEL CLADDINGS AT HIGH BURNUP

by

JONATHAN E. D. HAWES

*A thesis submitted to the University of Birmingham for the degree of*

*DOCTOR OF PHILOSOPHY*

*School of Metallurgy and Materials*

*University of Birmingham*

*October 2020*

# UNIVERSITY OF BIRMINGHAM

**University of Birmingham Research Archive**

**e-theses repository**

# ABSTRACT

When Zirconium claddings are exposed to irradiation and oxidation in reactor, after a certain period, they may undergo a change of hydrogen uptake behavior and in some cases an increased hydrogen pickup fraction. Hydrogen is present in reactor as a by-product of the oxidation, or through radiolysis of the coolant.  It may penetrate through the oxide and enter the underlying metal. Above a certain concentration, it precipitates as brittle Zr-hydrides degrading the cladding's mechanical properties.

This degradation is important since Zr based fuel claddings, in the form of rods, are used in light water nuclear reactors to encapsulate multiple $UO_2$ pellets. They act as the first barrier between the fuel and the reactor system. Clad failure would not only cause shutdown of the reactor (with related economic repercussions) but also potentially allow the leaking of radioactive fuel into the reactor system.

The oxide formed at the outer surface of the cladding (the surface in contact with coolant) acts as a barrier for further oxidation, since it grows by oxygen diffusion through a pre-existing oxide layer to the metal-oxide interface. The nature and morphology of this oxide therefore influences the rate of oxidation and H-uptake. There is a limit of hydrogen concentration in the cladding above which this parameter becomes life limiting.

The question of H-uptake and its mechanism has been present since Zr based alloys were used as cladding material, this has led to a large amount of literature being available on the topic. However, there are still aspects, which require better understanding, especially with the desire to use fuel to higher burnups. Different properties of the oxide have been studied in the past, including its chemical composition, microporosity, etc.

One of the properties that was mentioned to play a role regarding the increased hydrogen pickup fraction was the conductivity of the interface oxide layer. However, this aspect was not explored in irradiated materials, and the intrinsic properties of the interface were not explored at high resolution. To further examine the impact of this property, electrical resistivity of the oxide formed on the same alloy grade (Zircaloy-2 LK3/L) after different residence times in a boiling water reactor (3,6 and 9 cycles) was examined by a novel technique which used micromanipulators contacting different thicknesses of oxide produced by FIB. This technique brought local intrinsic resistivity information, with high spatial resolution, across the different oxides on irradiated materials, not possible with other techniques. The presence of an inner more conductive region was demonstrated.  Furthermore, it was shown that the thickness of this layer decreased from approximately 1500nm to 800nm from the 3-cycle to the 9-cycle sample. Additionally, the resistivity increased between the two. Surprisingly a generally higher resistivity was seen on the 6-cycle sample. This has been discussed in the thesis. These

results makes it possible to demonstrate the nature of the barrier layer in such materials, quantifying this property and its changes.

To further characterize this material, micro-compression of micro-pillars was performed on Zircaloy-2 LK3/L (autoclaved and 6-cycle) to fill gaps missing in the literature on the evolution of mechanical properties, in the vicinity of the metal-oxide interface, with residence time. An irradiated as well as autoclaved low-tin Zircaloy-4 were also measured to compare. A decrease in strength of oxide was seen with residence time for the Zircaloy-2 LK3/L series but not so clearly observed for the low-tin Zircaloy-4.

The distribution of alloying elements in Zirconium based alloys was shown to play a role on the hydrogen uptake behaviour. One alloying element currently under scrutiny is Nb. Two different Nb containing alloys, from pressurised water reactors, were studied to answer open questions about the speciation of Nb in the oxide of irradiated claddings. A Zr-2.5%Nb sample was studied with scanning transmission electron microscopy (STEM)-electron energy loss spectroscopy (EELS) and a low-tin ZIRLO sample with X-ray absorption near edge structure (XANES). Both sets of results showed Nb remaining metallic into the oxide and then an increasing oxidation state of Nb with distance into the oxide. Both sets of results also showed fully oxidised $Nb^{5+}$ to be present some distance into the oxide.

It has been shown that if hydrides precipitate, close to the metal-oxide interface, the subsequent oxide formed may also be less protective and allow easier ingress of oxidising and hydriding species. The hydrides close to the metal-oxide interface (in a low-tin Zircaloy-4) were examined with electron dispersive X-ray spectroscopy (EDS) and electron energy loss spectroscopy (EELS). In addition, the regions of oxide adjacent to hydride and metal were also compared with the same techniques. It was found that even though a change in chemical composition could be seen between the two areas the phase fractions of tetragonal and monoclinic zirconia appeared indistinguishable hence the increase in porosity in the region of oxidised hydride seen in the literature was concluded to be the most impactful difference between these two regions.

The work performed in this study contributes to the improved understanding of the hydrogen uptake mechanism in reactor. Parameters, which have been suggested to contribute to the changes in hydrogen uptake at high burnups, have been clearly quantified.

**LIST OF PUBLICATIONS**

Papers with content that is included partially or entirely in the thesis:

Hawes, J., Baris, A., Chiu, Y., & Abolhassani, S. (2020). Characterization of the conductivity of metal-oxide interface of zirconium based fuel cladding at low and high burnups. *Journal of Nuclear Materials*, *534*, 152133. https://doi.org/10.1016/j.jnucmat.2020.152133

Hawes, J. Warnicke, P. Burr, P. Ferreira Sanchez, D. Grolimund, D. Partezana, J. Chiu, Y. and Abolhassani. S. The speciation of Niobium in the oxide layer of an irradiated Low-Tin ZIRLO nuclear material (To be submitted)

Abolhassani, S., Baris, A., Hawes, J., Grabherr, R., Colldeweih, A., Bertsch, J., Chollet, M., Kuri, G., Martin, M., Portier, S., Ammon, K., Ledergerber, G., Limbäck, M., (2019). Towards an improved understanding of the mechanisms involved in the increased hydrogen uptake and corrosion at high burnups in zirconium based claddings. 19th ASTM International Symposium on Zirconium in the Nuclear Industry,

In addition, the work presented in this thesis has been presented at a number of conferences and meetings with conference proceedings, including the following:

Hawes, J., Baris, A., Vogt, D., Abolhassani, S. (2018). The Effect of Heating Zirconium Hydrides Studied by Electron Energy Loss Spectroscopy. International Microscopy conference, Sydney Australia

Hawes, J., Baris, A., R. Vanta., Abolhassani S. (2019). Investigation of the semi-conducting properties of oxides in the vicinity of the metal-oxide interface throughout lifetime of zirconium based fuel cladding. International FIB workshop, Dresden

Hawes, J., Baris, A., Warnike, P., Abolhassani S. (2019). The speciation of Nb in zirconium fuel cladding studied by SLS synchrotron using XANES spectroscopy. 3D Swiss Society of Microscopy meeting, Engelberg

**ACKNOWLEDGEMENTS**

I am deeply thankful to have been able to marry my wonderful wife Rachel during the timeframe of this PhD. I am thankful for her supportive attitude and constant love. She has made my life much better and I thank God for her.

*"giving thanks always and for everything to God",*
*"My grace is sufficient for you, for my power is made perfect in weakness."*
*Ephesians 5:20, 2 Corinthians 12:9*

# TABLE OF CONTENTS

**LIST OF ABBREVIATIONS**

| | |
|---|---|
| APT | Atom probe tomography |
| BCC | Body-centred cubit |
| BF | Bright field |
| BSS | Blind source separation |
| BWR | Boiling water reactor |
| DF | Dark field |
| EDS | Energy-dispersive X-ray spectroscopy |
| EELS | Electron energy loss spectroscopy |
| EFTEM | Energy-filtered TEM |
| EPMA | Electron probe micro-analysis |
| FCT | Face centred tetragonal |
| FEG | Field-emission gun |
| FIB | Focused ion beam |
| FWHM | Full width at half maximum |
| HAADF | High-angle annular dark field |
| HCP | Hexagonal close-packed |
| HUP | Hydrogen uptake |
| HPUF | Hydrogen pickup-fraction |
| KKL | Kernkraftwerk Leibstadt (Leibstadt Nuclear Reactor) |
| KKG | Kernkraftwerk Gösgen (Gösgen Nuclear Reactor) |
| LOCA | Loss-of-coolant accident MLLS |
| MLLS | Multiple linear least squares |
| PCA | Principal component analysis |
| PPT | Precipitate |

| | |
|---|---|
| PWR | Pressurised water reactor |
| ROI | Region-of-interest |
| SE | Secondary electrons |
| SEM | Scanning electron microscope |
| SI | Spectrum image |
| SIMS | Secondary ion mass spectrometry |
| SPP | Second phase particle |
| STEM | Scanning transmission electron microscope |
| SEM | Scanning electron microscope |
| SE | Secondary electron |
| TEM | Transmission electron microscope |
| TSSD | Terminal solid solubility limit of dissolution |
| TSSP | terminal solid solubility limit of precipitation |
| XANES | X-ray absorption near edge structure |
| XRD | X-ray diffraction |
| ZLP | Zero-loss peak |

# LIST OF FIGURES

# LIST OF TABLES

# 1 Introduction

## 1.1 Background

Light water reactors (LWR) comprise approximately 80% of the world's commercial nuclear reactors [1]. With more than three-quarters being pressurised water reactors (PWR) [1], and the second most common boiling water reactors (BWR). The general theory behind both reactors is similar with liquid water, used as a coolant and moderator in the reactor core, passing over nuclear fuel rods, which are present in the core as assemblies. The energy released from the nuclear reaction in the fuel is carried away and used as steam to drive turbines and create electricity. Heavy water reactors (HWR), which make up another 10% of the world's reactors, also work in a similar way but use deuterated water as a coolant; this allows the use of low enrichments of uranium or natural uranium as fuel since the heavy water moderates the neutrons less strongly than light water. Nuclear fuel rods consist of $UO_2$ cylindrical fuel pellets encapsulated in a tubular cladding material typically with a wall thickness of less than a millimetre and a length varying from 1.8 to 4.5 m [2]. An illustration of a BWR and PWR fuel assembly is given in Figure 1-1 [3]. A table of typical dimensions for fuel claddings and pellets is given in Table 1-1 [2]. The cladding is used to contain the $UO_2$ and prevent fission products from entering into the coolant. Clad failure would not only cause shutdown of the reactor (with related economic repercussions) but also potentially allow leaking of radioactive fuel into the reactor core, meaning workers themselves would be subject to radioactivity as well. Zirconium alloys have been used since the early 1950's as nuclear materials [4] and in the 1960's became the most commonly used material for fuel cladding in light water and heavy water reactors [4]. Their low thermal neutron capture cross-section means neutrons needed to continue the chain reaction in the core are less likely to be absorbed by the cladding material and hence contributes to a good neutron economy for the reactor. Zirconium also has good mechanical behaviour and satisfactory corrosion performance, particularly when it is alloyed with other elements (such as Sn, Nb, Fe, Cr, Ni). Two of the main limiting factors for the lifetime of the fuel cladding are oxidation and the hydrogen uptake (HUP) (or hydrogen pick-up), which are consequences of the waterside corrosion process in the reactor [5], [6]. Although newer alloys that display better corrosion performance have or are being developed, the problem of hydrogen uptake, especially at high burnups, still persists. Hydrogen, which can be produced on the waterside surface of the cladding or already be present in the coolant, may enter the cladding material by transporting across a pre-existing oxide layer to reach the underlying metal. When exceeding the

solubility limit this would result in the formation of brittle Zr-hydrides and hence the degradation of mechanical properties as well as the corrosion resistance.
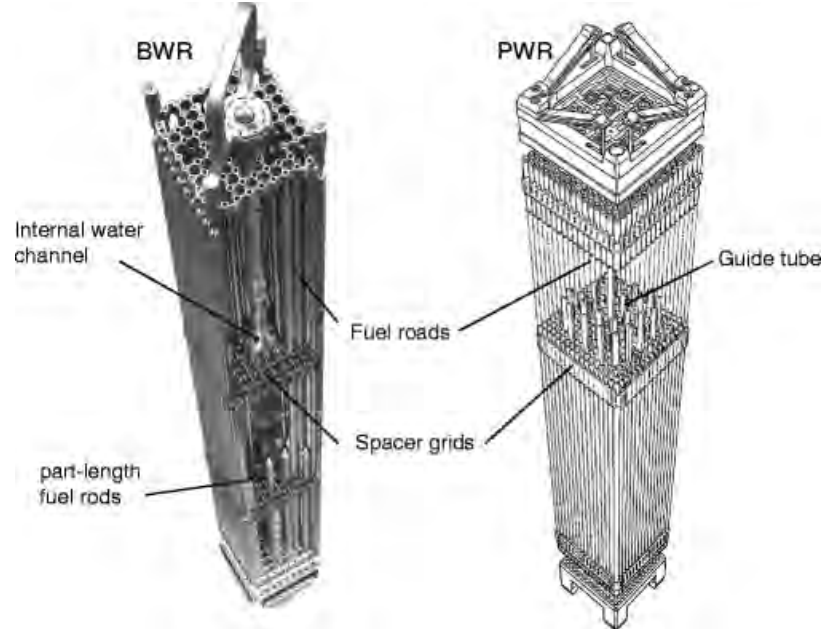


*Figure 1-1.Example of fuel elements for BWR and PWR reactors [3]*

| Feature | PWR | | | | | BWR | |
|---|---|---|---|---|---|---|---|
| | 14 × 14 | 15 × 15 | 16 × 16 | 17 × 17 | 18 × 18 | 9 × 9 | 10 × 10 |
| Cladding outer diameter (mm) | 10.16–11.18 | 10.75 | 9.14–10.75 | 9.50 | 9.50 | 11.00–11.20 | 9.84–10.28 |
| Wall thickness (mm) | 0.570–0.725 | 0.620–0.725 | 0.570–0.725 | 0.570 | 0.64 | 0.70–0.71 | 0.605–0.620 |
| Pellet – cladding diam. gap (mm) | 0.170–0.210 | 0.170–0.190 | 0.160–0.190 | 0.156–0.170 | 0.170 | 0.180–0.200 | 0.150–0.170 |
| Pellet height (mm) | 10.0–12.6 | 10.0–12.6 | 9.8–11.0 | 9.8–13.5 | 9.0–9.8 | 10.0 | 10.0–10.5 |

*Table 1-1. Typical dimensions of fuel claddings and pellets [2]*

# 1.2 Motivation and aims of the thesis

Researchers have shown that, by reducing the amount of hydrogen entering the cladding, the original properties of the material can be better preserved leading to longer residence times for the nuclear fuel [5]–[7]. This in turn has great benefits, as the reactors would need to be refuelled less often producing less highly radioactive waste. There would also be economic gain not only from purchasing or producing less fuel but also by reducing the amount of costly down time needed for refuelling. Despite decades of research on the topic of the mechanism of HUP in zirconium alloys, it is still not fully understood. Particularly what is lacking is a full understanding of hydrogen uptake during service in-reactor and even more so at higher burnups or residence times. This is because while there is much research on the topic, most are autoclave studies which do not necessarily describe the in-reactor behaviour [8]. For this reason this study focused on materials from different reactors with different residence times, even to higher burnups beyond the design limit of the claddings [9]. This is a challenge since radioactive material from reactor cores is of course not easy to handle, and special equipment and facilities are needed. The facilities at the Paul Scherrer Institute, where this thesis work was conducted, such as the Hot Laboratory and controlled microscopy laboratory as well as the material provided for the project made this possible. The interest in HUP, the mechanism in-reactor and at higher burn ups, comes not only from the desire to increase fuel efficiency and residence time but also because it has been demonstrated that the hydrogen pick-up fraction (HPUF) changes with the time spent in the reactor by Abolhassani et al [8]. In certain cladding alloys (e.g. LK3/L type Zircaloy-2 in BWR), it was shown to increase with increasing burnups; this phenomenon is termed "increased H-uptake". However, not all alloys behave in the same way. This implies that knowing the early and/or mid-life behaviour of a given cladding may not provide the complete information regarding the late-life behaviour of the cladding. For this, a more complete understanding of the mechanism of HUP is needed. This finding prompted a large amount of research to be undertaken, which is further discussed throughout this thesis. Since there are many factors which are known or expected to affect the HUP not all of them could be investigated during the timeframe of one PhD. Therefore, this work aims to investigate some of the factors affecting hydrogen uptake which have previously not been investigated, as well as to build on and add to study or characterisation conducted in the framework of this project and others.

The main aims of this thesis can be summarised as follows:

- To verify if the semi-conducting properties of the cladding oxide near the metal-oxide interface is influenced by residence time and burnup.

- To explore more in-depth the mechanical properties of the material on the two sides of the interface and reveal the changes present as a function of time and burnup.

- Furthermore, to examine the chemistry and crystal structure of the oxide in the case of a material showing little influence of time and burnup on the change of hydrogen uptake behaviour.

- Finally, to address a question that arose during the previous studies, to examine the oxide structure by means of electron energy loss spectroscopy for the oxide formed adjacent to a hydride found at the metal-oxide interface, as opposed to the oxide formed on a metal-matrix. This helped to verify if the oxide formed on a hydride phase shows a different structure or not.

In addition, the thesis will discuss and draw conclusions on how these factors will contribute and affect the hydrogen uptake mechanism. Together with findings from other studies, it will also aim to discuss and suggest which factors are most important to the hydrogen uptake mechanism and particularly the observed increased HUP at higher burnups.

The above mentioned aims were expressly chosen as areas which were lacking and needed further study. The motivation for choosing these aims will be discussed in more detail at the beginning of their respective chapters.

# 1.3 Structure of the thesis

In the following chapter, an overview is given of the current literature and understanding of the oxidation and HUP mechanism. The second half of that chapter is a list of factors which could affect the HUP of a Zr based fuel cladding in reactor, highlighting the factors which could contribute to the change in HUP seen for some alloys at high burnups. Since not all of these factors can be covered in the scope of one PhD thesis, more detail is given to those that are covered in the thesis. Chapter 3 covers the materials used in this work as well as some measured data, from the literature or material supplier, on the oxide thickness and hydrogen content of that material. Chapter 3 also outlines the different experimental techniques used. The subsequent Chapters 4-7 show the obtained. Each chapter includes a brief introduction as well as a discussion. Each chapter focuses on different techniques and in this way each of the four results chapters, as well as forming part of the whole thesis, could also potentially be read alone and the reader should still understand the purpose of the chapter as well as the main findings. Chapter 4 focuses on the electrical resistivity of the oxide formed in reactor on Zircaloy-2 LK3/L after 3 different residence times. This property was investigated using a novel technique developed at PSI. Chapter 5 is on the speciation of Nb in the oxide of two different Nb containing alloys irradiated in PWRs and studied with XANES or EELS. Chapter 6 covers the mechanical properties of irradiated and autoclaved alloys investigated by creating micro-pillars in the vicinity of the interface and compressing them. Chapter 7 uses EDS and EELS to examine hydrides at the interface and their effect on subsequent oxidation. Chapter 8 is a general discussion about the findings in relation to the current understanding of HUP particularly at high burnups. Chapter 9 are conclusions.

# Contents of chapter 2:

# 2 Literature review

## 2.1 Zirconium in the nuclear industry

Zirconium is the base element of nuclear fuel claddings. Pure Zr cannot withstand the reactor conditions; therefore, small amounts of other elements, such as Ni, Fe, Cr, Sn, Nb, are added. Zr alloys exhibit low neutron cross section, mechanical stability and corrosion resistance allowing its application in reactor. This has led to the development of a wide range of Zr based materials used as fuel claddings. Z. Duan et al. [10] show a compiled list of Zr based alloys used as claddings. In early stages of development, the content of alloying elements was varied and the materials tested to provide higher quality alloys. While a great deal has been learnt and well performing alloys have been produced, there is still much about the material behaviour and particularly degradation, including hydrogen uptake, which remains unknown [6], [11]. The Zircaloy family of alloys was one of the first and most predominant families to be developed. The Zircaloy-2 group of alloys has been used predominately in BWRs since the early 1970's [10]. Soon after, Zircaloy-4 was produced with a decreased amount of Ni and adjusted amounts of Fe and Cr to further improve corrosion and hydrogen uptake. Zircaloy-4 is predominantly used in PWR reactors where an over pressure of H is seen in order to supress radiolytic oxygen formation[12]. In Canada and Russia, zirconium alloys with Nb as the major alloying element in the place of Sn were developed instead containing 1-2.5% Nb. With improved corrosion and creep resistance, ZIRLO, and later on "Optimized ZIRLO", were developed as a successor to Zircaloy-4 to be used in PWRs. Although the list of alloys used in the industry is long and many newly developed alloys exist, this literature review will focus on the alloys used for the current study, i.e. Zircaoly-2 (specifically the LK3/L series), (low-tin) Zircaloy-4, (low-tin) ZIRLO, Zr-2.5%Nb.

## 2.2 Physical properties and effects of alloying

Zirconium assumes an HCP structure (alpha phase) up to 863 $^{\circ}$C; above that temperature it transforms to a BCC structure (beta phase) which can be stabilised with the addition of certain alloying elements even at lower temperatures. At very high pressures, pure zirconium exists as a hexagonal omega-phase. Even in the reactors with highest pressure such as pressurised water reactors (PWR), the

pressure is of the order of 100 bar, or 10 MPa, which is far from the required pressure for transformation. The pressure-temperature phase diagram of zirconium is shown in Figure 2-1. Zirconium is the 40th element in the periodic table, a transition metal with the relative atomic mass of 91.22 [13] and density of 6.511 g cm$^{-3}$. As the basis for nuclear cladding material, the most important advantage over other metals is zirconium's low neutron absorption cross-section of 0.18 barn [13]. The low neutron absorption cross-section lies at the root of the choice to use zirconium as a nuclear material.
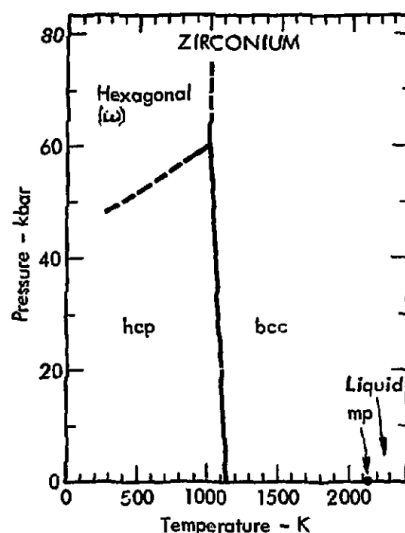


*Figure 2-1. The Pressure-Temperature phase diagram for pure zirconium [13]*

A large amount of work has been performed on the role of different alloying elements in zirconium alloys, and while there is still much debate about the exact role of each alloying element, the role and reason for the addition of the main alloying elements are briefly summarised next. These elements will then be discussed in individual sections further in the  literature review.

**Oxygen (O)** is an alpha stabiliser and has a high solid solubility in the Zr matrix. Small amount of O is present in Zr alloys to increase the phase transition temperature and increase the yield strength of the metal, although at larger values the ductility of the metal significantly decreases[10]. The Zr-O phase diagram is shown in Figure 2-2 [14] and the Zr-O Ellingham diagram in Figure 2-3 [6], [15].

**Tin (Sn)** is added to improve mechanical properties such as yield strength and creep resistance [16]. It also, in the absence of other alloying elements, helps to inhibit corrosion and reduce the harmful effects of N impurities in the material. However it has been shown that, at some level, Sn begins to

greatly lower the corrosion resistance of the material; as an example, in the case of Zircaloy-2, a study showed that above 1.5% the effect of Sn would be to reduce resistance to corrosion [17].

**Iron (Fe), Chromium (Cr) and Nickel (Ni)** are grouped together as beta stabilisers. All three have low solid solubility in Zr-alpha matrix and therefore precipitate as secondary phase particles (SPPs) and in the case of ternary precipitates, $Zr_2(Fe, Ni)$ and $Zr(Fe, Cr)_2$ can be mentioned. As well as these, binary precipitates could also be present such as $Zr_3Fe$, $Zr_2Ni$ or $ZrCr_2$ [10], [18].These elements are added to improve corrosion resistance. It has been shown though that it is not only the amount of added element but also the size, shape and distribution of SPPs (controlled by the processing route and heat treatment) which affect the susceptibility to corrosion [19], [20]. There is evidence that Ni can increase the hydrogen pickup fraction of a clad [21], [22], therefore in some alloys the amount of Ni was lowered and Fe increased for example in Zircaloy-2 and -4. Cr also improved the creep resistance and tensile properties of the material[23], [24].

**Niobium (Nb)** is also a beta stabiliser added to improve mechanical properties and counterbalance the detrimental effects of different impurities [25]. Alloys such as E100, E125, E635, Zr-2.5% Nb, M5, ZIRLO have high amounts of Nb rather than Sn with small amounts of other alloying elements, particularly usually Fe. It has been shown that Nb-containing alloys such as those just mentioned, have a lower hydrogen pick up fraction [8], [11], [26]. This phenomenon will be discussed in greater detail later in the thesis.

Evidently, other alloying elements have been tested, however, since they are outside the scope of this thesis, no further reference will be made to them.
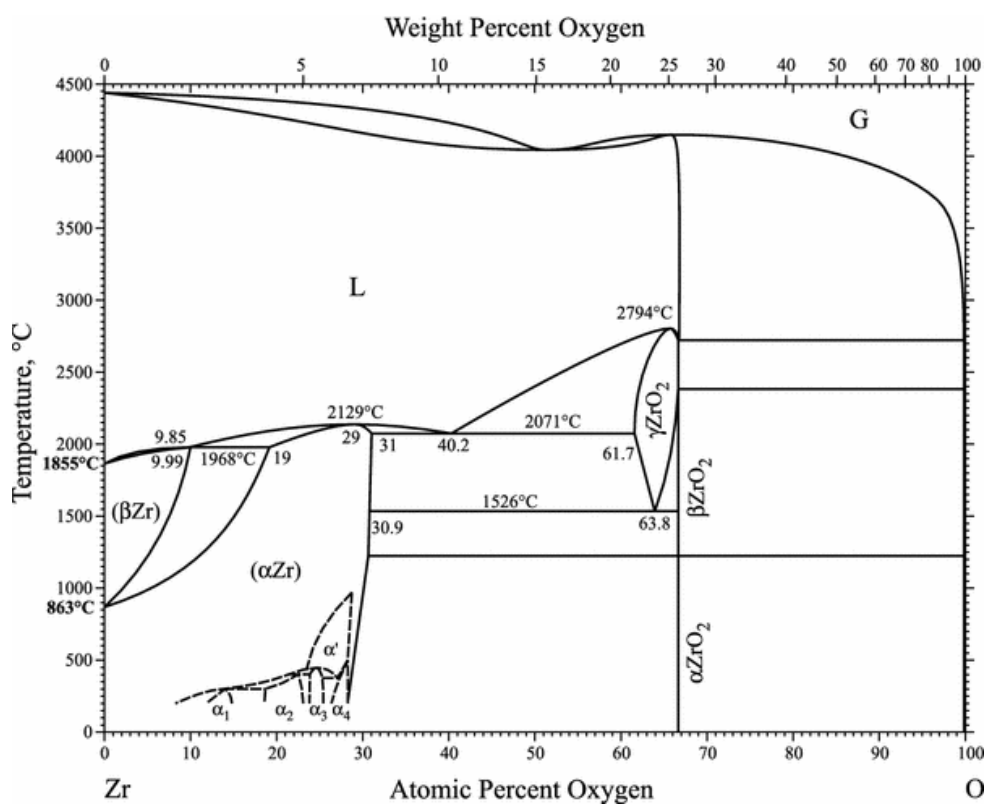
*Figure 2-2. The Zr-O phase diagram [14]*
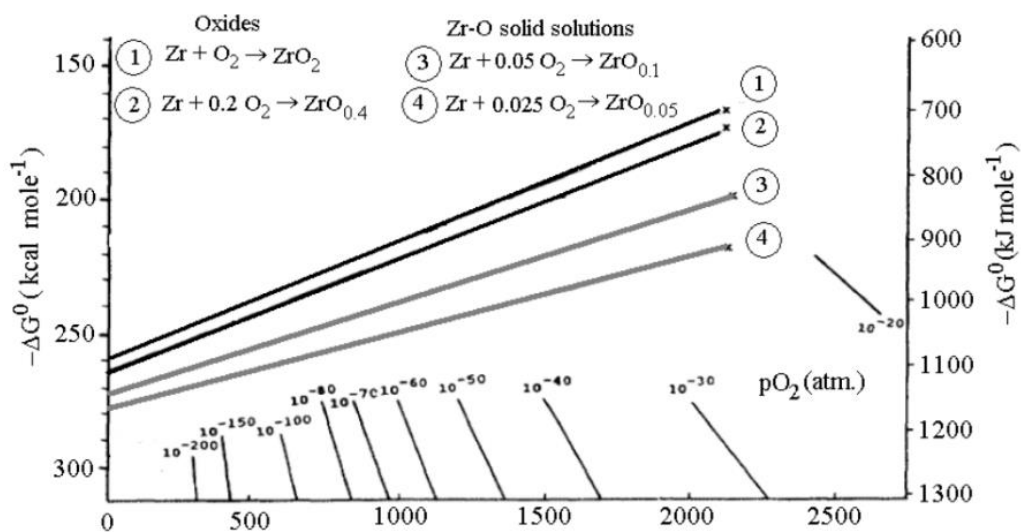


*Figure 2-3. The Zr-O Ellingham Diagram [6], [15]*

# 2.3 Oxidation

In the following section a general overview of the current understanding of Zr oxidation in water is outlined. The subsections are laid out in a chronological order beginning with initial or early oxidation and growth, then moving onto pre and post transition oxide growth. Transition is a term for the sudden increase in oxidation rate or deviation from cubic (or other exponent) kinetics. The oxidation scheme after transition is not defined by the term however different possibilities will be discussed in this chapter.

## 2.3.1 Early oxidation and subsequent oxide growth

Zirconium has a high affinity for oxygen and readily oxidises in air at room temperature forming a 2-5 nm thick oxide layer. The Zr-O phase diagram in Figure 2-2 shows how oxygen can be in solid solution with alpha–Zr up to 28.6 at.% O at 200°C and that its solubility increases with temperature up to 35 at.% at 2065 °C [6]. As presented in the Ellingham diagram (Figure 2-3), it is energetically more favourable for oxygen to be dissolved in the metal than to form an oxide; there will therefore be an oxygen saturated region ahead of the oxidation front with oxygen in solid solution. Oxide will only then form if the partial pressure of oxygen is higher than the dissociation pressure of the oxide, at a given temperature. It is therefore possible that during exposure to a reducing atmosphere, oxygen can dissolve into the metal substrate diminishing the oxide layer. However, such conditions are not those addressed by this thesis. The general equation for Zr oxidation in water, as the cladding will be in reactor, can be written as:

$$Zr + 2H_2O \rightarrow ZrO_2 + 2H_2 \qquad \textit{Equation 2-1}$$
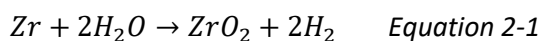
Whether the hydrogen produced is released into the water or enters the zirconium metal is of great interest and will be discussed in greater detail. Once the thin dense oxide layer is in place further oxidation of Zr will then take place at the metal-oxide interface by the migration of the oxidising species through the already formed oxide layer to the metal [27]. Growth of the pre-existing thin oxide scale is driven by the free energy of formation of zirconium oxide which has been shown to be ≈965 KJ/mol at 360 $°C$ [28]. The oxide formed at the early stages is dense and prevents rapid diffusion of different oxidizing species, such as $O^{2-}$ to the interface.

From the literature, one possible oxidation mechanism is provided below. For this mechanism, the following steps summarise only early oxide layer growth (this will be during the so-called pre-transition phase where the oxide is still dense and protective) [15]:

- Water molecules will physically adsorb onto the oxide surface and, at a defect site such as an oxygen vacancy. Oxygen from the water molecules will dissociate to fill an oxygen vacancy keeping the electrons from the two hydrogen atoms leading to the formation of charged oxygen ions [29] as well as two positively charged hydrogen atoms.

- Oxygen ions which are on the oxide surface can then be incorporated into the oxide scale at defect sites [15]. "The concentration of these defects at the surface clearly defines the rate of oxygen incorporation" [15]

- A negative oxygen vacancy concentration gradient, from the metal oxide interface to the outer surface (or a lower oxygen concentration near the interface), will exist because new defects are being formed at the metal oxide interface and are being filled by oxygen ions at the outer surface [11], [30], [31].

- The driving force is the oxygen gradient across the oxide; the rate limiting factor is oxygen ion diffusion via oxygen vacancies [15] which will lead to an oxygen concentration gradient from the oxide surface to the metal oxide interface.

- As mentioned before, in this configuration the assumption is that 'transition' has not occurred, meaning that the oxide scale is still dense and protective without porosity and cracking. The incorporated oxygen ions will diffuse through the oxide layer via point defects (oxygen vacancies or interstitials), line defects (dislocations) and grain boundaries until reaching the metal oxide interface [27]. It has been found that the diffusion coefficient of oxygen in $ZrO_2$ along grain boundaries can be $10^4$ times greater than lattice diffusion [32]. It is therefore suspected that almost all oxygen transported through the oxide film is via grain boundaries.

- Oxygen dissolution into the metal substrate will occur and give some diffusion distance where oxygen is dissolved in the metal (the distance of this depends on alloy type and other parameters such as temperature)[33]; once the solubility limit is exceeded, the oxide layer will begin to form. A more shallow oxygen distribution into the metal has been correlated with more rapidly growing oxide scales [15].

- When the oxygen ion reaches the metal-oxide interface, it reacts with zirconium cations to form a new oxide (Equation 2-2 and Equation 2-3). The formation of this new oxide releases electrons, $e^-$, which could then migrate through the oxide by a hopping mechanism to reduce the hydrogen ions at the cathodic site [34] shown in Equation 2-4.

$$Zr \rightarrow 4e^- + Zr^{4+}$$

*Equation 2-2*

and

$$Zr^{4+} + 2O^{2-} \rightarrow ZrO_2$$

*Equation 2-3*

$$4e^- + 4H^+ \rightarrow 2H_2$$

*Equation 2-4*
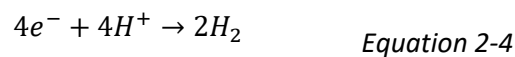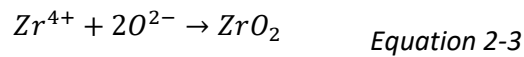
In this scenario, to maintain charge balance, either electrons must migrate outwards to reduce the $H^+$ at the outer oxide-water interface (cathodic site) or $H^+$ must migrate inwards (towards the metal) following which they could be 'picked up' and incorporated into the metal. The ingress of hydrogen (particularly at high burnups) and the proposed mechanisms of HUP will be discussed in a later section of the thesis. To summarise, the oxide is expected to have a lower chemical concentration of oxygen at the interface (i.e. a vacancy concentration gradient from metal-oxide interface to the outer oxide-water interface) as well as an electrical potential between the two sides of the oxide.

Oxygen vacancies are defects which are formed at the metal-oxide interface from the formation of new oxide and can be separated into two groups: neutral and oxidised vacancies i.e. $V_o$ and $V_o^{2+}$ [35]. Once an oxide exists neutral vacancies $V_o$ are present due to the metal dissolving neutral oxygen atoms from their positions in the oxide. For oxidised vacancies however, $V_o^{2+}$ electrons are forced to stay in the oxide [35]. The creation of charged vacancies and charged oxygen ions gives a potential across the oxide layer; this will cause the inward diffusion of oxygen ions and the outward diffusion of vacancies. The difference between the partial pressures of oxygen at the two interfaces will dictate the size of this potential i.e. a larger difference in partial pressures will give a larger potential difference and hence a faster oxidation. A parabolic vacancy concentration gradient is therefore expected with the highest vacancy concentration at the interface.

The phases present at the interface, their composition and structure have been the subject of several studies. For example, as mentioned above, the solid solubility limit of O in Zr at simulated PWR conditions (360 °C) is around 28 at% [6]. Such a value could be seen in the metal at the metal-oxide interface. However, the interface is continuously changing during oxidation, meaning equilibrium might not have the possibility to establish. Hence, metastable phases can form. Numerous authors have reported a variety of phases such as amorphous or omega phase [56], ZrO [57], Zr-30%O [58], Zr$_3$O [33] and a series of other different phases [59]. As well as these structures an oxygen saturated region is found in the metal side of the interface. During the transition, it is has been observed that

the thickness of the different phases or a combination of the layers decreases significantly, expected to be due to the lack of time for formation at faster oxidation rates [27].

### 2.3.2 Pre-transition oxide growth, kinetics and oxide structure

The mechanism proposed in section 2.3.1 is one of the proposed general oxidation mechanisms for zirconium alloys. This phase of oxidation is known as "pre-transition" and only lasts until the oxide is approximately 2-3 $\mu m$ thick [11], [36]. The growth of oxide has been well documented especially in autoclave studies such as in refs [11], [37]–[39]. It has been observed [40], [41] that at temperatures present in BWR and PWR's ($232° - 316°C$), the initial growth rate approaches a cubic rate although the exact exponent is dependent on cladding grade. Many authors have discussed the origin of this cubic rate and the deviation from parabolic growth seen in other metals, for example [39], [40], [42], [43]. It has been proposed that parabolic kinetics would only apply if grain boundary area per unit volume of oxide remained constant independent of oxide thickness. However it has been observed [39] that this is not the case. Due to the columnar growth of oxide grains in the direction of oxide growth compared to oxide film thickness, the grain boundary per unit area decreases, with increasing thickness. The resistance to mass flow is proportional to film thickness and therefore the cubic kinetics can be easily derived by setting the rate of film thickening , $\frac{dx}{dt}$, to be inversely proportional to the integrated resistance to mass transport (where x, the film thickness, is the resistance to mass transport). Thus the rate of film thickening is proposed to be [26]

$$\frac{\mathrm{dx}}{\mathrm{dt}} = \frac{\mathrm{k}}{\mathrm{x}^2} \qquad \textit{Equation 2-5}$$

And therefore:

$$\mathrm{x}^3 = \mathrm{Kt} \qquad \textit{Equation 2-6}$$

Giving cubic behaviour.

The actual relationship is more complex than described in the equation as there are many other factors involved, but it helps to show the origin of oxide growth for Zr alloys. The equation can therefore be written more generally as:

$$\delta = Kt^n$$

(Where $\delta$ is used to represent oxide thickness instead of $x$ as above).

Experiments undertaken at Pennsylvania State University [37], [44] "carefully measured" the exponent 'n' for various zirconium alloys, including some commercial alloys, in autoclave at 360°C with pure water using the general equation [37]. The results from their studies are shown in Table 2-1 and demonstrate a wide range for the exponent 'n' from well below 0.33 to almost 0.5.

*Table 2-1. Model alloys pre-transition kinetics constants in 360°C water autoclave experiments [37], [44]*

| Alloys group | K | n |
|---|---|---|
| Zr-Fe-Cr | 9.9 | 0.21 |
| Zr-Cr-Fe | 10.9 | 0.19 |
| Zircaloy-4 | 10.2 | 0.22 |
| Zirconium | 7.6 | 0.22 |
| Zr-Sn | 9.5 | 0.29 |
| Zr-Cu | 14.1 | 0.18 |
| Zr-Sn-Nb | 6.5 | 0.41 |
| Zr-Nb | 5.9 | 0.45 |
| ZIRLO | 6.7 | 0.37 |
| Zr-2 5Nb-0.5Cu | 8.4 | 0.31 |

As well as the changing size of oxide grains, and hence the change in grain boundary diffusion with oxide growth, other authors have proposed the following as the cause of sub-parabolic (slower than parabolic) oxide growth. The occurrence of obstacles which could include cracks (depending on orientation), pores and other inclusions leading to the hindering of oxygen ion migration [45], [46]. Compressive stress build-up in growing oxide [31], [47]. The build-up of electrical charges and fields across the oxide [42], [48].

During the pre-transition phase, the oxide is quite dense and protective containing tetragonal zirconia at variable concentrations depending on the alloy. The grain structure is mainly columnar but interspersed with equiaxed grains, although the transformation of columnar grains to equiaxed in the outer parts of the oxide has been reported [49]. There is still much debate about the meaning and effect of more equiaxed or columnar grains. Three examples are given to show how the presence of a mainly equiaxed structure has been reported in more corrosion resistant alloys [50], in faster corroding alloys [51] and also sometimes with no correlation at all [52]. It is clear that no definite conclusion has been agreed upon in the community. The stable phase of zirconia should be monoclinic at reactor temperature but it has been found that the compressive stresses in the oxide layer stabilise the tetragonal phase [36], [53]. These compressive stresses are due to the growth of new oxide and the Pilling-Bedworth parameter [54] (for this material approximately 1.56), and have been observed to be in the range of 200-500 MPa [55].

### 2.3.3  Post-transition oxide growth, kinetics and structure

After pre-transition growth, different alloys exhibit different post-transition growths. Figure 2-4, from ref [11] is a schematic representation which shows the kinetics of three groups of zirconium alloys: pure zirconium, alloys with one 'breakaway' transition, and alloys with oxides which show re-passivation and exhibit cyclic behaviour such as Zircaloy-4 and ZIRLO. For zirconium alloys, as the oxide grows the resistance to oxidation increases as the resistance is the oxide film thickness (section 2.3.2) therefore the oxide formed acts as a barrier (although imperfect) to further oxidation until transition (or breaking of the oxide) where rapid corrosion takes off. For some alloys, especially modern commercial alloys, a new layer of oxide forms after one transition and acts again as a barrier, temporarily slowing down further oxide growth. As a result, the alloy undergoes cyclic oxidation.
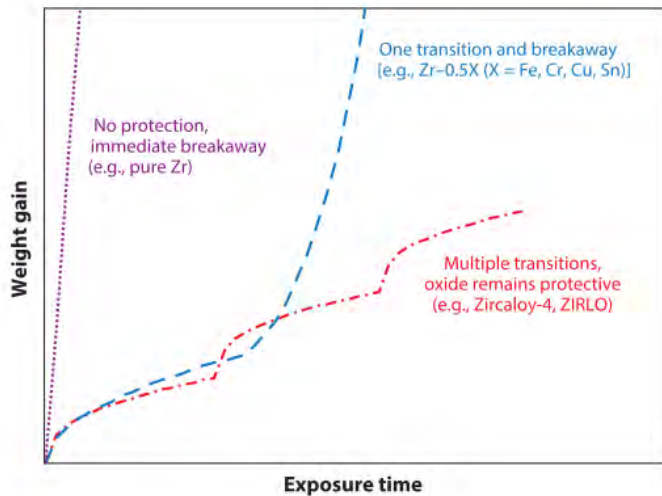
*Figure 2-4. Schematic representation of corrosion and transition in three groups of zirconium alloys pure zirconium, alloys with one 'breakaway' transition and alloys with oxides that show re-passivation and exhibit cyclic behaviour [11].*

Many hypotheses exist concerning the occurrence of a transition and it has been the subject of many studies [6], [46], [56]–[59]. Much debate still exists about the exact mechanism causing transition and what gives rise to the differing behaviour in different alloys. However, it has become clear that the transition is directly related to the breakdown of the protective dense oxide that exists close to the metal-oxide interface. Some mechanisms exist whereby 'short circuits' are present allowing the easy and quick penetration of oxidising species to the metal-oxide interface. The most common is the development of cracks or interconnected porosity thus causing the oxide to no longer be protective. Cracking and porosity could arise from multiple sources, of which the main causes are discussed in section 2.4.4. Periodic transitions have also been seen by analysis of the fossil oxide. Yilmazbayhan et al. [44] studied a sample of Zircaloy-4 oxidised in an autoclave at 360 ◦C for 784 days meaning the sample would have gone through many transitions. Ordered cracks were visible when imaged through a transmitted light microscope, or SEM (which can be seen in Figure 2-5), suggesting that large cracks and transition are strongly linked. Recent work [60], [61] showed how transition is not an instantaneous event but rather the corrosion rate varies and "up to 50% of subsequent cycles consist of the transitory period (i.e. period between minima and maxima)" [60]. Additionally, there is some argument that the time (and therefore distance) between transitions decreases and the distance of protective oxide reformed in the repassivation step decreases with more and more transitions, this has been particularly noted in the presence of hydrides [62], [63].
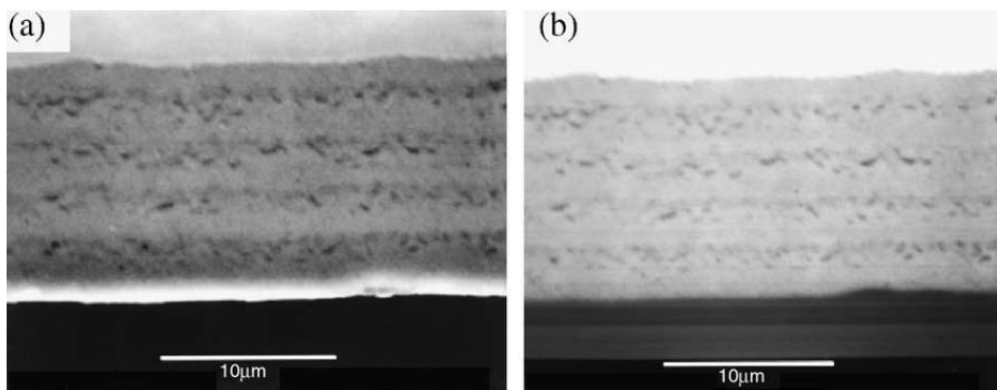
*Figure 2-5. (a) Secondary and (b) backscattered scanning electron images of oxide formed on Zr–2.5%Nb alloy exposed to 360 °C water for 784 days. [44]*

The idea of cyclical oxidation kinetics is well supported but the vast majority of these results come from autoclave studies. Due to the difficulty (and expense) of removing material from a reactor core, cladding, which has been corroded in reactor, is much more difficult to study. For the oxidation data the number of points and frequency between them is therefore much less than autoclave. For example, material from reactor is normally removed on a yearly time frame to coincide with the yearly cycle of reactor (e.g. 11 months service in Switzerland and one month maintenance/refuelling and reshuffling). Therefore, the corrosion profile vs time will have points every year compared to autoclave where result can be gathered when wished, even daily. Thus, there is still much debate into the exact corrosion kinetics of cladding inside reactor, especially in between the points of measuring since from autoclave studies transitions are expected to last less than one year. Therefore, it must be kept in mind throughout this thesis that the materials studied are from reactors and the examinations performed are ex-situ and 'snapshots' taken at a point in the life of the cladding. Whereas in reality the material, particularly at the metal-oxide interface, is continually changing. This means that observing a phenomenon, for example in a 9 cycle sample, may be true but it cannot be deduced that this is the state of the material all the time while it is in its 9th cycle. One possibility to verify the phenomenon of cyclic corrosion from in-reactor materials would be to examine the fossil oxide after a certain amount of time in reactor. Such obvious periodicity is difficult to routinely see from the fossil oxide of material corroded in reactor. However, Bossis et al do report seeing periodicity in cracks in fossil oxide of Zircaloy-4 and also that the distance (and therefore time) between them decreased [62].

## 2.4 The microstructure of Zr materials oxidised in reactor

In the scope of this PhD predominantly materials from reactor were studied with already grown oxide layers, which would be expected to have gone through transitions. Since it is currently impossible to directly observe and study these materials in the core during operation, the oxide formed in reactor is studied out of situ after the removal of the material from the core. From the materials studied even those with the thinnest oxides (average size 4.4µm) are expected to have gone through transition and the higher burn-up samples through multiple transitions and re-passivations. Some characterisation has already taken place on the reactor samples used for this PhD and thus there is already an understanding of the microstructure, with particular interest in the vicinity of the metal-oxide interface since this is where subsequent oxidation and HUP occurs.

### 2.4.1 Zircaloy-2 LK3/L morphology and structure

The PhD thesis of Adrienn Baris [64] focused a great deal on the characterisation and evolution of the Zircaloy-2 LK3/L series after different residence times in reactor (BWR for this material). Figure 2-6 shows SEM images of the metal-oxide interface for the 3,6,9 cycle Zircaloy-2 LK3/L series (from ref [64]). Since these materials were the same cladding grade, in the same reactor at similar elevations it could be well compared the change in material with residence time. On these samples the main microstructural changes observed were as followed;

- A highly irregular and undulated interface was seen on the 3 cycle material compared to the other samples.
- The 3 cycle oxide appeared much more crack free than the other samples. (the amount of porosity for these materials was also quantified using 3D FIB reconstruction. It was found the volume fraction of cracks in the oxide close to the metal oxide interface after 3 years was 0.19%, 2.3% after 6 years and 4.9% after 9 years. This will be further discussed in the Section 2.4.4)
- The amount of hydrides in the metal at the interface increased for these samples with residence time. (This was also quantified in the metal close to the interface and found to be approximately 1%, 21.1% and 26.3% for the 3,6 and 9 cycle material. Again this will be discussed further in section 2.4.4)
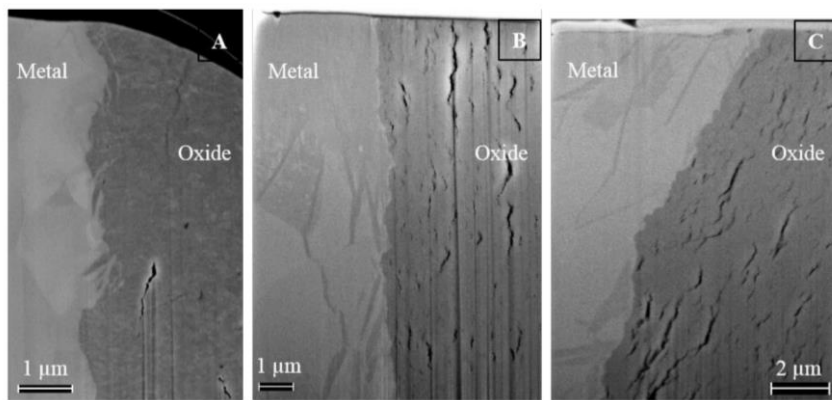
*Figure 2-6. SE images of the metal-oxide interface of the 3 cycle (A), 6 cycle (B) and the 9 cycle (C) LK3/L cladding segments. [64]*

In the same work, as well as in other publications such as from Abolhassani et al. [65] the chemical aspects such as the distribution of alloying elements and state of SPPs was examined. It was observed that in the metal the SPP number and size decreases as a function of residence time. After 9 cycles the SPPs in the metal have dissolved to a great extent, however some remnants containing Cr still existed. Therefore the bulk metal matrix is enriched with alloying elements. It was also found that hydrides in the metal repelled alloying elements particularly Fe and Ni.

The crystal structure of the 9 cycle claddings oxide has been object of a study in the laboratory [66] by synchrotron radiation. The major oxide phase observed has been reported to be monoclinic $ZrO_2$ and a very small ratio of tetragonal has been revealed by Micro-XAS analysis. This small phase has been mainly observed in the vicinity of the interface, however, not on a uniform and homogeneous distribution all along the interface. The results obtained in the laboratory for 3 cycle cladding show similar behaviour but with a slightly higher volume fraction of tetragonal (the exact ratio of tetragonal to monoclinic was not calculated due to its small quantity). These observations lead to the conclusion that the two oxide layers studied (the 3 and 9 cycle) near the interface have mainly a monoclinic crystal structure, however a slightly higher proportion of tetragonal is present in the low burnup oxide.

## 2.4.2  4 cycle low-tin Zircaloy-4 morphology and structure

The low-tin Zircaloy-4 material after 4 cycles in a PWR was also characterised structurally and chemically in the thesis of A. Baris [64], as well as in other publications for example [33], [67]. Figure 2-7 shows SEM images of the metal-oxide interface and the outer oxide. It was seen that compared to the oxide formed in early oxidation (i.e. the outermost 2-3µm) the crack volume fraction of the newest

formed oxide increased drastically from 0.004% volume to 4.25%. The oxide grains in this material were shown to have two types of morphology [67]; columnar and equiaxed. The columnar grains can be as long as 500 nm and have an average width of 30 nm. The columnar oxides were mostly free from cracks and usually parallel to the direction of the oxide growth. Mostly they were found to have a monoclinic structure. The equiaxed oxide grains are dispersed over the whole oxide, and they show cracks in their grain boundaries. The SPPs are seen to be depleted of Fe but still many remnant SPPs were seen containing Cr [64].
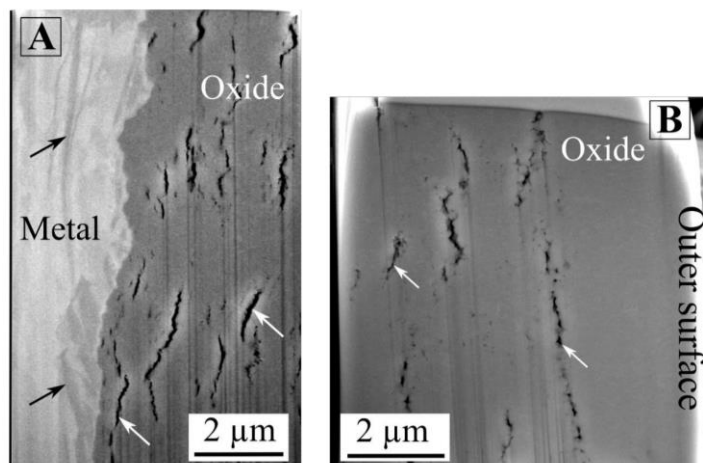


*Figure 2-7. SE images of 4 cycle low-tin Ziracloy-4. A) at the Metal-oxide interface Black arrows mark the hydrides, white arrows indicate the cracks. B) the outer oxide showing the outer 2.5-3µm with few visible small cracks. [64]*

### 2.4.3  3 cycle Zr-2.5%Nb morphology and structure

The Zr-2.5%Nb material after 3 cycles in a PWR was also characterised structurally and chemically in the thesis of A. Baris [64], as well as in other publications for example [33], [67]. Figure 2-8 shows SEM images of this material. Here it can be seen the morphology of this material is quite different to the previous two. In this material large $\beta - Zr$ phases can be seen and persist still after 3 cycles. It had been demonstrated that these large Nb phases can remain structured and metallic 1-2µm into the oxide depending on size and shape [67]. A more undulated interface was also seen particularly with the oxide front ingressing more near to the Nb structures, as can be viewed in Figure 2-8.
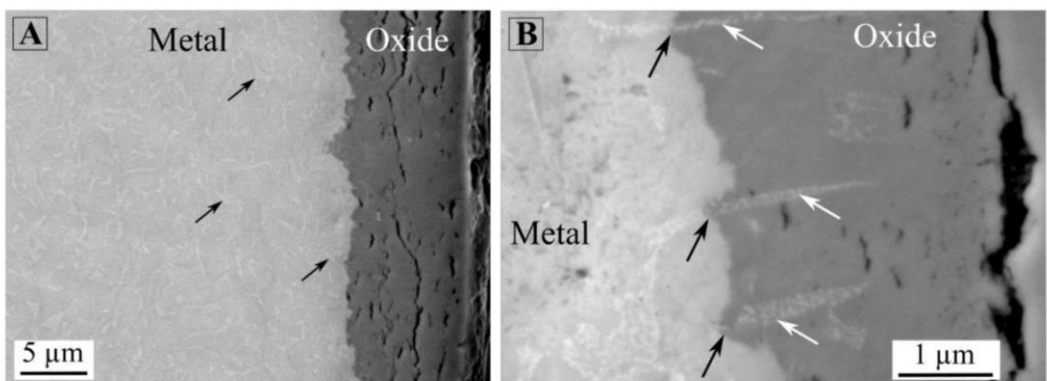
*Figure 2-8. SE images of the 3 cycle Zr-2.5Nb sample. (A): Outermost part of the cladding with the full oxide; (B): metal-oxide interface. White arrows show the Nb phases in the oxide phase. Black arrows indicate a more advanced oxide front in the metal surrounding the Nb phases. [64]*

In this material the oxide at the interface (1µm) had a decreased crack volume fraction, and the areas of less cracked oxide could be correlated to the positions of metallic Nb phases in the oxide. However after a distance of 1µm into the oxide the crack volume fraction was much higher at 3.8%. It was proposed that the more undulated interface results in a better stress distribution in the oxide. Which results in less cracked oxide at the interface. It was also suggested that "metallic Nb-phases in the oxide can improve the mechanical properties of the oxide acting as a composite component which will prevent the material from cracking at the interface. Nb-phases seem to act as obstacles for the propagation of the already formed small cracks." [64]. The increase in cracks away from the metal-oxide interface was suggested to be due to the oxidation of the Nb-phases, and the removal of their protective quality.

## 2.4.4 Porosity in the oxide

With the first transition the microstructure of oxide changes. The presence of interconnected cracks or radial cracks in the oxide layer would allow water molecules to permeate through the oxide layer thus reducing the diffusion distance from the oxide/water boundary to the metal/oxide interface this has been termed 'short circuits' [68]. These cracks have been systematically viewed in the oxide but only recently quantified. Baris et al. (2017) [64], [69] performed 3D reconstruction of LK3/L Zircaloy-2 oxide formed after 3 years, 6 years and 9 years in reactor. This was undertaken, due to the fact that it was previously shown LK3/L Zircaloy-2 cladding had a much higher oxidation and hydrogen uptake rate after 9 years compared to after 3 [8]. It was found the volume fraction of cracks in the oxide close to the metal oxide interface after 3 years was 0.19%, 2.3% after 6 years and 4.9% after 9 years. This is a significant increase which is expected to decrease the protectiveness of the oxide as residence time

increases. The 4 cycle low-tin Zircaloy-4 and 3 cycle Zr-2.5%Nb materials from PWR were also measured and all the results are shown graphically in Figure 2-9.
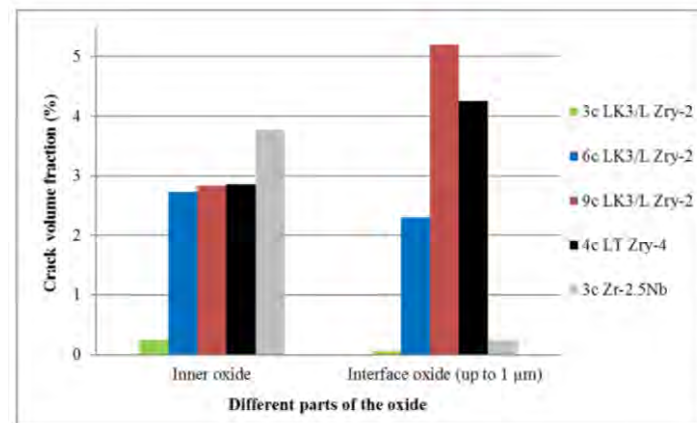


*Figure 2-9. Comparison of the crack volume fraction for different cladding grades and cycles in the inner and the interface oxide. Interface oxide: up to 1 μm from the metal- oxide interface; Inner oxide: the region between 1-3 μm from the metal-oxide interface. Inner oxide on 6 cycle LK3/: 1-2 μm from the metal-oxide interface. [58]*

The mechanism to which most of the large scale cracking is attributed is as follows. Once the thickness of the oxide reaches a critical level (usually in the region of 2-3 $\mu m$ the stress in the outer region of the oxide is no longer sufficient to stabilise the tetragonal phase. As more and more monoclinic phase forms the tetragonal phase can no longer be stabilised and it transforms to monoclinic causing cracking since the tetragonal-to-monoclinic phase transformation has an associated volume increase (3–7%) [70]. It has been claimed that the resultant cracking in the tetragonal region is the beginning of the post transition phase [36].

Other suggested mechanisms for the creation of porosity, as well as the aforementioned transition of tetragonal to monoclinic zirconia, are:

1. The delayed oxidation of secondary phase particles (SPPs), which exist due to the alloying elements added to zirconium metal. And a difference in Pilling-Bedworth ratios of oxidized SPP and zirconia. [16], [71].
2. Since the oxide is growing by anion transport, voids can initiate by coalescence of vacancies generated in the alloy by the Kirkendall effect when rejected solute diffuses away from the oxide/metal interface faster than matrix atoms diffuse towards it. [72]

3. At higher burn ups, once hydrogen has entered the zirconium metal, hydrides precipitate close to the metal oxide interface (see Figure 2-27 which shows hydrides in a zircaloy-2 sample after 9 cycles in reactor precipitated at the metal-oxide interface, as well as an SEM image showing the potential correlation between hydride and crack placement in the vicinity of the interface from ref [73]). The oxidation of these compared to the zirconium alloy metal matrix has been proposed [73]–[75] to also create porosity.

   a. It is proposed that this effect is due to the volume difference between hydride and metal matrix. Since a zirconium hydride would occupy a larger volume than the alpha matrix as the oxidation front would move inwards, if the hydrogen was not incorporated in the newly formed oxide, and both the region that was previously hydride and previously matrix transformed into similar oxide more space would exist in the region that was previously hydride; leading to more porosity (please see reference for calculations) [64].

   b. Other proposed theories how such precipitated hydrides at the interface could induce porosity are; since hydrides are brittle, this would lessen the ability for the metal matrix in the vicinity of the metal-oxide interface to incorporate stress and hence lead to cracking in the oxide [75].

   c. The presence of hydrides at the interface could allow easier incorporation of hydrogen into these hydrides, and hence the cladding, once hydrogen is near the interface leading to larger hydrides at the interface [74]

   d. Depending on the hydride phase, there could be miss match of coherency between the hydride and matrix thus leading to the easier formation of vacancies in the newly formed oxide [74].

A Baris [58] also quantified the volume of hydrides at the interface and correlated it with the crack volume fraction in the oxide at the metal oxide interface. Theoretical calculations showed that the larger volume of the zirconium hydrides (for the FCC $\delta$-hydride) at the interface could contribute to the formation of void space being adjacent to the Zr hydrides. Hence the hydride oxidation will allow for more porosity/cracking in the region of newly formed oxide compared to the metal matrix. Seen in Figure 2-10. A clear correlation was found with increasing hydride volume fraction and increasing crack volume fraction irrespective of alloy type and reactor type (BWR or PWR). It was calculated that approximately up to 50% of the cracks could be due to the presence of hydrides.
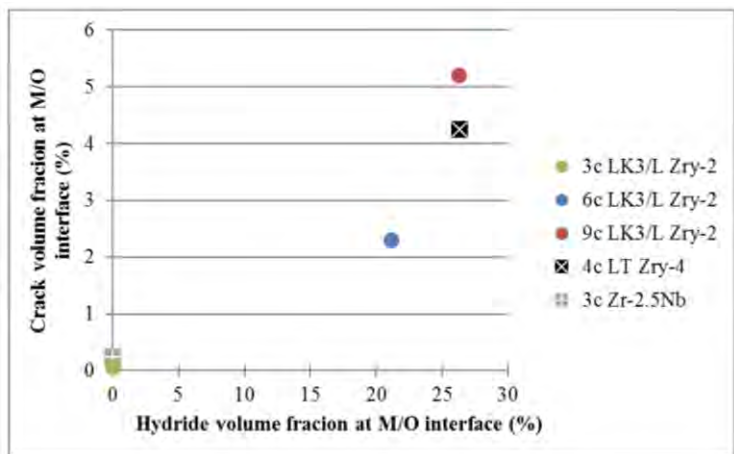
*Figure 2-10. The crack volume fraction in the oxide as a function of the volume fraction of hydrides in the metal for different claddings. Both parameters are taken into account close to, i.e. up to 1 μm from the metal-oxide interface. [58]*

# 2.5 Hydrogen uptake mechanisms

## 2.5.1 Hydrogen pickup fraction

As shown in Equation 1, hydrogen is also a product of the corrosion of zirconium metal in aqueous environments. However, not all the hydrogen produced enters the zirconium matrix and most recombines to form hydrogen gas which is released in the reactor coolant. To clarify, the two scenarios are described. Firstly, hydrogen, formed at the cathodic site (initially the water-oxide interface), recombines with electrons migrated from the anodic site i.e. at the metal-oxide interface, directly at the place of formation of hydrogen ions. Alternatively, the hydrogen can penetrate through the oxide layer eventually reaching the metal-oxide interface (recombining with electrons at the anodic site or directly in the metal) and enter the metal. This process is called hydrogen uptake (HUP). Since not all the hydrogen created will enter the metal cladding, the hydrogen pick up fraction (HPUF) is an important factor and is defined as:

$$HPUF = \frac{Hydrogen\ absorbed\ in\ cladding}{Hydrogen\ produced} \text{ [76].}$$
$\qquad$ *Equation 2-7*

The HPUF is strongly dependent on the alloy composition and the environment (e.g. water, steam, coolant additions in reactor). As an example, Hillner et al. [77] measured the HPUF of Zircaloy-2 in different environments above 330 °C and reported 2-7% HPUF in oxygenated water, 15-24% in degassed water, and 30-52% in hydrogenated water. It was previously thought that the HPUF was a constant throughout the lifetime of a component and depended on the material, but could vary depending on temperature or oxygen in the environment as well as reactor type [78]. This was refuted by Abolhassani et al. (2015) [8] who also demonstrated that in some cases, for example the Zircaoly-2 LK3/L series, "hydrogen pickup fraction gradually increased with the number of cycles in reactor" (see Figure 2-11).
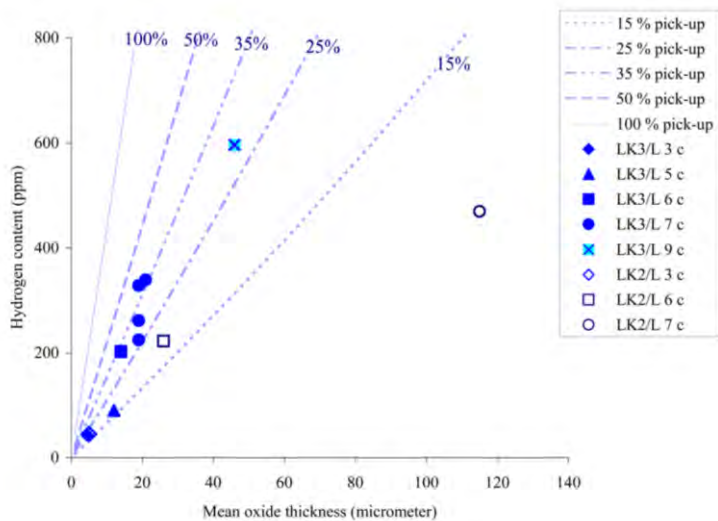
*Figure 2-11. Mean oxide thickness and total H-content of LK3/L and LK2/L type Zircaloy- 2 claddings irradiated in the same reactor. Dashed lines show the HPUF values. From ref [8]*

Other studies in autoclave [79] have shown that the instantaneous pickup fraction, which is the derivative of HPUF with respect to time, increases just before the oxide transition and that the overall pick-up fraction in the second cycle is higher than in the first cycle for repassivating alloy, displayed in Figure 2-12. Harada and Wakamatsu [80] showed that the rates of hydrogen pickup vary a lot during pre-transition as well as during the repeated cycles during post-transition. They found that as the rate of oxidation decreases, the rate of hydrogen uptake increases. This suggests that the hydrogen uptake behaviour is strongly linked with the oxidation.
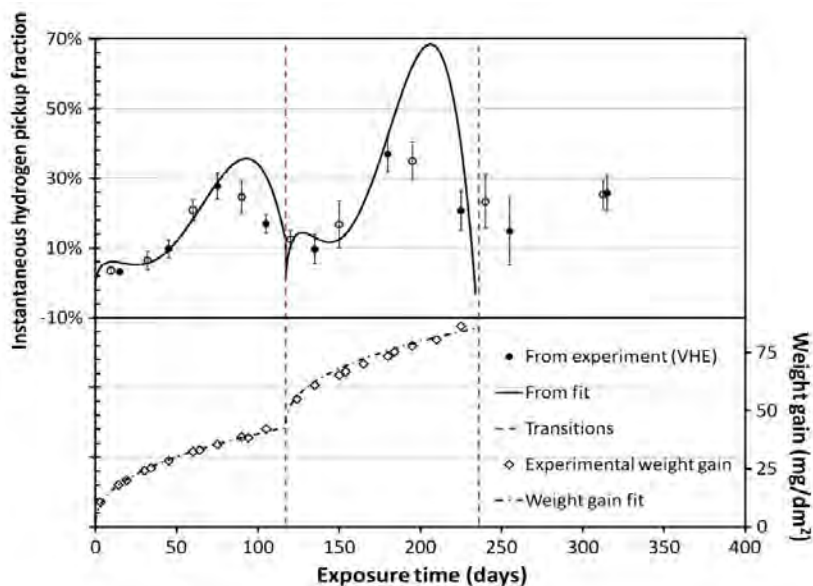


*Figure 2-12. Instantaneous hydrogen pickup fraction and weight gain as a function of exposure time determined experimentally for ZIRLO sheet. The weight gain fit and the instantaneous hydrogen pickup fraction determined from the weight gain and hydrogen content fits are also plotted. [79]*

# 2.6 Hydrogen transport through pre-existing oxide layer

Debate still exists on how hydrogen transports through the oxide to the underlying metal. A list of different mechanisms by which hydrogen can enter the metal is given below. These processes are likely to be competitive, and it is possible that different processes are dominant at different stages of oxidation.

Proposed mechanisms include:

1. Hopping of protons from $OH^-$ to $OH^-$ decorating the pores, or at oxide grain boundaries or cracks [81].

2. Solid-state diffusion of H molecules assisted by oxygen vacancies and dislocations. Implicitly, it is assumed that hydrogen diffuses as H+ [82]–[84].

3. Migration of hydrogen atoms via nanopores in the oxide film [68], [85].

4. Transport of hydrogen through or aided by SPPs [46], [86]–[88].

5. Another mechanism has recently been proposed on zirconia, claiming the hopping of protons on a hydrated surface $H_3O$ (although this has only been observed in the presence of water molecules) [89].

These proposed mechanisms can be classified in three categories.

## 2.6.1 Diffusion of hydrogen as a positive ion

The first two mechanisms assume that hydrogen migrates in the oxide layer as positively charged ions. In reality, it is expected that hydrogen ingress through the oxide is facilitated by more than one single mechanism and that both the first two mechanisms would be required as a way for positively charged $H^+$ to travel through the so called 'dense/protective' oxide. These are also expected to be the predominant mechanism in early stages of corrosion before transition. Ramasubramanian et al [90] proposed a model for hydrogen ingress through the oxide. By using the technique of isotope incorporation and exchange experiments the following method was proposed: hydrogen would transport through the bulk oxide through "hydrated pathways" on the surfaces of the oxide crystallites. Such "hydrated pathways" have been found in Zr-2.5Nb alloys, on the surfaces of oxide crystallites. They were found in the form of hydrogen isotopes as hydroxyls and hydrogen-bonded water, both out of reactor and in reactor. Other studies have also subsequently viewed hydrogen (or

often deuterium for doped experiments) along oxide grain boundaries in the form of hydroxides and deuterium oxides [91]–[93].

## 2.6.2  Migration of hydrogen atoms via pores in the oxide film

To expand on the third mechanism listed, porosity in the oxide layer can be separated into two different categories (and many sub-categories) contributing to two different mechanisms. It is important to illustrate this by returning to the idea of a post-transition oxide having a heavily cracked and porous outer layer as well as a denser inner layer close to the metal oxide interface. The first category of porosity consists of the large-scale cracks; when interlinked in the outer oxide, this could include large cracks in the radial direction. This, as previously discussed, would allow the penetration of liquid/coolant into the oxide layer and thus reduce the distance for oxidising and hydriding species to travel to the underlying metal. The second category of porosity consists of that which is contained within the protective inner layer and would usually be on the nano scale and not interlinked. Jing Hu et al [85] extensively studied the nanoporosity close to the metal-oxide interface for three different alloys using Fresnel imaging with TEM. They saw in each alloy, even very close to the metal-oxide interface, the existence of nanoporosity. Approximately a few hundred nanometres further away, more porosity could be seen in the form of interconnected 'nano-pipes' rather than isolated pores. They proposed the following mechanism: water can penetrate through the outer oxide by cracks to the inner oxide where numerous oxygen vacancies would be present. Water molecules could react with vacancies exothermically with the disassociation of H atoms to form molecular hydrogen. Either the $H_2$ molecules are relased at the oxide/water interface into the water, or they diffuse via 'nano-pipes' through the inner oxide until reaching near the metal/oxide interface. The $H_2$ molecules are proposed to dissociate naturally on the meta-stable oxide phase ZrO, if such phases were present. The H atoms that would form enter into the sub-oxide, and further diffuse through the distance of oxygen saturated Zr metalinto the underlying metal, eventually forming thermodynamically stable zirconium hydrides which in turn may that operate as sinks for other hydrogen atoms. A schematic diagram of the oxide according to this theory is shown in Figure 2-13. It is proposed diatomic molecular hydrogen can diffuse down channels even as small as 0.5nm in diameter. Since hydrogen is much smaller than oxygen, it has been suggested that the nanoscale porosity in the barrier layer has a greater effect on the hydrogen uptake than oxidation and that hydrogen ions could recombine at pores helping to stabilise them. The protectiveness of the inner oxide here would depend on the amount of interconnected nanoporosity. If present, the sub-oxide will facilitate hydrogen absorption into the bulk barrier layer by accumulating hydrogen on its surface (which would be a highly exothermic step

-111KJ/mol for ZrO and -50-70KJ/mol for Zr metal). It must be noted that such a "suboxide" ZrO is not seen in every material but has been seen more commonly in autoclaved materials [94]–[100] with only one publication on its presence in a neutron irradiated ZIRLO sample [101].This could be due to the faster corrosion rate in reactor compared to autoclave. The theory may therefore need some adjustments for when this phase is not present, but the idea of diatomic hydrogen diffusing through interconnected 'nanopipes' would remain valid.
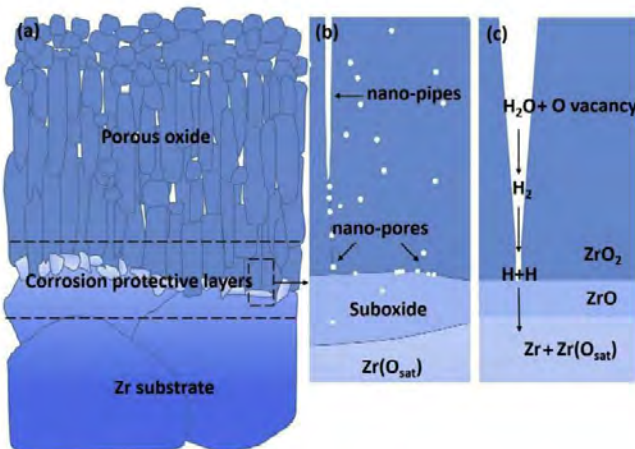


*Figure 2-13. Nano-pores and nano-pipes distribution in ZrO2 corrosion films. (a) Schematic of the size and distribution of nano-pores and nano-pipes in the oxide layer. Panels (b) and (c) show magnified cartoons of nano-pores and nano-pipes in the protective oxide near the metal-oxide interface. The change in colour in the metallic substrate reflects the oxygen content measured in previous work from the group. The panel on the right-hand side shows the proposed mechanism for H uptake. [85]*

Hatano et al. [86] used SIMS to study hydrogen distribution through the oxide layer. They concluded that "the rate of hydrogen uptake is controlled by the transport process through the oxide film" and that a gradient of hydrogen (actually deuterium) was seen from the outer surface to the metal-oxide interface. Using high resolution 3D NanoSIMS, Li et al. [102] examined how deuterium was distributed in the oxide of Zircaloy-4 oxidised in 360 °C 18 MPa pure heavy water for different lengths of time. It was also observed that a high concentration of deuterium can be seen in the outer oxide. Furthermore, a gradual decrease in the deuterium concentration from the outer to the inner oxide. In the oxide near the metal-oxide interface, deuterium was seen to be trapped in 'small cracks and pores' which is evidence that these defects act as routes for hydrogen to ingress into the metal (Figure 2-14).
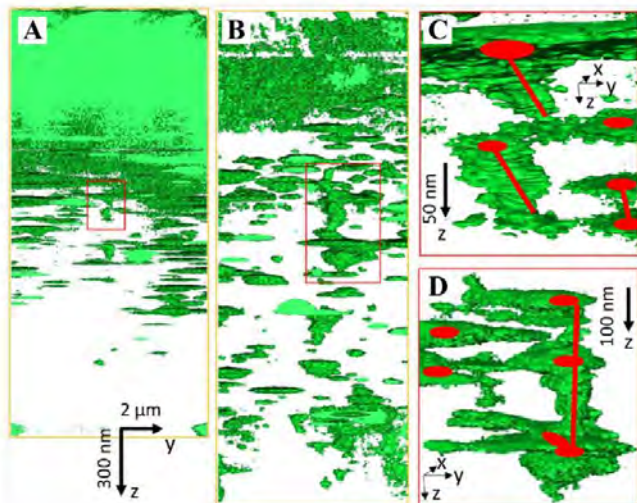
*Figure 2-14. 3D distribution of deuterium in oxidized Zircaloy-4 by NanoSIMS by Li et al. [102]. (A) and (B): samples oxidized for 61 days (pre-transition stage) and 106 days (around the oxidation transition), respectively. (C) and (D): magnified images of the red frames on (A) and (B). The green volume is the measured data while the red dots on (C) and (D) are suggestion of the real distribution estimated by the authors and the red lines are the possible paths for deuterium transport [102].*

### 2.6.3 Transport of hydrogen through or aided by SPPs

Extensive studies have been conducted on the role of SPPs on HUP. In the coming chapters, the role of each alloying element will be discussed in detail. Here, a brief explanation of the mechanism of how alloying elements and SPPs specifically affect hydrogen uptake is provided. It is claimed that SPPs which remain metallic in the barrier oxide layer act as local fast routes for H diffusion increasing the HPU [46], [86]–[88]. In their review, Motta et al. stated that "the effects of precipitate size and volume fraction are not well understood" [11], however it has been found that for a given precipitate volume fraction, a larger number of finer precipitates increase hydrogen pick-up fraction, possibly because more cathodic sites are available [34]. Although the results show correlation between the SPPs and the HUP, only assumptions exist as explanations. Three theories have been put forward to explain this phenomenon. Firstly, SPPs could take in and accommodate higher amounts of hydrogen compared to the matrix [86]. Secondly, it is possible that hydrogen can also have a higher diffusivity through the SPPs [86], [88]. Thirdly, metallic SPPs were considered to be the sites of proton discharge and the produced $H^+$ could then enter the metal [88]. In reactor, the alloying elements will redistribute due to irradiation induced dissolution throughout the component lifetime and thus have varying effects on the hydrogen uptake. This will be discussed in later sections.

# 2.7 Factors affecting hydrogen uptake

The aim of this thesis is to better understand the mechanism behind hydrogen uptake into zirconium-based fuel claddings in reactor, *in particular to help understand the causes for variation in hydrogen uptake throughout component lifetime, with emphasis on those alloys which show increased hydrogen uptake.* To do this, in the following section all the factors which can play a role on the hydrogen uptake are listed from the broadest factors down to the more specific ones. Research into this topic has spanned many years using a variety of techniques to answer many questions, therefore not all factors will be the subject of this work. The factors which were studied over the course of this thesis will be discussed in greater detail compared to the others. Additionally, due to the complexity of the problem and the many factors involved, there may be some overlap between the subdivided groups. The number of factors playing a role and their interconnectedness certainly has been the cause of much confusion and difficulties over the years. This list is an attempt to add some clarity to the problem. Although the following paragraphs are a thought experiment and compiled by personal reflection, the factors in the list are based on previous work either from the scientific community on the subject or from the project running at PSI. Hence, it is included here in the literature review as a compilation of factors which could affect hydrogen uptake in zirconium-based claddings. References are given as examples of different groups who have performed work on that topic.

## 2.7.1  Broad factors affecting hydrogen uptake

Starting from the most basic of reasoning, three parameters can be thought of that may affect initial hydrogen uptake into fuel cladding (this is assuming we have a system similar to that in LWRs, where nuclear fuel, contained in cladding, is in a core with light water as coolant):

1. Cladding material and structure
2. Fuel form and therefore clad form
3. Water chemistry and temperature

Since this work is focused on understanding a mechanism for pre-existing fuel claddings leading to their improvement rather than developing new claddings or fuel for new reactors, point two and three must be kept in mind but are not greatly touched upon in this thesis. The focus then is on the first

point. If the claddings are of a predefined size and shape and assumed to be zirconium based claddings (of one material rather than duplex etc.), that surprisingly leads to four variables only:

1. Which alloying elements are included and their quantities;
2. The microstructure of the material – including how the chosen alloying element are distributed (i.e. the effect of processing and heat treatment);
3. The fuel burnup / length of time in reactor;
4. And power history.

While four factors may not seem many, the problem arises that these 4 factors are extremely interlinked with points one and two mentioned above, having an almost infinite number of combinations. This is why such a large range of zirconium alloys (as described in section 2.1) exists, and these only cover a small range of the possible alloying element additions and processing routes.

## 2.7.2   Specific factors affecting hydrogen uptake

In previous sections the general mechanisms for the oxidation and hydrogen transport into the metal for zirconium based alloys used as claddings is discussed. Oxidation will occur and it is therefore the state and evolution of the grown oxide that will influence how easily hydriding species can ingress to the underlying cladding. To help understand HUP as residence time increases a specific list of all the variables that could affect H uptake follows:

1. Size of dense oxide, distance which is impermeable to coolant i.e. diffusion distance [64], [103]
2. Amount of defects in dense oxide and its structure [59], [64], [68], [104]
3. Amount of porosity once no longer dense [59], [64], [68], [104]
4. Grain size and orientation of underlying metal [105] ,[106], [107]
5. Electronic conductivity of oxide [48], [61], [108], [109]
6. Ability to withstand stress (either strength of oxide or ability of metal to incorporate stress) [31]
7. Shape of interface [64], [67]
8. Distribution of alloying elements and types [16], [26], [33], [71], [73], [92], [110]–[114]
9. Distribution of hydrogen already present, either in metal or oxide [64], [74], [75], [115]

Obviously not all of these topics can be covered in one PhD, therefore a particular interest was given to those which have the potential to make the most difference at higher burnups. A more thorough

literature review is conducted on the points which are a topic of study in this thesis. These are mainly points 5,6,8 and 9, however other points particularly 1 will require discussion.

## 2.7.3 Porosity and defects

The first three points taken from the above list are linked to porosity and similar defects in the oxide. Since the topic of porosity has already been much discussed, with its origin in section 2.4.4 and effect in section 2.6.2, only a small summary for each point is given:

1. As the oxide grows in the early pre-transition regime it is expected to be dense and crack free meaning any oxidising or hydriding species must travel from the water-oxide outer interface to the metal-oxide interface via diffusion. After a certain amount of oxide growth cracks will appear in the outer oxide allowing coolant to penetrate through the oxide. This is termed transition and is not an instant phenomenon but rather happens over some time with the dense inner oxide being reduced in size and hence speeding up the oxidation rate. The oxide will then repassivate as it grows and a new dense protective region increases in size. Most modern alloys are expected to exhibit cyclic growth with multiple transitions. There is some evidence that the time between transitions will decrease such that, at later life, this dense protective oxide will be thinner before transitioning.

2. In the dense barrier oxide, defects such as nano porosity or vacancies can also exist. While these are not large, or maybe not interconnected, they can be enough to permit coolant to penetrate through. The density of these will dictate the speed at which species can diffuse through the layer. The structure of this layer will also play a role since different alloys will exhibit different ratios of tetragonal and monoclinic oxide as well as grain size and shape.

3. Once the oxide is no longer dense and has coolant penetrating it, the amount or density of cracks may dictate the extent to which coolant enters the oxide. Although it is assumed that once a certain level of cracking is reached, coolant is penetrating the outer oxide with ease. This may mean even a heavily cracked outer layer still provides some protection depending on the extent of cracking [64]. A second effect suggested is that when a porous non-protective oxide layer is present on the top of the growing protective oxide, the hydrogen evolved at the cathodic site (now somewhere inside the oxide) has to diffuse through the non-protective layers in order to reach the water. Resulting in a hydrogen over pressure which will be established at the cathodic site because of the hydrogen gradient across the non-protective oxide layers [61].

### 2.7.4 Grain size and orientation of underlying metal

4. Since the metal grain size and texture is not expected to change greatly during component lifetime, this is one of the points not studied in this work. Zirconium based claddings are deliberately produced with crystallographic texture, with the c-axis of the HCP lattice parallel to the radial axis of the tube as shown in Figure 2-15 [105]. This is done to enhance the mechanical properties of the clad, particularly to minimise radiation induced creep. The oxide also will grow with a specific texture but this has been shown to depend on the stress accumulation from oxide growth rather than the underlying metal texture [106]. The same study also concluded that for the alloys Zircaloy-4 and low-tin ZIRLO, "substrate orientation does not significantly affect corrosion performance and H pickup in single phase zirconium alloys". However, other studies have reported different effects, demonstrating that the underlying crystallography influences the rate and crystal orientation of the oxide formed [107]. For example, when using EBSD over a larger area than that of one TEM foil, encompassing multiple zirconium metal grains, it was seen that substrate texture has a significant impact on local corrosion behaviour. Lattice matching between the metal grains and the oxide showed a faster local corrosion.
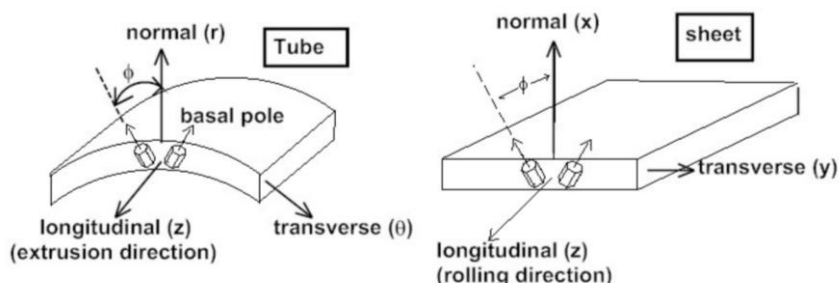


*Figure 2-15. Schematic diagram of the texture found commonly in Zirconium based fuel claddings with the normal to the basal plane pointing in the radial direction compared with the tube. [105]*

### 2.7.5 Electronic conductivity of oxide

5. From the current understanding of the corrosion process, electron transport and proton transport are partly interrelated processes. Either negatively charged electrons must migrate outwards through the oxide to reduce positive $H^+$ ions at the oxide-water interface; or $H^+$ ions

must ingress through the oxide to capture the electrons. The latter is unfavourable as the hydrogen, being very close to the metallic site, can cause a rapid ingress of hydrogen into the underlying metal and increase the hydrogen uptake. The addition of their currents results in the total cathodic current (i.e. electron current). Adrien Couet concluded in his PhD thesis that the driving force for HUP is the electrochemical potential gradient across the oxide layer. This potential gradient is mainly influenced by the electrical conductivity of the oxide meaning that if the conductivity of the oxide layer is low, a higher potential would build up [108]. Thus resulting in a higher HPUF. A schematic diagram from ref [108] is included to illustrate (Figure 2-16).
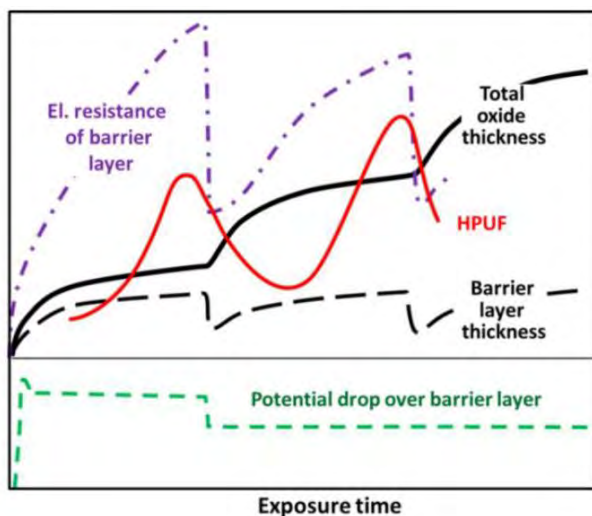


*Figure 2-16. Schematic of the variation of HPUF, resistance of the barrier layer total oxide thickness and barrier layer thickness in relation to exposure time of a sample in autoclave [108]*

Pure zirconia is an insulator with a wide band gap (5.2 eV) meaning it is difficult for electrons to transport across the oxide without additional energy levels (acceptor and/or donor) which can be introduced by impurities or dopants. It has been shown that sub-stoichiometric zirconium oxide has a higher conductivity than stoichiometric oxides [116]–[118]. $ZrO_{2-x}$ would act as an n-type semiconductor, in this manner fully ionised vacancies will act as electron donors and hence more electrons as charge carriers will increase the electronic conductivity of the material [116]–[118]. Previous attempts have been made to quantify the resistivity of the oxide by Electrochemical Impedance Spectroscopy (EIS) [61], [109], [119]–[124]. These works have given great insight into the conductivity/resistivity of the oxide. It has been shown that alloys with better electronic conductivity of the oxide display a lower HPUF. This difference can particularly be seen between Zr alloys containing Sn, like Zircaloy-4, and Zr-Nb alloys [61] and it is attributed to a lower proton ($H^+$) current through the oxide. There are some limitations to the EIS technique; firstly since the experiments are mostly performed

in autoclave conditions, there is an absence of irradiation and related in-reactor phenomena. Secondly, since the samples are immersed in electrolyte, it is not possible to have a direct measurement of intrinsic oxide resistivity but instead a bulk average is calculated across the whole sample and the exact thickness of the oxide probed is unknown. This technique has been successfully paired with weight gain measurements [61], [109], [120], [122], which can be correlated to oxide thickness but once again the electrolyte is expected to penetrate into the oxide through open pores and cracks, and hence may not give the intrinsic value for the oxide. Furthermore, the exact penetration distance in the oxide is unknown. There is currently only one known publication attempting to measure the conductivity of an oxide formed in reactor from Forsberg et al. [125]. That paper uses EIS to measure the resistivity of an oxide formed after 256 days in reactor, which can give good insight into the variation between autoclave and reactor in the pre-transition regime. However, samples with a longer residence time were not studied. It was found that oxides formed with irradiation in reactor had a lower resistivity (ranging from 10-50,000 times).

There is still debate about the exact role of certain dopants and impurities, particularly the variety of alloying elements and their distribution in the oxide. Recently, Couet et al. developed the 'coupled current charge compensation model' (C4) [42] to address the effect of an electrochemical potential gradient and the resultant electric field across the oxide, which is caused by the oxygen vacancies and other dopants like alloying elements. It is argued that a general oxidation mechanism of zirconium alloys should account for the existence of an electric field, or space charge, and should fulfil the condition that the cathodic current is equal in magnitude but opposite in charge to the anionic current so that the net current across the oxide is zero. Nb (2+) and Nb (3+) (as well as Fe(2+) and Fe(3+) if the quantity is high enough) have been suggested to compensate for space-charge variation (the build-up of positive charge at a certain place) in the oxide during corrosion [42], which can result in near to parabolic kinetics for corrosion. The removal of aliovalent dopants in the oxide (e.g. Nb 2+ and Nb 3+), either through clustering effects [114], [126], [127] or by increasing the oxidation state to 4+ and 5+, leads to an increase in space-charge which hinders the migration of oxygen vacancy diffusion in the protective oxide layer and results in a sub-parabolic oxidation kinetic [127]. Compensating for the build-up of space charge with aliovalent dopants that increase the electronic conductivity of the protective oxide favours hydrogen recombination near the oxide/water interface, thereby reducing the HPUF.

Recent evidence suggests that there is a correlation between the oxidation exponent and the HPUF. Two Zr-Nb alloys were tested in autoclave and it was found that the faster corroding alloy (closer to parabolic kinetics) had a lower HPUF (8%) compared to the slower corroding alloy (sub-parablic kinetics) which had a HPUF of 12% [128]. In-reactor data from LK3/L and LK2/L Zircaloy-2 reported similar behaviour i.e. higher HPUF for slower oxidizing alloy [8]. So far, the evolution of the oxide conductivity for the same alloy after different residence times in reactor has not been studied, to our knowledge. In addition, how this property varies with distance across an existing oxide is not possible to measure using the technique of EIS as this will give the resistivity of the oxide, which is not permeated by electrolyte, as a whole.

## 2.7.6 Ability to withstand stress

6. As new oxide is formed, due to the difference in volume between metal and newly formed oxide, the oxide will be under compressive stress and therefore the metal under tensile stress [31]. The ability of the system to withstand stresses will dictate the time and thus thickness before cracking will be caused in the oxide [31]. Therefore, the transition thicknesses may not always be the same and depend on when the stress reaches a critical level in the oxide. The measurement of the stresses in the growing oxide is not easy, however many authors have used different techniques and environments to study the phenomenon [55], [129], [130]. In Zircaloy-4, the stresses in the metal have been measured to not exceed 25MPa, whilst they reach 1.7GPa in the oxide [131]. It has also been seen that there is a decrease of stress at transition [11]. Under irradiation, particularly from neutrons, zirconium alloys have been seen to undergo complex changes in both microstructure and mechanical properties [110], [132]–[136]. One of the major effects is the creation of defects and particularly two different types of dislocation loops. A high number density of small <a> loops (on the prismatic plane {10-10}) are formed rapidly and can be either interstitial or vacancy in nature. The fraction of each is a strong function of irradiation temperature being between 50% and 70% vacancy <a> loops being observed at irradiation temperatures between 350 °C and 400 °C [133]. At approximately 300°C and then lower temperatures, interstial <a> loops become the most common. At higher fluences, there is significant nucleation of vacancy <c> loops (on the basal plane {0001}). Both defect types are expected in reactor. These defects are instrumental in 'irradiation hardening' and they are well known to increase the hardness and hence brittleness of the metal [110], [132]–[136]. Cockeram et al [133] showed that, after the initial irradiation hardening, the yield strength then decreased

for all the Zircaloy-2 and Zircaloy-4 samples tested at higher neutron fluences. This is shown in Figure 2-17 [133].
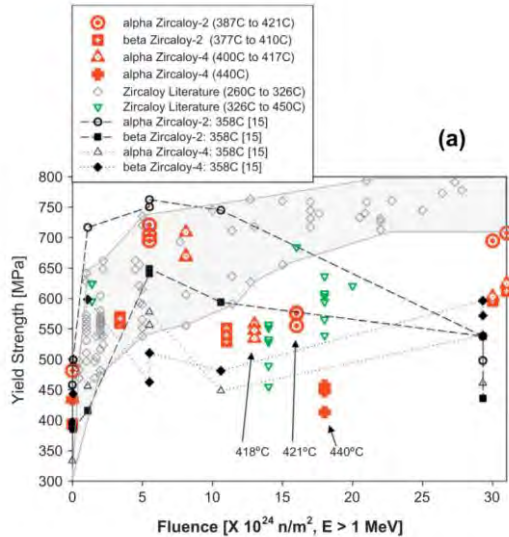


*Figure 2-17. Comparison of post-irradiated tensile data for Zircaloy irradiated nominally in this work at temperatures of 377–440 °C compared with Zircaloy literature results. In this figure yield strength is given [133]*

Colldeweih et al. [137] used micropillar compression tests to examine the metal and oxide on an LK3/L Zircaloy-2 cladding after 3 and 9-cycles in a BWR. It was found that the oxide of the 9-cycle material had a lower yield strength than that of the 3-cycle. This was attributed the higher amount of porosity in the 9-cycle. These results will be shown in Chapter 5 and compared with the results from this PhD also on the same cladding grade.

Hardening of the underlying metal matrix would mean the stresses created by newly forming oxide would struggle to be incorporated and hence lead to earlier cracking in the oxide. The second possible effect is that if an oxide were weaker, for example having more defects caused by irradiation or more porosity, this would also lead to earlier cracking of the oxide.

### 2.7.7   Shape of Interface

7. The shape of interface is potentially not a true factor as it depends on other things such as the rate of corrosion, SPP's or porosity. However, once an interface exists, it will affect subsequent oxide growth. It is briefly included here as it has been shown that all oxides have a metal-oxide interface that is undulated i.e. not a perfect straight plane. Abolhassani et al [67] examined the interface on three different alloys: Ziracloy-4, low-tin Zircaloy-4 and Zr-2.5%Nb, using TEM. It was found that the slower corroding alloy, Zr-2.5%Nb produced a more undulated interface than

the others and had a so called 'jigsaw' shape. A more undulated interface is expected to influence the alloy in two main ways. Firstly, it creates better stress distribution at the interface, leading to a lower crack density in the forming oxide. Secondly, a more undulated interface will increase the surface area at which oxygen can enter the metal. This effect is expected to be outweighed by the first but the exact relationship is still unknown.

### 2.7.8   Distribution of alloying elements and their types

8. Here we come to possibly the most complicated and interwoven point. Much work has been performed on the various alloying element additions, their distribution, SPPs, and the evolution of that distribution under irradiation and oxidation [16], [26], [33], [71], [73], [92], [110]–[114] to name only few. The study of the effect of individual alloying elements can be the subject of whole PhDs, for example for Fe [138]. It is therefore evident that not every aspect of this point can be covered. The main suspected effects on hydrogen uptake of major alloying elements, as well as how this may change with increasing time or burnup follows:
(intermetallics containing multiple alloying elements will also be discussed)

**Tin**

Many different zirconium-tin intermetallics can exist, as is seen from the phase diagram [139] in Figure 2-18. However, tin has an extended solid solubility at low concentrations in the Zr alloys [140]. At reactor temperatures and expected Sn concentrations (i.e. in the ranges for the standard alloys used in reactor: 0.5 to 1.5 wt%), $Zr_4Sn$ would be the expected structure but is very rarely observed (for example see EDS results from ref [64]). Sn was initially added to improve mechanical properties like yield strength and creep [16], but another benefit is that in some zirconium alloys, the oxide produced by corrosion adhered better to the metal surface than for pure zirconium [141].

The presence of tin in the ternary and quaternary alloys is not the same as in binary alloys. In some cases, the absence of tin, for other parameters being the same, Leads to an improved performance, whereas this is not systematically observed, Garner et al [142] studied the effect of the removal of Sn using two alloys: ZIRLO (containing Sn) and Zr–1.0Nb–0.1Fe (removed Sn). They concluded in the case of that alloy that "the removal of Sn leads to a delayed transition in the corrosion kinetics (~200 days) and a reduction in hydrogen pickup." This was attributed to less tetragonal oxide grains being stabilised, meaning larger and better-oriented

monoclinic grains could form. Less tetragonal grains available to transform, when no longer stress stabilised, would mean less cracking induced via this mechanism. Sn was also seen to give a more ordered oxide grain structure [142].
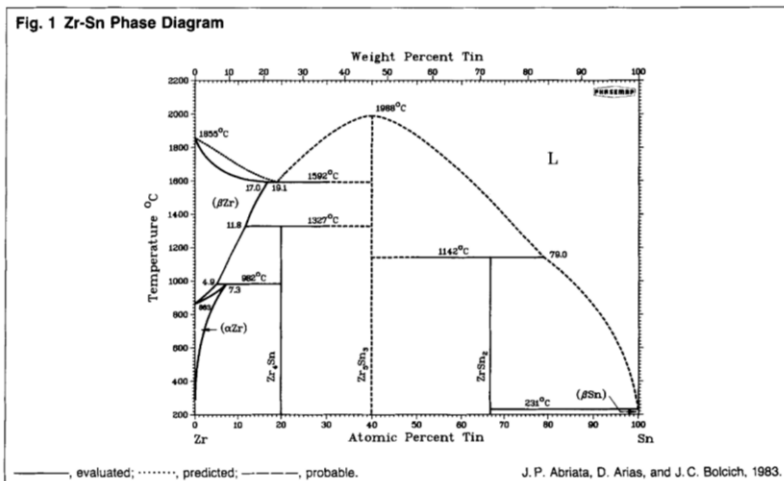


*Figure 2-18. The Zr-Sn phase diagram [141] The solubility limit of tin is higher than Fe and Cr,*

**Niobium**

A great deal of interest in Nb currently exists, and many newer alloys are Nb based alloys. In particular, 1%Nb alloys such as ZIRLO and M5 used for PWRs, have recently received much attention. The niobium solubility in zirconium is relatively low, around 0.5 wt% [143]. Meaning alloys containing 1%Nb are reported to form small precipitates usually $\beta - Nb$, that is 80 wt%Nb [144]. The phase diagram is given in Figure 2-20. However, the solubility of iron, chromium and nickel is even lower, and it is the relatively higher solubility of Nb that could play a role in the superior corrosion and hydrogen resistance seen in Nb-containing zirconium alloys [8], [114], [126]. As explained in the C4 model, oxidised Nb in solid solution (if found with an oxidation state less than 4+) could increase the conductivity of the oxide by increasing oxygen vacancy and electron mobility, which would aid in decreasing the overall hydrogen uptake. Previous studies have shown that Nb precipitates remain predominantly metallic some distance into the oxide layer, i.e. Nb precipitates display delayed oxidation compared to the Zr matrix [16], [67], [112], [145], [146]. Once these SPPs are oxidised, Nb atoms could gain oxidation states of 2+, 3+, 4+ and 5+. It is believed that the oxidation state of Nb atoms has a direct impact on the oxidation and H uptake kinetics of Zr-Nb alloys but the speciation of Nb through the oxide still remains unquantified. Previous studies on Zr-Nb alloys (Zr2.5%Nb, Zr1.0%Nb, Zr0.6%Nb, Zr0.5%Nb) had been undertaken at PSI using XANES [147], [148]. Those studies could not conclude a well-defined oxidation state for Nb (e.g. $Nb^{2+}$, $Nb^{4+}$or $Nb^{5+}$) and

hence a systematic spectroscopic study aiming at characterising the niobium speciation as a function of its position in the oxide layer of irradiated material is still lacking. Furthermore, other researchers have not yet demonstrated an unambiguous distribution of the different states [113], [128], [146], [149]. Within the field of microscopy, Bach et al. [150] used different Nb and Nb oxide standards to show how the Nb L edge could be probed with EELS and shifted depending on its oxidation state, see Figure 2-19. Hu et al [101] used this technique of EELS to investigate the speciation of Nb in a neutron irradiated ZIRLO sample. Again, a delayed oxidation of Nb SPPs was seen followed by a gradual increase in Nb oxidation state with distance into the oxide until reaching a maximum shift of 4.5eV and indicating Nb in a (5+) oxidation state. However, this study did not isolate the different regions matrix and SPP but rather only studied SPPs.
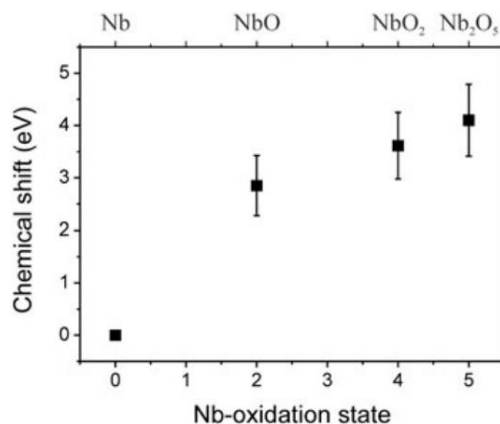


*Figure 2-19. Chemical shift of the Nb-L2,3 edges as a function of the Nb-oxidation state of the reference materials. The position of the Nb-L2,3 edges of Nb was chosen as a reference and subtracted from that of the other materials.*

Recent work [127] has shown evidence that under irradiation the amount of Nb in solid solution decreases by formation of nano precipitates or nano clusters. This reduction of Nb in solid solution is credited for the improvement of ZrNb alloy corrosion resistance, but according to the model should increase the HPUF.

For alloys containing higher Nb concentrations, such as Zr-2.5%Nb, large $\beta - Zr$ precipitates, 20 wt.%Nb form [67]. Debate still exists regarding the role of these large precipitates, of particular interest is the fact they have been observed to remain metallic some distance into the oxide [64], [67]. Baris et al [64] suggested having large metallic precipitates in the ceramic oxide may cause it to act as a composite allowing better accommodation of growth stresses or that they could act as buffers for crack propagation. Another effect, depending on the

processing route, is that these precipitates could form an unbroken metallic connection from the substrate through the oxide. Authors agree that although the exact mechanism is unclear **Nb additions decreases HPUF** (graphically shown in Figure 2-21 from ref [151]).



Figure 1   Zr-Nb Phase Diagram

J. P. Abriata and J. C. Bolcich, 1982.
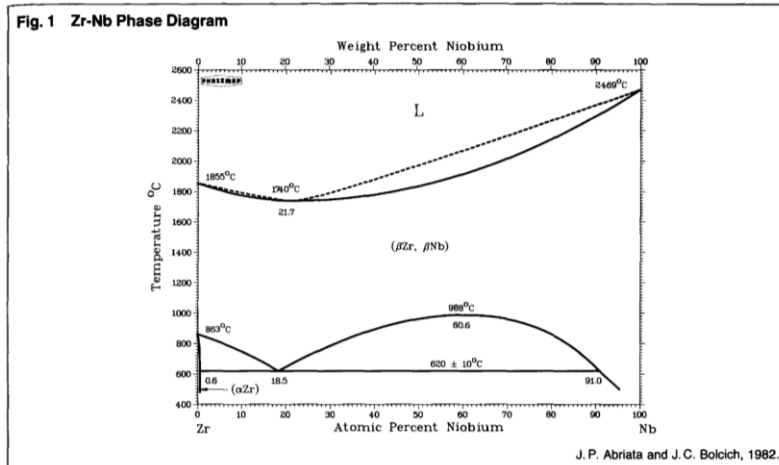
*Figure 2-20. The Zr-Nb phase diagram [144]*
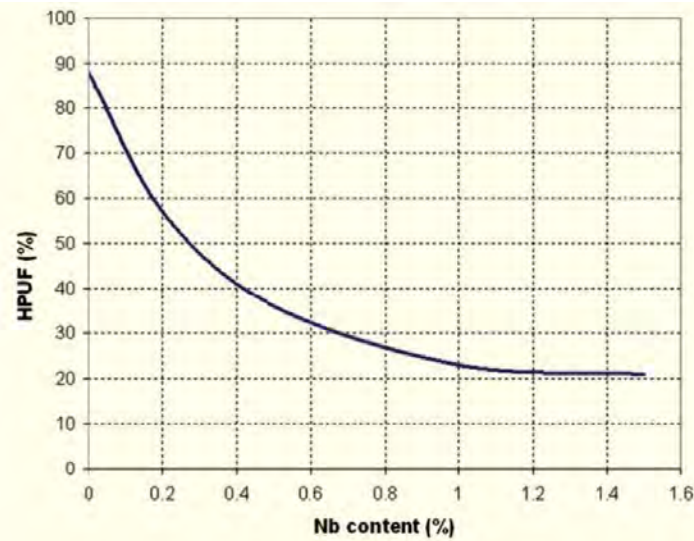


*Figure 2-21. Effect of niobium on the HPUF of zirconium on samples oxidised in water for 750 days [151]*

**Iron**

The Zr-Fe phase diagram can be seen in Figure 2-22 [152]. The solubility limit for Fe in $\alpha - Zr$ is extremely low at approximately 0.03 wt% at 730°C [152]. This means that in Fe containing alloys, Fe is more likely to form precipitates, especially intermetallics. In ternary and

quaternary alloys, Fe will form ternary intermetallics with other alloying elements such as Cr and Ni. Fe is difficult to remove during the manufacture of Zr metal and hence some small level of Fe impurity is always expected to exist in Zirconium alloys[4]. It is believed that Fe could act in a similar way to Nb to increase oxide conductivity, but it is unclear whether enough Fe would be in solid solution to make a significant difference. The heat treatment and the composition of the alloy can influence this point. Modified Zircaloy-2 with approximately double the concentration Fe (the so called hifi) has been shown to roughly half the HPUF [153].
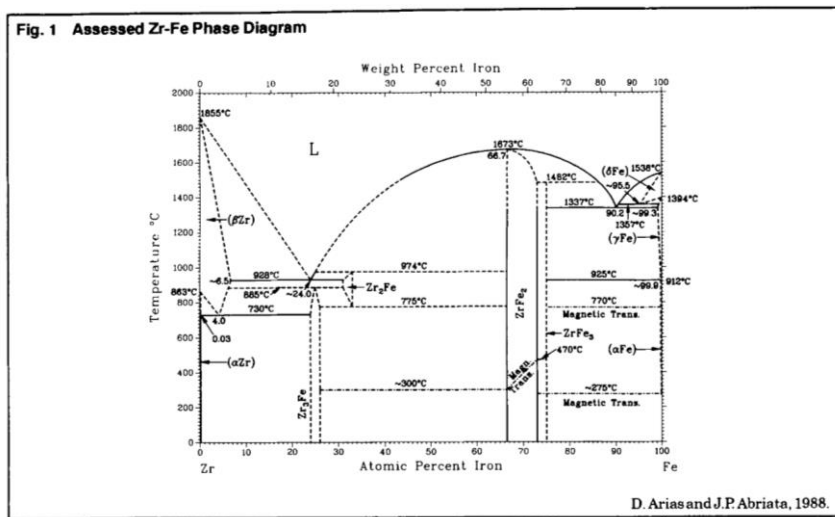


Figure 2-22. The Zr-Fe phase diagram [152]

**Chromium**

From the phase diagram shown in Figure 2-23 [154], in binary alloys (without other alloying elements), it could be expected that Cr would be found as a single phase or binary phase $Cr_2Zr$ at reactor temperature. However, as previously mentioned Cr is more likely to form intermetallics in Zr alloys containing other alloying elements. Cr is added to improve corrosion resistance although the mechanism for this seems to remain partly unknown [155]. It is known however that Cr containing SPPs show a delayed oxidation and that the precipitates dissolve slower than Fe [64], [156], [157]. It is postulated that as Cr containing alloys will still contain SPPs longer into life in the reactor (generally speaking the presence of SPPs reduces corrosion), Cr will improve the corrosion resistance of an alloy[157].
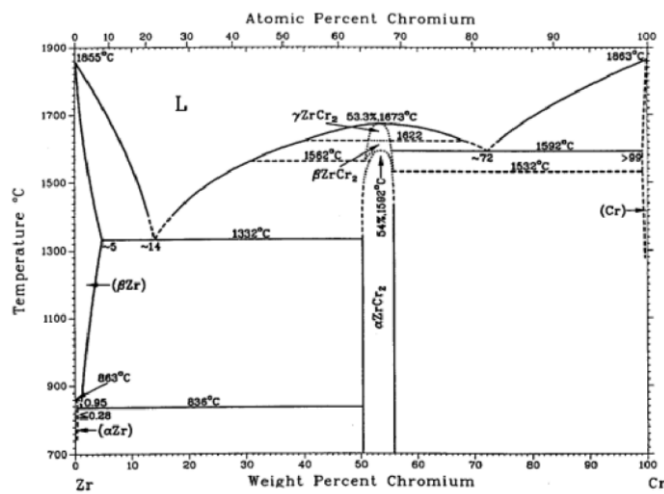
*Figure 2-23. The Zr-Cr phase diagram [154]*


**Nickel**

The phase diagram for Zr-Ni is shown in Figure 2-24 [154] which shows that there are many possible phases of Zr-Ni. However, in a similar way to Cr and Fe, Ni is more likely to form intermetallics in the concentrations found in zirconium fuel rod alloys. Small amounts of Ni have been shown to increases corrosion resistance, but at larger concentrations this affect may no longer hold. There is evidence that Ni can increase the hydrogen pickup fraction of a clad [21], [22]. Hillner argues that he high HPUF in Zircaloy-2 is mainly due to the Ni content. The explanation given is that Ni helps water dissociation and decreases the recombination of hydrogen and oxygen [77].
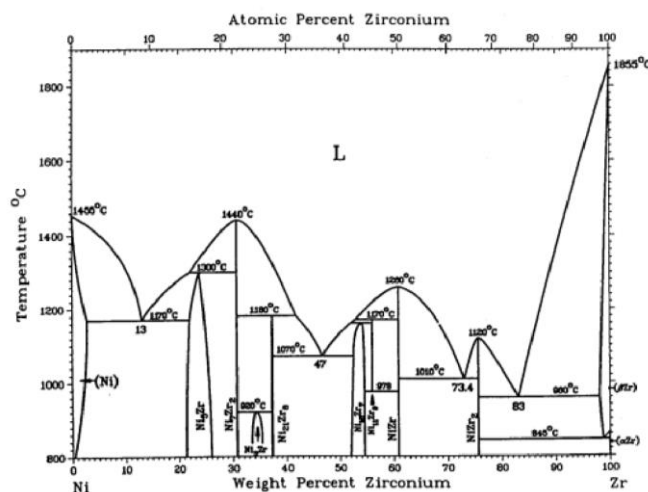


*Figure 2-24. The Zr-Ni phase diagram [154]*

Berry et al. [158] tried to assess the effects of various alloying elements by looking at the hydrogen absorption for various binary alloys. The results and the effect of the different alloying elements can be seen in Figure 2-25.
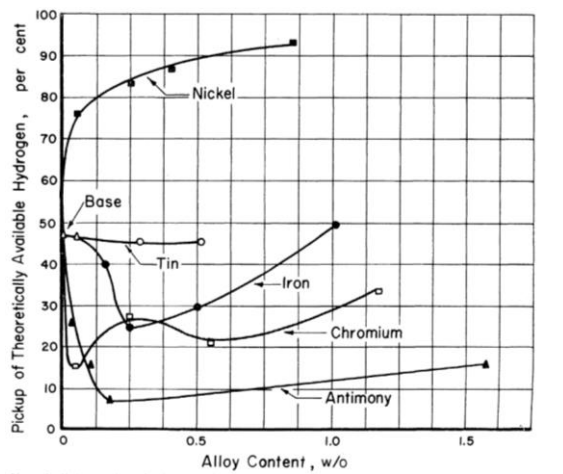


*Figure 2-25. The effect of different alloying elements on the hydrogen pickup fraction, after 575 days at 343 ∘C in water [158]*

**Intermetallics and evolution of alloying elements**

Although each of the main alloying elements is addressed separately in the previous section, it is stated that more commonly intermetallics or SPPs form. Some of the most common examples of these include; $Zr(Fe,Cr)_2$, $Zr_2(Fe,Ni)$. Zircaloy-2 contains both types of SPPs, while Zircaloy-4 has only $Zr(Fe,Cr)_2$ type SPP, as in this alloy, Ni is not usually added. A homogeneous distribution of SPPs is vital for the corrosion protection of Zirconium alloys and their role in HUP has already been discussed in section 2.6.3. The evolution of the distribution of elements with lifetime is of great interest. It is well known that once SPPs are in the oxide layer, they will begin to oxidise and dissolve, often exhibiting delayed oxidation. Irradiation can also create a similar effect in the metal causing alloying elements to diffuse out of SPPs. In her thesis, Adrienn Baris [64] studied the redistribution of alloying elements within the oxide layer on irradiated claddings using EPMA and TEM/EDS. Some key findings were that, for all alloys studied, an increasing concentration of Fe towards the outer surface of the oxide was seen, causing an Fe-rich region to be present in the outermost oxide in all claddings. This has shown to be from the outward migration of Fe but some Fe in this region could also be present from the Fe containing reactor materials and brough into contact by the coolant. Ni (where it is present) showed similar behaviour but to a lesser extent. Early in life, Fe and Ni

begin to diffuse out of SPPs under irradiation, but Cr is much slower and some Cr persist at the site of an SPP at extremely high burnups.

Other observations included alloying elements, particularly Fe and Ni which had left SPPs, would segregate to grain boundaries in the oxide; this was correlated with an increase in HUP. Sundell et al, using APT, also saw this phenomenon and confirmed that such grain boundaries showed an enrichment of hydrogen [92], [159]. Hydrides, in some alloys, were also shown to expel alloying elements and therefore be depleted compared to the Zr matrix (which is consequently enriched)[64]. The impact of this is still unclear. It was concluded that "irradiation induced high level dissolution of SPPs at extreme high burnups reduces the protectiveness of the cladding against increased oxidation in the Zircaloy-2 LK3/L type materials and most probably in other Zircaloy type claddings [64]."

### 2.7.9   Distribution of hydrogen already present, either in metal or oxide

9.  Once some hydrogen has entered the cladding, the distribution of that hydrogen will then affect subsequent HUP. Previous work postulate that the precipitation of hydrides in the metal, at the metal/oxide interface, will increase the rate of oxidation and hydrogen uptake and more hydrides will lead to a faster oxidation and hydrogen uptake [74], [75], [115]. The oxidation front will no longer be purely oxidising metal but also hydrides found at the interface. It is suggested [74] that the oxidation of this 'hydride rim' will lead to a change in microstructure in the newly formed oxide making it less protective and lead to faster degradation of the cladding (mentioned in section 2.4.4). The periodicity of cracks has been found to be higher in oxide layers formed on pre-hydrided samples with large hydride rims compared to hydrogen free metal samples [74]. Baris et al. [73] showed that crack position in the oxide, and hydride position in the metal were linked (Figure 2-27). Previous work has shown most zirconium based claddings contain a greater concentration of hydrides at the interface compared to the middle region of the cladding [73],[67] and in some clads which have inner liners, hydrogen could be drawn away from the interface and 'absorbed' into the liner [73] (Figure 2-26).

Within the same PhD project, it was also found that hydrides in Zircaloy-2 reject alloying elements and are therefore depleted of them while enriching the surrounding Zr matrix [73]. It was unknown if this was true in general for hydrides across different Zr materials and whether the newly formed oxide would be affected by this. That is to say, would the newly formed oxide

inherit the composition of the metal/hydride and would that consequently change the structure of the oxide. For example, Fe is a known tetragonal phase stabiliser, it was useful to know if the Fe concentration would be similar both in the oxidized hydride and in the adjacent metal matrix.
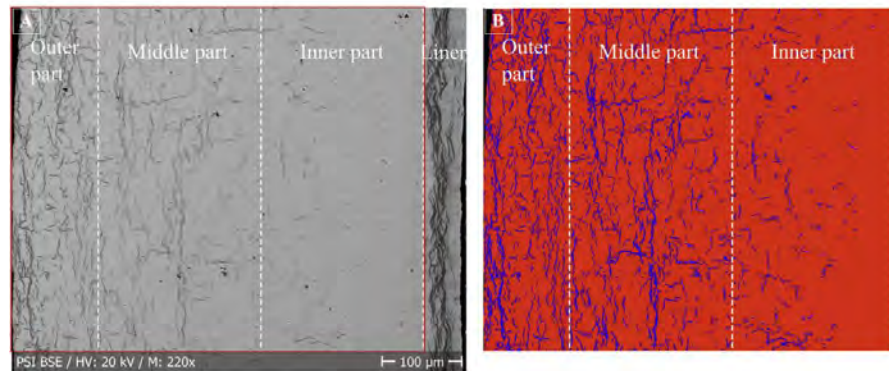


*Figure 2-26. An SEM BSE image to show the surface fraction of the hydrides in the different parts of the metal. White writing indicates the different regions as well as dashed lines (B): The same image where the metal is labelled by red and the hydrides by blue. The term "outer part" refers to the waterside of the cladding and "inner part" refers to the fuel side of the cladding.[73]*
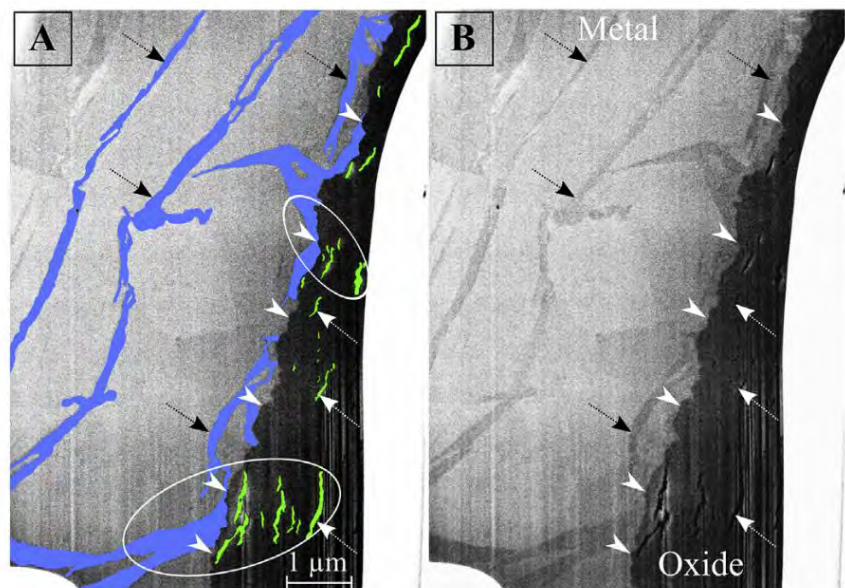


*Figure 2-27. An SEM image showing the hydrides (indicated with black arrows) in the metal and the cracks in the oxide (white arrows) at the metal-oxide interface (marked by the arrowheads). (A): Labelled image. Hydrides are in blue and cracks of the oxide are in green. Occurrence of a group of cracks along the extension of two hydrides to the metal-oxide interface is shown by the circled area. (B): Original image. [73]*

The Zr–H equilibrium phase diagram [160] shown in Figure 2-28 looks rather simple with only an hcp interstitial solid solution α-Zr(H) and two stable hydrides, the cubic phase $\delta$-hydride ($ZrH_{1.66}$) and the tetragonal structured ε-hydride ($ZrH_2$) and a (c/a < 1).
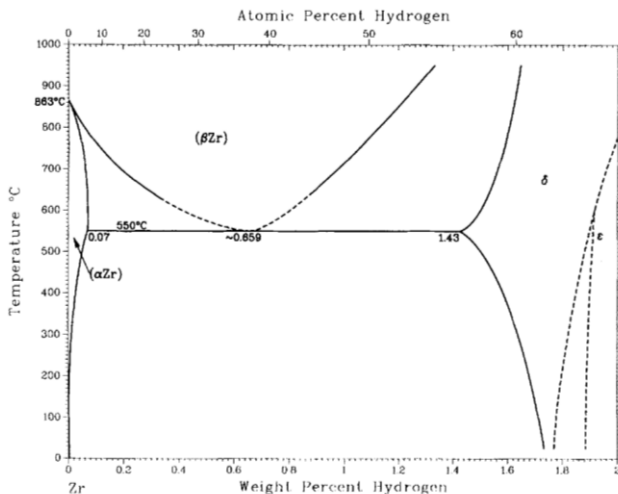


*Figure 2-28. The Zr-H phase diagram [160]*

However, the situation is more complicated in practice. Firstly the γ-hydride (ZrH) (tetragonal, c/a > 1), usually considered as metastable, is also frequently observed in non-equilibrium precipitation after quenching from a solid solution [161]. Secondly recent works have allowed the identification of a new hydride phase ζ, probably with composition $ZrH_{0.25-0.5}$ and metastable like $\gamma$-hydride ($ZrH$) [162]. There is still some debate regarding the hydride phase and structure within the metal. While the hydride phase predominantly observed at low temperatures is $\delta$-hydride [163], some authors suggest that the $\gamma$-hydride may also be present and even that, at high hydrogen concentrations (over 1000ppm), other phases are present [74], [164], [165]. Macroscopic hydrides, in the region of a few microns in size, are said to be composed of several smaller stacked hydrides or platelets [67], [163]. Recently (2018) two separate studies have shown an interfacial region of approximately 10-30nm between the $\alpha$-zirconium matrix and $\delta$-hydride but disagree on the phase. Hanlon et al. [164] performed low loss EELS and suggested the phase to be $\gamma$-hydride while Breen et al. [166], using high resolution TEM, suggest ζ- hydride. Both studies were performed on autoclaved materials without irradiation; so far this finding has not been confirmed on material subject to irradiation in reactor.

# 2.8 Short summary and objectives of thesis

This literature review gives a small insight into the vast amounts of work done on the topic of corrosion and hydrogen uptake in zirconium-based alloys and the large steps forward in scientific understanding and alloy production. On the other hand, it also shows is the complexity of the problem with many interlinked factors and changing parameters. In some instances, the literature not only disagrees, but seems to have directly contradicting results. Further research is therefore still necessary to better understand the hydrogen uptake mechanism especially in reactor. The aim and subject of this thesis is particularly to research the causes for increased hydrogen uptake seen at high burnups in reactor for some alloys. The literature review covers a list of factors which could affect this change in uptake at high burn ups, in section 2.7.2. It must also be  mentioned that there is possibility for other missed or not yet known factors to contribute to the HUP. From this list, certain points which were suspected to be impactful at higher burnups, were chosen to be studied over the course of this PhD work and the main aims of the thesis are outlined as follows:

- To measure the local resistivity/conductivity of the oxide in the same alloy after different lengths of time in reactor to identify the correlation between residence time and the conductivity of the oxide. To achieve this, a technique developed in the lab was further improved where the local resistivity/conductivity of the oxide layer can be studied in irradiated claddings.
- To measure the intrinsic mechanical properties in the vicinity of the metal-oxide interface for irradiated claddings as well as the same alloys oxidised in autoclave without the presence of irradiation.
- To study the distribution of Nb in the oxide from irradiated Nb containing Zr alloys and particularly it's speciation with respect to position in the oxide.
- To study the hydrides found at the metal-oxide interface in irradiated claddings, their structure and effect on the newly formed oxide as well as their effect on the chemical distribution in the vicinity of the metal-oxide interface.

With respect to  the points listed above, the literature review also discusses the so-called 'barrier layer of newly formed oxide' which is suggested to remain dense and mostly uncracked [92], [167]; there is therefore always a need for species to diffuse through it. The size and protectiveness of this barrier layer is an important topic which will also form a significant part of this thesis.  Some authors have

recently suggested that it is in fact the size of this impervious barrier as well as the amount of nano-porosity (of size 0.5-3nm) and the interconnection of such porosity, that governs the protectiveness of this barrier oxide and hence the corrosion rate [59], [71], [94], [99]. Although there is a certain agreement in the scientific community about the existence of a layer, generally called barrier layer, the question still remains about its thickness and its continued protectiveness after long residence time. In this sense, the question of the presence of such a layer and its structure, size and effect will be investigated.

In summary, it is expected that both the size of this inner layer and its protectiveness/ density play a role in determining the hydrogen uptake.

# Contents of chapter 3:

# 3 Materials and experimental techniques

## 3.1 Materials

To study different factors affecting HUP the following materials were used; the reasoning for choosing each of them is also given as follows:

1. Zircaloy-2 grade LK3/L irradiated for 3, 6 and 9-cycles in a BWR, as well as autoclaved tube of the same material. This material has been part of a large project and has been studied in detail to understand the evolution of cladding through lifetime. The semi-conducting properties of the oxide formed remained to be characterised. Hence, this material was chosen to attempt to characterise the electrical resistivity, or semi-conducting properties, of the oxide formed at different stages in life. In addition to this, micro compression tests were carried out on the 6 cycle material to compliment similar tests which had already been performed on 3 and 9 cycle samples. This was to develop the understanding of the evolution of the materials intrinsic mechanical properties especially at and around the metal-oxide interface.

2. Low-tin Zircaloy-4 irradiated for 4 cycles in a PWR. This material was chosen for study of the hydrides particularly at the metal-oxide interface, by means of TEM. It had been previously shown that a high volume fraction (approximately 25%) of the interface was hydrides.

3. Zr-2.5%Nb irradiated for 3 cycles. This material was chosen to add further characterisation to what had already been performed in the lab [8], [64], [67], [168]. The desire was to compare two different Nb containing alloys with two types of Nb SPPs ( the micro structure of these materials will be discussed further in chapter 5 section 6.1.1 and 6.1.2). Particularly this alloy was used in this thesis for EELS analysis of the Nb oxidation state.

4. Low-tin ZIRLO (1%Nb) irradiated for 3 cycles (guide tube material, in this case 1 cycle is equivalent to 18 months rather than 12). It was supplied as part of the MUZIC program to answer a specific question; The speciation of Nb near the interface using XANES and the comparison with other Nb containing alloys.

One of the interesting features of this PhD work is that it is carried out towards the end of a huge amount of work, which has been performed on these materials, at PSI in the frame of a research project on the oxidation and hydrogen uptake. Parallel to these studies, researchers from other

institutions and universities had examined some of these materials. These materials have previously been characterised with many techniques to help better quantify and understand the evolution and degradation of zirconium fuel claddings in reactor during lifetime. This is especially true for the Zircaloy-2 LK3 samples, as it is possible to look at the same material over a whole lifetime and even to extended burnups (9-cycle).

### 3.1.1  Zircaloy-2 LK3/L Grade

All Zircaloy-2 samples used in this study were of the same grade (LK3/L), from the same reactor and the elevations of the segments are very similar. This allows the direct comparison of the materials after 3, 6 and 9 cycles and is interesting to see the change throughout lifetime and even to extremely high burnups (9 cycle) which is beyond design [9]. The cladding material was designed by Westinghouse Electric and the designation "/L" indicates that the fuel cladding has an inner liner to enhance the Pellet-Cladding Interaction (PCI) resistance [169]. All samples were irradiated in the same reactor (Kernkraftwerk Leibstadt, KKL) in Switzerland. The composition of the alloy as well as the measured data such as oxide thickness and hydrogen content were published in ref [8] and are shown here in Table 3-1 and Table 3-2 respectively. The measured data from ref [8] is also plotted in Figure 3-1 and Figure 3-2 for ease of viewing. The parameter Log A is a cumulative annealing parameter and described as $A = \Sigma t_i e^{-Q/RT_i}$, [170], [171] where i is the $i^{th}$ heat treatment (after the last β-quench) at Ti (K) temperature for $t_i$ (h) time, R is the gas constant and Q is the activation energy for precipitate growth [171], here equal to 63 000 cal/mol [172],[157]. Table 3-2 also includes the measured data from 5 and 7 cycle samples of the same material, this is included for completeness even though those samples were not studied in the frame of this PhD.

*Table 3-1. The composition of the LK3/L fuel rod with Zr as balance [8]*

| LK3/L composition | Sn | Fe | Cr | Ni | Fe+Cr+Ni | O (ppm) | Si (ppm) | log A |
|---|---|---|---|---|---|---|---|---|
| wt% | 1.34 | 0.18 | 0.11 | 0.05 | 0.34 | 1320 | 70 | -14.2 |
| at% | 1.02 | 0.29 | 0.19 | 0.077 | 0.557 | | | |

*Table 3-2. Measured data showing the oxide thicknesses and hydrogen content of the LK3/L cladding after different service times [8]*

| Number of cycles | Peak burnup (MWd/kgU) | Segment elevation for oxide thickness measurement (mm) | Mean oxide thickness (µm) | Segment elevation for $H_2$ measurement (mm) | Total hydrogen content (ppm) |
|---|---|---|---|---|---|
| 3 | 44.6 | 2005 | 4.4 (±0.7) | 2002 | 44 |
| 5 | 59.6 | 2005 | 12 | 2002 | 90 |
| 6 | 66.9 | 2005 | 14 | 2002 | 202 |
| 7 | 67.4 | 1998 | 19 (±1.4) | 2004 | 261 |
| 7 | 67.6 | 1995 | 21 (±0.9) | 2000 | 339 |
| 7 | 73.3 | 1998 | 19 (±2.3) | 2004 | 328 |
| 7 | 73.0 | 1998 | 19 (±2.3) | 1995 | 224 |
| 9 | 89 | 2039.5 | 46 (±2.5) | 2045 | 595 |
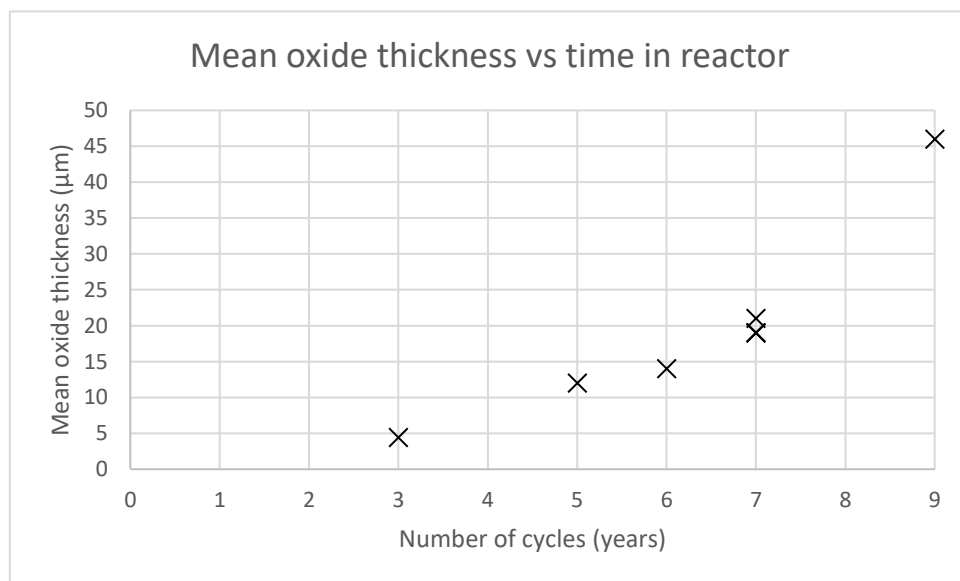


*Figure 3-1. Mean oxide thickness plotted against number of cycles (years) in reactor for the material Zircaloy-2 LK3/L. Four results are available at 7 cycles . The data was measured in ref [8]*
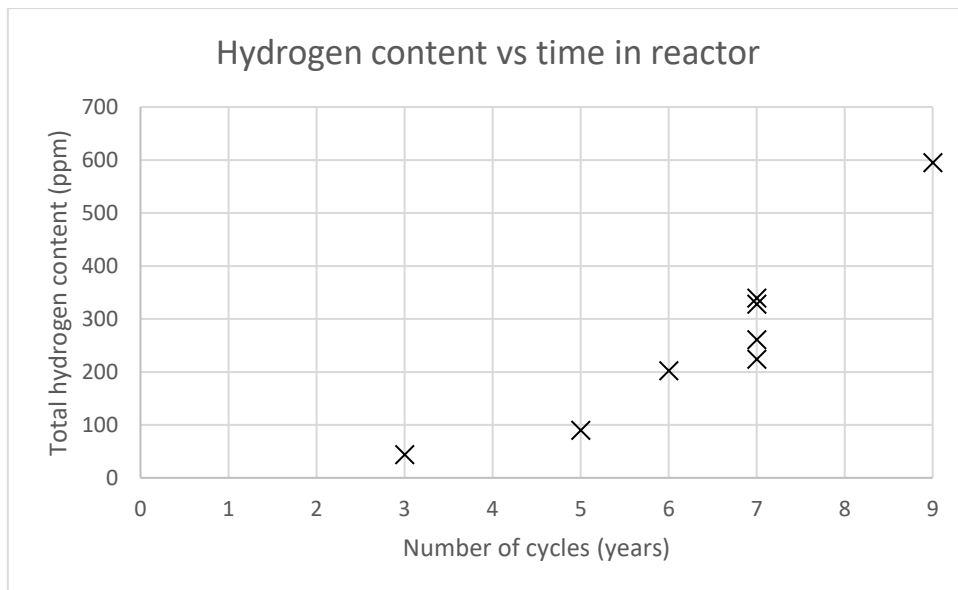
*Figure 3-2. The clad hydrogen content plotted against number of cycles (years) in reactor for the material Zircaloy-2 LK3/L. Four results are available at 7 cycles. The data was measured in ref [8]*

### 3.1.2 Zr-2.5%Nb

This material is one of the two Niobium alloys studied in this project. The cladding was produced by Framatome GmbH and irradiated for 3 cycles in KKG (kernkraftwerk Gosgen), PWR in Switzerland. The composition of the cladding as well as the heat treatment are shown in Table 3-3 similarly to the previous material the measured data for this material and specifically the sample set studied such as oxide thickness and H content are shown in Table 3-4 also published in ref [8].

*Table 3-3. The composition of the Zr-2.5Nb. HT: heat treatment; PRX: partially recrystallized condition [8]*

| Composition | Nb | Fe | Si (ppm) | C (ppm) | O (ppm) | H (ppm) | HT |
|---|---|---|---|---|---|---|---|
| wt% | 2.5 | 0.07 | 60 | 180 | 1170 | 10 | 500°C PRX |
| at% | 2.438 | 0.114 | | | | | |

*Table 3-4. Parameters of the analysed segment and for the full Zr-2.5Nb rod [8]. *From one data point.*

| Residence time (cycle) | Segment elevation (mm) | Burnup (MWd/kgU) | Rod max oxide thickness (µm) | Rod available data for H content (ppm) |
|---|---|---|---|---|
| 3 | 869 | 41.4 | 16 | 70* |

### 3.1.3  Low-tin ZIRLO

The composition and heat treatment of the alloy are shown in Table 3-5. This material differs to the others in the thesis as it is actually guide tube material, from Millstone (USA), rather than fuel cladding. Since the material is subjected to similar core conditions and a comparable burn up and the topic studied was the oxidation behaviour of Nb it is accepted the comparison is valid between this material and fuel cladding material. Such details are provide in Table 3-6. The piece received had an oxide ranging from $1.4 \mu m$ to $2.5\ \mu m$. The full oxide thickness of this segment of material is 8-10 $\mu m$.

*Table 3-5. Composition of the low-tin ZIRLO guide tube with Zr as balance. HT: heat treatment; RXA: Recrystallized and annealed.*

| Composition | Fe (wt%) | Sn(wt%) | Nb(wt%) | Heat treatment |
|---|---|---|---|---|
| wt% | 0.1 | 0.7 | 1.0 | RXA |

*Table 3-6. Data on low-tin ZIRLO from time in reactor- residence time and burn up*

| Residence time (number of cycles) | Burnup (MWd/kgU) |
|---|---|
| 3 | 63 |

### 3.1.4  Low-tin Zircaloy-4

This material, from Framatome GmbH, is similar to the LK3 Zircaloy-2 cladding but contains less Sn, slightly more Fe and Cr and does not contain any Ni. This material is used in PWRs and was irradiated in KKG. The Table 3-7 shows the composition and heat treatment. The measured data from this material is shown in Table 3-8 [8]. Here extra information is given about the oxide thickness and

hydrogen content as a function of rod elevation, this illustrates the variation that is possible even on a single rod.

Table 3-7. Composition of the low-tin Zircaloy-4 fuel rod with Zr as balance [8]. HT: heat treatment; SRA: stress relieve annealed.

| Composition | Sn | Fe | Cr | C (ppm) | O (ppm) | H (ppm) | HT | SPP mean size (nm) |
|---|---|---|---|---|---|---|---|---|
| wt% | 1.20 | 0.22 | 0.107 | 140 | 1730 | 8 | 504°C SRA | 190 |
| at% | 0.914 | 0.356 | 0.186 | | | | | |

Table 3-8. Measured data showing the oxide thicknesses and hydrogen content of the low-tin Zircaloy-4, at different elevations after 4 cycles. [8]

| Residence time (cycle) | Segment elevation (mm) | Rod Burnup (MWd/kgU) | Rod maximum oxide thickness (μm) | Hydrogen (ppm) |
|---|---|---|---|---|
| 4 | 1468 | 51.1 | 59 | |
| 4 | 353 | 51.1 | 7.5 | $52.2 \pm 5$ |
| 4 | 1561 | 51.1 | 25 | $209 \pm 19$ |
| 4 | 2525 | 51.1 | 44 | $367 \pm 31$ |
| 4 | 3120 | 51.1 | 56 | $460 \pm 44$ |

# 3.2 Experimental techniques

Throughout this PhD work five main groups of instrumentation and techniques were used, these are listed here:

1.  Scanning Electron Microscope/ Focused Ion Beam (SEM/FIB)
2.  Transmission Electron Microscope (TEM) – with Electron Energy Loss Spectroscopy (EELS) and Energy Dispersive X-ray Spectroscopy (EDS)
3.  Synchrotron studies
4.  Micro-mechanical – micro-compression tests
5.  Conductivity measurements

## 3.2.1 Scanning Electron Microscope with Focused Ion Beam

A Zeiss NVision 40 dual-beam FIB/SEM system with a field emission gun (FEG) at Paul Scherrer Institute has been used to prepare TEM lamella, image samples, micro-machine the shapes and deposit electrodes for conductivity measurements as well as the measurements themselves being performed inside the SEM and finally it was used to micro-machine micro-pillars for compression tests. This FIB system uses a Ga+ source that can be operated from 5 keV to 30 keV and from pA to nA range. A high current ion beam was typically used to cut and mill the sample while a low FIB current was used to polish the sample or deposit different materials (e.g. Pt, C). The option is also available to use the electron beam to deposit materials with the benefit of no Ga contamination, but this is a much slower process and only used when necessary. The specific application of this instrument will be expanded upon in each relevant section.

## 3.2.2 Transmission Electron Microscopy

Initially two TEMs were used at PSI. A JEOL 2010, equipped with a $LaB_6$ cathode and an INCA EDS system of Oxford Instruments, was mainly used for learning, screening, imaging and crystallographic study. The second was a JEOL 2200FS with cold FEG source and an Omega filter, used for imaging and EELS. An FEI TALOS F200X TEM, at the University of Birmingham, was also used. It is equipped with a brighter X-FEG gun and with 4 EDS detectors (ChemiSTEM technology) in order to achieve high speed chemical measurements on a nano scale EDS mapping and line scans. A JEOL ARM200F, at the University of Oxford, equipped with a cold FEG was used for high resolution EELS with a Gatan

Quantum 965 ER GIF. The latter two microscopes were mainly used in STEM mode. The EELS spectral images were acquired in both low loss and core loss energy ranges with spatial drift corrected. For each spectrum the zero-loss-peak (ZLP) alignment, which was used for energy calibration, and principal component analysis (PCA) were carried out by using open source software HyperSpy [173].

**Electron Energy Loss Spectroscopy and Energy Dispersive X-ray Spectroscopy– EELS and EDS**

EELS is a well established spectroscopy technique used in the TEM [174]–[180]. When electrons pass through a thin foil, a fraction will undergo inelastic scattering, losing some kinetic energy. The energy loss due to the inelastic scattering can be measured by means of specific spectrometers fit into the TEM column at different positions, giving information about the structure and composition of a sample. EELS is the counterpart to the more commonly used Energy Dispersive X-Ray Spectroscopy and a brief comparison is shown below in Table 3-9.

*Table 3-9. A short comparision between the techniques EDS and EELS*

| EDS | EELS |
|---|---|
| **Advantages** | **Disadvantages** |
| – Easier to use | – Currently more difficult to use |
| – Common technique | – Less common |
| – Sensitive to elements with higher atomic numbers | – Worse at detecting heavier elements |
| | – Samples should be thinner for a good signal to noise ratio which can make sample preparation difficult |
| **Disadvantages** | **Advantages** |
| – Lighter elements such as oxygen have a lower energy and a high absorption in the detector, making the quantification less accurate | – Better spatial resolution (can in principle map individual atoms) |
| – Worse energy resolution ~ 10 eV | – Larger energies are detected ($E_{initial} - \Delta E$) |
| – Can only identify elements present not structure and speciation | – Good at detecting light elements |
| | – Very good energy resolution which is dependent on the electron beam energy distribution and detector accuracy and can be <1eV |

| | |
|---|---|
| | – Can give information on chemical bonding and speciation |
| | – Can be used to determine the crystal structure not only elements present (fingerprint) |

A typical EELS spectrum is shown in Figure 3-3 to briefly explain the origin of the different features used for analysis from ref [180].
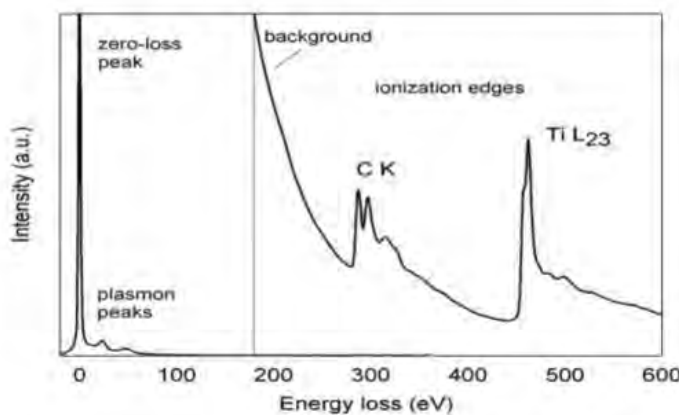


*Figure 3-3. EELS spectrum of a 20nm thin titanium carbide specimen recorded with a 200 kV TEM equipped with and energy filtering spectrometer (from ref* [180]*)*

The zero-loss peak corresponds to most of the electrons losing no energy (or such a small loss the collision is considered elastic). The width of this zero-loss peak is usually around 0.2–2 eV [180] and reflects mainly the energy spread of the electron source and the resolution of the spectrometer.

Two distinct regions can be thought of in EELS: the low loss region containing plasmon peaks, and the core loss region.

a- The plasmon peaks, in contrast to a single-electron excitation, are a collective excitation which occurs in almost all solids and is described in terms of the generation of plasmons which form the plasmon peaks. "When a fast-moving electron passes through a solid, the nearby atomic electrons are displaced by Coulomb repulsion, forming a correlation hole (a region of net positive potential of size ~1 nm) that trails behind the electron. Provided the electron speed exceeds the Fermi velocity, the response of the atomic electrons is oscillatory, resulting in regions of alternating positive and negative space charge along the electron trajectory." [179]

A transmitted electron causes an oscillation in electron density and this in turn produces a backward force on the causing it to lose an average energy:

$$E_p = \left(\frac{h}{2\pi}\right)\omega_p$$

Where h is planks constant and;

$$\omega_p = \left( \frac{n_e^2}{\epsilon_0 m} \right)$$

Where $n_e$ is the density of the atomic electrons electrostatically coupled with the solid and m is the effective mass of them.

b- The high loss, or core loss, results from the inelastic interactions of electrons with single atoms.

As mentioned above the majority of the electrons pass through the sample, without interacting inelastically, in the region of 90-95% for thin samples. The high loss peaks can therefore be very small in comparison with the zero loss peak and thus difficult to identify on a spectrum. At energies roughly over 50 eV the number of scattered electrons is much lower, but still distinctive "ionisation edges" are seen. The edges are formed when an inner shell electron absorbs enough energy (from the incident electron) and is excited above the fermi level (fermi level is the highest energy state occupied by electrons in a material at absolute zero). The energy-loss of the transmitted electron is then an indicator of that interaction. This allows the identification of particular elements and even the comparison of the same element at different oxidation states.

**TEM sample preparation with FIB**

TEM lamella must be very thin for electrons to pass through, in the region of 1-3 mean free-paths for an electron in that material. Preparing TEM lamella by FIB is now a very common method, but it is still difficult to routinely produce high quality lamella. The problem is especially exasperated by the fact that the most common area for TEM lamella for this project is the metal-oxide interface where two materials with different hardnesses must be polished simultaneously. The large amount of porosity present sometimes in the oxide also adds to the problem. The foils used in the current study were prepared following previous work specially developed to prepare TEM lamella at the metal-oxide interface for this material [181], which was detailed. A detailed step by step process is also given in the PhD thesis of Adrienn Baris [64]. It should be noted that the technique of Ga FIB has been reported to possibly induce some artefacts such as oxide phase transformation [182] particularly from tetragonal to monoclinic due to stress relaxation. Also the induction of hydrides due to fibbing has been reported [164] and there is the possibility of contamination from the Ga and other artefacts

[181]. The effect of these artefacts and possible ways to reduce them are discussed in ref [181]. In relation to this work the following steps were taken to reduce the impact of artefacts on results. TEM lamella with an inacceptable level of Ga present were excluded. An important point for this thesis is to verify that the hydrides studied were not artefacts, this could be done by isolating a hydride before FIB polishing. Another way to verify the true presence of a hydride is that while FIBbing large amounts of hydrides could be seen in the samples containing high measured amounts of hydrogen but not in others. For example seen in 9 cycle but not in the 3 cycle. Then once the lamella had been prepared using the same conditions hydrides could be seen in those samples they were expected in but not in the others. Therefore it was verified that in this study the hydrides studied were in fact features of the sample rather than artefacts. However one should be aware of the potential issue the induction of hydrides may cause.

### 3.2.3 Synchrotron studies

Synchrotron X-ray measurements were carried out at the X05LA/microXAS beamline at the Swiss Light Source (Paul Scherrer Institute, Switzerland). Monochromatic hard X-rays from the Si(111) double crystal monochromator of the beamline were focused down to approximately 0.8 µm (horizontal) × 0.7 µm (vertical) spot using a pair of Rh-coated Kirkpatrick-Baez (KB) mirrors (shown in Appendix C). Fluorescent X-rays were measured using an energy-dispersive solid state KETEK drift detector, oriented at grazing exit angle with respect to the sample surface. Chemical maps of the ZIRLO sample were measured in X-ray fluorescence mode using monochromatic X-rays with an incident energy of 19.1 keV. X-ray absorption near edge structure (XANES) spectra were measured in fluorescence mode over the Nb K-edge. The transmitted X-rays were measured using an Eiger4M area detector.

### 3.2.4 Micro-compression tests

**Micropillar fabrication with FIB**

The FIB/SEM mentioned in section 3.2.1 was used to prepare micropillars for micro-compression tests. Within the SEM the metal-oxide interface of the claddings were examined and the metal and the oxide regions near the interface could be selected. Subsequently pillars were fabricated in those regions. The preparation consisted of 2 steps of FIB polishing. This scheme is based on the work from Volket and Lilleodden [183] as well as micro-pillar work performed at PSI, as a feasibility study on similar irradiated materials [137]. The first step can be described as the 'rough cuts' defining the placement

of the pillar and removing enough material to allow the compression tip to correctly compress the pillar without contacting the substrate. These we typically carried out with a milling current of 6.5nA, an outer radius of 10 $\mu m$ and inner of 3.5 $\mu m$. The second step is the 'polishing' step with the aim to get a good uniform pillar here a low beam current 150 pA was used to reduce the contamination and improve the surface. This process produces pillars with a known taper. It was attempted to create the pillars as similar as possible but this of course is impossible due to the variation in the materials (especially from oxide to metal) so the dimensions of each set of pillars was recorded.

For the compression experiments four regions were studied, viz. Bulk metal, Oxygen saturated metal (i.e. the metal at the metal-oxide interface), Newly formed oxide (i.e. oxide at the metal-oxide interface), Bulk oxide. For each region in each alloy seven pillars were made with the dimensions between 2.0-2.6µm diameter and between 3.8-6µm in height. The aim was to have an aspect ratio ($\frac{upper\ diamter}{height}$) of 2 which is within the recommended values[23], [137].

**Micro-Compression tests**

A nano-indenter was used to perform micromechanical tests. The tests were performed with the MTS G200 nano-indenter at PSI, using a flat diamond punch tip. During the experiment the pillars were compressed at a fixed displacement rate, 33nm/s, to a specified maximum displacement 1µm. At maximum displacement, the load was held for a period before unloading. The compression test delivered load versus displacement data with a load resolution of 50 nN and a displacement resolution of 0.01 nm. A more detailed step by step explanation can be found in [137]. After the compression tests, the compressed pillars were once again taken to the SEM for analysis. This helped to verify if any pillars had not been properly compressed but instead buckled or deformed in some other way. This screening allowed the removal of incorrect compression data. Post analysis of the pillars also could be correlated with each compression test data and helps to explain some specific features.

From the compression tests the load vs displacement data available were used with the measured dimensions of each pillar, to obtain the stress and strain, calculated using the equations;

$$\sigma = \frac{F}{\pi r_{top}^2}$$

And

$$\epsilon = \frac{\Delta l}{l_o}$$

Where $\sigma$ is stress, F is applied force or load, $r_{top}$ is the radius at the top of the pillar.

And $\epsilon$ is strain and $l$ is length or height of pillar.

It should be noted that to use these formula the taper was not taken into consideration and only the diameter at the top of the pillar was used. This because the stress build up has been found to be at the top of the pillar by Ilchuck et al [184] and thus it was found to be more accurate to take this value. In order to ensure a good compression test without any influence on the compression tip by the surrounding material any is was assured that the pillar was more than 3μm above the crater remenants.

### 3.2.5 Conductivity measurements

Based on a method recently developed [185], [186], a novel experimental technique for measuring the high resistivity of oxide on irradiated fuel claddings locally was further developed and employed. The details of the method are described here.

**Technique outline and instrumentation**

The SEM/FIB described in section 3.2.1 was used to micro-machine the samples into a shape usable for the experiment. Subsequent to the micro-fabrication of segments, micromanipulators from Imina Technologies dedicated for such measurements were used to measure the conductivity. The overall experiment has 4 steps as follows:

a. micro-machining of the wedges at metal-oxide interface
b. deposition of Pt electrodes by electron beam
c. measurement of conductivity by micromanipulator
d. cutting under the electrodes to measure the exact thickness of underlying oxide.

The details of the experiment are further outlined below: first, the outer oxide is removed using a high current in the FIB. Then the current is reduced to create a wedge shape from the inner oxide at a small angle of 2° w.r.t. the metal-oxide interface, leading to a wedge with varying oxide thickness. Platinum electrodes can then be deposited over this wedge. In this manner, beneath each electrode a band of

oxide with increasing thickness is present, before reaching the underlying Zr metal (Figure 3-4a). Furthermore, there was also one electrode deposited where no oxide was left i.e. on the polished metal. This was used as a reference of the whole circuit without containing any thickness of oxide for each wedge. To complete the circuit an electrode was also prepared on polished Zr metal at a given distance (usually in the region of 100-300 μm) away from the wedge, and at an orientation perpendicular to the surface of the wedges. Figure 3-4a depicts this configuration. The area of Pt electrode deposited for every oxide thickness was kept constant at a size of 4 μm x 8 μm. The electrodes were all deposited using the electron beam and the thickness of the Pt deposition was kept in the range of a few hundred nanometres.

Using micromanipulators inside the SEM both the metal electrode and the wedge oxide electrode can be contacted simultaneously to form a circuit. Included in the circuit is an ammeter capable of reading very low currents, hence high resistances (in this case a Keithly 6487 pico-ammeter). When a voltage is then applied, the circuit will consist of the metal region, the thin Pt depositions and a certain thickness of oxide. This oxide thickness varies, depending on which electrode is contacted with the micromanipulator. During this experiment, a DC voltage of 0.1 V was applied. Although higher voltages did prove to give less error for larger oxide thicknesses (or much higher resistances), this low voltage was chosen to ensure the voltage limit (the so-called breaking voltage) was not reached and to be consistent with previous work [185], [186]. Higher voltages were sometimes employed to measure higher resistances when the oxide was thicker. A schematic diagram of the circuit set-up when contacted with micromanipulator is shown in Figure 3-4b. An example of the position of electrodes on the oxide is shown in Figure 3-5. The micromanipulator tips can be observed in operation inside the SEM in Figure 3-6a and the contacting of the electrodes is shown in Figure 3-6b.
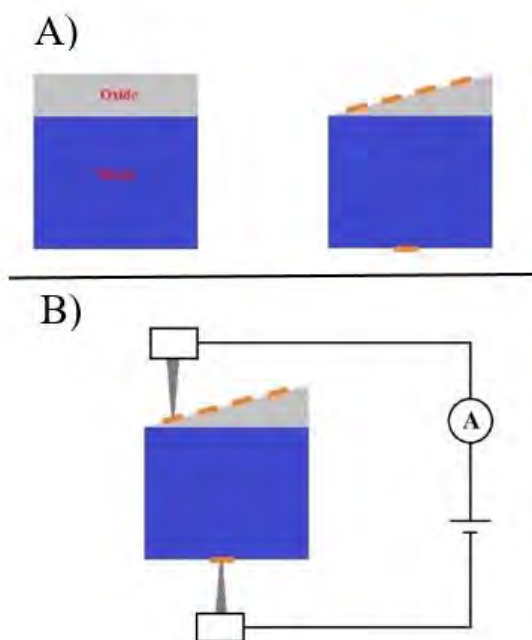
*Figure 3-4. Schematic diagram of the set up used to measure conductivity A) shows the oxide wedge with the deposited electrodes (exaggerated) and one electrode deposited a distance away on the metal B) shows the micromanipulators contacting the first oxide electrode and the metal electrode deposited in a different place to form a circuit.* [185], [186]
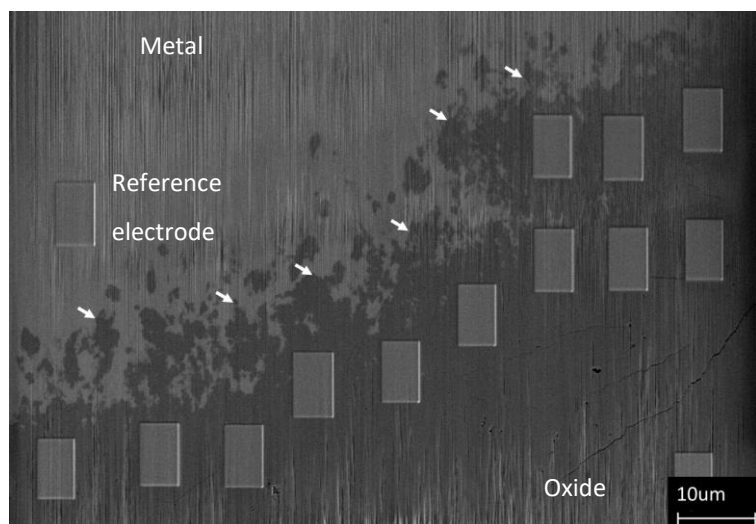


*Figure 3-5. SEM image of electrodes deposited onto the oxide wedge for 3-cycle sample. The metal (in bright contrast) and oxide (in dark contrast) regions of the wedge are indicated. The electrodes can be clearly seen on the oxide and an additional electrode was deposited on the bare metal region to allow a reference value to be measured i.e. the resistance of the circuit without containing any oxide. Arrows point to the approximate region of metal-interface, due to the angle of polish.*
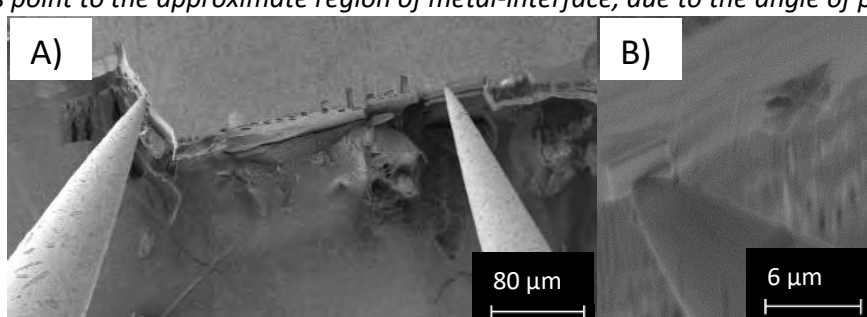
*Figure 3-6. SEM image of the 9-cycle sample, a) Micromanipulator tips and setup in the SEM ready to measure the electrodes, distance between the two electrodes is approximately 200 µm. b) Illustrating the contact between micromanipulator tip and electrode*

**Determination of oxide thickness under each electrode**

After the conductivity measurement, each electrode on the oxide was cut to reveal the exact oxide thickness beneath it, this was done using the SEM/FIB and examples are shown in Figure 3-7. The majority of electrodes were cut in two different locations in an attempt to find the minimum oxide thickness, due to the undulating nature of the oxide. The oxide could be viewed when the contrast is enhanced as the darker material. Effort was made to determine this minimum oxide thickness but the possibility of the existence of a thinner section of oxide, due to undulation, under the electrode must be kept in mind. In the oxide layers with a thinner average thickness, larger percentage change would exist if an unknown undulation was present. For some electrodes, covering very large thicknesses of oxide, only space for one cut was available; in these instances, attempt was made to watch the cutting procedure for any large irregularities in oxide thickness. In the case of thick oxides, region with much smaller thickness values was not observed except in the 6-cycle sample. Figure 3-8 is included to give examples of the extreme undulation found in the 6 cycle sample.
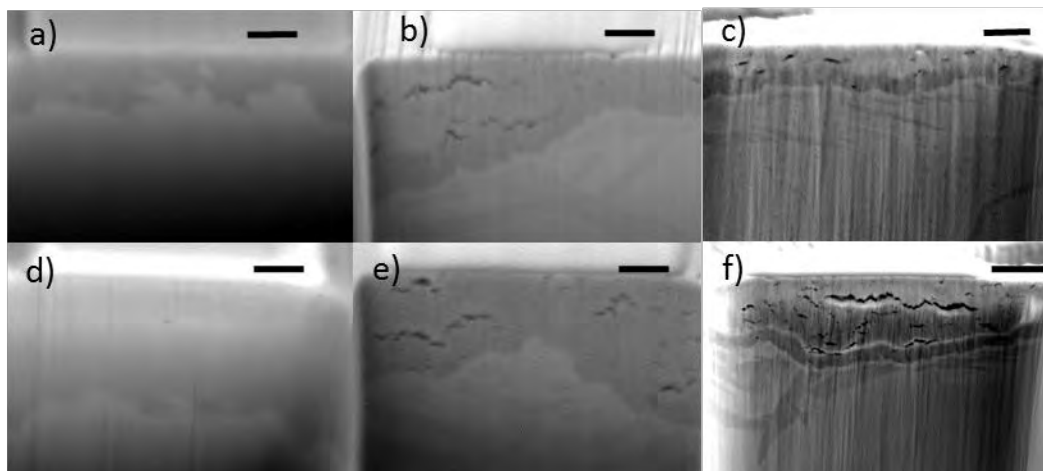


*Figure 3-7. Undercuts beneath electrodes after conductivity measurement. a/d shown 3 cycle material, b/e show 6 cycle material, c/f show 9 cycle material. The darker contrast region corresponds to the oxide, and in the 6 and 9 cycle cracks can be seen in this region. Scale bar represents 1µm*
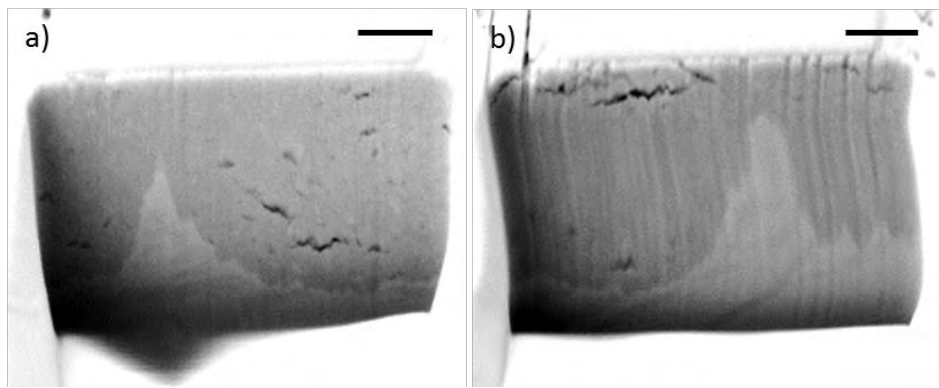
*Figure 3-8. Undercuts beneath 6 cycle electrodes after the conductivity measurement showing the possible irregular undulation of the interface. Scale bar represents 1μm*

**Calculation of results and assumptions**

The resistivity values were calculated from the measured resistance for each electrode using the formula,

$$\rho = \frac{RA}{l},$$
<div align="right"><em>Equation 3-1</em></div>

Where $\rho$ is resististivity, R is resistance, A is area, and l is length.

To calculate the resistivity in this manner some assumptions were made. As can be seen in Figure 3-5, besides the electrodes on the oxide wedge there were also reference electrodes in contact with the metal in the wedge to measure the resistance of the set up using the conductivity of metal Zr as our base point or reference point. The measured resistance, using these reference electrodes of the Zr metal with such setup ranged between 30-150 ohms, and hence was considered negligible compared to the measured resistance values from the oxide electrodes in the range of $10^4 - 10^9$ ohms. Thus one assumption was that the setup together with the conducting metal has a very low resistance.

The creation of a contact between a semi-conductor (here substoichometric oxide) and a metal (electrode) in the semi-conducting field is the precursor for the fabrication of low voltage drop diodes and it is quite well known. However, in order to verify, if the deposition of Pt plays a role on the modifications of the measurements, the conclusion from bulk studies performed previously [187] is reported here. The study used various electrode metal materials on zirconium oxides [187], and it was concluded that "No visible effects of electrode materials on the specimen current of Zircaloy oxides

are found [187]." With these assumptions in mind it is clear that the importance of this work lies within the comparison between the materials and hence any effects which may arise would be systematic and the comparison still valid.

Therefore, it is concluded the assumption that "the object length contributing to the high resistivity being probed is solely the thickness of oxide beneath the electrode", is valid. For these calculations always the minimum oxide thickness found under each electrode is used as length. Although every electrode was built to have the same dimensions of 4 µm x 8 µm, the thickness of underlying oxide was not constant over the whole area of Pt, as it can be clearly seen from Figure 3-7. This undulation has been reported many times and is a well known phenomenon [38], [67], [68] with the area of an average protrusion calculated to be approximately 0.9 µm x 0.9 µm in the 3-cycle material. Hence, the path of the current beneath each of the electrodes cannot be totally known. For this reason, a minimum value of resistivity was calculated using the protrusion area (the average area of a metal protrusion into the oxide) and a maximum calculated using the total electrode area. An average of these two values has been adopted for this study (Tables are shown in the appendix A).

## 3.3 Division of experimental work

This thesis work could not have been completed to the same standard and including such a variety of techniques without the help of others, this section is included to give credit to those who contributed and who gave help with the experiments performed. The beamline scientists Peter Warnicke, Dario Sanchez and Daniel Grollimund are acknowledged for operation of the micro-XAS beamline during the synchrotron campaign. Dario also processed the XRD 2D patterns to create 1D spectra I could then analyse. Patrick Burr is acknowledged for his work in computing the reliability of the XANES fitting (this is shown in appendix C). Guanze He performed the operation of the JEOL ARM at oxford which was used for EELS and he is thanked once again for this. His help and advice in how to analyse the core loss EELS performed on the Nb containing sample is also acknowledged. Although the processing and analysis of the data was performed by myself. Dr. Gnanavel Thirunavukkarasu helped me to operate the TALOS at Birmingham and is thanked. Andrej Bullemer is thanked for his help with equipment and sample preparation in the hotlab. The preparation of the ZIRLO alloy sample was performed by Dr. Pia Tijeland and her team. In addition the many people who helped train and give advice on the operation of the experimental equipment, particularly electron microscopes at PSI are thanked. Elisabeth Muller, Adrienn Baris and of course my supervisor who gave much guidance and training Sousan Abolhassani.

# Contents of chapter 4:

# 4  Conductivity measurements

## 4.1 Introduction

As previously discussed in Section 2.7.5 it is claimed that the conductivity of the oxide plays a significant role in the corrosion kinetics and hydrogen pickup. To briefly summarise, one of the hypotheses is that increasing oxide resistivity would decrease the mobility of electrons from the metal-oxide interface to the oxide-water interface. This in turn would increase the electrical potential across the oxide and hence the driving force for the ingress of $H^+$ [11], [26], [61]. To measure this property a novel technique was employed. Using micromanipulators (MMA) in an SEM, the resistivity of the oxide at a certain point could be directly measured. This technique has been explained in greater detail in Section 3.2.5. The aim of this was not just to determine the inherent (in the absence of external parameters) resistivity of an oxide grown in reactor, which is already a difficult process, but also to investigate how this property changes with time or burnup. To do this one alloy (Zircaloy-2 LK3/L grade) was examined after 3 different residence times, 3, 6 and 9 cycles in a Swiss boiling water reactor (Kernkraftwerk Leibstadt, KKL). Details about these samples can be found in Section 3.1.1. It is important to note here that this material had already been shown to change its HPUF throughout lifetime with the HPUF of the cladding being 17%, 34% and 30% 3,6 and 9-cycles respectively [8]. This finding forms the basis for the motivation for the extensive characterisation and comparison of its high and low burnup samples [8], [64], [65], [69], [73], [137]. It is important to add to the characterisation how the semi-conducting properties change with residence time and to correlate this to the change in hydrogen uptake behaviour since this property was identified as a possible factor which could cause the increase of hydrogen uptake at high burnups[61], [64], [108], [186]. This question, to our knowledge, has never been studied. The strength of this work is that multiple samples with varying irradiation/residence times were studied and the inner oxide of these samples could be directly compared, giving local resistivity data throughout the oxide with high spatial resolution.

## 4.2 Results

A detailed description of the technique and set up used to acquire the results in this section is included in chapter 3 section 3.2.5. To increase the reliability and the statistics of the results three measurements were performed on the 3 and 9 cycle materials, two on the 6 cycle sample. By doing this each time a different wedge in a different region of oxide was probed so as to ensure a good

average over a large distance of oxide (each wedge was roughly 100μm in size and the wedges were usually separated by 50-200μm).

## 4.2.1 Examination of resistivity of control samples

Because of the novel set up and therefore the non-standardised testing there was a desire to first further verify the reliability of the measurements and the setup. To do this, the resistance of different control samples was measured in the SEM/FIB using the micromanipulator. The chosen materials were a $10M\Omega$ resistor, a p-doped silicon with a known resistivity of $0.01\text{-}0.2\Omega.m$ and ZrO powder. Micrographs indicating the samples during measurements for these references can be seen in Figure 4-1, Figure 4-2 and Figure 4-3 respectively. Furthermore, it is considered that many Zr to Zr reference electrodes measured in each trial of the experiment, are also "internal" references.

Measurement of the resistor consistently returned values of $10M\Omega$ within a 5% deviation. The doped silicon had Pt electrodes deposited (of dimensions 4 μm x 8 μm) and was measured at applied voltages between 0.1V and 1V. Using the area of electrodes and being tested a mean value of 0.043 $\pm$0.010 $\Omega.m$ was measured, which is in good agreement with the known resistivity. For ZrO powders the aim of the test was to confirm the linear response of resistance vs distance between the micromanipulator tips, as well as the effect of varying the applied voltage. Furthermore, it was planned to study a sample without any FIB alteration, so that the material does not contain any Ga contamination. Different powder particles were contacted with the micromanipulators across different distances and the resistance was measured. One example of the measurement configuration and the ZrO particles can be seen in Figure 4-3. The results are plotted in Figure 4-4 and confirm a linear response furthering the reliability of the set up (the values for distance may vary due to the non-uniform shape of the particle). This gave a value of resistivity of 6.6 x 10$^{-6}$ $\Omega.m$ $\pm$2.5 x 10$^{-6}$ $\Omega.m$ with the assumption that the contact tips were of 1.5 μm x 1.5 μm. At certain positions, the applied voltage was varied between 0.05V and 1V. The returned resistance remained constant with a maximum deviation of +/- 10%. This confirms an ohmic response as expected; this may facilitate in the future the increase of the applied voltage for highly resistive materials in order to reduce the effect of 'noise' within the system. For example a rough limit of the measurable resistance attainable is, for 0.1V in the magnitude of $10^9$ $\Omega$, for 1V in the magnitude of $10^{10}$ $\Omega$ and for 10V in the magnitude of $10^{11}$ $\Omega$. It also showed the resistivity of ZrO is much closer to that of metal rather than oxide.

1 mm
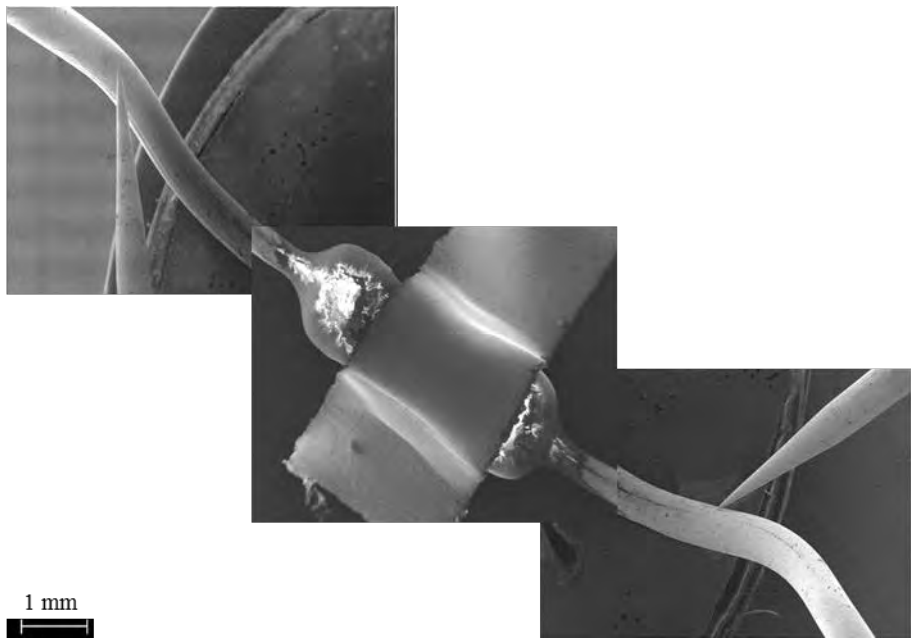
*Figure 4-1. The measurement of a 10MΩ resistor with the two tips contacting the wire on either side of the resistor. The two sides are shown here separately, since the object is too large to be captured in one SEM image. Here there is direct tip metal contact without an electrode. Only resistance was being measured not resistivity.*



1 mm
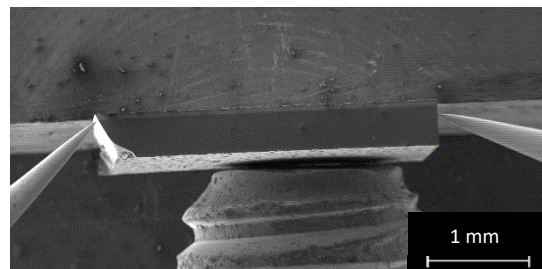
*Figure 4-2. The measurement of p-doped silicon wafer, here tips can be seen in position with silicon of length of 3.4 mm*
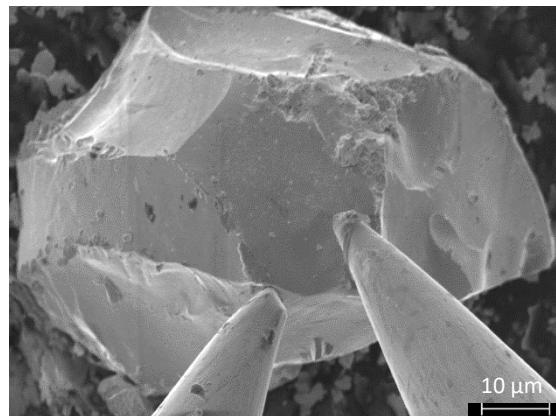
*Figure 4-3. Micromanipulator tips contacting a particle of ZrO with a small separation distance. The tips are located perpendicular to each other so that the tip at the bottom of the image is touching the side of the sample and the other is touching the top is the sample. To match the configuration of the tips in the main experimental setup.*
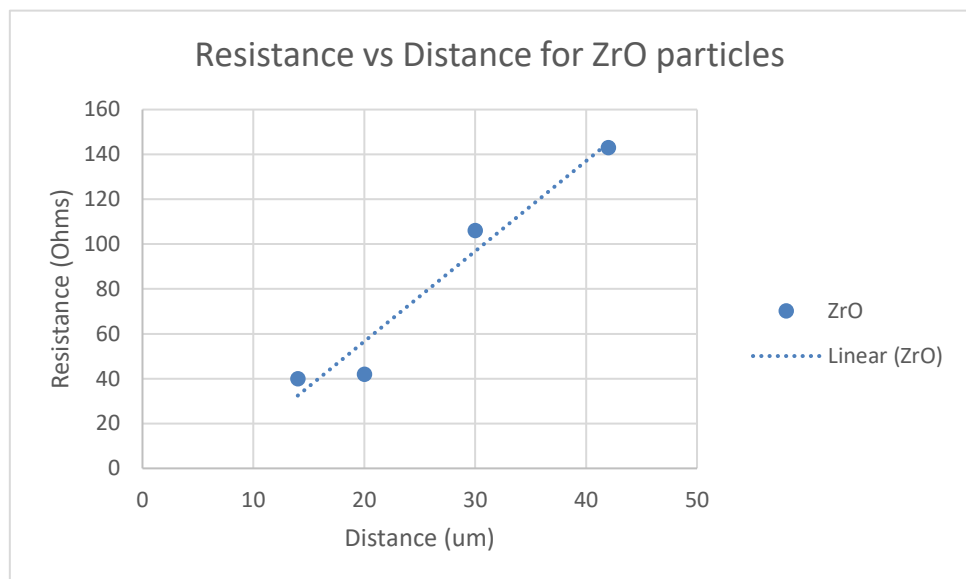


*Figure 4-4. Graph of the resistance measured with a 0.1V applied across varying distances. Results show a linear trend so that the resistance increases with the distance probed, and resistivity remains constant as the particle has a uniform composition.*

### 4.2.2   Results from resistivity measurements of the oxide for Zircaloy-2 LK3 after 3,6 and 9-cycles

The full oxide thickness formed on the examined cladding, after 3 cycles, 6 cycles and 9 cycles in reactor, is 4.4 µm, 14.0 µm and 46 µm respectively. However, the interest of the research focuses on the last oxide formed on the cladding since that is the oxide formed at that stage of life and is expected to be the oxide which dictates subsequent oxidation/HUP. This layer in the case of Zr and its alloys is

always the last layer in contact with the metal-oxide interface. For this reason, the property of the oxide in the vicinity of the interface is of interest for the understanding of the mechanisms involved in oxidation and hydrogen uptake. This allows a direct comparison of the oxide formed at low, intermediate and high burnups.

Tables containing the resistance measurements for the various electrodes and their respective minimum oxide thicknesses for all materials and all campaigns can be found in appendix A. From those results, the resistivities could be calculated as described section 3.2.5. In each table, as well as the minimum thickness measured under each electrode and the measured resistance of that electrode, there is the lower and higher calculated resistivity values (calculated from a minimum or maximum area). Then a resistivity value taken from the average of these possible minima and maxima is provided.

To best display the data first the results for each of the three materials are shown separately and then together. These are shown as Figure 4-5, Figure 4-6 and Figure 4-7 for the 3, 6 and 9 cycle respectively. For each material four graphs are given (as a, b, c, d in the figures). a) and b) both show the resistivity vs the minimum oxide thickness however, in the case of b) just showing the values at thin oxide thickness to ease visualisation. The 'average resistivity' values are displayed in these graphs. c) shows also the resistivity vs the minimum oxide thickness data but on a log scale. Please note that while it appears that some resistivity values are close to zero for some oxide electrodes; this is an effect of the units. And it must be kept in mind that even the lowest resistivity values for oxide regions, which are in the range of $10^{-2}$ $\Omega.m$ are still 5 orders of magnitude higher than that of the reference electrodes (metal-metal). The resistivity of zirconium metal is in the range of $10^{-6}$ $\Omega.m$. This comparison can be clearly viewed in d). Figure 4-8. shows all the data points for the 3 materials on the same graph for comparison. They are laid out in the same way as Figure 4-5, Figure 4-6 and Figure 4-7.

In Figure 4-5 (3-cycle material) two separate regions can be seen, the points before 1500nm show a lower resistivity which increases with distance away from the interface. The points after this distance appear to plateau at approximately 6000 $\Omega.m$. In the first region the points show a parabolic trend although there is some observed scatter. In Figure 4-5 some points have a lower resistivity than other measured points at similar distances, for example two points approximately 2000nm into the oxide and some closer to the interface. These could be caused by undulations i.e. a smaller distance of oxide being present under the electrode than was measured as it could have been missed if a jagged 'jigsaw' interface existed with a region of metal extending under the electrode. Another possibility is the existence of metallic SPPs which could shorten the distance of resistive oxide under the electrodes (more likely in shorter distances of oxide of few hundred nanometres). This point is further discussed

in the discussion section for this chapter. In Figure 4-6 (6-cycle) there appears to be a difference between the first and second trial. From the first trial, it seems that there is an inner more conductive region until roughly 100nm, which also follows a parabolic trend. However, from the second trial no such region can be clearly seen except a few points with lower resistivity 200nm into the oxide. A plateau region is again seen at higher distance from the oxide but at higher resistivities with more scattered results than the 3-cycle. In Figure 4-7 (9-cycle) an inner more conductive region can also be seen until a distance of less than 800nm. Then again a plateau with a similar resistivity to the 3-cycle but a larger scatter. The results will be discussed in the following section.

**Zircaloy-2 LK3 (3 cycle)**
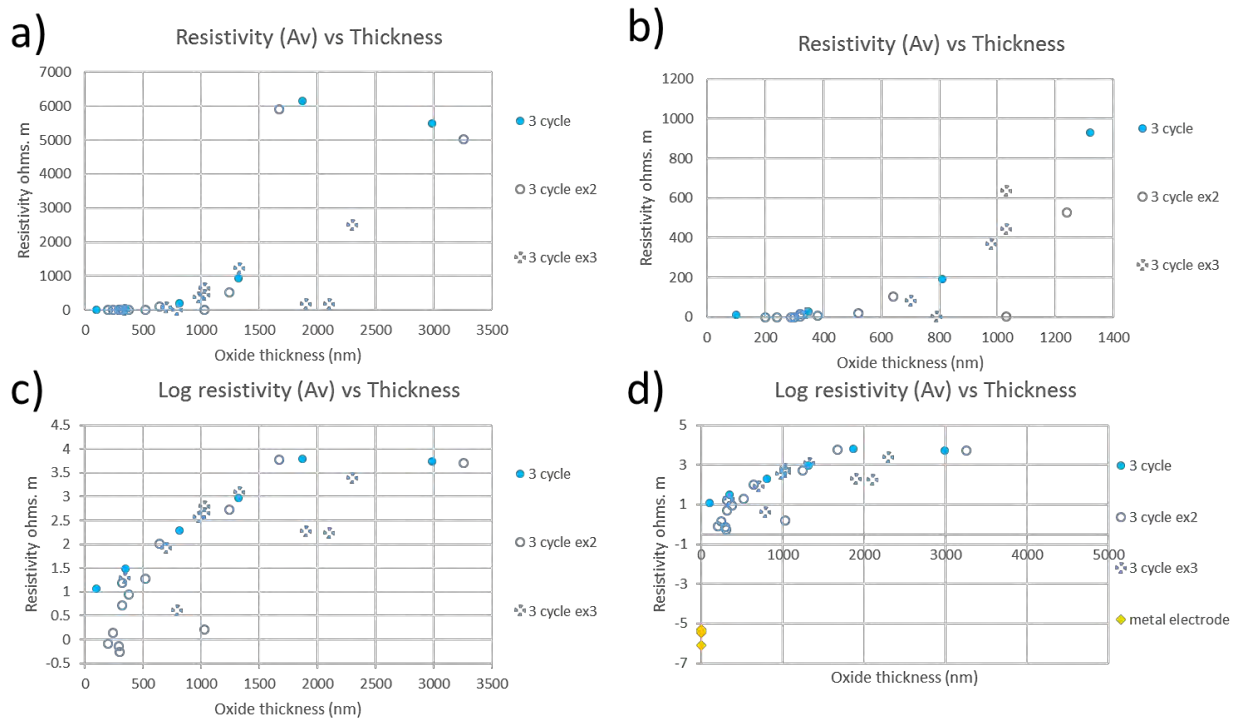


*Figure 4-5.a) graph showing the resistivity vs minimum oxide thickness for 3 cycle Zircaloy-2 LK3 oxide. b) Is a selection of points from graph (a) expanded to show the trend at thin oxide thicknesses. c) Graph showing the log of resistivity vs minimum oxide thickness for 3 cycle Zircaloy-2 LK3 oxide. d) Same as graph (c) but also including the resistivity values of the Zr reference electrodes for reference. Each point is a different electrode on the oxide wedge.*

**Zircaloy-2 LK3 (6 cycle)**
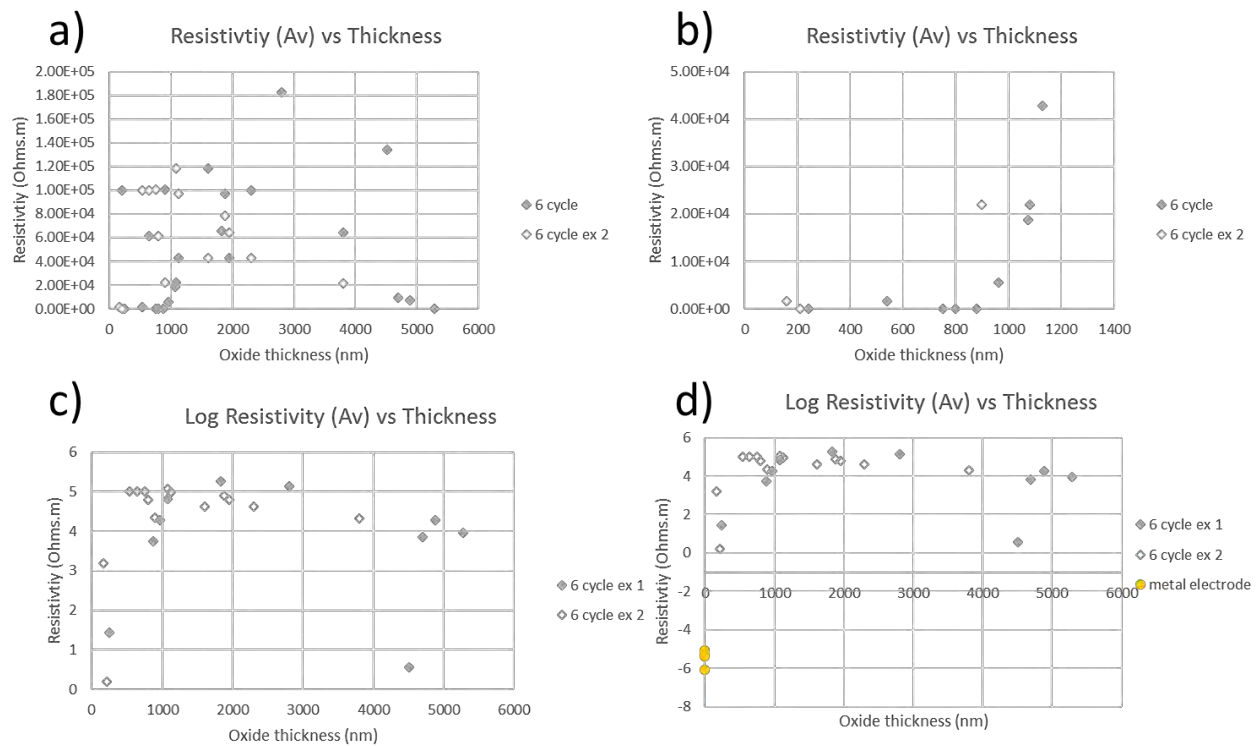


*Figure 4-6. a) graph showing the resistivity vs minimum oxide thickness for 6 cycle Zircaloy-2 LK3 oxide. b) Is a selection of points from graph (a) expanded to show the trend at thin oxide thicknesses please note the change in scale compared to Figure 4-5b and Figure 4-7b. c) Graph showing the log of resistivity vs minimum oxide thickness for 6 cycle Zircaloy-2 LK3 oxide. d) Same as graph (c) but also including the resistivity values of the Zr reference electrodes for reference. Each point is a different electrode on the oxide wedge.*

**Zircaloy-2 LK3 (9 cycle)**
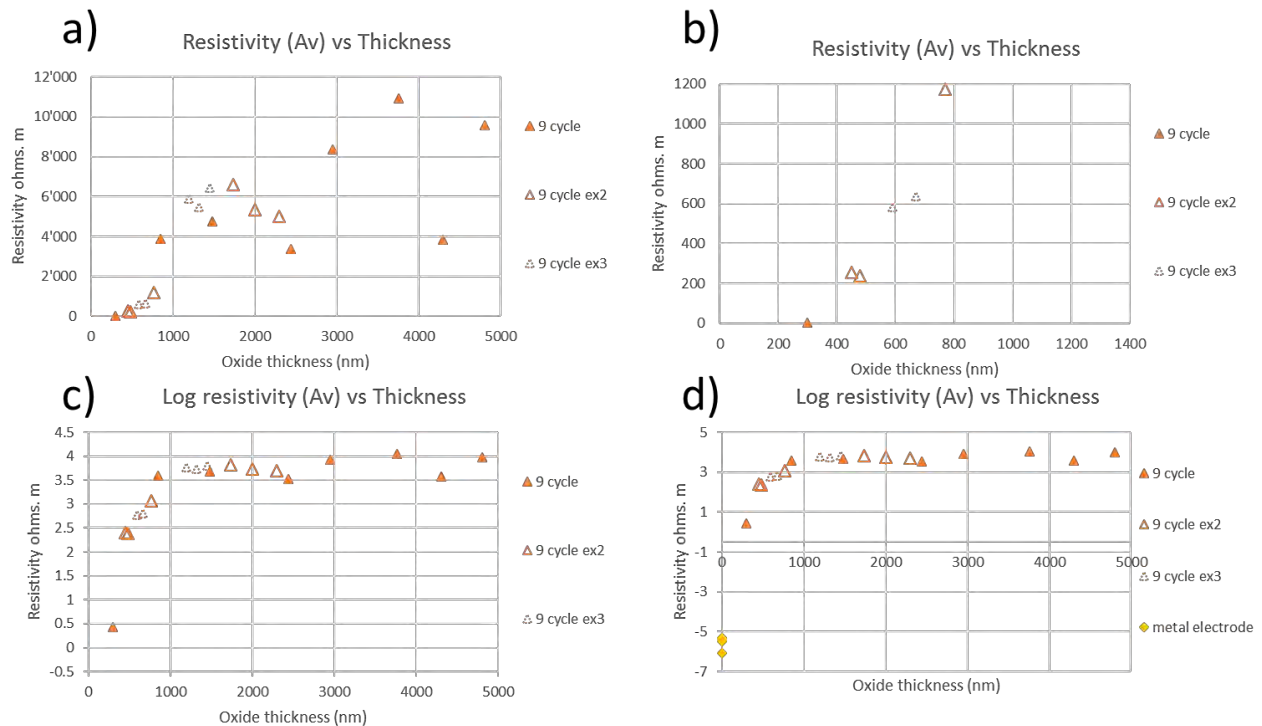


Figure 4-7. a) graph showing the resistivity vs minimum oxide thickness for 9 cycle Zircaloy-2 LK3 oxide. b) Is a selection of points from graph (a) expanded to show the trend at thin oxide thicknesses. c) Graph showing the log of resistivity vs minimum oxide thickness for 9 cycle Zircaloy-2 LK3 oxide. d) Same as graph (c) but also including the resistivity values of the Zr reference electrodes for reference. Each point is a different electrode on the oxide wedge.

**Zircaloy-2 LK3 (3,6 and 9 cycle)**
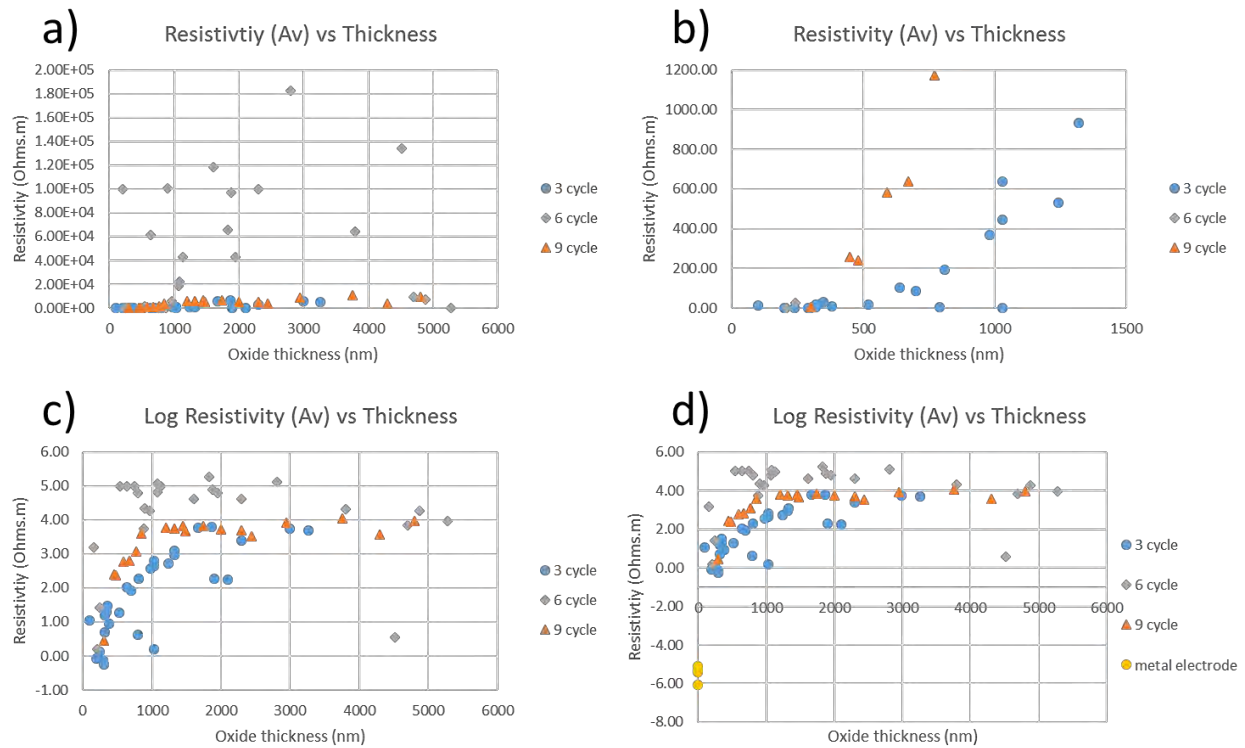


*Figure 4-8. a) Graph showing the resistivity vs minimum oxide thickness for 3,6 and 9 cycle Zircaloy-2 LK3 oxide which are displayed as blue circles, grey diamonds and orange triangle respectively. b) Is a selection of points from graph (a) expanded to show the trend at thin oxide thicknesses. c) Graph showing the log of resistivity vs minimum oxide thickness for 9 cycle Zircaloy-2 LK3 oxide which are displayed as blue circles, grey diamonds and orange triangle respectively. d) Same as graph (c) but also including the resistivity values of the Zr reference electrodes for reference. Each point is a different electrode on the oxide wedge.*

# 4.3 Discussion

### 4.3.1  The scope of the micromanipulator technique

The advantages of the current method are as follows:

I.    The technique so far has shown good repeatability within the scope of measurements, the deposition of Pt electrodes facilitates the use of micromanipulator and the confidence about the complete and repeatable contact between the micromanipulator and the sample. Performing the experiment within the SEM makes it possible to visualise the placement of micromanipulator and its contact with electrodes.

II.   The small scale of this experiment allows the probing of exact locations within the oxide; this gives local resistances for known thicknesses of oxide.

III.  The micromachining with FIB allows selecting the regions of interest with accuracy and creating electrodes at sensitive regions of the sample.

IV.   This setup has shown the possibility of direct resistivity measurements for irradiated samples.

V.    As it is possible to create miniature cross sections, it is possible to demonstrate that at very small distance from the metal-oxide interface, the samples of the same material after different residence times will not behave similarly.

In the following, the precautions to be taken to provide a satisfactory experiment are listed:

I.    The sample preparation and the FIB polishing will influence the amount of damage induced by ions and the quality of surface. Which in turn could modify the properties of the oxide and its resistivity. Therefore, care should be taken to provide a surface that is as clean and intact from ion implantation and amorphization as possible.

II.   With many cables and electronics of micromanipulator inside the SEM, care must be taken to install the micromanipulator in correct positions on its stage, with respect to the SEM gun and to consider that the displacement of micromanipulator should be within the range that is tolerated in the SEM.

III.  The metal-oxide interface of different alloys and after different stages in the reactor, have

very variable morphology. This would lead into a more or less undulated oxide at the interface. As an example, in the case of 3-cycle oxide a large variation of resistivity is observed for thinner oxides. This large variation can be directly correlated to the large undulation of the oxide at interface (as an example please refer to Figure 4-8, where a group of points between 200-300 nm show much lower resistivity and to Figure 3-8). The large undulations induce some uncertainty in the exact determination of the oxide thickness for thin oxides. Although the precaution should be taken to interpret the results, this is not a limitation of the technique but rather a specificity of the material examined in this study.

IV. The comparison of the resistivities measured by this technique with measurements performed by in situ EIS on unirradiated Zircaloy-4 and Zr 2.5%Nb [61] gives results that are not comparable. The results of that study give oxide resistivity in the range of 2-10 $M\Omega.$ m (for inactive materials) for oxide thicknesses in the range of 1-8 µm, that is to say 100-1000 times higher compared with current results. From the tables in Appendix A it can be observed that the maximum resistivity values are higher than the average values; and it might be more adapted to take that number. However, as the environment in which the materials are immersed will be different in the two cases, the influence of environment and temperature should not be neglected. As an example, the resistivity of deionized water is known to be quite high (in the range of 1.80E+07) [188]. This could influence the outcome of measurements. Furthermore, the in situ EIS is a bulk technique and cannot be compared with the current method, which shows a local high spatial resolution evaluation of these properties. To make further comments similar materials should be measured with the two techniques. Otherwise, it will not be possible to judge if the intrinsic properties of the regions studied are different, or the methodologies are causing this difference. It must be reminded that the current study is on irradiated materials, whereas the EIS was on unirradiated. Forsberg et al. [125] found a difference ranging from 10-50,000 times when comparing irradiated and non irradiated material so that the irradiated claddings showed a lower resistivity.

V. It is assumed all the current is traveling perpendicular to the electrode and metal-oxide interface whereas the actual path of the current cannot be known.

VI. These measurements are designed to examine the intrinsic properties of the material after different residence times, but it should be made clear that the oxide is expected to have differing resistivities in reactor (due to elevated temperatures, different pressures, different environment and irradiation conditions).

### 4.3.2 The influence of residence time on the resistivity of the oxide

The fact that the different samples show different results, under identical measurement conditions, indicates that the variation in results is a real observation. As was mentioned before, one of the hypotheses [42] regarding the mechanism of hydrogen uptake of a zirconium based fuel cladding is that the resistivity of the oxide has a direct relationship with the HPUF during oxidation. In other words, hydrogen pickup fraction would increase with increasing oxide resistivity. In the case of different cladding materials with different chemistry and heat treatment, prior to irradiation, this has been shown by in situ EIS [61]. The role of irradiation and residence time in-reactor on the semi-conducting properties of the oxide, remained to be verified. It is of interest to correlate the resistivity of the oxide with the change of HPUF for the same type of cladding material after different residence time.

Using the micromanipulator method, for the first time, the resistivity of oxide formed in-reactor on a Zircaloy-2 at low and extremely high burnups could be directly measured and compared. In Figure 4-8 the oxide resistivity is plotted against the distance from the metal/oxide interface for a Zircaloy-2 LK3/L after 3,6 and 9 cycles in reactor.

The observations from these results can be summarised as follows:

- Both the 3 and 9 cycle oxides have a region with lower resistivity close to the metal/oxide interface. Some data points could suggest this is also the case for the 6 cycle material but the results are more scattered.

- Within that region, the resistivity increases with distance, in the direction away from the interface, until plateauing with values in the range of 6-10 $K\Omega.\,\text{m}$ for the 3 and 9 cycle. while values approximately one order of magnitude higher are also seen for the 6 cycle oxide.

- The distance of these lower resistivity regions is not the same for all materials. Approximately this above-mentioned region extends up to a distance of 1500 nm in the 3-cycle material and 800 nm in the 9-cycle material. In the case of the 6-cycle cladding the increase to a higher value extends to not just one value but rather a difference between the two trials (hence regions) exists. High values of resistivity are seen both after 200nm into the oxide and 1000nm into the oxide.

- As shown in Figure 4-8D, the conductivity of the oxide is much (5~6 orders of magnitude)

lower than that of metal.

***The role of oxygen content and chemistry of the oxide on resistivity***

Literature ([8], [32], [33], [64], [67]) has suggested that the oxide in fact consists of two different regions, an outer heavily cracked porous layer and an inner dense impermeable layer. It has been suggested that coolant can penetrate into these outer cracks and hence only the inner dense layer, predominantly acts as a barrier to the penetration of oxidizing species [8], [32], [33], [64], [67]. The inner dense layer would then be an oxygen diffusion layer, and hence an oxygen vacancy gradient formed across this region, following a parabolic trend could be expected with the highest vacancy concentration being at the metal/oxide interface [189], [190]. It has been shown that sub-stoichiometric zirconium oxide has a higher conductivity than stoichiometric oxides [116]–[118]. $ZrO_{2-x}$ acts as an n-type semiconductor, as fully ionised vacancies will act as electron donors increasing the electronic conductivity of the material [116]–[118]. The same observation has been widely reported on titanium oxide ([191]–[193]) which is known to share many similarities with zirconium oxide. Other metal-oxide systems such as ZnO have also been shown to exhibit similar behaviour [194]. If there was a diffusion governed dense inner oxide layer it could be expected that the conductivity of this region would also follow a parabolic curve with highest conductivity (hence lowest resistivity) closest to the metal/oxide interface, where the highest oxygen vacancy concentration exists. This is the case for the 3 and 9-cycle materials. There could be several reasons such a region may not be so clearly seen in the 6-cycle sample, the first being that if at that stage of life the material had just gone through transition, or was going through, there may not be such a large diffusion layer present. Secondly the intrinsic oxide resistivity may be higher due to the morphology or microstructure of oxide. It should also be noted that the oxide is not uniform and especially with the well developed oxide at higher burnups it could be possible that certain areas of oxide are at different stages of life. For example if in a certain area a large crack was found this might mean at that place no protective oxide has been built up.

Although the cuts under each measurement have not been individually chemically and structurally characterised, complementing results obtained using different characterisation techniques help to further interpret the current results. For instance, thorough chemical analyses of the metal-oxide interface in the 3,6 and 9 cycle clads have been performed using EPMA, as well as TEM on the 3 and 9 cycle samples, to examine the chemistry across the interface [64]. The oxygen concentration from EMPA data with spatial resolution between 200-300nm is given in Figure 4-9 to provide a comparison between the three materials, with particular interest in the region close to the metal/oxide interface,

published in [64]. As can be seen in Figure 4-8b) for the 3-cycle material, we do detect a parabolic trend for the intrinsic resistivity of the material. In the case of the 9-cycle sample, the same is valid although extended to a shorter distance. It could be argued that such a trend is also seen in the 6-cycle material particularly from the first campaign on this material. This trend of increasing resistivity matches well, for the 3 and 9 cycle samples, with the oxygen profiles obtained from the EPMA measurements performed on the same samples, shown in Figure 4-9. As it can be observed, the oxygen profile in the case of the 3-cycle cladding increases to the stoichiometric oxide at a longer distance, compared to the 9-cycle oxide. In other words, the oxygen diffusion profile exists for all samples; but is extended to a shorter distance in the 6-cycle sample and shorter again for the 9-cycle sample. Surprisingly, the distances are quite similar even when measured by these two very different techniques, of two very different properties (i.e. the chemical composition and the resistivity). Here, the comparative behaviour is sought, rather than the exact quantitative values.

The correlation between the sub-stoichiometric oxide regions and their resistivities, together with the knowledge that oxides with higher oxygen vacancy concentration (sub-stoichiometry) show lower resistivity as seen in [116]–[118] leads to the suggestion that in this case it is oxygen vacancies that lead to the existence of a more conductive region, close to the interface. This observation suggests that i) the materials have an inner dense region governed by diffusion; ii) the size of this diffusion layer decreases with time in reactor. The positive finding of this study is that the diffusion layer is still present and relatively large in the case of the 9-cycle material, which is a material used as an experimental sample for exploring the limits of performance of this cladding and its residence time is beyond design [9]. However, the current measurements demonstrate that even the 9 cycle material still does show a more conducive region that will protect the underlying metal; Nevertheless, with a different kinetics being present between 3, 6 and 9 cycles.

It should be noted that these samples are 'snapshots' of the evolution of this cladding material in reactor and it is expected that the oxide and the protective part of it are constantly changing. It is expected that these samples will be going through a cyclical process of build up of protective oxide which, if it is free enough from cracking and porosity, will act as diffusion barrier to further oxidation and H uptake. Then break down of this barrier, followed by the subsequent build up of new protective oxide. As previously discussed in section 2.3.3 due to the difficulty of working with material from reactor there is a limited number of data points and hence it is not possible to know for each of these samples exactly where the sample is in relation to its evolving oxidation kinetics.

It has been demonstrated that most alloying elements dissolve from the secondary phase particles (SPP) and increase the matrix concentration of each element [69], [73]. It is clear that alloying

elements could also have an impact on the conductivity of the oxide if they are in solution. However, knowing that all alloying elements could play a role and their effects could also cumulate or counter balance each other [42] once their concentrations increase in the oxide as a function irradiation, their impact will require a much more in depth analysis and is outside the scope of this study. Certain facts however can be assumed. If large SPPs remained metallic it is possible these could act as metallic short circuits for electrons through the resistive oxide. In the 3-cycle sample many remnant SPPs containing mostly Cr could still be seen [69], [73]. Cr containing precipitates have shown a delayed oxidation with respect to the matrix, at early stages of their oxidation [16]. Whereas in the 6 and 9-cycle materials these would mainly have dissolved. This lowering of resistivity may be seen from results when a point less than 200nm of oxide thickness displays a much lower resistivity (Figure 4-5). However, it could also be due to the undulated metal-oxide interface of such material at low burnups, as seen in the case of 3-cycle LK3/L.

Another way the alloying elements may affect this parameter is that according to the C4 model [42], [195] Fe could act as a dopant in the oxide and compensate for space charge if it was found in an oxidation state of 2+ or 3+, but in a concentration level that can satisfy that model. Normally Fe would not be found in the matrix in high enough quantities for this (as was the case in that study [195]) , but with the enriched matrix due to irradiation and SPP dissolution it may become more of a possibility. However, from the studies of Baris, et al.[64] , it can be seen that the Fe concentration near the interface shows an opposite trend to what would be in favour of this suggestion. Meaning that the more conducting 3-cycle interface has much less Fe than the least conducting 6-cycle interface.

***The role of the structure of the oxide on resistivity***

Further to the chemical analysis, the microstructure of the metal-oxide interface has been analysed in depth and it has been demonstrated that the 9-cycle oxide near the interface is much more porous, as mentioned before for the crack volume fractions, please refer to chapter 2 section 2.4.1. The role of porosity on the different properties of the oxide has been discussed [196], [69], [73],[23]. It was shown that the porosity increases the resistivity of the oxide [196]. Therefore, it can be concluded that at least two factors are clearly at the origin of the differences of conductivity between the materials. The stoichiometry of the oxide in the vicinity of the interface, with the 9-cycle oxide having a thinner sub-stoichiometric region, and a higher oxide porosity. The case of 6-cycle seems to be also correlated to the above phenomena. However, the trend is not homogeneous.

One more factor, which has been the topic of several studies in the field of oxidation of Zr based alloys, is the ratio of tetragonal zirconia present in the oxide film and its impact on the oxidation. To correlate

this crystallographic property to the conductivity, seems to be a big challenge, for that it is necessary to perform direct measurement at nanometric scale of the two properties (crystal structure of the oxide and its conductivity), and if possible simultaneously or in parallel. Such measurements will be very demanding. Therefore, bulk data here from the literature on these alloys given in section 2.4 of the literature review will be discussed.

The crystal structure of the 9-cycle cladding has been object of a study in the laboratory [66] by synchrotron radiation. The major oxide phase observed has been reported to be monoclinic $ZrO_2$ and a very small ratio of tetragonal has been revealed by Micro-XAS analysis. This small phase has been mainly observed in the vicinity of the interface, however, not on a uniform and homogeneous distribution all along the interface. The results obtained in the laboratory for 3-cycle cladding show similar behaviour but with a slightly higher volume fraction of tetragonal (the exact ratio of tetragonal to monoclinic is not calculated due to its small quantity). These observations lead to the conclusion that the two oxide layers (of 3 and 9-cycle) near the interface have mainly a monoclinic crystal structure, however a slightly higher proportion of tetragonal is present in the low burnup oxide. Therefore, as the measurements cover quite large areas and knowing that the measurements are repeated for 3 consecutive campaigns, the statistics are sufficient to provide a representative image of the average crystal structure of the two oxide layers; including the statistically present tetragonal phase in each case. In other words, it can be claimed that the measurement probes monoclinic zirconia with a given ratio of tetragonal in both cases. Unfortunately such data is not available for the 6 cycle cladding however it would be very surprising if the ratio of tetragonal to monoclinic was massively different from what is seen in the 3 and 9 cycle claddings.

It must be noted that the bulk tetragonal zirconia known in the industry, is always stabilised by large concentrations of different oxides such as yttria, scandia, or ytterbia. Therefore, their composition is not comparable to the phases observed in Zr claddings. Furthermore, their conductivity could not be used as a comparison.

***Correlation of results to HUP***

One other aspect of corrosion can be discussed in the following. Oxidation of Zr based alloys, in particular in the case of autoclave oxidation, shows a cyclic behaviour [11], [197], meaning that the oxidation process starts at a given rate, it reaches a maximum and then slows down to a minimum rate. In such cases, it has been shown that the correlated hydrogen uptake has a delayed behaviour, either lagging behind and most often increasing in such conditions. This behaviour can be well

revealed in autoclave, where the number of samples collected are very large and the oxidation time between two samples can be quite short. In the case of reactor samples, such frequent and condensed sampling methods are not conceivable and samples are scarce. Thus, these corrosion cycles can't be revealed in the same manner. A fuel rod, is extracted from the reactor after a certain number of years (cycles), and the oxidation stage could be anywhere in between two periods. Furthermore, it is possible that such behaviour is even absent in reactor. Therefore, in the case of the 6-cycle cladding, the different campaigns performed on different regions of the specimen, could, to some extent reflect these differences. In the case of the 9-cycle however, the overall trend, does seem to go in the direction of smaller conducting distance in the 9-cycle oxide compared to the 3-cycle.

The presence of zirconium monoxide has not been detected in the claddings studied here. Therefore, the measurement of a ZrO particle has been carried out only as reference, as reported in the chapter of results. It is also worth noting that the resistivity of this ZrO phase is 5 to 6 orders of magnitude smaller than the oxide at the interface, which means that it is much closer to metal, than to the most conducting oxide measured in the current studies.

Having measured the resistivity profiles of the material after three different residence times, it is necessary to determine the correlation between the variation of resistivity and the variation of hydrogen pickup fraction (HPUF) of the cladding for these two different residence times. The HPUF of these claddings is determined in previous studies. It is observed that the HPUF of the 3, 6 and 9 cycle materials is approximately 17%, 34% and 30% respectively. It is interesting to note that the HPUF is even higher for the 6 cycle than for the 9-cycle sample.

From all our observations and the discussions above, it can be concluded that the material has changed behaviour; leading to different properties, including a change of resistivity. It is demonstrated to a great extent that this change is a consequence of the change of composition (i.e the oxygen concentration of the zirconia as well as the variation of alloying elements present in the oxide at the metal-oxide interface) and the change of micro-porosity. The fact that the resistivity near the interface changes from interface until a distance of 800nm and 1.5 µm (for 9-cycle and 3-cycle respectively), means that close to the interface, an inner, more electronically conductive, layer of oxide is formed. In general, this study has confirmed that the resistivity of the 6-cycle and 9-cycle cladding close to the metal-oxide interface (as an example at a distance of 500 nm from the metal-oxide interface) is higher compared to the 3-cycle sample. This finding corresponds well to the hypothesis that resistivity of the oxide near the interface plays a role on the HPUF and increased resistivity will increase the HPUF.
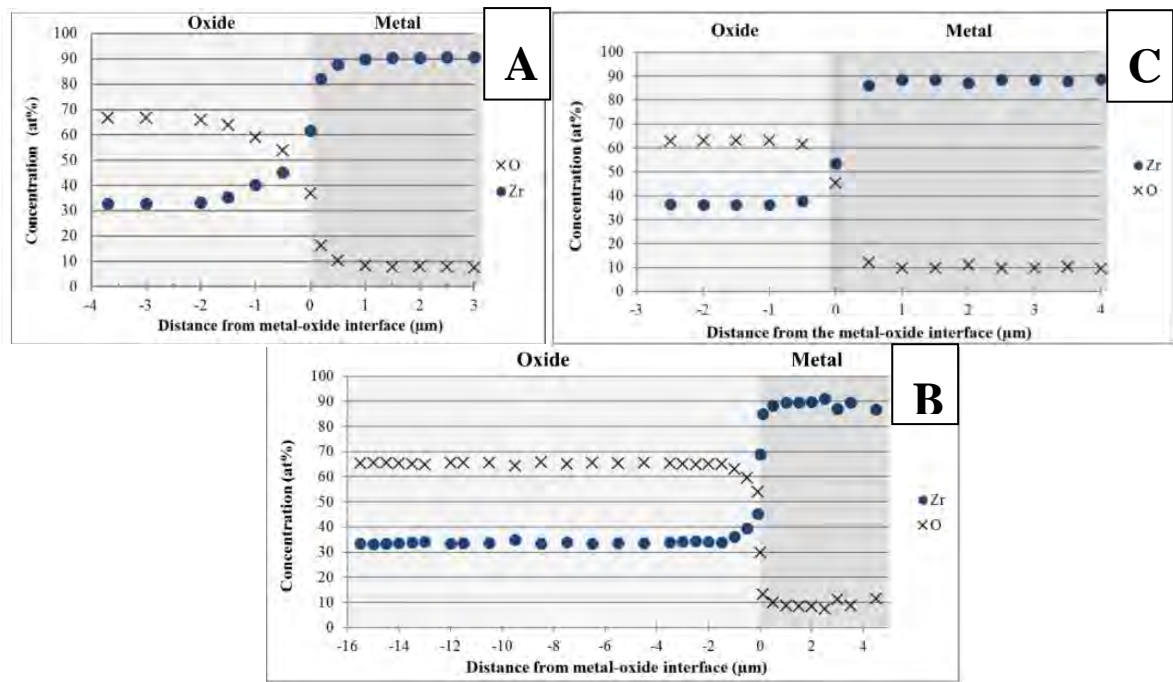
Figure 4-9. EPMA data of the Oxygen concentration in the vicinity of the metal/oxide interface. a) shows the 3-cycle material , b) shows the 6-cycle and c) shows the 9-cycle material. A much longer region of sub-stoichiometry can be seen for the 3-cycle material. Spatial resolution is 200-300nm for these measurements. These figures are extracted from ref [64].

# 4.4 Conclusions

- The intrinsic resistivity of oxide in the vicinity of the metal-oxide interface varies as a function of distance from the interface.

- An inner more conductive region has been identified in the oxide close the interface.

- Above a given oxide thickness, the value of resistivity plateaus although some scatter is still observed as a function of thickness.

- The resistivity of the 6-cycle and 9-cycle cladding at a given distance from the interface, before the values reach the plateau, is higher than that of 3-cycle cladding.

- The values of maximum resistivity seem to be similar between the 3 and 9-cycle materials, however higher values are reached in the 6-cycle material.

- These findings agree with the hypothesis that the increased hydrogen pickup fraction can be correlated to the increased resistivity of the oxide at a given distance from the interface.

- The comparison of results with previous studies on the same set of materials (by means of electron microscopy, 3-D FIB and EPMA) shows that the cause of this increased resistivity is an increased oxygen stoichiometry and in general chemical compositional changes in the oxide, and also owing to an increased micro-crack and micro-pore in the microstructure.

# Contents of chapter 5:

# 5 Micro-mechanical testing

## 5.1 Introduction

In this chapter, the evolution of the intrinsic mechanical properties, both in the metal and the oxide of Zirconium-based fuel claddings, will be discussed. As stated in the literature review if the oxide is intrinsically not strong enough to withstand the stress, cracking may already happen in the newly grown protective oxide. This weakening of the newly formed oxide could come from the introduction of porosity or other defects [64], [137]. Large scale cracking of the inner newly formed oxide would be disadvantageous as it may suggest that it is impossible to have any notable distance of protective oxide to act as a diffusion barrier, and hence oxidation and hydrogen uptake could occur uninhibited. Because of this, there is an interest in the intrinsic mechanical properties of the interface region of different alloys, and the manner in which they change with residence time under irradiation. Building on the previous micro-pillar work mentioned in section 3.2.4, further micro-mechanical testing was carried out with the aim to quantify both the strength and Young's modulus of different regions in two different alloys. Both metal and oxide pillars were tested and for the sake of continuity the term 'strength' will be used for both. However, it should be kept in mind that due to the difference in failure mechanisms between metals and ceramics the terms yield strength (metal) and fracture strength (oxide) are the appropriate terms.

In this chapter, an autoclaved and a 6-cycle Zircaloy-2 will be compared with those previously studied in [137]. In addition to those, a low-tin Zircaloy-4 material will be reported, both an autoclaved sample and a 4-cycle material, irradiated in a PWR. This was to add further insight into the variation between irradiated and non-irradiated materials and compare the behaviour of a different alloy in a different reactor type. Further details of the materials examined are available in chapter 3.1.1 and 3.1.4. The technique is described in section 3.2.4.

Four different regions were examined for each sample:

1. Bulk metal
2. Oxygen saturated metal (i.e. the metal at the metal-oxide interface)
3. Newly formed oxide (i.e. oxide at the metal-oxide interface)
4. Bulk oxide

# 5.2 Results

## 5.2.1 Preparation and compression of micro-pillars

Figure 5-1a gives an example of positioning of the pillars in relation to the interface before the FIB rough cuts, and Figure 5-1b displays those pillars once the rough cut is finished. Figure 5-2a,b,c,d gives examples of four pillars prepared from the four different regions, for the Zircaloy-4 active 4-cycle sample. Figure 5-3 shows the same pillars as those in Figure 5-2 after the compression test. The same procedure was carried out for all 4 samples. As mentioned before, the dimensions of individual pillars are required to calculate the stress vs strain curves. Table 5-1 gives the average aspect ratios for each set of 7 pillars in the various regions for the four samples tested. It can be seen from that table that for a set of pillars in the same region, they are generally quite similar whereas some variation exists from region to region, e.g. from metal to oxide. This is mainly due to the fact that different regions have different properties, thus using similar milling parameters while FIBbing affects them differently. Care was taken to attempt to keep pillars as comparable as possible, but due to the changing material and the many FIB technical issues, this was not always possible.
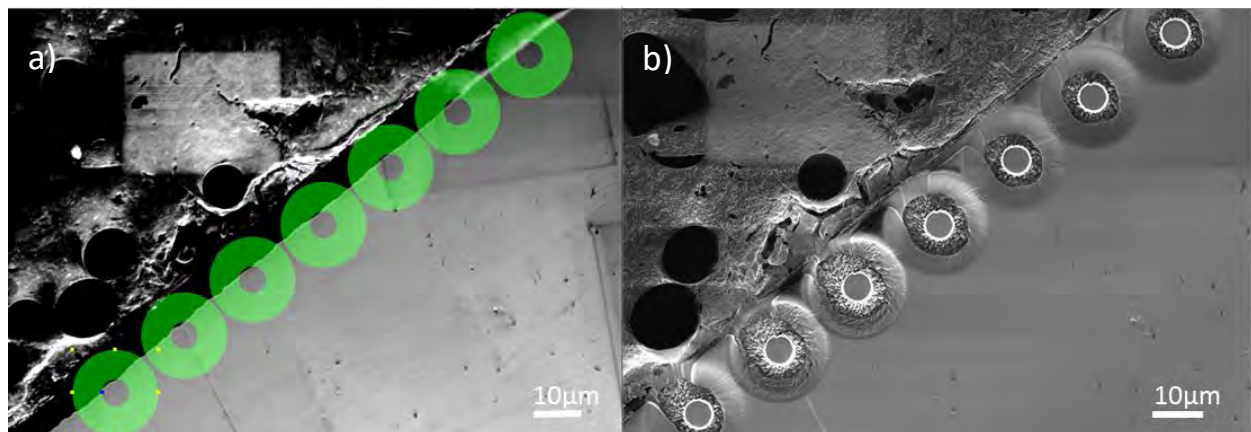


*Figure 5-1. The first steps of creating pillars for compression (example of Zircaloy-4, 4-cycle). A) shows the selection of areas to be milled in the rough cuts step here pillars are being made in the region of metal at the interface. B) the completed rough cuts to create pillars in the metal at the interface.*
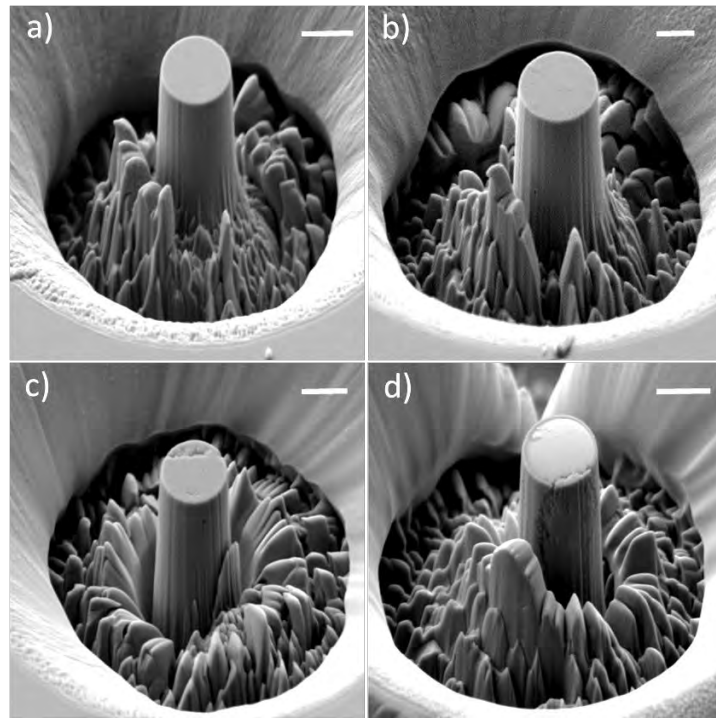
*Figure 5-2. Examples of completed and polished micropillars in the material low-tin Zircaloy-4 (4 cycles). A),b),c) and d) show pillars from different regions; bulk metal, metal at interface, oxide at interface and bulk oxide respectively. The scale bar in top right hand corner corresponds to 2µm for all.*
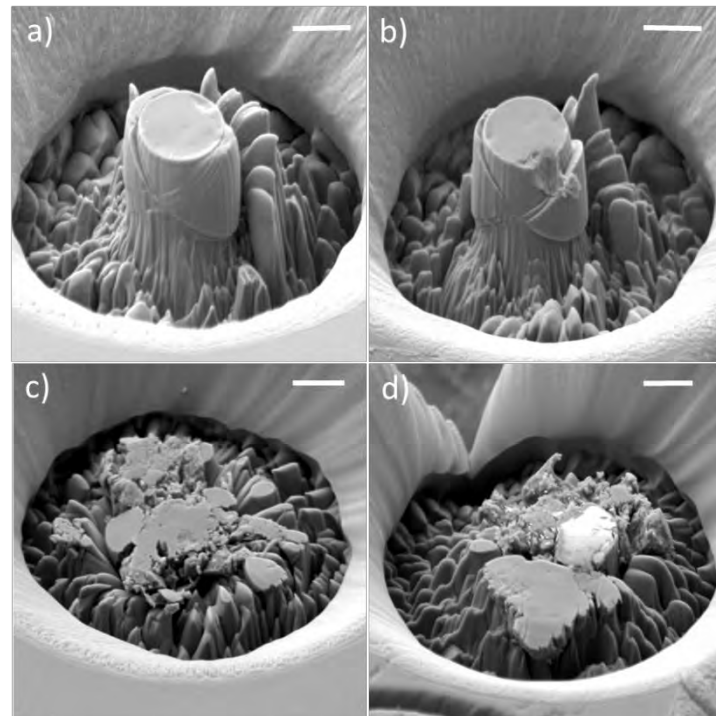


*Figure 5-3. The same pillars from the material low-tin Zircaloy-4 (4 cycles), shown in Figure 5-2, after compression. A),b),c) and d) show compressed pillars from different regions; bulk metal, metal at interface, oxide at interface and bulk oxide respectively. The scale bar in top right hand corner corresponds to 2µm for all.*

*Table 5-1. The average aspect ratios from seven pillars in a similar region for each of the four samples as well as the standard deviation of those values. 'IF' is short for interface*

| Sample name | Position | Aspect ratio | Error |
|---|---|---|---|
| **Low-tin Zircaloy-4 (autoclaved)** | Metal | 2.45 | 0.22 |
| | Metal at IF | 1.95 | 0.14 |
| | Oxide at IF | 2.04 | 0.04 |
| | Outer Oxide | 2.04 | 0.06 |
| **Low-tin Zircaloy-4 (4 cycle)** | Metal | 1.73 | 0.17 |
| | Metal at IF | 2.10 | 0.06 |
| | Oxide at IF | 1.97 | 0.07 |
| | Outer Oxide | 1.88 | 0.13 |
| **Zircaloy-2 LK3/L (autoclaved)** | Metal | 2.12 | 0.42 |
| | Metal at IF | 1.76 | 0.09 |
| | Oxide at IF | 2.14 | 0.11 |
| | Outer Oxide | 2.11 | 0.05 |
| **Zircaloy-2 LK3/L (6 cycle)** | Metal | 2.25 | 0.03 |
| | Metal at IF | 1.67 | 0.09 |
| | Oxide at IF | 1.59 | 0.12 |
| | Outer Oxide | 1.62 | 0.06 |

Generally, a group of seven pillars were produced at the same time with the same parameters and hence would be quite similar. Occasionally, errors with the FIB caused the destruction of a pillar and extra pillars were subsequently created, still with similar parameters. When creating pillars in different regions i.e. metal or oxide, the same FIBing parameters would create different shaped pillars due to the difference in material. Therefore, different parameters were sometimes used for different areas in the sample. For example, longer dwell times were needed to mill the same depth in oxide as in metal. This meant that although effort was made to create the pillars as similar as possible, there exists some variation between pillars and particularly between groups of seven pillars. This can be observed in the variation in dimensions in Table 5-1. Another issue that should be taken into consideration is the drift from the sample while milling. This varies from sample to sample and result in a non-symmetrical pillar. Since the samples were embedded and fixed in the holder by screws, the drift was usually very small but sometimes noticeable, especially for longer milling times of the small

pillars. An example of where this appears to have occurred is given below as Figure 5-4 (pillar number two in the metal at IF for low-tin Zircaloy-4 autoclaved).
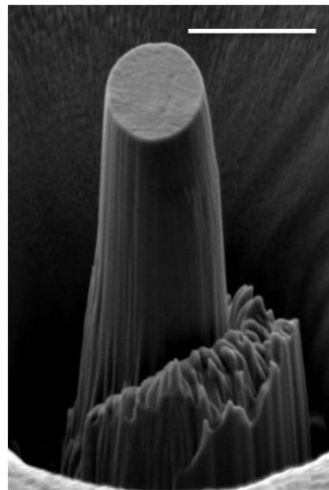


*Figure 5-4. Micro-pillar (labelled number 2 of 7) from the metal at IF region in the autoclaved low-tin Zircaloy-4, given here to illustrate one of the possible inconsistencies between pillars. It appears the the milling may have drifted or something else caused the slight non-symetry of this pillar. The scale bar corresponds to 3μm.*

### Location of interface micropillars

Since the pillars had a diameter of between 2-2.6 μm, the centre of the pillars were approximately 1.5-3 μm away from the interface both in the metal and in the oxide, while the bulk metal pillars were over 50 μm away. Care was taken to be close to the interface but to avoid having other phases in the pillars (i.e. to be in the metal and not contain any oxide). However, due to the large undulation seen in some of the oxides, the possibility of small amounts of unseen 'other phase' cannot be totally excluded. The distance of pillars in the bulk oxide from the interface of course varied with the size of oxide layer. In the tests on oxide, large displacements caused by pillar failure can be observed. This is due to the indenter tip going down rapidly after a failure of the brittle material, until the sensor could catch up and terminate the test.

### Observation of post compression micro-pillars

A clear difference can be observed in the post compression images (Figure 5-3) between the metal pillars and oxide pillars which can be explained by the brittle vs ductile response of the materials. It can be seen (in Figure 5-3) that for pillars in the metal after yielding, there is some plastic deformation whereas for oxide pillars there is brittle failure. These behaviours are characteristic and expected, both for the ductile metal and for brittle ceramic.  From the compression tests, the load vs displacement data is available; by using the measured dimensions of each pillar, the stress and strain can be

calculated using method and equations given in section 3.2.4. By looking at the post compression pillars and correlating them to the test results, certain pillars were excluded due to a failed test or a buckled pillar. For the set of 28 pillars, 1-3 would generally have to be excluded. For example, in the data displayed in Figure 5-5 and Figure 5-6 pillars 1 and 6 had to be excluded from the set in the metal at the interface due to invalid tests.

## 5.2.2  Load-displacement and subsequent stress-strain curves

In this section, the load-displacement data and the caclulation of stress-strain curves are described. The stress-strain curves are shown in Figure 5-5 for the low-tin Zircaloy-4 (4 cycle) obtained from the four different regions, viz. bulk metal, metal at the interface, oxide at the interface, outer oxide. It can be seen from those compression results that initially there is a (relatively) straight steep increase in stress with small amount of deformation, this is the region of elastic deformation (i.e. before yield). Figure 5-6 shows the same information but zoomed in on the initial part of the curve to show the region before failure. This region is used to calculate the Young's modulus. All metallic pillars, whether in the bulk metal or in the oxygen-rich metal, show an elastic region, with a yield point which is very reproducible, followed by a plastic region. The latter displays a bigger deformation capacity for the bulk metal. In the case of the oxide pillars, the situation is different which is expected knowing that the ceramic oxide will show a brittle fracture. Therefore, as the results show, the pillars show an elastic behaviour prior to failure, with a more scattered strength between the pillars.

As can be seen from Figure 5-5 and Figure 5-6, the start of this straight gradient is not always exactly at 0,0. This may be due to a slight misalignment of the indenter or a small angle mismatch between the indenter and pillar, which could be caused by the sample not being perfectly flat or some artefact on the indenter tip. Because of this, to calculate the Young's modulus, points at the beginning and end of the elastic region were excluded leaving only a straight gradient. Although it must be stated that because of the small size of the pillars and the imperfect nature of the material and tests, the gradient was not always perfectly straight hence a fit was used, which was generally very close to the data points.

The stress vs strain curves are also given here for the other three samples tested (autoclaved Zircaloy-4, autoclaved Zircaloy-2 LK3/L and 6 cycle) and are given as Figure 5-7, Figure 5-9 and Figure 5-8 respectively. The form of the curves is generally quite similar for the different regions over the samples tested however the values do differ indicating a change in material.
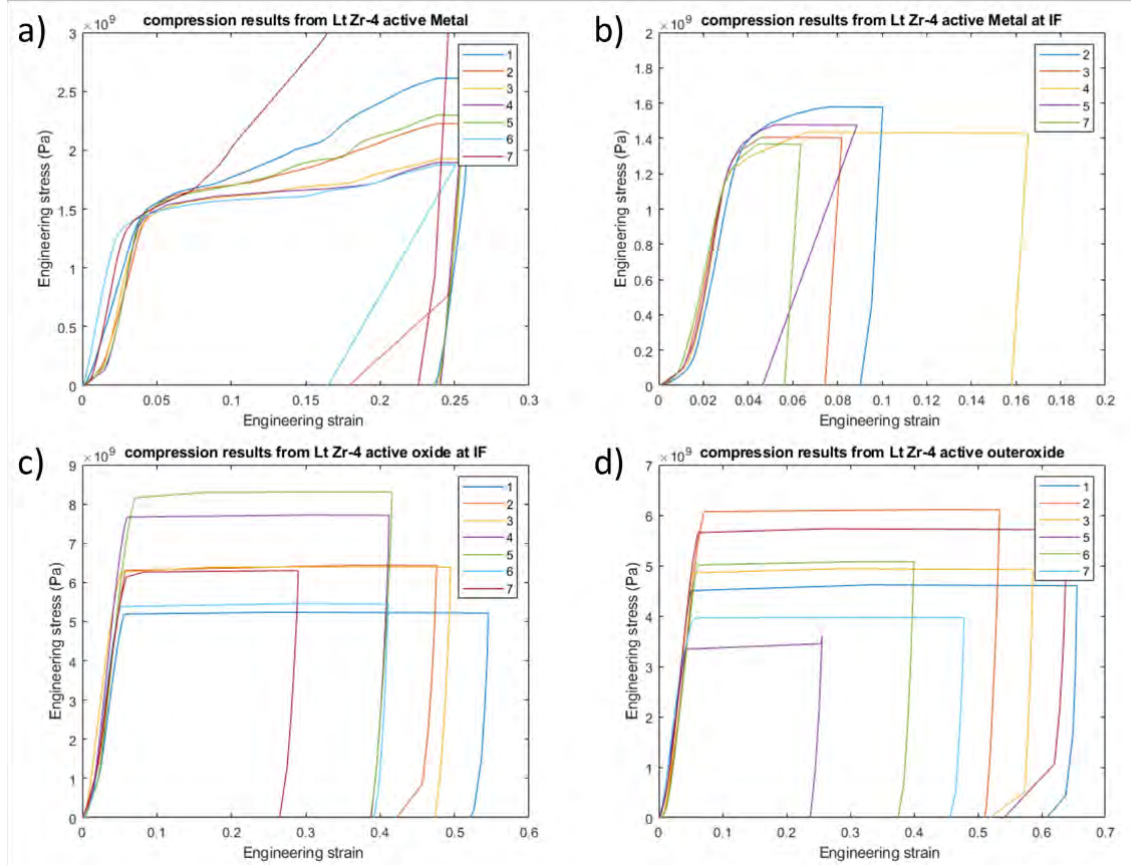
*Figure 5-5. Stress vs strain curves for the pillars in the four different regions tested in the 4 cycle low-tin Zircaloy-4. a) the results from the pillars in the metal region, b) the results from the pillars in the metal at the interface region because of inaccurate or incomplete tests test 1 and 6 are not included, c) the results from the pillars in the oxide at the interface and d) the results from the pillars in the bulk oxide.*

**4-cycle Low-tin Zircaloy-4**
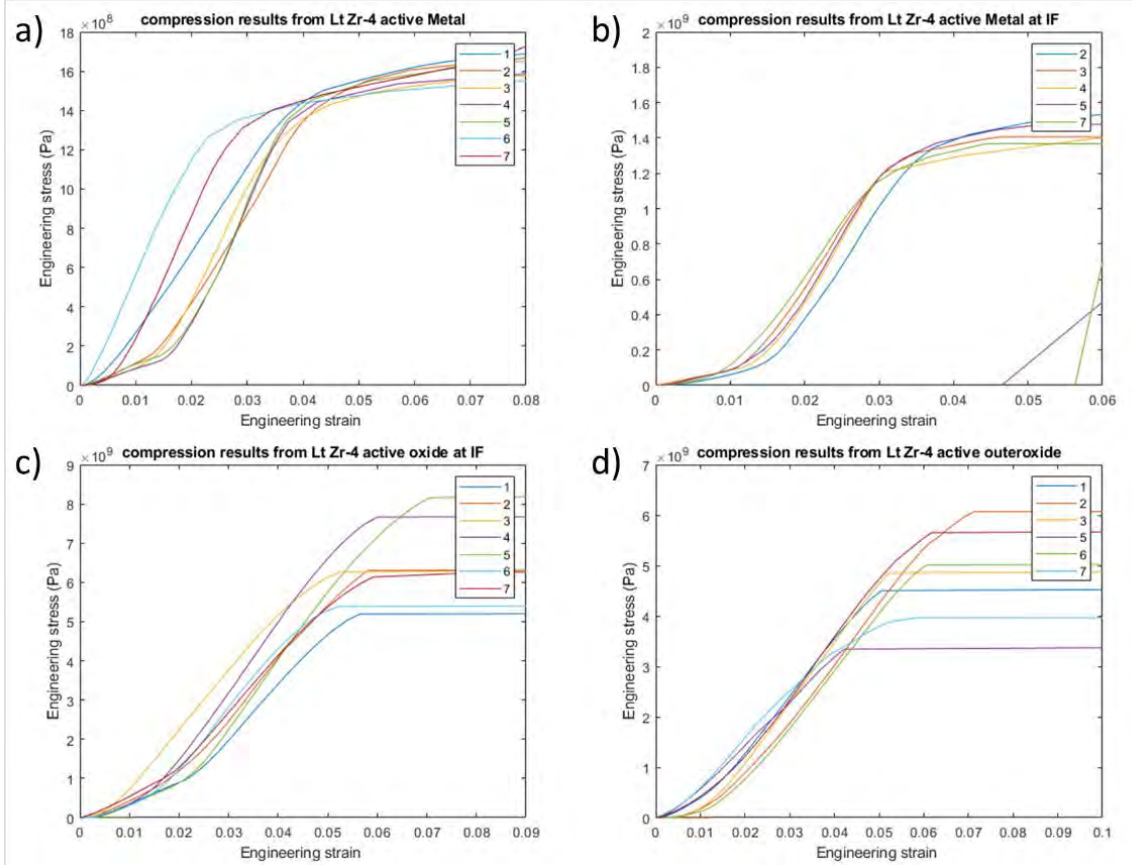


*Figure 5-6. Stress vs strain curves for the pillars in the four different regions tested in the 4 cycle low-tin Zircaloy-4 here the region before failure is focused upon from Figure 5-5. A) the results from the pillars in the metal region, b) the results from the pillars in the metal at the interface region because of inaccurate or incomplete tests test 1 and 6 are not included, c) the results from the pillars in the oxide at the interface and d) the results from the pillars in the bulk oxide.*
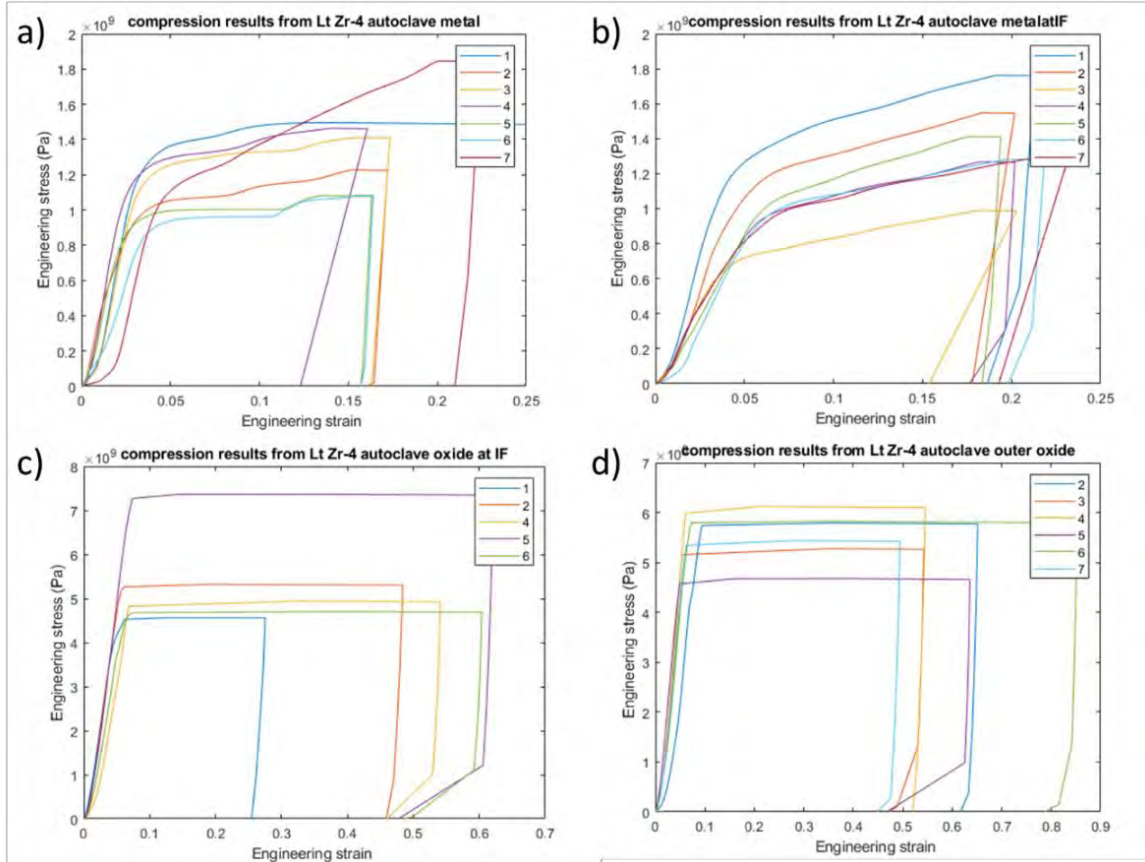
*Figure 5-7. Stress vs strain curves for the pillars in the four different regions tested in the autoclaved low-tin Zircaloy-4. A) the results from the pillars in the metal region, b) the results from the pillars in the metal at the interface region, c) the results from the pillars in the oxide at the interface because of inaccurate or incomplete tests test 3 and 7 are not included and d) is the results from the pillars in the bulk oxide. Due to inaccurate or incomplete tests, test 1 is not included*

**6-cycle LK3/L Zircaloy-2**
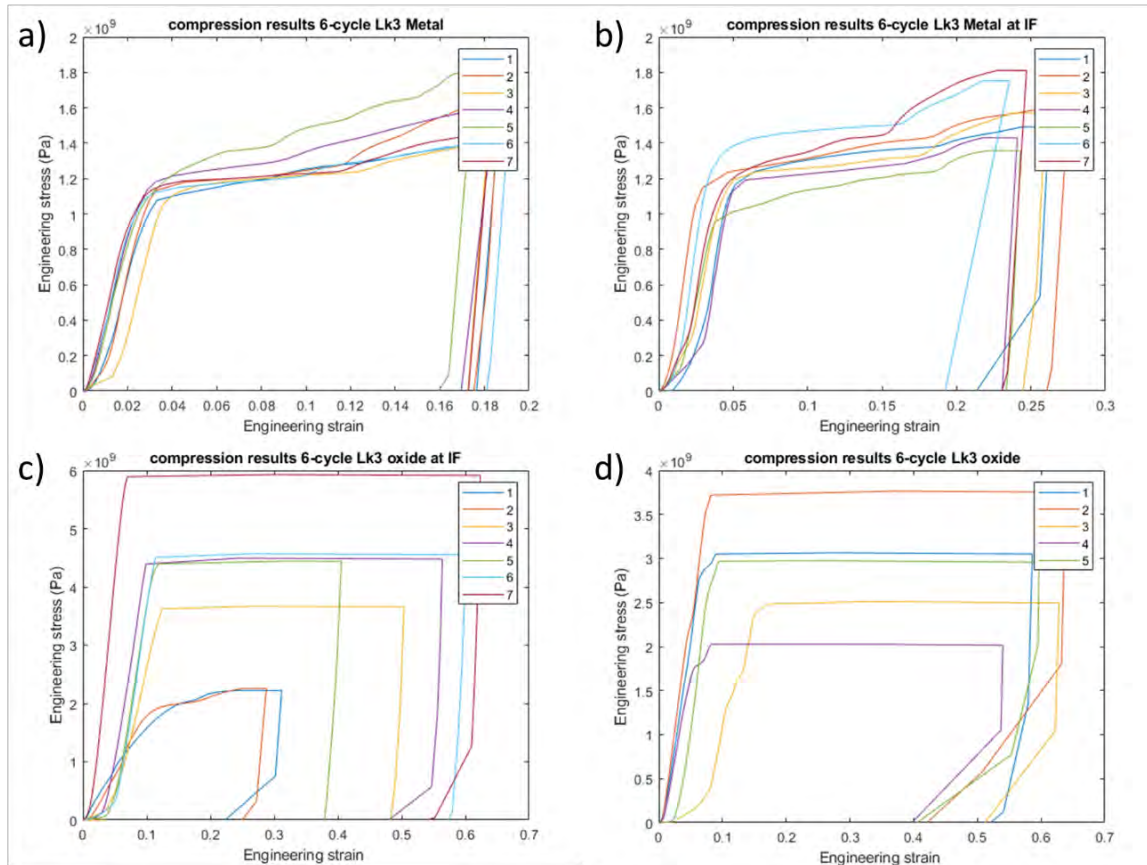


*Figure 5-8. Stress vs strain curves for the pillars in the four different regions tested in 6 cycleLK3/L Zircaloy-2. A) the results from the pillars in the metal region, b) the results from the pillars in the metal at the interface region, c) the results from the pillars in the oxide at the interface and d) is the results from the pillars in the bulk oxide. Due to inaccurate or incomplete tests, test 6 and 7 are not included*

**Autoclaved LK3/L Zircaloy-2**
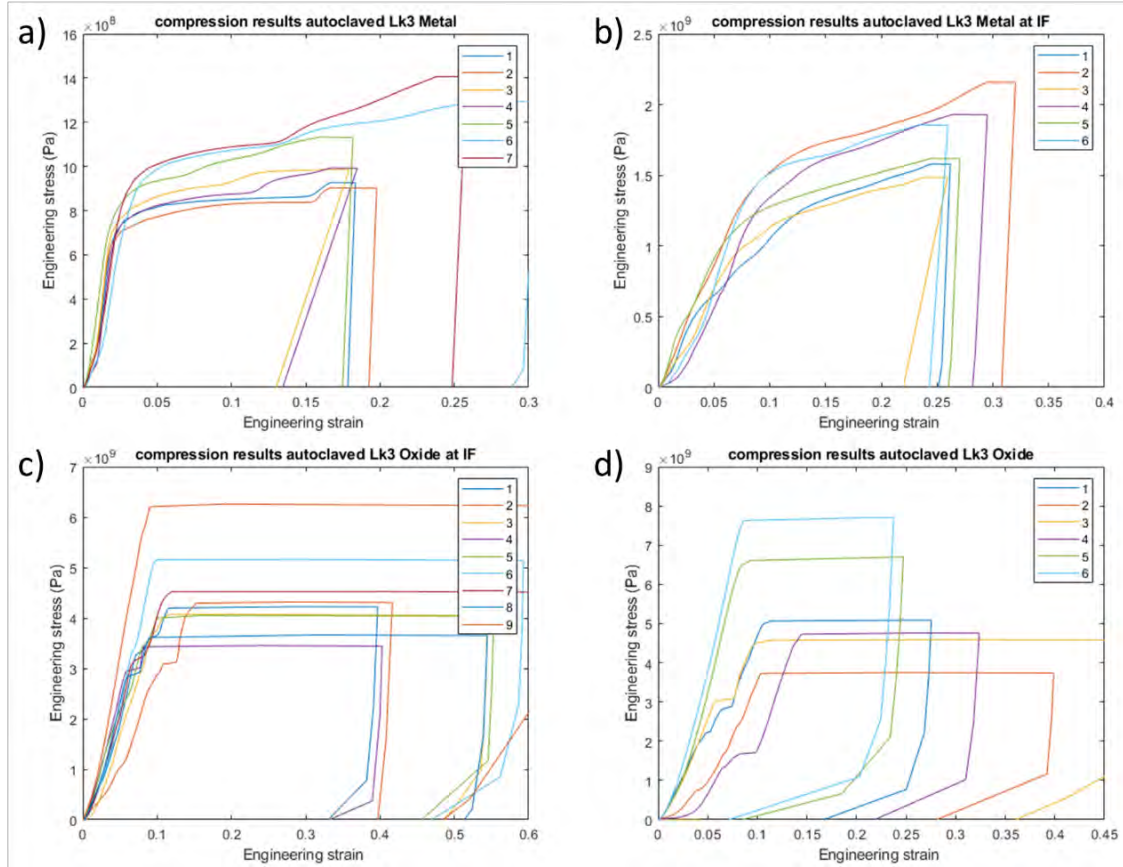


*Figure 5-9. Stress vs strain curves for the pillars in the four different regions tested in the autoclaved LK3/L Zircaloy-2. A) the results from the pillars in the metal region, b) the results from the pillars in the metal at the interface region, c) the results from the pillars in the oxide at the interface, extra pillars were made in this region and labelled 8 and 9 and d) is the results from the pillars in the bulk oxide. Because of inaccurate or incomplete tests, test 7 is not included*

### 5.2.3 Young's Modulus and Strength

Graphs showing the Young's modulus and strength of the LK3/L series (autoclaved and 6 cycle as well as the results from the 3 and 9 cycle LK3/L which had previously been tested [137]) are shown in Figure 5-10 a,b,c,d and Figure 5-11a,b,c,d respectively. Graphs showing the Young's modulus and strength for the four samples; Zircaloy-2 LK3/L (autoclaved and 6 cycle) and low-tin Zircaloy-4 (autoclaved and 4 cycle) together with the 3 and 9 cycle LK3/L which had previously been tested [137] are shown in Figure 5-12 and Figure 5-13 respectively. In all figures a,b,c,d correspond to the four regions: bulk metal (a), metal at interface (b), oxide at interface (c), bulk oxide (d). In the graphs 0 cycles represents autoclaved material. The values for the oxide at the interface for the 3 and 9 cycle were not available from [137]. The exact values are tabulated and shown in Table 5-2.

In Figure 5-10 (Zircaloy-2 LK3/L), the bulk metal and the metal at IF can be seen to increase in modulus and strength between the autoclaved metal and irradiated 3-cycle. For example, the strength from $0.79\pm 0.1$Gpa to $1.1\pm 0.1$Gpa in bulk metal and from $1.2\pm 0.15$Gpa to $1.3\pm 0.2$Gpa in the metal at IF. At higher residence times, these values then decrease again to values close to the unirradiated, except for the strength of the 9-cycle metal at IF which does not follow the trend. However, this point has very large error bars. In the oxide at IF, the change between the autoclaved and 6-cycle is small and within errors $4.5\pm 1.0$Gpa and $4.1\pm 1.3$Gpa respectively. In the bulk oxide, a clear trend of decrease in strength can be seen with residence time, however the 6-cycle sample is more similar to the 3 than 9-cycle. From autoclaved to 9-cycle, the change is $5.4\pm 1.4$Gpa to $1.3\pm 1.2$Gpa.

In Figure 5-11, the results from the low-tin Zircaloy-4 are given as well as the results from Figure 5-10. In the bulk metal and metal at IF, a similar effect of hardening with irradiation can be seen; higher residence times were not tested to see if this property would then decrease again at higher levels of irradiation. In the oxide, Zircaloy-4 does not seem to decrease in strength between the autoclaved and irradiated sample the way the Zircaloy-2 sample does. In the oxide at IF, an increase in strength is seen from $5.2\pm 1.1$Gpa to $6.0\pm 1.1$Gpa. The values in the oxide are $5.5 \pm 0.5$Gpa and $5.4\pm 1.1$Gpa for the autoclaved and irradiated sample respectively.

The results in this section will be discussed in the following discussion chapter.

*Table 5-2. Data on the Young's modulus and strength of all the alloys tested for the different regions tested. The error is one standard deviation from a group of 7 pillars. The symbol \* indicates data which was not collected in this thesis, but has been collected previously in the scope of the project and is taken from ref [137]. Also included are values from ref [198] of unirradiated Zircaloy-4 bulk measurements.*

| Sample | Position | Average Young's Modulus (Pa) | Error on Modulus (Pa) | Average Strength (Pa) | Error on Strength (Pa) |
|---|---|---|---|---|---|
| **Zr-2 LK3/L (autoclaved)** | Metal | 4.47E+10 | 6.18E+09 | 7.93E+08 | 6.61E+07 |
| | Metal at IF | 2.06E+10 | 4.62E+09 | 1.18E+09 | 1.54E+08 |
| | Oxide at IF | 5.60E+10 | 1.32E+10 | 4.50E+09 | 9.66E+08 |
| | Outer Oxide | 7.64E+10 | 1.71E+10 | 5.43E+09 | 1.44E+09 |
| | | | | | |
| **Zr-2 LK3/L (3 cycle)\*** | Metal | 6.23E+10 | 5.20E+09 | 1.10E+09 | 1.00E+08 |
| | Metal at IF | 3.90E+10 | 7.40E+09 | 1.30E+09 | 2.00E+08 |
| | Oxide at IF | | | | |
| | Outer Oxide | 4.20E+10 | 2.70E+10 | 2.73E+09 | 1.40E+09 |
| | | | | | |
| **Zr-2 LK3/L (6 cycle)** | Metal | 5.22E+10 | 2.98E+09 | 1.06E+09 | 3.93E+07 |
| | Metal at IF | 4.94E+10 | 5.76E+09 | 1.13E+09 | 7.29E+07 |
| | Oxide at IF | 6.42E+10 | 2.69E+10 | 4.10E+09 | 1.27E+09 |
| | Outer Oxide | 4.57E+10 | 9.04E+09 | 2.79E+09 | 5.88E+08 |
| | | | | | |
| **Zr-2 LK3/L (9 cycle)\*** | Metal | 3.95E+10 | 4.00E+09 | 9.00E+08 | 1.00E+08 |
| | Metal at IF | 3.64E+10 | 8.40E+09 | 1.50E+09 | 5.00E+08 |
| | Oxide at IF | | | | |
| | Outer Oxide | 3.99E+10 | 1.33E+10 | 1.29E+09 | 1.17E+09 |
| **low-tin Zr-4 (autoclaved)** | Metal | 4.46E+10 | 8.48E+09 | 9.95E+08 | 1.28E+08 |
| | Metal at IF | 2.36E+10 | 7.35E+09 | 8.52E+08 | 1.35E+08 |
| | Oxide at IF | 1.03E+11 | 1.26E+10 | 5.17E+09 | 1.11E+09 |
| | Outer Oxide | 1.10E+11 | 1.03E+10 | 5.52E+09 | 4.62E+08 |
| | | | | | |
| **low-tin Zr-4 (4 cycle)** | Metal | 5.19E+10 | 9.31E+09 | 1.30E+09 | 2.55E+08 |
| | Metal at IF | 5.62E+10 | 2.88E+09 | 1.08E+09 | 3.66E+07 |
| | Oxide at IF | 1.48E+11 | 1.60E+10 | 6.02E+09 | 1.06E+09 |
| | Outer Oxide | 1.19E+11 | 1.45E+10 | 5.38E+09 | 1.10E+09 |
| **Literature[198] Zircaloy-4** | Metal | 1.00E+11 | 4.00E+9 | 6.00E+8 | |
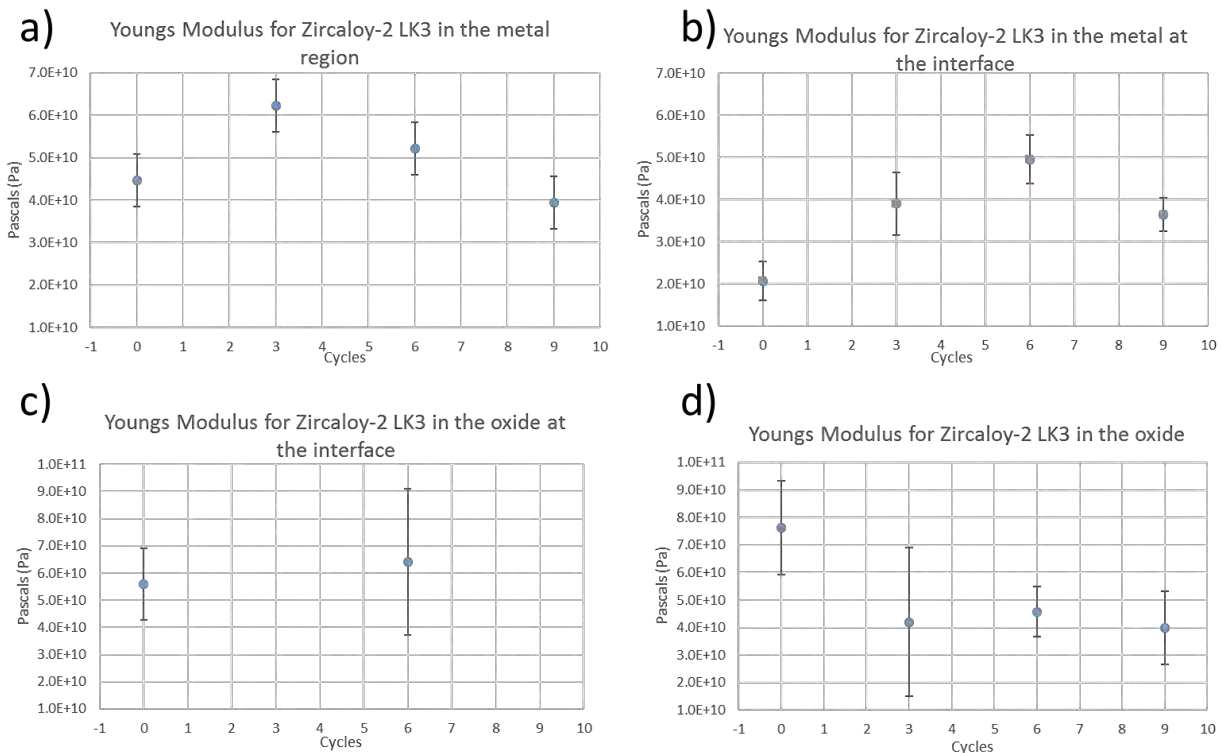
Figure 5-10a,b,c,d. The Young's modulus for Zircaloy-2 LK3/L after various residence times (shown as cycles). A) Young's modulus in the bulk metal region, b) in the metal at the interface region, c) in the oxide at the interface region, d) in the bulk oxide.
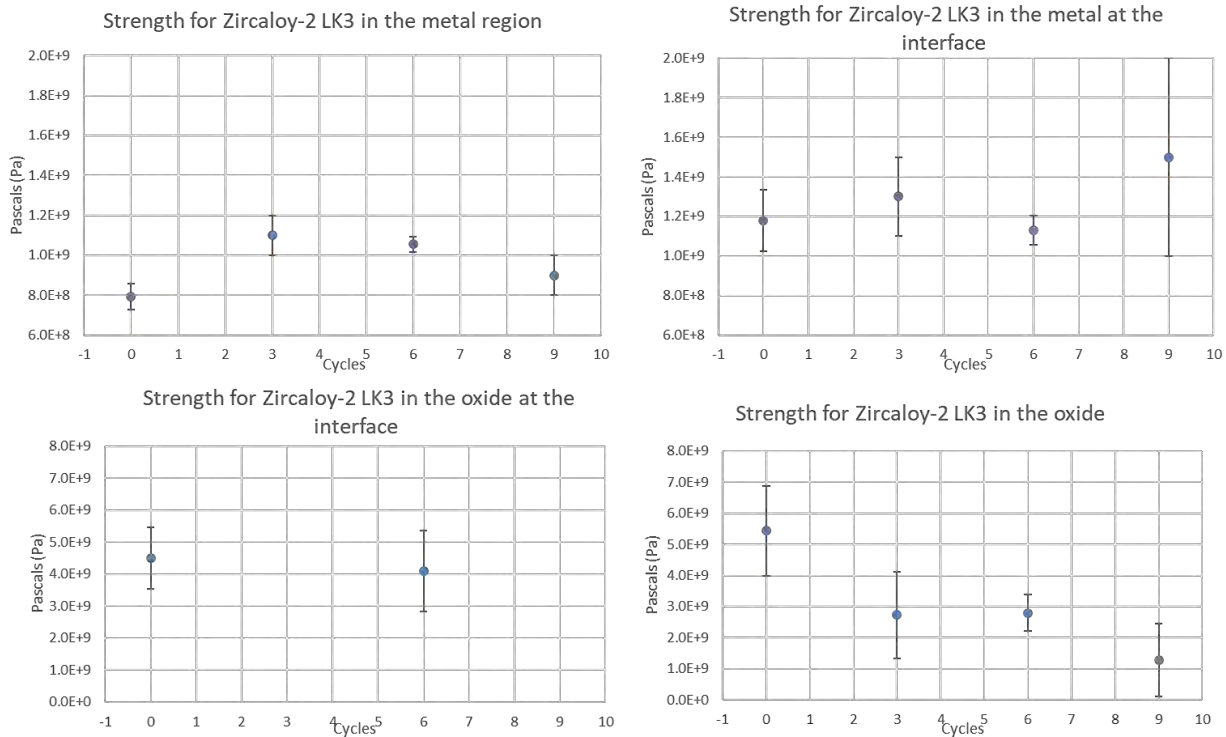


Figure 5-11a,b,c,d. The strength for Zircaloy-2 LK3/L after various residence times (shown as cycles). A) strength in the bulk metal region, b) in the metal at the interface region, c) in the oxide at the interface region, d) in the bulk oxide.
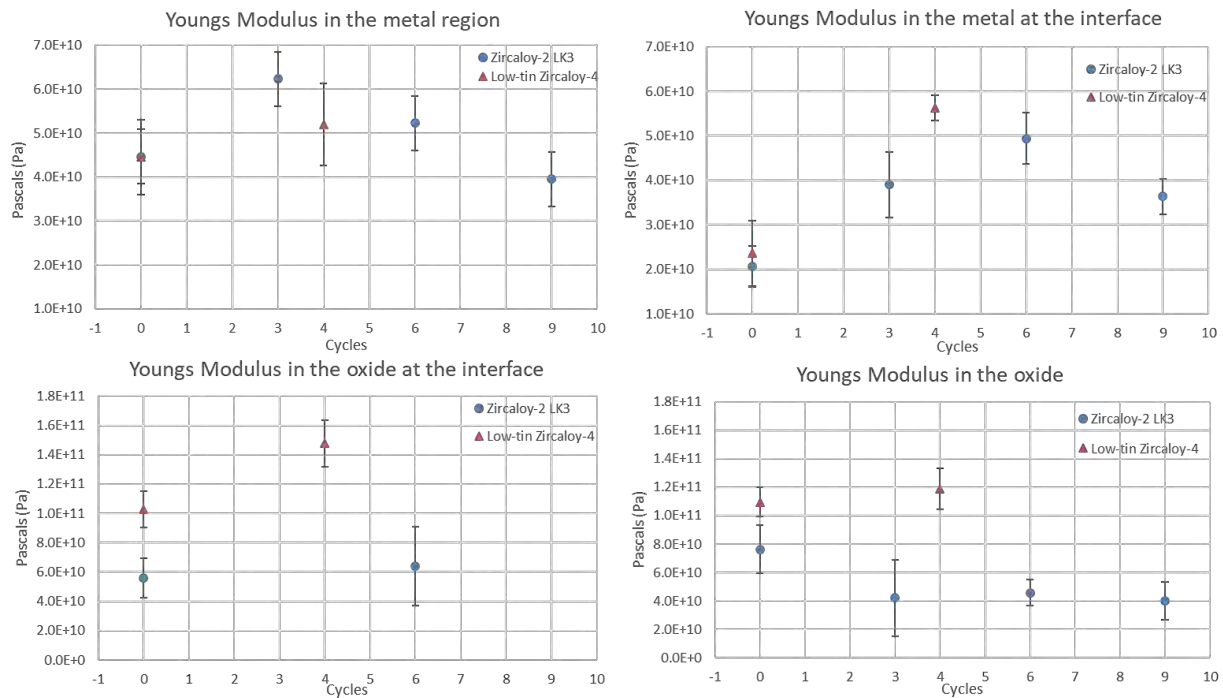
*Figure 5-12a,b,c,d. The Young's modulus for 2 materials; Zircaloy-2 LK3/L and Low-tin Zircaloy-4 after various residence times (shown as cycles). A) Young's modulus in the bulk metal region, b) in the metal at the interface region, c) in the oxide at the interface region, d) in the bulk oxide.*
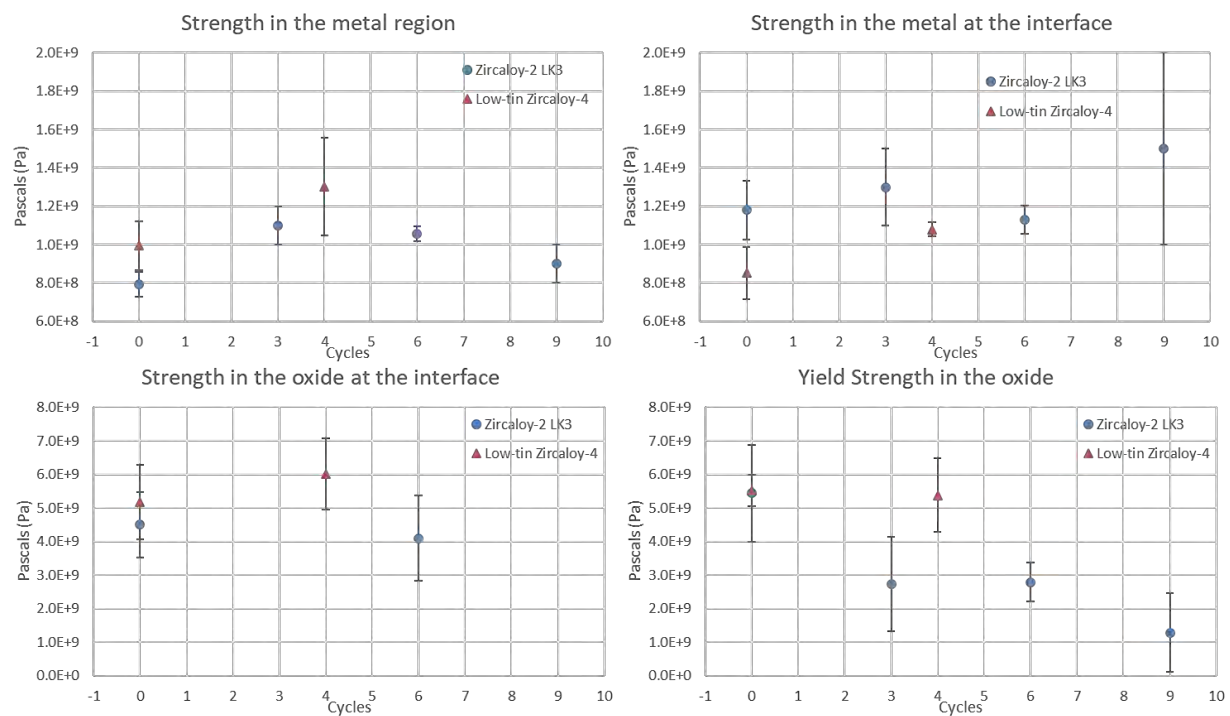


*Figure 5-13a,b,c,d. The strength for 2 materials; Zircaloy-2 LK3/L and Low-tin Zircaloy-4 after various residence times (shown as cycles). A) Young's modulus in the bulk metal region, b) in the metal at the interface region, c) in the oxide at the interface region, d) in the bulk oxide*

# 5.3 Discussion

The methodology of using a FIB/SEM to select certain areas of a sample and create micro-pillars to compress has allowed the probing of intrinsic mechanical properties in the vicinity of the metal oxide interface even for highly irradiated materials. Due to the size of the regions of interest and types of materials, this would not be possible with any other technique and, to the best of our knowledge, has not previously been performed [137]. The size of the pillars was partly dictated by the size of the regions wished to be studied (roughly 1-3μm); in the case of oxide pillar, it was partly dictated by the need to be large enough to encompass enough oxide grains to be considered a polycrystalline pillar [137]. This is important to be representative of the oxide layer. The size of pillar was kept the same in the metal and the oxide to help with comparability of geometrical factors between metal and oxide pillars and also with the pillars previously made in the aforementioned study of 3 and 9 cycle LK3/L. Even though this size of pillar may not be optimum for the grain size found in the metal since the average grain diameter is approximately 3μm for Zircaloy-2 and 4μm for Zircaloy-4, the metal pillars cannot truly be single crystal or polycrystalline but they could be considered as a bicrystal. However, while this may increase the scatter of results, it is still concluded that results are comparable to each other.

## 5.3.1 Scope of experiments and confidence of results

As mentioned above, all tests that showed an incomplete or inaccurate compression, have been removed from the results. Thus, after this screening it could be argued that the presented values are reliable. Therefore, the standard deviations of average values could represent some real variation between the different regions of the material, as well as a certain degree of inaccuracy of measurement. In the metal regions' tests, good agreement was generally seen between the compression results with the standard deviation of one set of 7 pillars being relatively low (between 5% and 31%), seen as the error bars on each point and given in Figure 5-12 and Figure 5-13. However, the possibility for larger scatter still exists and can be seen in a few data points, for example in the metal pillars at the interface for low-tin Zircaloy-4 (4 cycle) sample. A few reasons could cause such scatter. For example, as previously mentioned, in the metal the pillars are not expected to be truly monocrystalline but rather include some grain boundaries and hence the position of grain boundaries within each pillar cannot be totally reproducible. Also intrinsically, due to the nature of materials and especially irradiated materials, the metal phase cannot be considered to be totally uniform. SPPs and

irradiation induced defects as well as hydrides can all contribute to the non-uniformity and hence scatter of results. With 7 tests per region, the statistics can be considered reliable for evaluation but due to occasional failed tests, some data points only have 5 or 6 tests; this may slightly reduce the statistics on that data point.

The oxide pillars show a larger scatter (between 9% and 90%), particularly the strength. This is known to be a feature of brittle materials and ceramics [199], and has also been shown to be the case for zirconia [200]. The scatter may have been further exacerbated by the fact that the oxide often contains many cracks and small scale porosity. It may be the case that some pillars contained large cracks or a higher volume of porosity compared to the average for that region [64]. While this did increase the error, the number of tests in each region stipulates that the data should still be of value even if a larger number of tests would ideally be required to give a more exact value for the intrinsic properties. It should be noted that this porosity and non-uniformity of the oxide is also an important feature; in fact the larger scatter demonstrates this about the oxide.

Another issue which must be considered is the introduction of uncertainty due to the production of pillars by FIB. It is well known that FIBing can introduce artefacts to this material [181] which could potentially affect the properties. However, in this study it can be quite confidently concluded that due to the low beam current used for polishing the beam damage, Ga implantation and amorphization induced would be very small in comparison to the size of the pillar (approximately a hundred nanometers compared with the 2-3µm pillar diameter).

In regards to the testing, despite all the possible variation between pillars, dimensions and materials results seem to be quite reproducible. Pillars that were not properly compressed were removed as they were easily identified. However, small irregularities or inconsistencies may come in from a number of sources during testing. For example, a difference in angle between the tip surface and the pillar would result in the beginning of compression having a shallower gradient than expected. This is often seen in the stress strain curves and these points were not included when calculating the modulus. Misalignments between the tip and pillar may cause non-uniaxial compression and hence the stress distribution throughout the pillar may not be uniform causing premature failure. For some oxide pillars, the initial stress-strain gradient is not constant but rather exhibits one or more quick jumps or increases in strain (see Figure 5-9). This could be attributed to the cracking in the oxide and the sudden collapse of existing cracks, or the nucleation of new ones from small porosities.

### 5.3.2  The influence of residence time on the change of micro-mechanical properties of Zircaloy-2

*Metal results*

By examining Zircaloy-2 LK3/L after different residence times in the same reactor, which eliminates many other factors and allows for a direct comparison of properties with residence time, the evolution of the mechanical properties could be compared. Additionally, the examination of an autoclaved sample allowed for useful insight into the effect of irradiation on this material. Since there are many data points to compare, the metal is considered first. When comparing the non-irradiated (autoclaved) and 3-cycle material, an increase of roughly 70% is seen both in the value of modulus and strength. This can be explained by the well-known effect of irradiation hardening [132], [133], [201]. When Zr-alloys experience neutron irradiation, the microstructure is affected. The neutrons knock Zr atoms out of their normal sites and generate defect vacancies and interstitials. The defects then tend to migrate and form two types of dislocation loops (see 2.7.6 for further details). Both types of loops are obstacles for dislocation movement and hence increase the strength and hardness of the irradiated material. Furthermore, the structure of the SPPs will change under irradiation and usually dissolve, with the rate of dissolution depending on the alloying element and SPP size [69].

The results from bulk metal (Figure 5-10a and Figure 5-11a) suggest that at higher residence times and hence greater doses, the alloy reduces in stiffness and strength. It is expected that the effect of irradiation would quickly saturate [201]. A study by Cockeram et al. [133] testing the yield strength of Zircaloy-2 and Zircaloy-4 as a function of neutron fluence showed that initially, with small amounts of neutron irradiation, the yield strength quickly increased and then either plateaued with an additional small increase or decreased. In the case of the alloys studied here, the change occurring in the material is expected to be more complex since irradiation is not the only parameter influencing the component's life time in reactor, but oxidation, hydriding and other dimensional changes together with the impact of the fuel also play a role. Furthermore, forces exerted on the cladding; will lead to creep and growth which change the shape and microstructure of the clad. It is therefore expected that these other parameters would cause a difference of behaviour in comparison with the results obtained in the study by Cockeram [133].

In addition, as previously mentioned, hydrogen entering the cladding will be in solid solution and as more hydrogen enters, the solubility limit will be reached and hydrides will form. It is postulated that the brittle behaviour of claddings increases with hydrogen content [7], [198], [201]. However, as described in the literature in section 2.7.9 Yagnik et al. [198] demonstrated that hydrides have a smaller impact on the mechanical properties compared to the fluence. It is therefore suggested that

since the results from the tests in the metal show a trend of increasing strength and initial stiffness in the reactor, and then a decrease in these properties at extended residence times, the main factor for this would be the neutron irradiation as shown by Cockeram [133]. However, the factors previously mentioned may play a minor role in the evolution of metallic mechanical properties with residence time.

A similar but non-identical trend is seen in the results of the metal at the interface. All points for LK3/L series show a decrease in modulus but an increase in strength compared to the bulk metal. Here, two points should be kept in mind: near the interface, a 'transition zone' is expected [8] with oxygen dissolved ahead of the oxide corrosion front; secondly, close to the interface is where a higher amount of hydrides are found to be precipitated.  Up to 25% of the volume of metal at the interface was found to be hydride in the 9-cycle cladding [64]. Both of these points are expected to make the material more brittle. The distribution of hydrides at the interface has been suggested to account for the increased variation in the point in the metal at IF for the 9-cycle sample [137]. It is also reiterated that the results of 3 and 9-cycle claddings were taken from the literature. In the metal close to the interface region of the 3-cycle material, only 3 micro-pillars were available showing fairly irregular stress vs strain curves [137].

### Oxide results

The pillars in the oxide, both at the interface and bulk oxide, do not plastically deform in the same way as metal pillars but rather show brittle failure which is typical for ceramic materials. They also exhibit higher modulus and strength. There are only data points available at the interface from the autoclaved and 6-cycle sample since these are not available from ref [137]. However, in the case of the 3-cycle cladding, the oxide layer being only 4 µm thick, the information could also be used to compare with the interface oxide data for autoclaved and 6-cycle samples in this study.

The study of autoclaved cladding was carried out as a reference for the nature of the metal and the oxide prior to irradiation. However, besides this comparison, this autoclaved material provides very useful information about the nature of the oxide not previously observed. Knowing that the interface region should act as a barrier layer, it is expected that the oxide shows a stress which is higher than the bulk oxide. This, however, proves to be incorrect. The bulk oxide of this autoclaved material shows a higher strength compared to the oxide close to the interface. The explanation of this behaviour can be found in the previous observation, that the oxide layers formed on the Zircaloy-2 material preserve their microstructure even after they are some distance away from the interface and that the penetrating of water/coolant into the oxide is via large radial cracks in the outer oxide [64].

By comparing the bulk oxide measurements of all four samples, it appears there is a decrease in strength as a function of residence time with the 6-cycle being more similar to 3-cycle than 9-cycle. This decrease in strength in the oxide is most probably attributed to the increase of porosity or cracking in the oxides from 3-9 cycles, as shown in [64] where the crack volume fractions were found to be 0.19%, 2.73% and 4.9% for the 3,6 and 9-cycle oxide respectively. For the oxide at the interface, in the two sets of available results, the properties seem to be comparable.

### 5.3.3 The influence of in reactor corrosion on low-tin Zircaloy-4

In order to examine if the nature of the alloy and the type of reactor influence the change of properties, one cladding from a PWR was studied and was compared with the autoclaved sample from the same material. A low-tin Zircaloy-4 was selected. Similar to Zircaloy-2, the factors mentioned above in section 5.3.2 should have the same influence here. Between the non-irradiated and irradiated sample, an increase both in modulus and strength in the metal was seen, which is again mainly attributed to irradiation hardening. From this data, it cannot be extrapolated how the material may react towards high burn ups being subjected to more irradiation.

In the oxide both close to the interface and in the bulk, the strength increases or stays approximately the same in the 4-cycle compared to autoclaved. This is in contrast to the Zircaloy-2 sample where an unambiguous reduction in strength is seen. Both the interface oxide as well as the bulk oxide is stronger than oxide in Zircaloy-2. It is suggested that either one of two things may best explain this if it is a true finding. Firstly, the autoclaved zircaloy-4 sample had been autoclaved longer and had a much larger oxide layer than the autoclaved zircaloy-2 sample (i.e. approximately 20µm compared to 6µm); this might suggest the oxide on the Zircaloy-4 sample had been through more transitions and hence more cracked. This may mean that the Zircaloy-4 oxide is intrinsically stronger than that of Zircaloy-2 but such a large reduction with strength is not seen from autoclaved to irradiated because the two autoclaved oxides are not comparable. The second option would be that this phenomenon is real and the decrease in strength seen due to irradiation in Zircaloy-2 does not happen in Zircaloy-4.

## 5.4 Conclusions

- The metal of a Zircaloy-2 LK3/L is shown to increase in 'strength' due to irradiation hardening at early stages of residence time in reactor. However, after a certain time (between 3 and 6 cycles in this case) this effect saturates and begins to soften again. The same trend of increased 'strength' could be observed in low-tin Zircaloy-4 between non-irradiated and irradiated, but due to the lack of high burnup samples it cannot be confirmed if the trend would continue to match.

- Generally, a higher strength was seen in the metal at the interface, which was correlated, with the oxygen saturated metal. However since the size of the pillar was larger than the expected size of this zone and could not be directly at the interface due to undulation, only a portion of the pillars would be oxygen saturated metal.

- In the oxide of Zircaloy-2 LK3/L, a decrease in strength could be seen with residence time with the 6-cycle sample being more similar to the 3-cycle than the 9-cycle. This finding was correlated with the increase in porosity found in the oxide.

# Contents of chapter 6:

# 6 The oxidation and role of Niobium

## 6.1 Introduction

In this chapter the question of the oxidation of Nb, in Nb containing alloys will be addressed with the aim to discuss and link the findings to hydrogen uptake. Oxidation behaviour and hydrogen uptake of Zr alloys can vary greatly with even small changes to alloying element composition and distribution. For this reason, there is a desire to understand the speciation of such alloying elements in the oxide layer[42], [75], [112], [113], [147], [148], [202], [203]. A particular interest in the speciation of niobium exists as the Nb containing alloys usually show a lower hydrogen uptake [11], [26], [112], [147], [148]. In comparison, alloys like Zircaloy-2 used in the boiling water reactors (BWR) and Zircaloy-4 used in pressurised water reactors (PWR) show higher hydrogen uptake [8].

In this chapter two techniques have been used; XANES and EELS. Both are spectroscopy techniques one using X-rays as incident beam and the other electron beam, and were employed for specific purposes, according to their strengths and weaknesses. Firstly XANES was used because of it's high sensitivity and detection limit, being able to detect signal from Nb even down to the ppm range [204]. This should give a highly accurate information about Nb speciation at a certain point (here the beam size is approximately than $0.7 \times 0.8 \ \mu m^2$). Including all the Nb whether it is found as SPPs, or in the matrix or however it is distributed. Because the beam is expected to cover multiple features each spectrum acquired is expected to include contributions from different sources, with the Nb having potentially different states, and hence will require deconvolution. This will be discussed and expanded upon in the current chapter.

EELS was chosen to complement XANES since the extremely small spot size in STEM EELS (even possibly as small as 1 nm) allowed the probing of distinct features such as SPPs, cracks, matrix etc. The detection limit of EELS to trace amounts of alloying element however is not as high. Making the study of Nb in solution or matrix very difficult. Two different Nb alloys were used for the XANES and EELS studies. For XANES a low-tin ZIRLO described in Chapter 3.1.3 and for EELS a Zr2.5%Nb described in Chapter 3 section 3.1.2 . This is because TEM work had already been performed on this material and similar ZIRLO material (including EELS on this material) [101], [168], [205] and what was lacking was XANES. Whereas the EELS work on Zr 2.5%Nb would add something missing in the

characterisation of that material. Also since both materials were Zr-Nb alloys the behaviour of Nb should be comparable in the two alloys.

X-ray diffraction patterns were also acquired in parallel to fluorescence maps of the low-tin ZIRLO sample. It was hoped that oxidised phases of Nb could be identified in this way. While this work is not yet complete, other results are available, from the subsequent data analysis, including insights into the presence of monoclinic and tetragonal phases in the oxide. Hence, the XRD data is included in this chapter along with discussion on the relation of these findings to the Nb speciation.

In the following in order to provide a description of the phases present and also the size of precipitates in each of the two materials examined the microstructure of both material as studied with TEM will be provided, including the results from previous researchers.

### 6.1.1 Microstructure of low-tin ZIRLO

This material is described in chapter 3 section 3.1.3. The family of ZIRLO alloys have been to a great extent studied, for example in these references and many more [26], [101], [112], [114], [141], [197], [202], [206]. G. Sabol in ref [141] well describes the development of ZIRLO alloys. As previously mentioned ZIRLO alloys contain 1.0 wt% Nb and are known to form roughly spherical $\beta - Nb$ SPPs (containing 80% Nb). These alloys contain also other ternary Fe-Nb containing SPPs and are expected to be of the composition $Zr_{0.5}Nb_{0.3}Fe_{0.2}$ [168], although other SPPs containing more iron could be present and have been seen in similar alloys with higher Fe content. It was also shown that under irradiation these SPPs would show depletion or dissolution just as with other SPPs. However, because of the high initial Nb content, and probably also the slow mobility of Nb, the $\beta - Nb$ SPPs showed less dissolution/depletion than other similar SPPs containing other alloying elements [168]. Included here in Figure 6-1 is an EDS map of a standard un-irradiated ZIRLO sample taken from reference [205]. This Figure is included to show particularly the distribution of Nb as that is the subject of this chapter and to contrast its distribution with that of the Nb found in Zr-2.5%Nb shown in the next section 6.1.2.
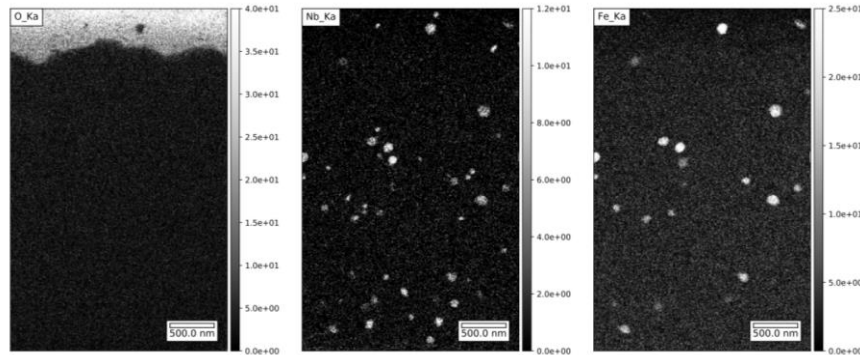


*Figure 6-1. EDS showing the distribution of Nb and Fe SPPs in an unirradiated ZIRLO taken from reference* [205]

### 6.1.2 Microstructure of Zr-2.5%Nb

This material is described in chapter 3 section 3.1.2. To add to the characterisation of this material STEM-EDS was carried out at the University of Birmingham on the FEI TALOS, as well as EELS at the University of Oxford on the JEOL ARM200F which will be subsequently shown and discussed. This was

not only to better understand the material but particularly to show the distribution of Nb with high spatial resolution and decide how and where best to study with EELS. Figure 6-2 and Figure 6-3 show the EDS results as well as high angular annular dark field (HAADF) images for two TEM lamella, one which previously belonged to the project (Figure 6-2) and one which was newly made by myself (Figure 6-3). In contrast to ZIRLO (and most other 1% Nb alloys) in the case of Zr2.5%Nb it can be clearly seen that large Nb-rich phases with microns in length or size are formed. From previous work on this material [67] these are known to be $\beta$-Zr containing up to 20% Nb. In the same study it was also shown that at $1\mu m$ distance into the oxide these Nb phases remained metallic and structured. Further into the oxide they begin to dissolve and oxidise. Although the presence of oxygen signal in an SPP could be a direct indication of the fact that the phase is oxidised. The exact oxidation state of Nb cannot be determined from EDS and hence EELS was employed to examine the speciation of Nb in its various possible positions. To do so multiple EELS spectrum images were acquired using the JEOL ARM200F. Table 6-1 includes the semi-quantitative EDS values from Figure 6-2 and Figure 6-3, and other maps, for both the metal matrix and the Nb phases, in the metal-side of the interface. The values for regions inside the oxide are not given as this will vary depending on distance into the oxide. Figure 6-4 is included to show the percentage composition of Zr and O across the metal and oxide. The drop of concentration of Zr (in form of sharp peaks) in the oxide corresponds to cracks in the oxide (not shown here). Previous work on this material by A. Baris [64] quantified the amount of cracking in the oxide close to the interface (within 1µm) to be much lower than that of the rest of the oxide 0.25% compared to 3.15%. From Figure 6-2 and Figure 6-3 it can be seen how at a distance from the interface where Nb begins to dissolve there is also an enrichment of Nb in and around cracks. It is shown previously that Nb (and Fe) will tend to migrate to free surfaces and hence be found on crack surfaces [16], [156].
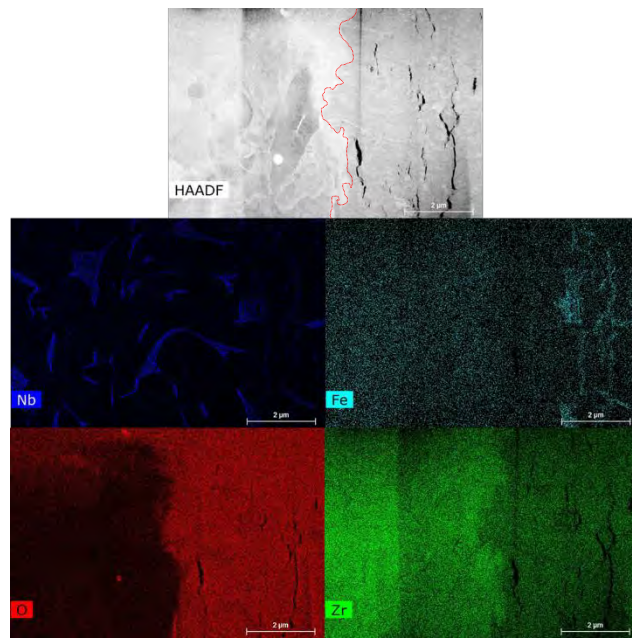
*Figure 6-2. Micrograph of the metal-oxide interface of a 3 cycle Zr- 2.5Nb TEM lamella. The red dotted line on the HAADF image marks the interface. The scale bar is 2 μm*
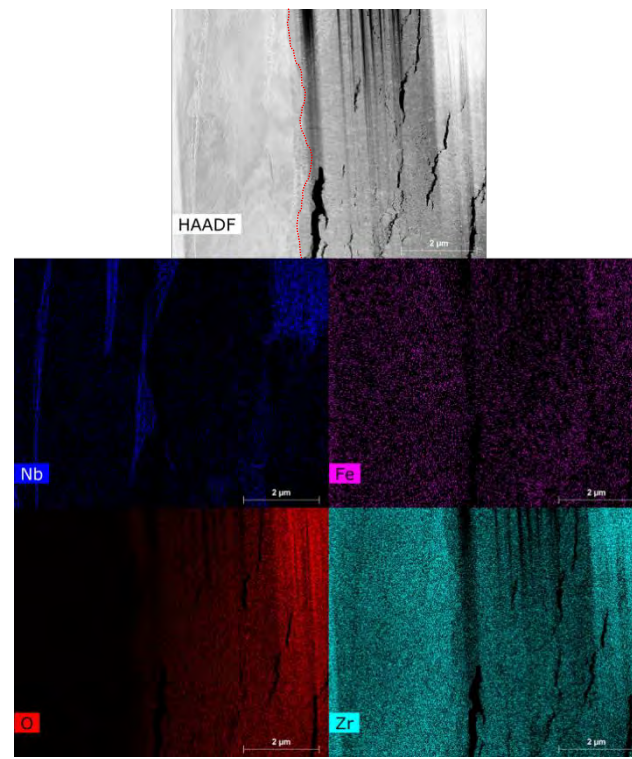


*Figure 6-3. Micrograph of the metal-oxide interface of a 3 cycle Zr- 2.5Nb TEM lamella. The red dotted line on the HAADF image marks the interface. The scale bar is 2 μm*

*Table 6-1. Semi-quantitative values from EDS for both metal matrix and Nb rich phase for Zr-2.5%Nb after 3 cycles of iradiation.*

| Phase | O (at%) | error | Fe (at%) | error | Zr (at%) | error | Nb (at%) | error |
|-------|---------|-------|----------|-------|----------|-------|----------|-------|
| metal matrix | 0.78 | 0.33 | 0.945 | 0.28 | 96.72 | 1.08 | 1.285 | 0.625 |
| Nb rich phase | 0.525 | 0.095 | 0.915 | 0.555 | 84.62 | 2.12 | 15.87 | 1.65 |
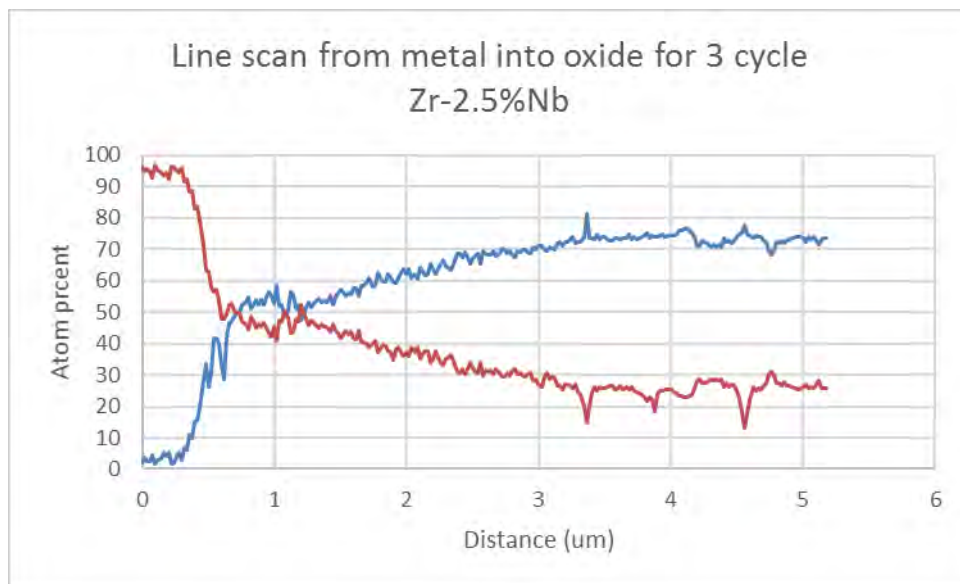


*Figure 6-4. EDS line scan moving from metal to oxide in the 3-cycle Zr-2.5%Nb showing the normalised atomic percentage of Zr (red) and O (blue).*

## 6.2 Synchrotron data acquisition and processing of ZIRLO

### 6.2.1 Acquisition of spectra

An SEM image of the studied sample can be seen in Figure 6-5, along with other elemental signals during the Synchrotron campaign. The fluorescence images show the frontiers of the sample, and the major elements present in it. Platinum and copper signal are acquired to determine the limits of the sample and can be used as a control. The sample was also imaged and measured in SEM and more details as well as material details can be found in section 3.1.3.
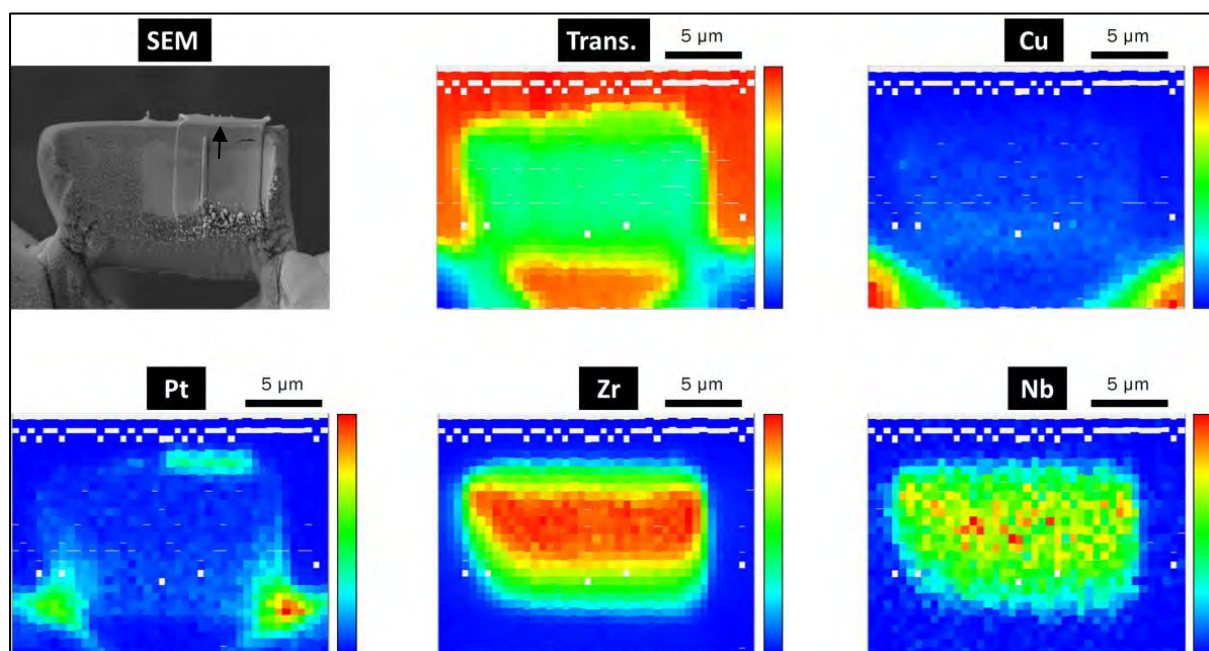


*Figure 6-5. X-ray florescence images of the low-tin Zirlo sample (left to right): SEM image, transmission total, Copper, Platinum, Zirconium, Niobium. The polished section can be clearly seen in the SEM image and this contains the analysed region.*

In order to analyse the speciation of Nb in the metal and in the oxide, a "point line-scan" was performed with the beam moving perpendicular to the metal/oxide interface from metal into the oxide with a predetermined step size of 200 nm. The approximate distance, placement and direction are marked with an arrow on Figure 6-5. At each 200 nm interval, 10 spectra were acquired and

averaged to improve statistics and reduce noise. Some of the spectra acquired had to be discarded due to anomalies and due to technical issues and hence three points have reduced statistics of 7 or 8 spectra averaged rather than 10. These points were the 3rd, at 0 μm, 7th, at 0.8 μm, and the 11th, at 1.6 μm.

## 6.2.2 Data processing

An evolution of the Nb signal when moving from metal to oxide was observed, to quantify this energy shift and shape change standards with known speciation were used. XANES scans were acquired for the following Nb standards: Nb metal, NbO (2+), $NbO_2$ (4+) and $Nb_2O_5$ (5+). The resulting fluorescence spectra from each point in the line scan was fit using linear combination of these (normalised) standards using the Athena software and an in-house fitting Python script. The fit was based on minimising either the $R^2$ value or the root mean square error (RMSE) between the model and the measurement. The model spectra is defined as

$$\mu_{model} = a \cdot \mu_{Nb^0} + b \cdot \mu_{Nb^{2+}} + c \cdot \mu_{Nb^{4+}} + d \cdot \mu_{Nb^{5+}}$$

Where $\mu_i$ is the spectra of the $i$-th standard, with the constraints that the concentration of each standard in the model was between [0,1]. [207]

$$0 \leq a, b, c, d \leq 1$$

And that the sum of all standards added up to 1

$$a + b + c + d = 1$$

The portion of the spectra used for fitting the standards was in the energy range of 18950-19150 eV, which was chosen based on a sensitivity analysis provided in the Appendix C. Fitting for $R^2$ and RMSE yielded equivalent results.

As was previously mentioned earlier results [147], [148] reported an averaged oxidation state of Nb across the oxide layer. The procedure to acquire spectra at given distances from the metal-oxide interface, was used to obtain local information in the oxide. Still it appears that the measured spectra do not correspond to one single standard and thus are formed from a mixture of different Nb oxidation states even at a single point of inspection. In order to find out the relative fractions of each of the oxidation states the described analysis was performed.

### 6.2.3 X-ray diffraction acquisition and analyses

In addition to the above-mentioned measurements, X-ray diffraction patterns were acquired, using the Eiger4M area detector, across the whole sample at intervals of 300 nm in both horizontal and vertical directions. The beam diameter (FWHM please see Appendix C) was approximately 0.8 μm (horizontal) × 0.7 μm (vertical) as before for this data collection and the beam had an energy of 19.1 keV. The software XRDUA was used to analyse the resultant diffraction patterns and create semi-quantitative models of the phase fractions of the phases Zr, monoclinic $ZrO_2$ and tetragonal $ZrO_2$. For a more accurate calculation of the monoclinic vs tetragonal content in the oxide, specifically to account for the texture, the Garwie-Nicholson equation [208] was used. Where I represents the intensity of the relevant peak i.e. $It - ZrO_2(101)$ represents the intensity of the tetragonal (101) peak. And $R_{t/m}$ represents the phase fraction of tetragonal compared to monoclinic.

$$R_{t/m} = \frac{I\,t-ZrO_2(101)}{I\,m-ZrO_2(\bar{1}11)+I\,t-ZrO_2(101)+I\,m-ZrO_2(111)} \qquad \textit{Equation 6-1}$$

The error on this expression was calculated using the general formula for error calculation and is shown in Equation 6-2. Here for simplicity $x$ represents $I\,t - ZrO_2(101)$, $y$ represents $I\,m - ZrO_2(\bar{1}11)$ and $z$ represents $I\,m - ZrO_2(111)$. $\Delta x, \Delta y, \Delta z$ represent the errors on $x, y, z$ respectively.

$$error = \sqrt{\left(\frac{y+z}{(x+y+z)^2}\Delta x\right)^2 + \left(\frac{-x}{(x+y+z)^2}\Delta y\right)^2 + \left(\frac{-x}{(x+y+z)^2}\Delta z\right)^2} \qquad \textit{Equation 6-2}$$

# 6.3 XANES of Niobium in low-tin ZIRLO

As the photon beam moves from metal across the metal-oxide interface and subsequently further into the oxide the XANES signal shows a clear shift in both edge energy and white line intensity. Examples of the Nb fluorescence spectra can be seen in Figure 6-6. The displayed spectra have a spatial separation of 200 nm and are all included i.e. the first spectrum has a position of 400 nm away from the interface in the metal and the last 2.2 μm away from the interface in the oxide. 0 μm represents the metal-oxide interface, negative the metal and positive the oxide.
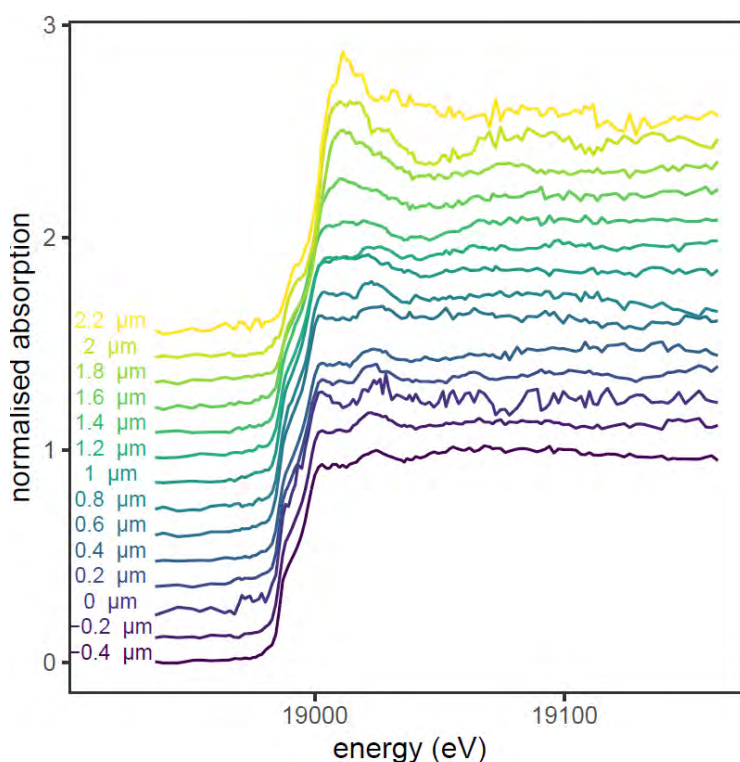


*Figure 6-6. Nb fluorescence spectra moving from the metal into the oxide with spatial separation on the sample of 200 nm. All spectra have been normalised, and are offset vertically by 0.125 for ease of viewing.*

To quantify the evolution of spectra, as mentioned in section 6.2.2, each spectrum was fit as a linear combination of Nb standards. The spectra of individual standards can be viewed in Figure 6-7. This procedure allows calculating the best mathematical fit from the given reference spectra, the percentage included from each standard corresponds to the percentage of Nb atoms in that state, i.e. metallic or different oxidation states. Examples of the resultant fits are shown for the XANES spectra in the metal and 2 μm into the oxide in Figure 6-8. All four reference-spectra were included in the

fitting for each point. The resulting percentages from the best fit for each spectrum, of the line scan, are displayed in Figure 6-9. In Figure 6-9 a distance of 0 µm represents the metal-oxide interface, negative the metal and positive the oxide.
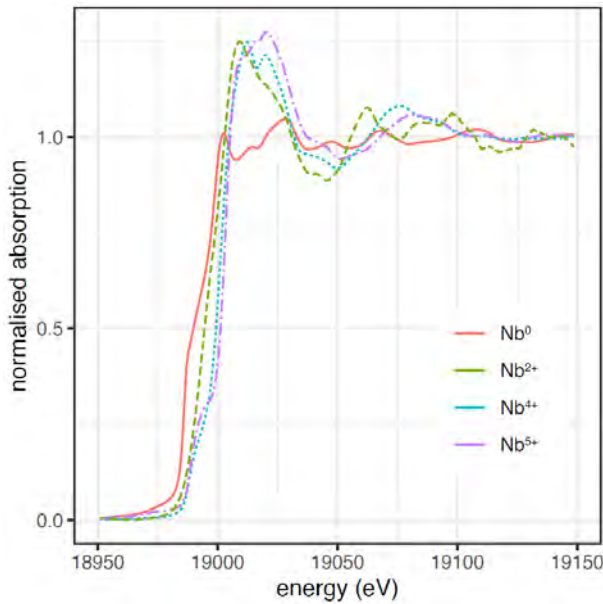


*Figure 6-7. Four XANES standards used for linear combination fitting. The four standards are Nb foil (metallic), NbO, NbO2, N b2O5. All spectra have been normalised.*
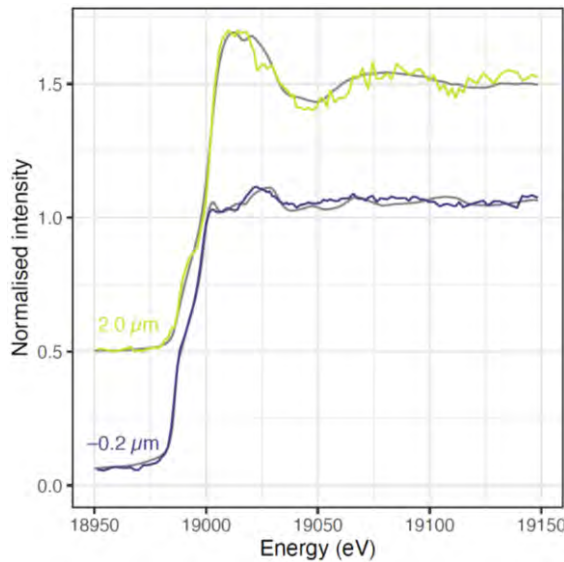


*Figure 6-8. Examples of linear combination fitting where the coloured line represents the spectra (as per Figure 6-6) and grey line represents the linear combination fit, one spectrum is taken in the metal part of the sample (-0.2 µm) and one spectrum is taken 2 µm into the oxide. The results from the fitting for each point, including these two, are given in Figure 6-9.*
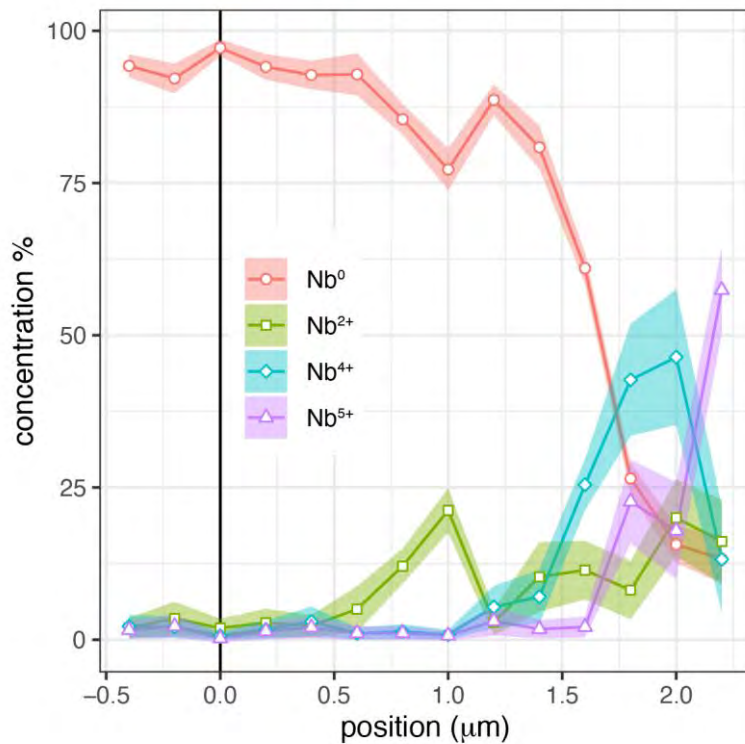
*Figure 6-9. The resulting constituent percentages for each position across the sample. The lines and points show the best linear combination fitting of the four reference standards. The shaded area represents the variation in fit when considering all solutions with residual error within 1% of the best fit.*

### 6.3.1  Verification of fitting confidence

Fitting the standards has a level of uncertainty associated with it, partly due to the noise-to-signal ratio of the measured spectra, and partly due to the effect of local atomic environment, which are different between the sample and the standards. While the local environment is not expected to affect the energy of the absorption edge, it may affect the structure of the spectra after the edge. To provide further confidence on the results presented above, the sensitivity of the results was tested against (a) the choice of spectral energy range used for fitting and (b) variations in the fitting parameters near the best-fit solution. Although (a) may lead to large uncertainties if the spectra are cut at values just beyond the edge, this uncertainty become vanishingly small when a suitably large spectral range is considered – see Appendix C for details.  On the other hand, (b) exploring the variations of fitting parameters near the best-fit solution provides an estimate of uncertainty caused by the noise in the signal. This is plotted as a shaded area in Figure 6-9, which depicts the range of possible solutions that yield a residual error within 1% of the best-fit solution (represented by point). More details are

provided in the Appendix C. This uncertainty increases in the oxide as a function of distance from the metal-oxide interface. However, it remains sufficiently small to provide confidence on the key findings.

The four standards used are the stable Nb oxides NbO, $NbO_2$ and $Nb_2O_5$. In Figure 6-9 $Nb^{2+}$ decreases at 1.2 µm into the oxide, but the $Nb^{4+}$ only begins to appear in meaningful concentrations only after 1.4 µm, this might suggests that the $Nb^{3+}$ state could potentially exist in the region in between. However, the residual error using these four standards remains small for all points, including those where a $Nb^{3+}$ state might be expected (see Appendix C), which indicates that if there were any contribution of $Nb^{3+}$ it would necessarily be a small one. Still, to examine the contribution if a $Nb^{3+}$ standard was present it was possible to obtain such a spectra from other researchers and hence these results are shown in the following section (6.3.2)

As with any XANES analysis, there are additional sources of error that are not accounted for here which introduce noise into the data, these could arise from many sources such as; magnetic and electrical fields from equipment or elsewhere, cosmic rays or activity, beam instability, changes to the surrounding environment as well as others. This accounts for some of the uncertainty within these measurements and was previously mentioned as the signal to noise ratio. When observing the first 2 points in Figure 6-9, these measurements are taken from the metallic portion of the sample, and hence we expect 100% of the Nb to exhibit a $Nb^0$ charge state. However, the unconstrained fitting procedure obtains a lower residual error by including small additions (up to 5%) of the other standards. Additions such as these are expected to be from the ultra thin 2-5 nm oxide formed on zirconium alloys even at room temperature but also by the noise in the signal. Nevertheless, these uncertainties appear to be small and do not reduce the trend of increasing oxidation state as the distance from the metal-oxide interface increases. Which is in line with expectations and in agreement with previously reported observations.

### 6.3.2  Incorporation of the $Nb^{3+}$ standard obtained from external researchers

As mentioned above, it was expected that the contribution of the $Nb_2O_3$ standard oxidation state should be small; however, it was necessary to verify this point, and to provide a complete evaluation of the effect of each state. To improve the validity of results and also to verify clearly this point, at the late stages of the progress of this research, a XANES spectrum of $Nb_2O_3$ oxide acquired in a different laboratory has been obtained. After its calibration, it was used to perform once more the fit, using the previous four standards as well as the $Nb_2O_3$ standard. Results of this new fit are presented in Figure 6-10. From these results, it can be observed that the oxidation state increases gradually from a state

of 2+ to a state of 5+ including the state of 3+. A small amount of $Nb^{3+}$ can be observed close to the interface as the concentration of $Nb^{3+}$ oxide seems quite small, a certain uncertainty exists in its quantification. However, this early oxidation of Nb at the metal-oxide interface is not surprising and could have two origins. The first one is the surface oxidation of the specimen which varies in thickness depending on their oxidation properties, and the methods of preparation. The irradiated materials show a bigger tendency for such oxidation. The second origin of such signal is the oxidised Nb in the oxide matrix in that location. It would be expected that Nb in the oxide matrix had oxidised but since the values are not much higher than on the metal side of the interface it is difficult to conclude for definite. If some oxidation of Nb is present, its quantity is small with respect to the total content of metallic Nb present. This finding further consolidates the fact that the early oxidation states of Nb in the Zr-Nb alloys (in this case the ZIRLO alloy) are indeed below the state of 4+ as required to satisfy the C4 model for reduced hydrogen uptake (refer to section 2.7.5).
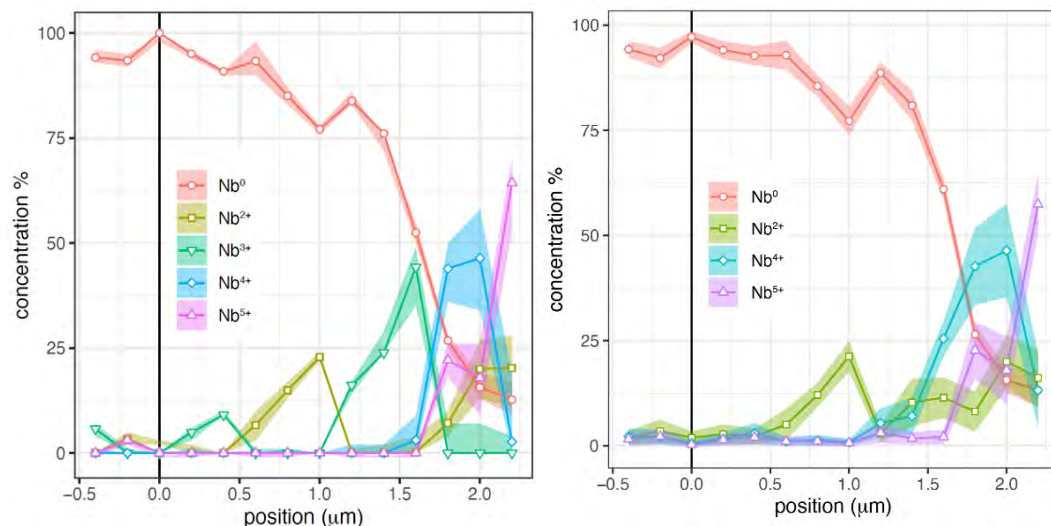


*Figure 6-10. The resulting constituent percentages for each position across the sample. The lines and points show the best linear combination fitting of the five reference standards. The shaded area represents the variation in fit when considering all solutions with residual error within 0.1% of the best fit. Figure 6-9 with only four standards is also provided for comparison.*

# 6.4 Micro-XRD of $ZrO_2$ in low-tin ZIRLO

XRD patterns were taken with a step size of 300 nm in both the horizontal and vertical directions across the whole sample. This allows high spatial resolution XRD information across the whole sample to be taken and, in the case of this material, can provide the tetragonal and monoclinic phase fractions in the oxide. The superposition of all 2D diffraction patterns, can be seen in Figure 6-11.a and in Figure

6-11.b the resultant integrated 1D spectrum is provided as intensity vs 2θ. Furthermore, example of diffraction pattern from one pixel, in 2D and the 1D resultant are also provided in Figure 6-11.c and Figure 6-11.d.

The distribution of different phases along the sample can be observed in Figure 6-12. Texture exists in the metal part of the interface and regions with differently oriented grains can be viewed using this technique. For example Figure 6-12b shows the intensity of Zr grains with the (101) orientation. The tetragonal and monoclinic phases seen in the oxide side of the sample are explored in more detail, with the aim to examine the tetragonal content as a function of distance from the interface.
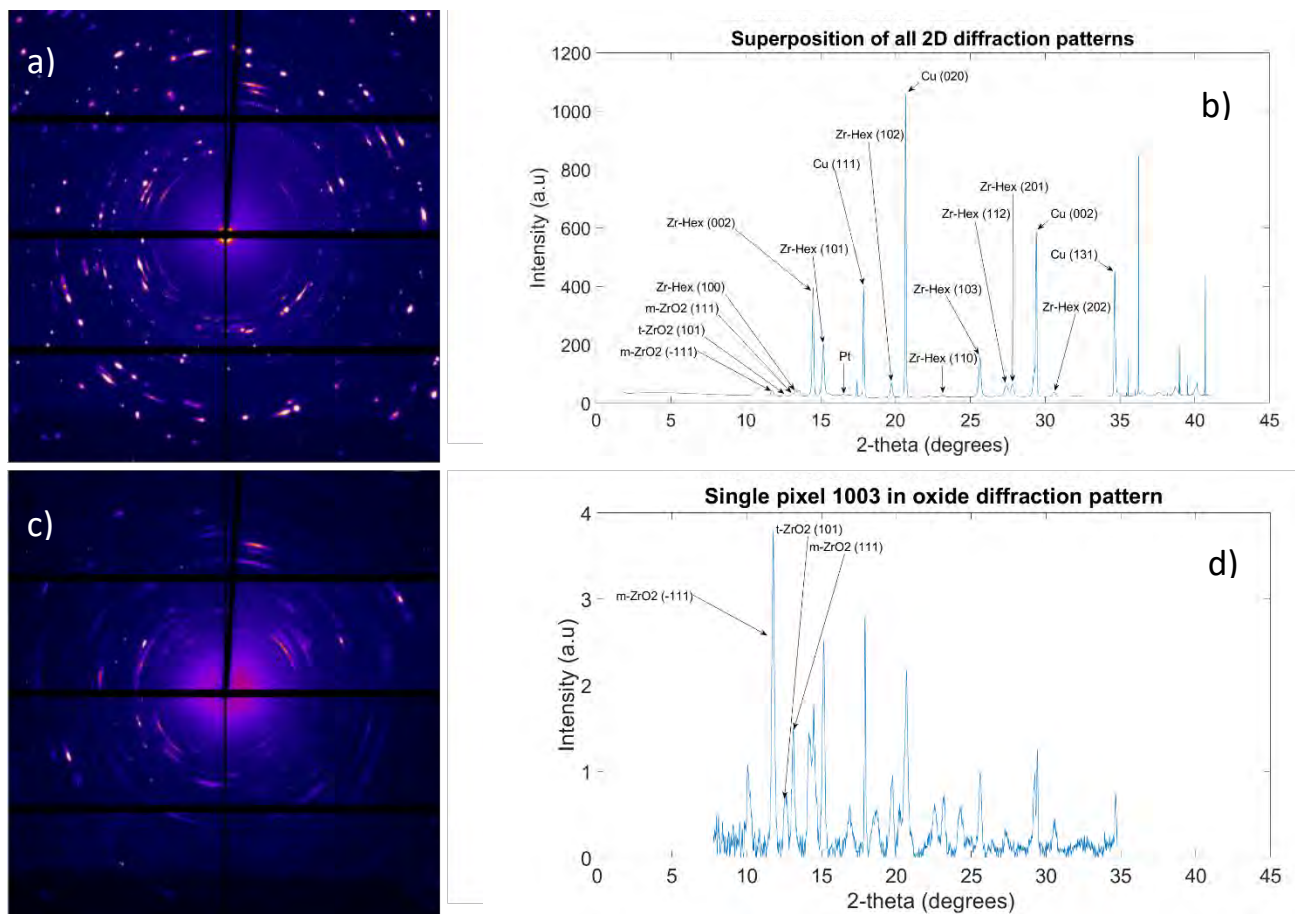


Figure 6-11. a) Superposition of all 2D diffraction patterns from each 300 nm x 300 nm pixel.  b) the resultant 1D spectrum which is a sum of all diffraction patterns taken over the sample. Here the background has been removed. The copper signal originates from the copper grid used as sample holder, and is the most intense signal. The other phases are shown. c) The individual 2D diffraction from one point of the sample (beam diameter less than 1µm) and the 1D spectrum from this 1µm beam region. The beam located in the sample's oxide region, is at the origin of "better observed" monoclinic and tetragonal peaks.  It is worth noting that the ratio of tetragonal to monoclinic in this specific spectrum is in the range of 12%.

The ratios of hexagonal Zr, tetragonal and monoclinic oxide phases are represented, for one column of pixels, perpendicular to the metal-oxide interface in Figure 6-13. The XRDUA software was used to provide the ratio of different phases as a function of distance from the interface (Figure 6-13a). The software calculates the ratio of different phases, using the intensities of related XRD peaks for each phase without taking into consideration the texture parameter. Therefore, the resultant phase ratios presented in that Figure can only give an approximate distribution of these phases providing a qualitative information. In Figure 6-13b the superposition of the tetragonal $(101)$ plane (in green) and the monoclinic $(\bar{1}11)$ plane (in red) are given. These are the same as Figure 6-12 c and d, and are included in this way to provide a qualitative visual information about the distribution of these phases in the oxide near the metal-oxide interface. It is however possible to distinguish the preponderance of tetragonal phase near the interface. In order to perform a quantitative analysis of the tetragonal content, the Garwie-Nicholson equation for tetragonal content was used. The results are displayed in Figure 6-14 for the same pixel line perpendicular to the interface as was used in Figure 6-13. Each data point is only one single XRD spectrum (1D from one 2D dataset). This approach increases the accuracy and the resolution of the information. The calculation of error bars is shown in section 2.2.3. and they are provided here to show the reliability of each data point. It can be seen that when low amounts of signal, and therefore oxide phases, are present the error is much higher but this is reduced to an adequate size once in the oxide.

Two observations can be made; firstly, the highest amount of tetragonal phase is seen closest to the metal-oxide interface, this has been reported previously from TEM [44], [55], [67] and Synchrotron results. Secondly, the placement of tetragonal is not uniform parallel to the metal-oxide interface, instead what appears to be islands, or at least regions of higher intensity, of tetragonal can be seen and these do not appear to correspond with either areas of thick or thin oxide growth. These are marked with white arrows on Figure 6-13.b.
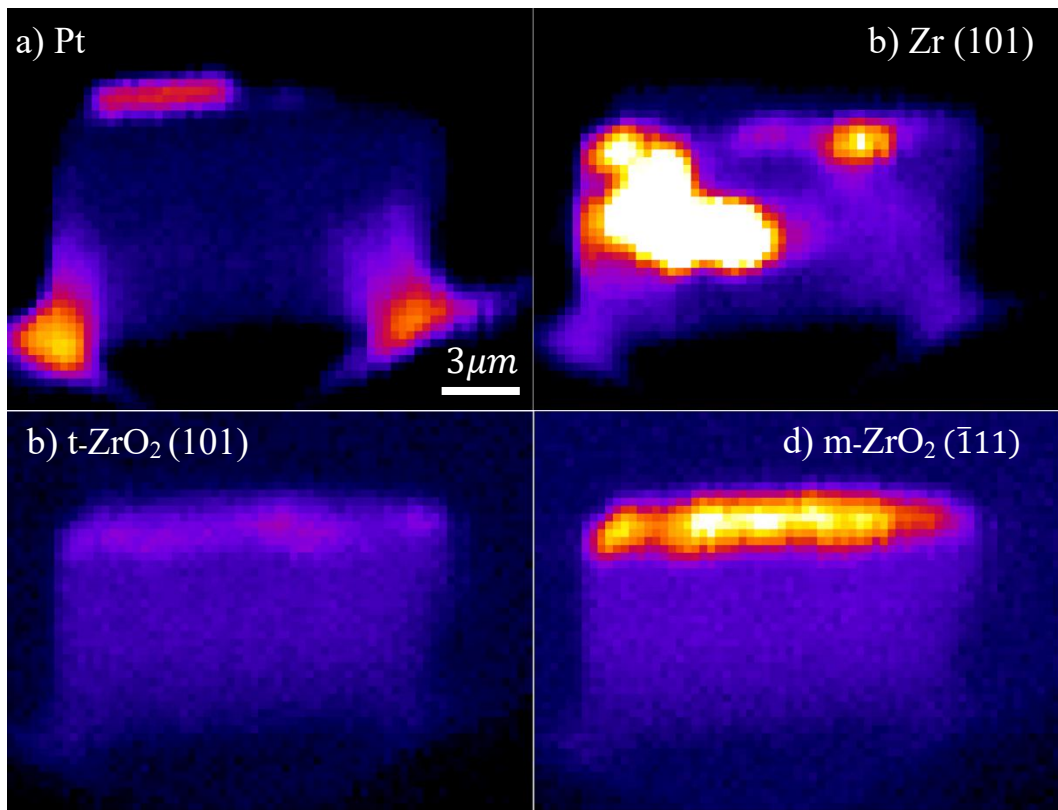
Figure 6-12. a) Intensity map of XRD signal for platinum shown as a marker for the sample; to give the position and outline for intensity maps: b-d. b) Intensity map of XRD signal for Zr (101), c) for tetragonal $ZrO_2$ (101) peak and d) for monoclinic $(\bar{1}11)$ $ZrO_2$ . Each pixel corresponds to one diffraction pattern and pixel size is 300nm x 300nm.
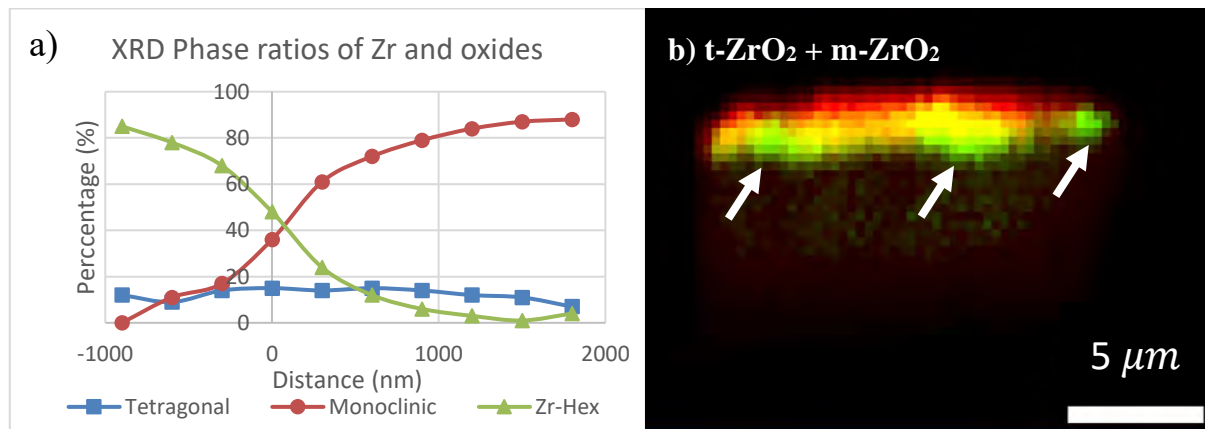


Figure 6-13. a) XRD phase ratios of Zr hcp and two oxide phases perpendicular to the metal-oxide interface for a single pixel data set. b) The superposition of the tetragonal and monoclinic intensities from Figure 6-12 is provided for comparison. As observed, the tetragonal phase ratio is preponderant close to the metal-oxide interface (white arrows).
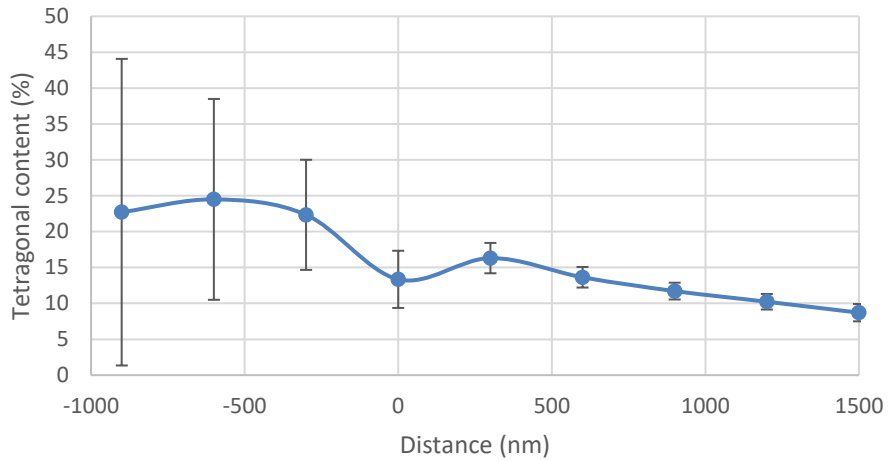
*Figure 6-14: The tetragonal content of the oxide as a function of distance from the interface, in the region close to the area studied for XANES. The interface is estimated to start at position of 900 nm on the graph. As the fomula only contains terms for oxide phases when the beam is in the metal the values are not reliable since the intensity mainly comes from noise, hence the first three data points (from 0 to 900 nm) show a larger error bar. The XRD spectrum of those three points contains a large metallic peak.*

# 6.5 EELS of Zr-2.5%Nb

The acquisition of these EELS datasets is described in section 3.2.2, all the data acquired shown in this section comes from point, line and maps acquired on the JEOL ARM200F equipped with a cold FEG used for high resolution EELS with a Gatan Quantum 965 ER GIF, in STEM mode. Figure 6-15 is included to help illustrate the different regions probed with EELS R1-R8 are the different spectrum images acquired where red is a map and yellow is a line. The green box shows the area of the EDS map displayed in Figure 6-3.
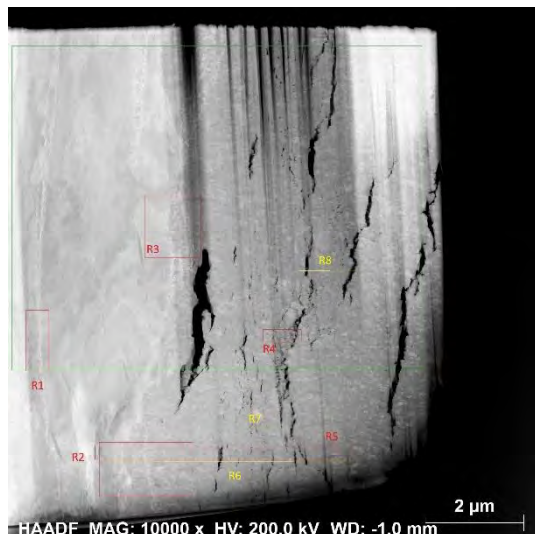


*Figure 6-15. HAADF STEM image of Zr-2.5%Nb lamella. Annotation shows the differently probed areas; Red is an EELS SI, Yellow is an EELS line scan and green is the placement of the EDS map shown in Figure 6-3.*

For each point low loss, the O K edge as well as the Zr and Nb L3 and L2 edges were acquired. It is well known that this alloy displays large Nb rich phases which have been identified as $\beta - Zr$ [64], [67], these can also be clearly seen in the EDS maps shown in Figure 6-2 and Figure 6-3. Figure 6-16 shows a BF image from one of these regions in the metal it's position correlates with R1 in Figure 6-15. Figure 6-17 shows spectra from both the metal matrix and an Nb rich phase in the metal. These can be used as internal standards. It is important to have these, since due to the energy resolution and stability of the microscope and detector, as well as their alignment and calibration, for the spectra acquired the exact values of the peak positions could differ from other reference values. The change in peak energy and peak intensity of spectra from the internal references can be used to indicate a change in the

material. Of interest here is the Zr L3 edge and the Nb L3 edge, for both peaks a shift towards higher energies indicates oxidation, this phenomenon has been used many times, not only in this field, to examine the oxidation of Nb [97], [101], [150], [205], [209], [210]. Although Nb is expected to also be present in the matrix the expected value is lower than 0.5wt% and hence, with the sensitivity of EELS, it can be very difficult to show the state of Nb at a position in the matrix. Since this material has been subjected to three cycles in reactor, and hence a fairly high level of irradiation, Nb is known to diffuse out of Nb phases and into the matrix. This is also seen from the EDS quantification in Table 6-1 which agrees that the Nb in the $\beta - Zr$ phases is less than the expected value of 20% and higher in the matrix than the 0.5 wt% expected. Especially in regions close to Nb phases where a higher content of Nb is seen.

Although irradiation would induce non-equilibrium solid solubility and higher concentrations of alloying elements can be observed in the Zr matrix after long-term irradiation, in the case of Nb alloys, a certain concentration of the dissolved Nb is reported to precipitate further in the form of nano-size $\beta - Nb$ needles. [25], [211]. The non-uniformity of the distribution of Nb in the matrix means that even pixel to pixel there can be a difference in spectra and the Nb L$_3$ peak is not always seen in the matrix and when it can be seen it is small. It is well reported that Nb rich phases remain metallic and structured some distance into the oxide layer [16], [64], [67]. At a distance into the oxide, these will oxidise and dissolve in the matrix. In these regions which were previously Nb rich phases there is now higher amounts of Nb found in the matrix, this facilitates easier probing of the Nb oxidation state on dissolved Nb rich phases. Because of the high spatial resolution of EELS it has been possible to separate out the different regions and features. Thus, not only the distance into the oxide layer for a given spectrum is important, but also its position. Figure 6-18 shows spectra from the following features; a structured metallic Nb rich phase, Nb in the metal Zr matrix, Nb in the oxide matrix in the inner oxide (0.7μm from interface), a region which contained an Nb rich phase before but is now oxidised (3.6μm from interface). These are included to give examples of the spectra from different features/regions and four of the spectra used to analyse the peak shift shown in Figure 6-19. The four spectra in Figure 6-18 are given as examples of spectra on different features and do not represent every spectra on a similar feature, for example one feature is named as oxidised Nb phase but the spectra from every oxidised Nb phase is not expected to be the same, it is in fact this variation which is being studied. The spectra are included to give examples of the type of spectra encountered on these different features and to show visually the evolution of the spectra. The peak centrum positions for the ZrL3 and NbL3 edges from Figure 6-18 are also given numerically in Table 6-2 to help illustrate the changes.

A similar process was then carried out for many positions, and therefore sufficient spectra were obtained. All spectra were acquired with a channel width per pixel of 0.25 eV, and dispersion of 0.25eV. Meaning that electrons will detected in one channel or another due to variation from the energy distribution from the electron source. This is also the case when aligning the ZLP leading to the error on single spectrum peak positions being 0.5eV. The results are plotted in Figure 6-19, showing the peak centrum position for the Nb L3 peak as a function of distance with respect to the metal-oxide interface, (I.e. perpendicular distance from the metal-oxide interface).

Negative numbers indicate distance in the metal from the interface and positive distance into the oxide from the interface, 0 being the metal-oxide interface. Different markers are used to show if the spectra were acquired on a structured Nb rich phase (I.e not dissolved in the oxide) (triangle) or on the matrix (circle). Here if an area was previously SPP but now that phase is fully dissolved it is given the same marker as matrix. Two markers are also included in red to indicate the internal standards in the metal. As stated in the literature review section 2.7.8 it has been shown how the shift in Nb L edge can be used with EELS to show the oxidation state of Nb. Please refer to Figure 2-19.
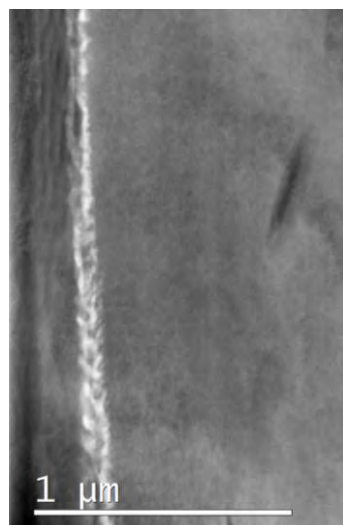


*Figure 6-16. Bright Field STEM-TEM image showing a Nb rich phase (white) surrounded by Zr metal matrix*
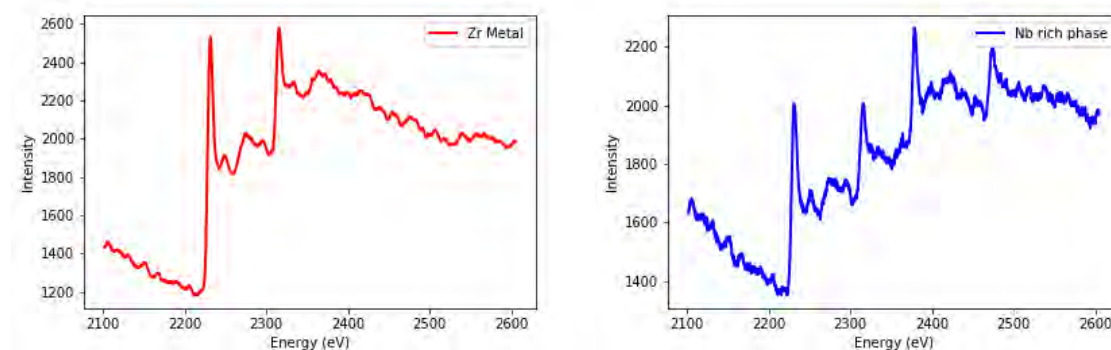
*Figure 6-17. The EELS spectra from two positions; a) from the Zirconium metal matrix. b) from a Niobium rich phase in the metal. The L3 and L2 peaks from metallic Zr can be clearly viewed in both spectra whereas the Nb L3 and L2 edges can only be clearly seen in b). the peak centrum values are as follows: a) Zr L$_3$ – 2231.75eV, Zr L$_2$ – 2316.0 eV b) Zr L$_3$ – 2231.75eV, Zr L$_2$ – 2316.0 eV, Nb L$_3$ – 2379.75eV, Nb L$_2$ – 2474.5eV*
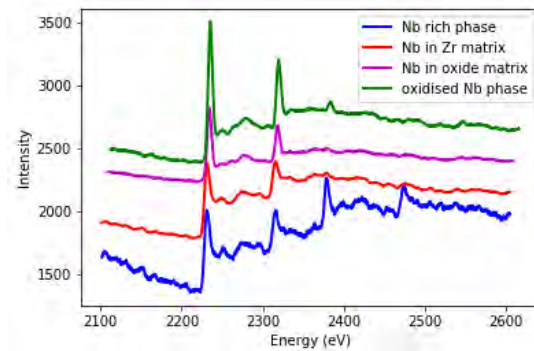


*Figure 6-18. Four typical EELS spectra from the following positions; a structured metallic Nb rich phase (blue), Nb in the metal Zr matrix (red), Nb in the oxide matrix in the inner oxide (magenta), a region which contained a metallic Nb rich phase previously but is now oxidised (green).*

*Table 6-2. The numerical values of the Zr L3 and Nb L3 peak centres from four different regions also shown is their position perpendicular from the metal-oxide interface. Negative numbers represent position measured in the metal and positive in the oxide. Reference values from the 'EELS atlas'\* are also given.*

| Feature analysed | distance from metal oxide interface (um) | Zr L3 peak | Nb L3 peak |
|---|---|---|---|
| Reference values (Metal) | | 2222.0 | 2371.0 |
| Structured Nb phase | -2.5 | 2231.75 | 2379.75 |
| Nb in the metal matrix | -2.7 | 2232.0 | 2379.75 |
| Nb in the oxide matrix | 0.8 | 2234.25 | 2380 |
| oxidised Nb phase | 3.6 | 2234.5 | 2384.25 |

\*Reference for metal peak positions from Gatan's EELS Atlas at https://eels.info/atlas
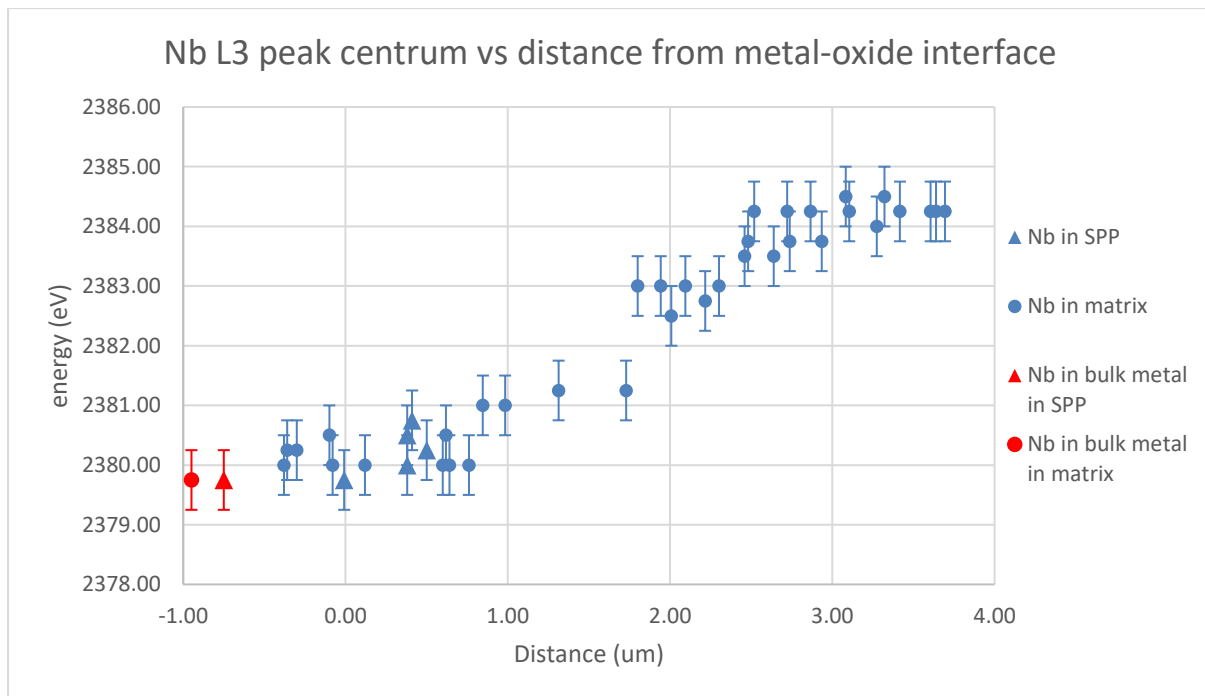
*Figure 6-19. Peak positions of the Nb L3 edge vs the perpendicular distance from the metal-oxide interface, 0 marks the interface with negative values being in the metal and positive values being in the oxide. Values from the bulk metal at a distance of 2-3 um from the interface are used as internal standards and shown in red.*

In Figure 6-19 a clear trend is observed where an increasing energy shift, which is correlated to an increasing oxidation state, is seen as the distance increases from the metal-oxide interface. This is until a maximum shift of 4.5eV is seen which indicates $Nb^{5+}$. The fact that specific shifts can be measured at specific positions with such high energy resolution and particularly spatial resolution is the power of these results and these will be discussed further in the discussion section of this chapter. Another feature of interest is the many cracks found in the oxide layer, as already mentioned at the distance from the metal-oxide interface where Nb is dissolved many cracks exist and these cracks are often seen to be decorated with Nb (and small amounts of Fe) as seen in Figure 6-2. Since the origin and morphology of the cracks is of great importance to the oxidation and hydrogen uptake properties of the cladding these features were also examined using EELS. In general the trend and shifts were quite similar to that of Figure 6-19. Large peaks were often seen at the edges of cracks which would not just be the result of higher Nb content but also thinner material at crack edges would increase the signal to noise ratio. One interesting observation is that Nb peaks from cracks often had large FWHM or irregular shapes two example spectra are given in Figure 6-20. Two possible explanations for this could be; either Nb exists in multiple oxidation states in this region and hence actually the peak is made up

of multiple smaller peaks, or it is an artefact of the low intensity due to the small amount of material and there are not enough counts to form a symmetrical peak.
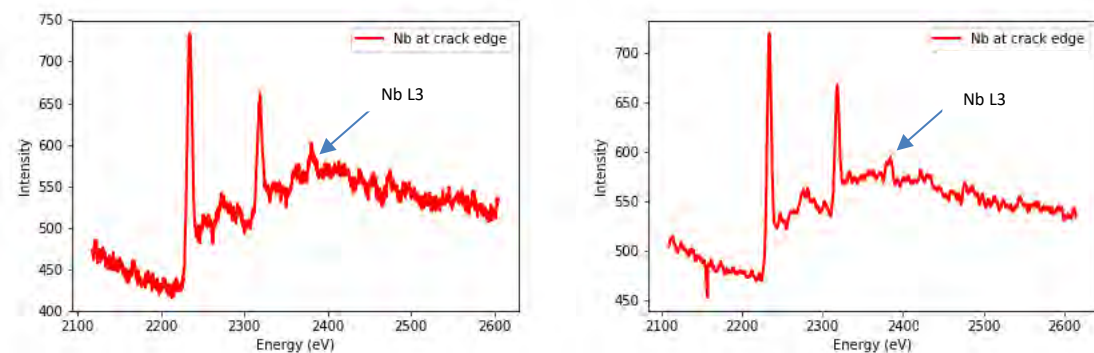


*Figure 6-20. Two examples of the unusual shaped Nb L3 peak often found at the edge of cracks*

### 6.5.1 Summary of results for this chapter

In Figure 6-9 (XANES) it can be seen that the Nb in the oxide of the low-tin ZIRLO remains predominantly metallic until 1.2-1.4 µm into the oxide. However, after approximately 0.5 µm into the oxide, certain amounts of $Nb^0$ are oxidised into $Nb^{2+}$, and at 1.4 µm distance from the interface, the remainder of the $Nb^0$ signal starts to drop and rapidly is replaced by increasing amounts of $Nb^{4+}$ and then $Nb^{5+}$.

A similar result is seen in Figure 6-19 (EELS) of Zr-2.5%Nb.  The distances are also quite similar, additional information that is brought shows that although mostly the shift is small and within the expected scatter, in some places within the first micron of oxide, a shift larger than the error can be seen which may indicate small amounts of oxidation. For example, 3 points are taken on an SPP from 0.38-0.41µm into the oxide. The peak is seen at 2080.0-2080.75 a maximum shift of 1eV, this suggests small amounts of oxidation on the outer side of the SPP (the edge which is furthest into the oxide). At distances of 2.5µm into the oxide the maximum peak shift of 4.5eV is observed and at 3µm the shift begins to plateau with almost all the points showing an approximate shift of 4.5eV.

The XRD results on low-tin ZIRLO reveal the presence of tetragonal phase in the oxide. Due to the small concentration of the Nb oxides, these oxides could not yet be revealed in the data.

# 6.6 Discussion

The aim of this section of the thesis has been to study, in depth, the speciation of Nb in the oxide, near the metal oxide interface, to verify two points: a- is there any $Nb_2O_5$ ($Nb^{5+}$) present in the oxide. b- What is the exact speciation of Nb as the distance from the metal-oxide interface increases? The interest for this information stems from the observation that in the case of Nb containing alloys, the speciation of Nb influences the charge compensation near the interface and thus can reduce the HPUF in these alloys. According to the theory, previously mentioned, this will only be the case if Nb is found in solid solution with an oxidation state of less than 4+ [42]. A state of $Nb^{5+}$ is also of interest as other researchers have shown the presence of $Nb_2O_5$ at the water-side oxide [212]. These authors claimed that the presence of this $Nb_2O_5$ oxide near the outer oxide promotes the reduction of $H^+$ closer to the coolant and thus further reduces the ingress of hydrogen into the metal substrate. By comparing the results obtained from two techniques on two Nb alloys a more comprehensive understanding about the speciation of Nb could be drawn.

The speciation of Nb in low-tin ZIRLO measured by XANES is shown in Figure 6-9, the advantage of that technique is that all the Nb over a large volume can be measured and then the signal may be de-convoluted to show the relative percentages of each Nb phase (for the standards which exist). In parallel Figure 6-19 shows the speciation of a Nb in a Zr-2.5%Nb measured by EELS, the advantage of this is the spatial resolution allowing the accurate probing of specific positions and features. In contrast to XANES EELS spectra in this application are not possible to deconvolute (e.g separate the exact percentage of Nb oxide which causes the peak shift) since the spectral feature under examination is purely a peak shift rather than a whole spectrum change. If the two peaks exist in parallel and shift is too small to be resolved between them it will appear as a single peak with a shift between the two positions. In the case of our spectra, as the intensity of signals were low, it was decided to report only the peak shift and deconvolution was not performed. While deconvolution was possible for the XANES signal without using other techniques it is impossible to know exactly what is being probed, i.e. the region examined would contain all phases present in that area. It must be mentioned that the part of the reason the deconvolution was more feasible was due to the large volume of material probed (this was related to the beam size as well as the thickness of the sample studied), as well as the better signal yield further improved by averaging approximately 10 spectra. So it can be seen the two techniques complement each other well.

*Delayed oxidation and metallic Nb in the oxide*

From both sets of results it appears that Nb remains metallic in the oxide, both in the SPPs and in the metal matrix in the vicinity of the interface. Whereas, in the region between 1-2 µm into the oxide a shift of 1.5eV is seen which is halfway between a total shift of 3eV to Nb$^{2+}$ here it is assumed from this observation that most likely approximately 50% of the Nb is oxidised to a (2+) state. The possibility that different combinations of Nb oxidation states make up this shift cannot be excluded. However, the XANES results have clearly shown the absence of Nb4+ close to the interface thus the suggested case is certainly the most probable since if it were the combination of metallic and a higher oxidation state with a larger shift of 4.5eV this should be resolvable. Therefore, if there are contributions from multiple other oxidation states they should be small. It is important to note that all the points in that region are found in the matrix, this, as well as the general lack of points in that region, was because no Nb rich phases were found at that distance. It is definitely not the case that no Nb rich phases exist in that region but more coincidence that for the lamella studied they were either not found or the lamella were not appropriate for EELS study. Indeed even in Figure 6-2 structured Nb phases (previously shown to be metallic [67]) were seen extending up to a distance of almost 2 µm and potentially remaining metallic the whole distance, particularly when still linked to the metal. Therefore it is expected that Nb remains metallic in SPPs for a greater distance than in the matrix. With the results from the XANES study it is difficult to assess the distance Nb SPPs remains metallic in ZIRLO as they are of different composition compared to that found in the Zr-2.5%Nb alloy. The secondary phase in ZIRLO is a $\beta - Nb$ rather than $\beta - Zr$, i.e. it is an intermetallic with 80% Nb Furthermore, the morphology is spherical, whereas in the case of Zr-2.5%Nb a lath-type structure is observed. Also the size of precipitates is much smaller. Nevertheless, within the first micrometre of oxide on the low-tin ZIRLO almost all the Nb remains metallic (but this percentage does decrease slightly as distance increases from the interface). Other studies on these two different type of SPPs suggest that $\beta - Nb$ SPPs are more likely to stay metallic for longer in the oxide compared to $\beta - Zr$ [128], [206], [213]. These results would tend to agree with the above mentioned finding, but due to the lack of SPPs studied at greater distances into the oxide with EELS it cannot be concluded. The solid solubility of Nb in the Zr matrix is in the range of 0.4 to 0.6 wt% depending on different types of alloys, in the case of the ZIRLO alloy, 0.5 wt% is claimed to be in the solid solution [213]. Since approximately 50% of the signal is coming from the SPPs and 50% from the matrix if the Nb in the matrix had oxidised a much smaller percentage of the signal, and therefore of the Nb should be metallic. The finding that Nb remains metallic (in the SPPs) to these distances into the oxide layer is not new and is in good

agreement with other studies on Nb alloys [16], [67], [112], [145], [146]. But the finding that Nb remains predominantly metallic even in the matrix up to a distance of approximately 1 μm, to our knowledge has not been shown before.

After the first micrometre it is also useful to correlate the two sets of results. At this distance in Figure 6-9 it can be seen about 25% of the Nb is in a (2+) state. This fits well with the EELS at that distance which, as previously mentioned, could show 50% of the matrix is in a (2+) state. In other words if 50% of the XANES signal comes from Nb in the matrix and 50% of that was $Nb^{2+}$ 25% of the signal should show $Nb^{2+}$. The distance, which this situation continues, does not perfectly match with the two data sets with a slight increase in the metallic XANES signal and then rapid oxidation. Whereas it seems to extend further in Figure 6-19. There are a few possibilities for this; firstly, the materials themselves are different and while they both contain Nb and hence have many similarities the difference in morphology, especially the Nb phases and distribution, is expected to create some differences in the oxidation of Nb across the oxide. Secondly, just by looking at the points at 1 μm and 1.2 μm on Figure 6-9 it looks like they are going against the trend and it could be possible that at that position there is a larger amount of Nb SPPs or some particularly large ones. Thirdly, it has already been mentioned about the lack of points on Figure 6-19 between 1 and 2 μm and with this small amount of statistics, it is difficult to exactly determine the average behaviour in this region.

### Nb oxidation state at a distance from the interface

In both samples it seems that large amounts of $Nb^{5+}$ is present. In Figure 6-9 slightly over 50% and significantly above the uncertainty limit, is observed at 2.2 μm into the oxide. Unfortunately this was the edge of sample studied and it is not clear what would happen at greater distances into the oxide, if the trend were to continue of increasing oxidation further into the oxide one could assume all the Nb would oxidise to a (5+) state at some distance. This however cannot be concluded from this dataset. From the EELS shown in Figure 6-19 it does seem that the shift plateaus towards the maximum possible shift of 4.5eV which is evidence that the significant majority of Nb was fully oxidised. This is interesting as there is still debate about the presence of this species and its role in hydrogen pickup. Our findings evidence that at some distance from the metal/oxide interface, most of the Nb is observed to oxidise to the highest oxidation state. However, this transition to the 5+ oxidation state of Nb may occur at a distance into the oxide that may be considered beyond the protective barrier layer, that is, in the porous monoclinic oxide that may not provide a rate-limiting

barrier for further oxidation and H pick-up [85], [92], [167]. It must be noted that at a specific distance from the metal-oxide interface, all Nb (both in the SPP and that in the matrix), should be oxidised, and therefore, no further change should be observed above that distance. From these results, it does seem most probable that that state is for Nb to be in a fully oxidised 5+ state although further study would be needed to confirm if this is a true and constant phenomenon. The low-tin ZIRLO alloy examined by XANES, contains a certain amount of Sn in its composition, and thus it cannot be compared exactly with the Zr-2.5%Nb alloy which does not contain Sn. However, as mentioned, the family of ZIRLO alloys have been examined with TEM [101], [168], in all cases delayed oxidation of beta-Nb precipitates was observed. The delayed oxidation of $\beta - Nb$ precipitates in the oxide has been regularly demonstrated, both in irradiated state as well as in autoclave [16], [67], [101], [168]. The similarities between the results from both these samples is interesting, and while because of the different techniques a direct comparison is not perfect they have been used well in conjunction to complement each other.

*Impact of the results on hydrogen uptake*

These findings have implications on the H transport kinetics, as $Nb^{2+}$ and $Nb^{3+}$ have been suggested to compensate for space-charge variation in the oxide during corrosion [42], resulting in parabolic kinetics. The removal of aliovalent dopants in the oxide (e.g. $Nb^{2+}$ and $Nb^{3+}$), either through clustering effects [114], [126], [127] or by increasing the oxidation state to 4+ and 5+, leads to an increase in space-charge, which hinders the diffusion of oxygen vacancies in the protective oxide layer and result in a sub-parabolic oxidation kinetic [127]. However, in that case, it is claimed that the HPUF will increase.

Aliovalent doping as described above, also affects the kinetics of HPUF. In order to complete the electrochemical corrosion cell, charge must be transferred from the metal/oxide interface (anode) to the oxide/water interface (cathode). This is primarily achieved through electronic transport through the oxide from the metal side towards the water side, but can also be partially fulfilled by proton transport in the opposite direction. Thus, aliovalent dopants that increase the electronic conductivity of the protective oxide favour hydrogen recombination near the oxide/water interface, thereby reducing the H pick-up fraction [42], [214]. It is known and has been previously stated that small changes to the alloying element Nb can result in large differences in the HUP of a material but this works shows that there still are many ways in which Nb acts similarly from alloy to alloy. This finding

could help to come to a more complete understanding of the role and behaviour of Nb in Zirconium based nuclear materials under irradiation.

## 6.6.1  Discussion regarding XRD results

The XRD results (performed on low-tin ZIRLO) while not the main focus of the synchrotron campaign provide interesting information about the crystal structure of zirconia that is to a certain degree in agreement with the results observed by previous researchers. It also helps to better understand the structure of the most recently formed oxide and give clues about how this may be correlated with the speciation of Nb in that position. The oxide structure near the interface shows the presence of tetragonal $ZrO_2$. The highest amount of tetragonal is seen in the first point in the oxide with approximately 16% of the oxide being tetragonal phase. The tetragonal content seems to gradually decrease with the distance from the interface. Due to the uncertainty about the signal intensities, it is not possible to explore the peaks at a distance of 2 micrometre from the interface, due to the size of the sample and the intensity of the peaks, which reduces gradually as the beam goes out of the sample and into the air. A certain periodic increase and decrease of tetragonal would be expected, as observed in other materials [70]. However, the maximum content of tetragonal phase is in the region between 300 and 600 nm from the interface.  Interestingly the tetragonal ratio is high in the region where the speciation of Nb in the oxide is mostly metallic, and the $Nb^{2+}$ gradually starts to appear. It could be argued that the presence of metallic beta-Nb particles in this region (i.e. close to the metal-oxide interface), which are more compliant than the oxide, will accommodate the stresses in the oxide, close to the interface and will allow the existence of the tetragonal metastable phase.

It must be mentioned that in this study, the zirconium monoxide (ZrO) observed quite often in autoclaved materials [94]–[100] but also a thin layer on a similar neutron irradiated ZIRLO sample [101], has not been revealed. The reason for this could be the resolution limit of current XRD measurement (the ZrO revealed by that study [101] was in the range of 30 to 50 nm wide, extending from the metal to the oxide). It should be mentioned that while such ZrO phase has been often reported in autoclave materials such reports are rare for irradiated materials [101].

This sample examined in the present study, having only 2.4 μm oxide (the total oxide thickness of the segment has been in the range of 10-12 micrometres), it can be assumed that the oxidation has passed the transition phase. However, the current results show a structure in the vicinity of interface which

points towards the presence of a dense layer near the interface, that leads to a barrier layer promoting low ingress of hydrogen through that part of the oxide, into the underlying metal.

## 6.7 Conclusions

- Both sets of results indicated a trend of increasing Nb oxidation state in the oxide with increasing distance from the metal-oxide interface.

- Both sets of results agree that Nb remains predominantly metallic within the first micron of oxide but with an increasing amount of Nb being oxidised to the $Nb^{2+}$ state.

- Both sets of results show that Nb remains metallic even in the oxide matrix in this region. It is expected that the majority of the Nb oxidation occurring is the Nb in solid solution and both sets suggest that approximately half of the Nb in the matrix could be oxidised to a $Nb^{2+}$ state at a distance of approximately 1μm.

- After the first micron, the results appear to diverge slightly with the Nb in the ZIRLO sample appearing to remain metallic for a greater distance into the oxide. This would be in agreement with other work since the two materials have two different types of Nb SPPs. However, it cannot be shown that the metallic Nb at a distance of 1-1.4μm in the ZIRLO sample is found in SPPs (although it is suspected) and the lack of SPPs studied in the Zr-2.5%Nb sample at this distance may mean the overall Nb state could be different. The exact comparison of the two materials with respect to SPP dissolution is not reasonable as ZIRLO contains β-Nb SPPs (80% Nb) and 2.5%Nb contains β-Nr SPPs (20% Nb).

- The XRD results show the ZIRLO sample to have a considerable amount of tetragonal phase in the oxide close to the metal oxide interface. The highest phase fraction of tetragonal was found to be approximately 16% at the closest point to the interface examined. This amount then decreased with distance from the interface to approximately 8% at a distance of 1.5μm. Due to the size of the sample it cannot be concluded if this trend would continue until the oxide contained no tetragonal or if cyclic behaviour may be present or some other behaviour.

- The tetragonal oxide was also found to vary in concentration even between points at the same perpendicular distance from the interface. Such that 'islands' or regions of higher tetragonal concentration were found rather than a continuous layer at the interface.

# Contents of chapter 7:

# 7 Hydrides and their impact on newly forming oxide

## 7.1 Introduction

As described in the literature review (section2.7.9) it is expected that once hydrogen has entered the Zr metal in concentrations above the TSSP, hydrides will begin to precipitate. The amount and location of hydrides, particularly those at the metal-oxide interface, will influence further oxidation and hydrogen uptake. Previous work postulates that the precipitation of hydrides in the metal, at the metal/oxide interface, will increase the rate of oxidation and hydrogen uptake and more hydrides will lead to a faster oxidation and hydrogen uptake [74], [75], [115], [215], [216]. The oxidation front will no longer be purely oxidising metal but also hydrides found at the interface. It is suggested [74] that the oxidation of this 'hydride rim' will lead to a change in microstructure in the newly formed oxide making it less protective and lead to faster degradation of the cladding. It was observed by TEM that there was a link in highly irradiated claddings between the position of hydrides near the interface and porosity in the oxide (please see Figure 2-27).

As is also discussed in section 47 there is still debate about the phase and structure of the zirconium hydrides particularly those found in reactor samples. Specifically, the presence of a small interfacial hydride between hydride and matrix and the effect of hydrides on the distribution of alloying elements. Then how this will affect the subsequently grown oxide.

Hence this chapter will aim to report the findings on two things:

1. The composition of hydrides at the metal-oxide interface found in irradiated claddings in a Zircaloy-4 material to compare with those studied previously.
2. The structure and composition of newly formed oxide which had formed on a sample with hydrides present at the interface. Particularly to compare the differences between the regions of oxidised hydride and oxidised metal.

To investigate these two points, the technique of TEM/STEM was employed using both EELS and EDS. Firstly the JOEL 2200 FS was used to investigate the area in the vicinity of the metal-oxide interface visually and with EELS. After this, it was decided that the higher spatial resolution of STEM and STEM-EELS or STEM-EDS would be useful to add to the characterisation of these regions. Hence also the FEI

TALOS F200X TEM and the JEOL ARM200F described in section 3.2.2 were used for EDS and EELS respectively. Particularly low-loss EELS was of interest as it had been shown by Dash et al. [217] that the monoclinic and tetragonal phases of zirconia showed a peak shift in the 4p plasmon peak of 0.8eV from 41.5eV to 42.3eV. Woo and carpenter [218] used the low loss EELS spectrum to differentiate between different hydride phases, showing hydrides to have a larger plasmon energy loss than the Zr alpha matrix. A table of the peak positions from the literature for different hydride and oxide phases is given in the Appendix D. The material chosen was Low-tin Zircaloy-4 after 4 cycles in the PWR KKG in Switzerland. Details about the material are given in section 3.1.4and section2.4.2. This material was chosen as it had already been shown to have high amounts of hydrides at the interface [64] and some TEM samples were already produced and present in the lab. Also included in this chapter is the analysis of some EELS data previously acquired in SuperSTEM Darsbury.

It should be noted that the metal-oxide interface and the oxide structure, for this material, had already been studied by TEM in previous publications [33], [67]. It was found that the oxide has long columnar grains surrounded often by equiaxed grains, some small (10-50nm) tetragonal grains were present in the grain boundaries of columnar monoclinic grains. Therefore what was lacking was chemical information, particularly about the distribution of alloying elements, and information on the phase ratios of tetragonal and monoclinic. Although Synchrotron studies have been used in the past to show the fraction of tetragonal phase to be between 4-15% in the first $0.5\mu m$ from the interface for various zirconium claddings [38], the data being from unirradiated material, needs to be further examined for the irradiated alloys. The technique of EELS employed here should give better spatial resolution and allow the probing of oxide close to the hydride as well as close to the metal, hence corresponding to oxidised hydride and oxidised metal.

# 7.2 Results

## 7.2.1 EDS of 4 cycle low-tin Zircaloy-4

To be able to compare results more in-depth, the same sample was probed by EDS and by EELS for different purposes. Figure 7-1 shows the HAADF image of the sample along with the elemental distribution of the different constituent elements. Using the HAADF image and the oxygen map the metal-oxide interface can be clearly seen. In this section only the EDS spectra will be reported. However, using multiple linear least square (MLLS) fitting (on EELS spectra) on a low loss spectrum image (SI) the areas of metal and hydride could be quickly differentiated. This will be shown in the subsequent section to keep EDS results and EELS together for ease of comparison. One area was particularly selected for further study as it included a hydride extending almost perpendicularly from the metal-oxide interface. This would mean that as the oxide front oxidises inwards both areas that are hydride and metal will be oxidised. Hence, either the hydrogen in the hydride will be 'pushed back' into the metal or will be incorporated in the oxide. Also of interest is whether the oxide inherits the chemical composition of the metal near the interface as it moves inwards. Figure 7-2 shows EDS maps of this region with a hydride precipitate adjacent to the interface. From Figure 7-1 and Figure 7-2 it can already be seen visually that the hydrides contain less Fe and possibly less Cr than the matrix. Figure 7-3 shows a Zr $(Fe,Cr)_2$ SPP between two hydrides; once again, especially the Fe content can be seen to be higher in the matrix than the hydride. The visualisation of such variations might not be always easy with such maps, however the quantifications can demonstrate more precisely these variations. These EDS maps are spectrum maps meaning that each pixel is a full EDS spectrum and the quantification in Table 7-1 comes from many (hundreds) of pixels in a similar region. The areas of quantification are marked in yellow boxes on Figure 7-2 and Figure 7-3. Therefore, the data can be considered as averaged and reliable for one quantification box. It should be kept in noted that only one area of oxide adjacent to hydride and matrix was compared so while the values for those boxes may be reliable it cannot be claimed that every oxide adjacent to matrix or hydride would share the same values. Furthermore, even within similar phases (e.g. different regions of the metal matrix) the value may still vary as the alloying elements are not always uniformly distributed. For example, closer to an SPP the matrix is more enriched. Therefore, in the table a range is given to indicate the results from 2-3 different quantification areas as well as an error which is one sigma for one quantification area.
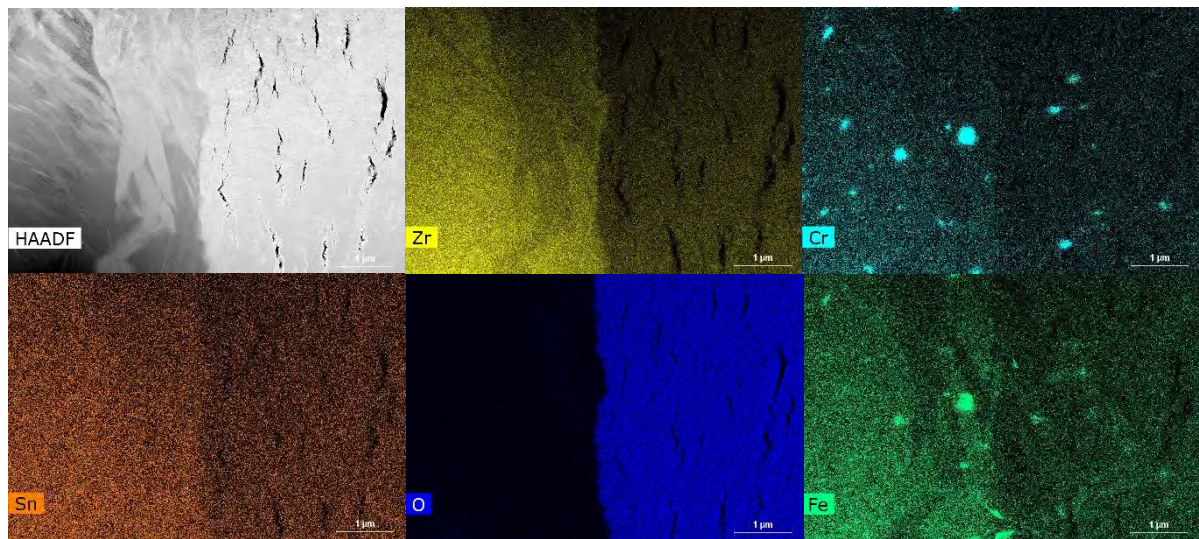
*Figure 7-1. HAADF overview image of a 4-cycle low-tin Zircaloy-4 metal-oxide interface, the EDS maps for the main constituent elements are given as labelled. Scale bar is 1µm*
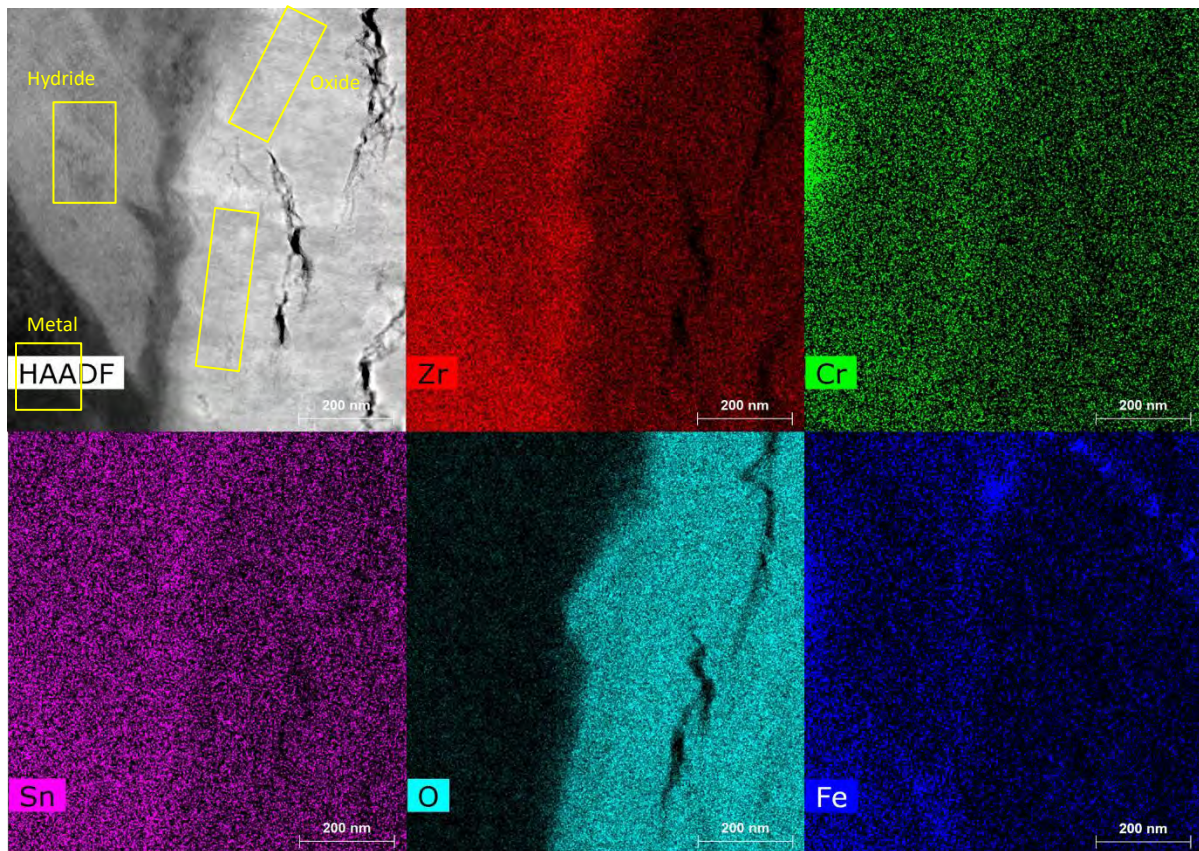
*Figure 7-2. HAADF image of a 4-cycle low-tin Zircaloy-4 metal-oxide interface and hydride adjacent to it. The phases metal, hydride and oxide are marked in yellow. The EDS maps for the main constituent elements are given as labelled. Scale bar is 200nm*
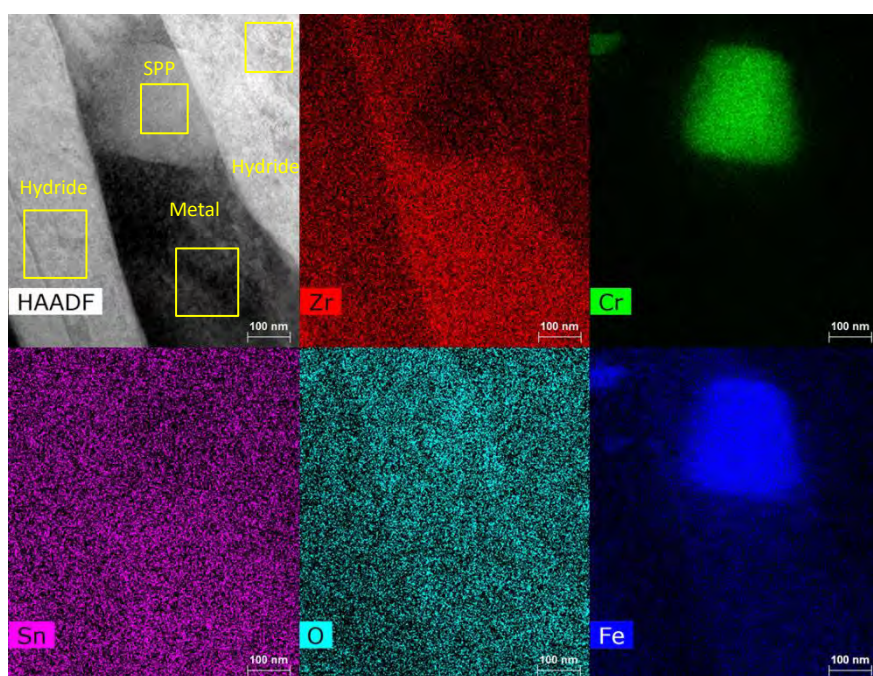


*Figure 7-3. HAADF image of a 4-cycle low-tin Zircaloy-4 showing an SPP between two hydrides. The phases metal and hydride are marked in yellow. The EDS maps for the main constituent elements are given as labelled. Scale bar is 100nm*

*Table 7-1. Quantification of constituent elements of different regions found in a 4-cycle low-tin Zircaloy-4, by EDS. The quantification ranges for metal and hydride come from multiple regions.*

| Region | O (at%) | error | Zr | Error | Fe/Zr (at%/at%) *100 | Error | Cr/Zr (at%/at%) *100 | error |
|---|---|---|---|---|---|---|---|---|
| Metal matrix | 0.81-3.34 | 0.27 | 93.50-95.57 | 2.98 | **2.07-2.15** | 0.15 | 0.04-0.15 | 0.03 |
| Hydride | 0.00-8.35 | 0.18 | 89.61-95.13 | 2.90 | **1.08-1.20** | 0.1 | 0.04-0.06 | 0.03 |
| SPP in the metal | 2.56 | 0.13 | 58.21 | 2.20 | **26.50** | 1.35 | 40.0 | 0.18 |
| Oxide adjacent to metal | 55.75 | 0.58 | 42.87 | 2.48 | **2.36** | 0.16 | 0.00 | 0.00 |
| Oxide adjacent to hydride | 61.8 | 0.71 | 37.58 | 2.69 | **0.88** | 0.08 | 0.05 | 0.02 |

From these results, even if they are considered semi-quantitative, some clear points can be noted. Firstly as found with hydrides in irradiated Zircaloy-2 claddings [64] hydrides in this material also reject alloying elements particularly Fe with the concentration being roughly two times higher in the matrix compared to hydride. Secondly, this phenomenon is then inherited by the oxide causing a higher concentration in the oxide which was previously Zr matrix compared to that which was previously hydride.

### 7.2.2 EELS of 4 cycle low-tin Zircaloy-4

The three distinct areas namely Zr metal matrix, hydride and oxide have different low loss EELS spectra, which are shown in Figure 7-4, together with the regions in the SI which they come from. Also in Figure 7-4 the low loss spectra for the hydride and metal are given on the same axis to demonstrate the shift of the first peak which has been designated as the bulk plasmon peak [100], [218]–[220]

whereas the other broader peak is assigned as an electronic transition of the Zr 4p level. This state is designated as "$4p^{-1}4d, \epsilon d$, and has been well documented for transition metals with less than half-filled conduction band d levels" [219] and should not shift between hydride and metal. For the metal spectrum, the peaks are at 16.7±0.25eV and 39.7±0.25eV, and for the hydride 18.8±0.25eV and 40.2±0.25eV. Using the values from the literature (see table D-1 in appendix D) the hydride plasmon peak could be positioned between $\gamma$ and $\delta$ hydrides. For the bulk oxide, the three peak centres are at 14.7±0.25eV, 25.3±0.25eV and 42.1±0.25eV. These three peak have been designated as firstly bulk plasmon peak, secondly 'collective excitations' and thirdly 4p plasmons [217]. Of interest here is the final peak which according to Dash et al. [217] exhibits a 1.1eV shift between $ZrO_2$ monoclinic (41.2eV) and tetragonal zirconia (42.3eV).

In Figure 7-5a and b MLLS fitting is performed using the spectra of metal and hydride. This allows quick separation of the two phases throughout the sample. In addition to this, it is possible to map the shift of the plasmon peak which can reveal shifts in-between the two measured peaks. This is shown in Figure 7-5c. The colour bar ranges from black (i.e. 18.9eV) to white (i.e. 16.5eV) which indicates maximum shift of 2.4eV. Hence, the green colour indicates a shift of 0.8eV, which would be in-between the peak positions for the two measured phases of metal matrix (16.8eV) and hydride (in this case 18.7).
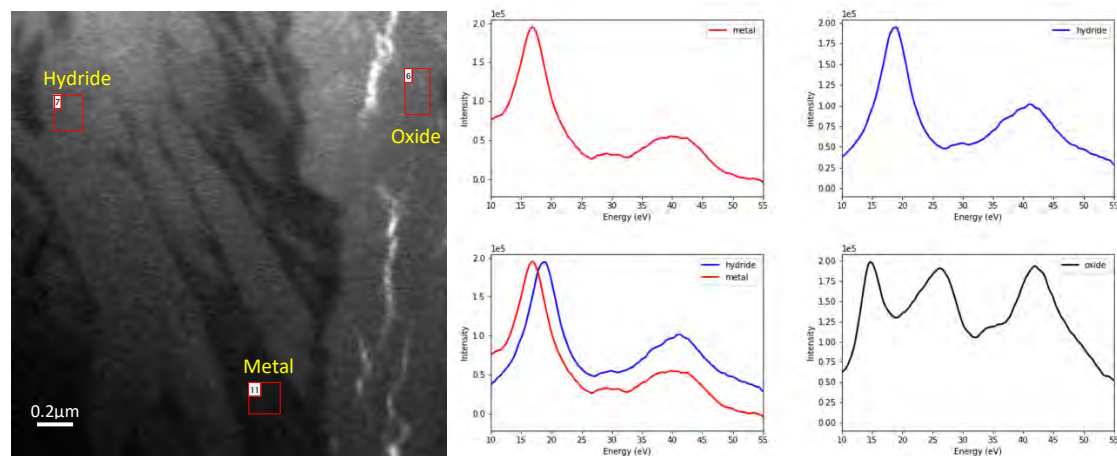


*Figure 7-4. Spectrum image from a 4-cycle low-tin Zircaloy-4. Red boxes show the selection of pixels to be summed and yellow writing indicates the phase at that region. The low loss EELS spectra (with ZLP removed) from the different regions are given and labelled as metal, hydride and oxide. The hydride and metal spectra are also displayed on the same axis to view the shift in plasmon peak.*
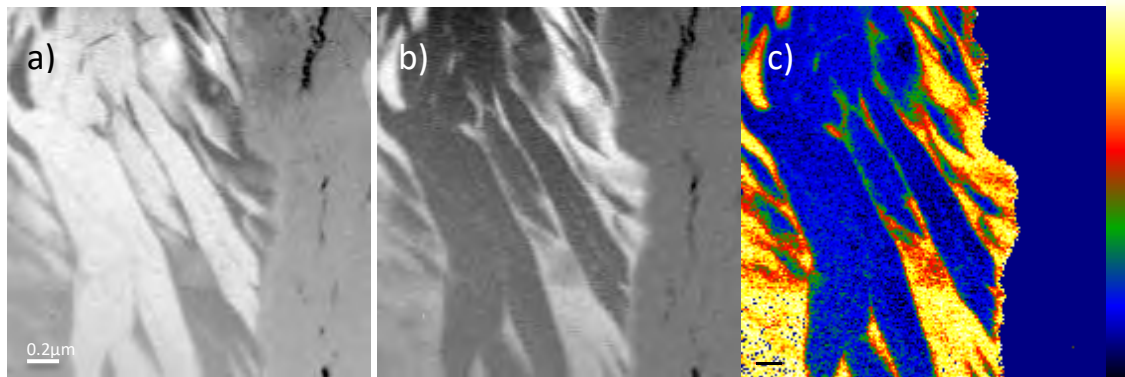
*Figure 7-5. Spectrum image from a 4-cycle low-tin Zircaloy-4. a) MLLS fitting from a low loss EELS spectra of hydride. b) MLLS fitting from a low loss EELS spectra of metal. c) Peak shift map with respect to the plasmon peak position of hydride. The colour bar ranges from black (i.e. 18.9eV) to white (i.e. 16.5eV) which indicates maximum shift of 2.4eV.*

Once the phases present were clearly characterized in the metal, to study the difference between the areas of oxidised hydride and oxidised metal the same region as is shown in Figure 7-2 was examined by comparing the low loss EELS spectra. Figure 7-6a shows the BF image with the selected area for EELS mapping in a green box, Figure 7-6b maps the plasmon peak shift for the hydride/metal. From this figure, it can clearly be seen that an area of metal exists between the hydride and oxide rather than be in direct contact with the oxide at the metal-oxide interface. By further examining the spectrum in this area, shown in Figure 7-7, the metal between the hydride and oxide can be seen to match with that of oxygen saturated metal from ref [205]. Figure 7-6c maps the peak shift for the third oxide peak, the 4p plasmon. If there were a difference in the phase composition (i.e. monoclinic and tetragonal) it would be expected that a shift in the 4p plasmon peak could be seen. Whereas in this case no clear difference between the areas of oxidised hydride and oxidised metal can be seen. By analysing the SI in this way, every pixel is individually assessed. As well as this method, to gain a more statistically relevant information, the spectra for the two areas were also summed and are shown in Figure 7-8. Again the spectra are so similar that any shift in peak position due to the difference in tetragonal phase fraction could be considered negligible.
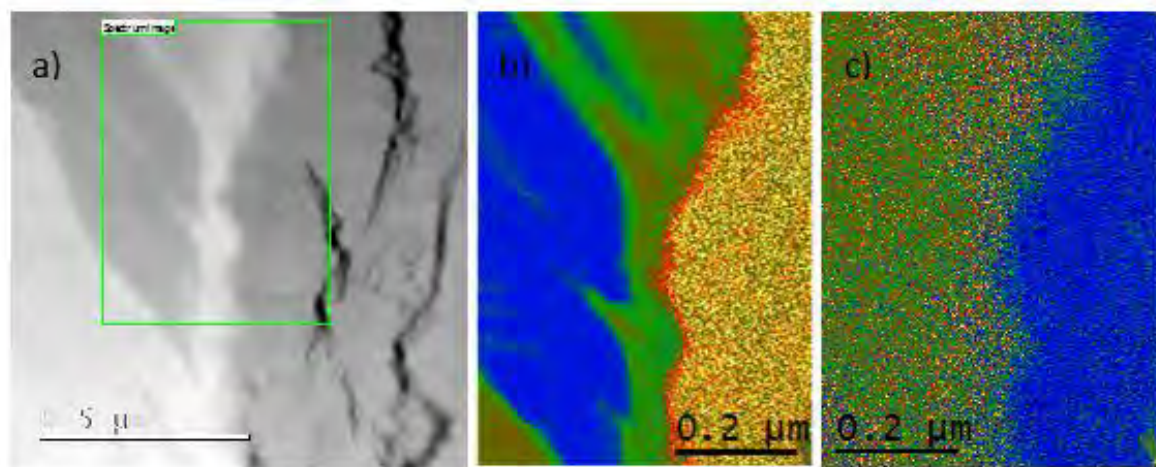
*Figure 7-6. 4-cycle low-tin Zircaloy-4 with a hydride extending from the metal-oxide interface a) BF image showing the selection of the area for low loss EELS mapping in a green box. b) Peak shift map of SI with respect to the plasmon peak position of hydride (here hydride is blue and metal is green). c) Peak shift map of SI with respect to the bulk oxide 3$^{rd}$ peak position no clear difference can be seen in different regions of the oxide.*
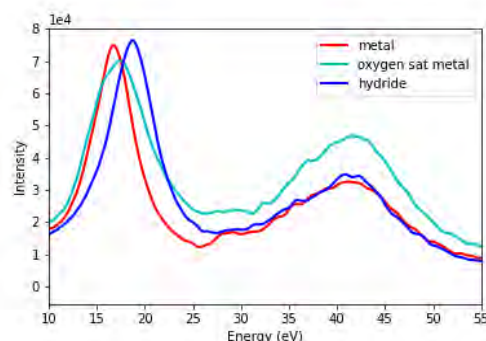


*Figure 7-7. Low loss EELS spectra summed from multiple pixels in three regions found in the SI presented in Figure 7-6: Metal, hydride and oxygen saturated metal*
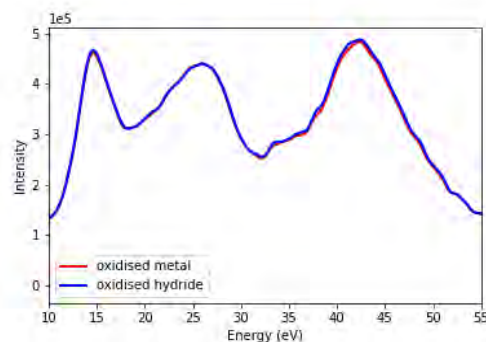


*Figure 7-8. Low loss EELS spectra summed from multiple pixels in two regions found in the SI presented in Figure 7-6: oxidised metal and oxidised hydride*

As mentioned in the introduction to this chapter it was also possible to analyse some data previously acquired at very high energy with high spatial resolution. This data was used to investigate the question of a 'hydride shell' as discussed in in Section 2.7.9. That is the possibility of the hydride precipitate having a different phase and composition as an interface between it and the metal matrix, suspected to contain less hydrogen. In Figure 7-9 an interface of a hydride is shown and the peak shift is mapped. An interfacial region (green) can be clearly seen in-between the metal (red) and hydride (blue). The spectra for these regions are shown in Figure 7-10. However, as will be further discussed there could be multiple explanations for this result.
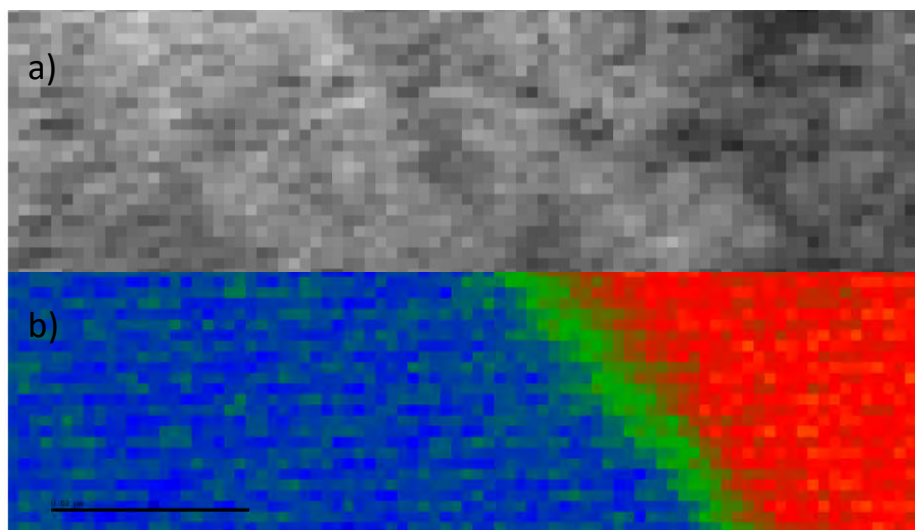


*Figure 7-9. a) SI of Interfacial region between hydride and metal. b) Peak shift map of SI with respect to the plasmon peak position of hydride (here hydride is blue shift of 0eV, interface is green shift of approximately 0.8eV, metal is red shift of approximately 1.9eV). Scale bar represents 20nm*
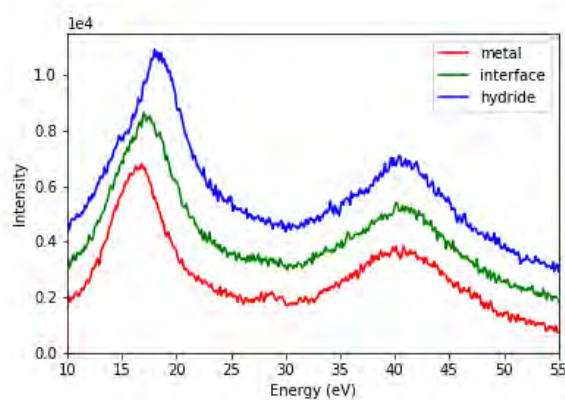


*Figure 7-10. Low loss EELS spectra from the three regions identified in Figure 7-9: metal peak centrum at 16.8eV, interface peak centrum at 17.6eV and hydride peak centrum at 18.7eV*

# 7.3 Discussion

### 7.3.1 *The distribution of alloying elements in the vicinity of the metal-oxide interface*

The results in this chapter give preliminary evidence to answer interesting questions still open about the role of hydrides and their oxidation. The results agree with previous work on Zircaloy-2 LK3/L [64] since in this material, low-tin Zircaloy-4, hydrides were also seen to be depleted of Fe and hence the matrix, particular at the boundary between hydride and metal, was enriched. The amount of Fe, quantified in the matrix, was found to be in the region of two times higher than the hydrides in several hydrides studied. From these results, it is difficult to confirm if the phenomenon is also present for Cr but they suggest that the matrix had a slightly higher Cr concentration. Keeping in mind that the Cr in the $Zr(Cr, Fe)_2$ shows a slower dissolution rate compared to Fe and also there are more Cr remnant SPPs in low-tin Zircaloy-4 [64], [67]. This observation is a further confirmation of this behaviour, also seen here from Figure 7-1. Hence, it is understandable that less Cr is present in solid solution and therefore more difficult to confirm the rejection of Cr from hydrides. However, the fact of Fe depletion from hydrides in two different alloys irradiated in two different reactors would suggest that this is a general phenomenon and it would be suspected that Zr hydrides in other Zr alloys under irradiation would show the same behaviour.

In the oxide at the metal-oxide interface (within first few hundred nanometres), the amount of Fe was found to be much higher, approximately three times higher, in the area adjacent to metal matrix compared to the hydride. This would strongly suggest that as the oxidation front moves in, the newly formed oxide inherits the chemical composition from the underlying material, which in this case being a metal-hydride mix would results in a non-uniform distribution of Fe in the newly formed oxide. The effect of this finding on HUP is not known. However, two interesting possibilities are mentioned here. Fe is a known tetragonal stabiliser and hence this may also have an effect on the monoclinic-tetragonal phase ratio of newly forming oxide. If Fe were in high enough amounts, and in an oxidation state less the $Fe^{4+}$, according to the suggested C4 model [42] this could influence the conductivity of the oxide by acting as a dopant and hence would reduce the HPUF.

### 7.3.2 Structure of hydrides and their impact on newly formed oxide

From Figure 7-6 it can be seen that hydride is not directly in contact with the metal-oxide interface but rather approximately 100nm of metal is between them. This has been shown to be the oxygen saturated metal and this effect has also been confirmed in other TEM lamella of the 9 cycle LK3 material (shown in Appendix D). This is an interesting finding which to our knowledge has not been shown before. One possibility would be that hydrogen in hydrides is 'pushed back' into the metal rather than being incorporated into the oxide since the hydride is not in direct contact with the oxide and is separated by the oxygen saturated metal region. If this is truly the case it would have large repercussions for the HUP mechanism, meaning that once hydrogen is in the metal it is not any more released as the oxide front moves inwards. Also it will mean that the hydrides at the interface become larger and hence further modify the protectiveness of the new oxide and further reduce the protectiveness of the oxide.

Low-loss EELS is not the only way to separate the regions of Zr hydrides and Zr metal matrix but does provide another fast and relatively easy way to do so with high spatial resolution. However, by using the technique of fingerprinting alone it is not clear which hydride phase is present in the vicinity of the interface. This is because the plasmon peak position is consistently between the literature values of $\gamma - ZrH$ (18.3eV) and $\delta - ZrH_{1.66}$ (19.2eV). In addition, an interfacial region between the hydride and the matrix was seen on all hydrides examined but was sometimes very small and ranged from 5-15nm. This is also the case for the hydrides assessed at the interface in 9 cycle LK3/L material. With these results it is difficult to confirm if this is a true interfacial region with a different hydride phase, or an artefact of the technique. The proposed hydride phases [164], [166] which could act as hydride shells contain a smaller amount of hydrogen than the hydride, and also have an intermediate peak shift in between that of metal and hydride. Therefore, it is unclear in this intermediate interface region (Figure 7-9 and Figure 7-10) if this plasmon peak shift comes from the presence of another phase or is an artefact of mixing the two signals from metal and hydride. these results show that low-loss fingerprinting is a powerful and rapid technique but in this case cannot be used alone. An additional technique such as a diffraction technique or high resolution TEM is needed to confirm the structure of these hydrides.

From Figure 7-6c and Figure 7-8 it is shown that there is a negligible difference in the third peak of the oxide low-loss spectrum between the areas of oxidised hydride and oxidised metal. From this initial investigation, no difference could be seen in the tetragonal-monoclinic phase fraction of the oxide in the vicinity of the metal-oxide interface of a hydride/metal mixture using this method. It must be

noted that using this method only a small region was probed however even when examining the whole oxide TEM lamella no observable difference could be seen. Although this question needs further investigation; it appears that both oxidized hydrides and oxidized metal matrices produce a similar phase ratio of tetragonal to monoclinic. Having examined this lamella to make a more general statement might need more statistics. Nevertheless, the difference in chemical composition between the areas does not seem to impact largely the phase fraction of different zirconia oxides. And this finding confirms the theory presented in [64], that the increased volume of the hydride when compared to the $\alpha$-Zr matrix would induce only porosity in the newly formed oxide, without inducing any change of phase fraction of oxide.

# 7.4 Conclusions

- Hydrides are seen close to the metal-oxide interface however they are separated from the oxide by the oxygen saturated metal.

- Hydrides are depleted of Fe and Cr and the surrounding metal matrix enriched so that approximately two times the amount is found there.

- The newly formed region of oxide (approximately 300nm) was seen to inherit the chemical properties of the underlying metal/hydride so that an enrichment of Fe could be seen in the oxide adjacent to Zr metal matrix.

- No difference could be seen in the shape and peak positions of the low loss EELS spectra between the area of oxide adjacent to metal and oxide adjacent to hydride, implying that the ratio of tetragonal to monoclinic zirconia is similar in the two areas.

# Contents of chapter 8:

# 8 General discussion for the thesis

In this thesis, each results chapter is followed by a discussion applicable to that chapter, both on the techniques involved in that chapter and the results therein. In this final discussion chapter, a more general approach is taken to discuss the findings of the thesis as a whole as well as their influence on the hydrogen uptake. How the findings fit in with the current understanding of the mechanism of hydrogen uptake and the causes of its increase at high burnups will also be discussed.

A list was formulated of potential factors which could influence the HUP and cause the increase in HUP seen at high burnups for some alloys (see chapter 2 section 2.7.2.). It has been suggested that the microporosity in the oxide increases as a function of residence time [64], which was partly correlated to the hydride volume fraction at the metal-side of the interface. To verify some of these factors and to investigate others, different techniques were used during this PhD. They are: TEM/STEM (particularly EELS and EDS), SEM/FIB, XANES, micro-XRD and Micro-pillar compression testing. In addition to these techniques, a large amount of effort during the PhD went towards further improving a novel technique developed at PSI to measure the local intrinsic resistivity properties of oxide grown on irradiated fuel claddings.

This chapter will have three sections. The first section will consider the physical properties studied in chapters 4 and 5. Subsequently these findings will be discussed in the light of all studies performed on Zircaloy-2 cladding in this study as well as in the literature. The second section will deal with the chemical and crystallographic data obtained on different claddings. The last section will discuss the topic of the barrier layer.

## 8.1 Physical properties of the oxide and their role on HUP

As mentioned above, this section will consider the physical properties studied in chapters 4 and 5, discuss these findings in the light of all studies performed on Zircaloy-2 cladding from this study and those obtained in the past. The impact of these findings on the hydrogen uptake will also be discussed.

### 8.1.1 Summary and discussion of conductivity measurements

To study the electrical conductivity of the oxide layer, the Zircaloy-2 LK3/L series was selected. This alloy had already undergone a large range of characterisation due to the fact that samples were available after different residence times (or cycles) in KKL a BWR, even to burnups beyond design (9-cycle) [9]. Furthermore, the samples were carefully selected to reduce the number of variables that could influence the direct comparison of the claddings with different residence times. Hydrogen content and oxide thickness measurements had also been performed on these samples [8] and it was found that the HPUF was not constant through lifetime and that it increased with residence time for this material. The chemical composition of the cladding was examined to a high resolution both by means of EPMA and TEM [64] and the impact of irradiation on the dissolution of precipitates as a function of number of cycles was measured. The localised mechanical properties and electrical resistivity were also measured in this work.

The experimental procedure and the reliability of the results has been discussed at length in section 4.3.1, however a short summary of the main points is given here. While this technique has some very powerful advantages, the limitations must also be discussed. The fact that it is novel and adapted to the specific problem to be studied allows for new information to be brought but also means the method is not routinized. In other words, due to the fact that an oxide interface changes from one region (or even one micrometre to another) and the conducting layer acting as electrode is very fragile, the experiment is very operator-dependant. However, the measurement of reference standards (shown in section 4.2.1) brought further confirmation about the reliability of the set up. The aim was to make the test results as comparable as possible thus the electrode size and the set up was kept as constant as possible. Due to the undulated nature of the metal oxide interface, an element of chance on the placement of electrodes was present, and each 'wedge' was different. This meant that the distance of oxide underneath each electrode could not be fully known until after the measurement: the electrodes had to then be destroyed to be cut and reveal the thickness of oxide underneath. This This created difficulty determining whether the result for that electrode was correct, or if it was an error due to poor contact between the tip and the electrode during the experiment (or poor adhesion of the electrode to the oxide). To try to account for this, each electrode was measured a minimum of three times with the tips being taken off the electrode and replaced between each measurement with the Keithly ammeter.

In the current state of the experiment, it is not possible to exactly know the path of electrons from one electrode to the other. The contribution of the metal and circuit is very small compared to that of oxide therefore it is considered that only the oxide contributes to the high resistivities and that the shortest distance of oxide will dictate the resistivity of that electrode. In addition, it is assumed that

all the current is going through the bulk of the oxide in a perpendicular direction to the metal-oxide interface, but this may not be the case. As previously mentioned, large amounts of undulation can be seen in this material, and in the case of the 6-cycle material, large irregularly shaped undulation are sometimes observed (refer to Figure 3-8). Another practical limitation is that the experiment may be considered somewhat slow as much FIBbing was required to prepare the sample and a new wedge needed after each measurement. Were the process faster, one option could entail making larger wedges with larger electrodes. This could provide two benefits: firstly, it would account for some of the undulation and give a more reliable averaged value for a region, secondly it would reduce the measured resistance by having a larger area for the current to pass through and thus higher resistivities could be measured. However, the small size of electrodes had the advantage that small regions could be studied with high spatial resolution.

At present, the reason for the results from this study to differ by large amounts (approximately 10-1000 times) compared to in-situ EIS studies [61] is still not fully understood. This was discussed in detail in chapter 4 section 4.3.1. To our knowledge, there is only one study on the resistivity of the oxide formed on irradiated Zr alloys using EIS by Forsberg et al. [125]. In that publication, a difference ranging between 10-50,000 times was found when comparing irradiated and non-irradiated materials. It is therefore plausible for this difference to be a true phenomenon due to the difference in materials. However, without directly comparing the same material with EIS and our technique, it is impossible to conclude on this question. As mentioned in Section 4.3.2, it was our desire to also measure autoclaved material using this technique: an autoclaved sample of LK3/L with a 6μm oxide was tested but it appeared unfortunately that the resistance was too high to be measured by our set up. This confirms that the non-irradiated material has a higher resistivity, however the exact value of this resistivity was above the specification of our setup. Nevertheless, the fact that different results were confirmed with two or three separate trials, with identical set ups and the same material after different residence times, shows that the resistivity is being measured and the comparison is valid. The finding that the resistivity of the oxide can vary with position has, to our knowledge, never been shown before on irradiated or non-irradiated samples. The same is true for the comparison between the extent of an inner more conductive region in a similar alloy after different residence times. These results agree with the literature that a more conductive oxide layer will show a lower HPUF [42], [61], however these results also show that it is not only the conductivity of the oxide, but also the size of the inner conductive region (which is expected to be correlated with an inner diffusion layer) that is important. The size of these regions are approximately 1500nm for 3-cycle, 200nm or 1000nm for 6-cycle and less than 800nm for 9-cycle. The two numbers for the 6-cycle material come from two sets of results where the evidence suggests different regions of oxide have different sizes of conductive

oxide. It is suggested that at this time the oxide is going through transition. Without other measurement techniques providing the data in the same region, it may be difficult to validate the exact experimental values of oxide resistivity using this technique, but it still has managed to bring forward important information about the semi-conducting properties of the oxide and the evolution of this property with residence time, i.e. on different samples with different burnup and hydrogen uptake properties.

### 8.1.2  Summary and discussion of micro-mechanical testing

To investigate the intrinsic mechanical properties of the oxide and metal, micro-pillar compression was employed. The technique had already been used in the lab at PSI during a feasibility study [137] where the Young's modulus and strength of the 3-cycle and 9-cycle LK3/L was compared. To add to this study and to go further, it was decided to also test the 6-cycle and an autoclaved LK3/L and also attempt to fabricate pillars in the oxide as close as possible to the interface. Also, to add further insight into the effect of irradiation and compare different alloys in different reactors, an autoclaved low-tin Zircaloy-4 was compared to a 4 cycle low-tin Zircaloy-4.

This technique allows for the selection of small regions; in the case of this experiment it allowed the probing of the material on both sides of the metal-oxide interface as well as the bulk metal and oxide. The pillars had a diameter of between 2-3μm (but usually closer to 2μm). This size was chosen to be consistent with the study mentioned previously, so that geometrical factors would be constant. However, smaller pillar size are possible to produce in the FIB and may be better by more accurately selecting the desired region. For example, the pillars made had a larger diameter than the expected oxygen saturated region in the metal at the interface and thus did not solely give information from that feature.

Seven pillars per region were produced in 4 different regions, totalling a number of 28 pillars in each of the four samples. With 7 tests per region, the statistics can be considered as good but due to the occasional failed test (roughly 1 in 12), some data points only have 5 or 6 tests, which in turn increase the error on that data point. These failed tests were removed with the correlation of the test results and the post compression pillars in the SEM which gives confidence about the tests results presented.

As discussed in section 3.2.4, this is a standard methodology, however uncertainty could still arise from a number of sources. The most impactful was deemed to be geometrical inconsistencies

produced from the FIB milling. Because of these, the dimensions of each pillar were recorded and used when calculating the stress-strain curve for that test. This should improve the accuracy in the values presented. However, since every pillar had small variations in form and size, this is expected to contribute to the scatter. It should still be kept in mind that the scatter of results from the same region (i.e. oxide) also brings information about that region.

The metal pillars in the Zircaloy-2 LK3/L generally followed the expected trend described in the literature of irradiation hardening, with initial irradiation followed by a saturation of that effect and a subsequent reduction in strength. The point from the 9-cycle material at the interface [137] did not appear to follow this trend and it was suggested that it could be due to the high amount of hydrides seen in the metal at the interface in this sample. In the oxide of this alloy, a reduction of strength was seen with residence time with the 6-cycle oxide being more similar to the 3-cycle than the 9-cycle. It was proposed that this change is due to the differing amounts of porosity found in the oxide [64].

The low-tin Zircaloy-4 appeared to follow the same trend in the metal, however without the high burnup samples it is unknown whether it would continue to follow the trend. In the oxide however, such a clear decrease in strength between the autoclaved and 4-cycle sample was not observed. Two theories are proposed to explain this. Firstly, the two autoclave samples may not have comparable oxides since the Zircaloy-4 oxide was much larger than the Zircaloy-2 oxide (20µm compared to 6µm). This may mean that if the Zircaloy-4 sample was tested at the same stage of oxidation, a higher strength would be seen for the autoclaved sample and thus a reduction between the autoclaved and irradiated sample would be seen. Secondly, such a reduction in oxide strength may not occur in this low-tin Zircaloy-4 material.

### 8.1.3  Comparison of different properties of the Zircaloy-2 LK3/L material as a function of residence time

From the results obtained in chapters 4 and 5, it may be concluded that the conductivity and mechanical properties of the oxide evolve as a function of residence time so that the thickness of conducting layer gradually reduces and the fracture strength of bulk oxide gradually decreases. The comparison of these data with the literature [64] shows that some of the causes of these trends could be revealed in the composition and microporosity studied there. As an example, the oxygen concentration of the oxide has slightly changed with the number of cycles as shown from EPMA. The comparison of the different claddings demonstrates a slight decrease of the thickness of the

substoichiometric layer of the inner oxide as the residence time increases. Furthermore, the Fe concentration of the 3, 6 and 9-cycle in the inner oxide is not identical, with the 6-cycle oxide being richer in Fe compared to the other two.

These changes in chemistry could play a role in modifying the mechanical properties and the conductivity of the interface, however it is difficult to create a direct correlation at this stage although clear trends exist in particular for the substoichiometry as shown in 4.3.2. It can be seen that for this material, one factor cannot be simply isolated as the single factor causing the increase of HUP at high burnups but rather multiple factors are seen to evolve with residence time and are proposed to increase the HUP. It should be kept in mind that the HPUF for these materials is 17%, 34% and 30% and the additional H content (in other words, the increase of the amount of H between those cycles) is 44, 168 and 393 ppm for the 3,6 and 9-cycles respectively. The additional oxide thickness is 4μm, 10μm and 36μm respectively. The proposed factors are as follows: the conductivity of the inner oxide, the strength of the oxide and the porosity of the inner oxide [64]. Study on this alloy shows that while a higher conductivity will increase the HPUF, a thinner or less protective (more porous) 'barrier layer' will increase the total amount of oxidation and HUP.

# 8.2 Chemical properties in the vicinity of the metal-oxide interface

This section will consider the chemical properties studied in chapters 6 and 7 and discuss these findings in relation to the literature, as well as their impact on the hydrogen uptake.

### 8.2.1 Summary and discussion of the Nb speciation studied in the oxide of Nb containing alloys

To study Nb in the oxide layer, two techniques were employed. Firstly, XANES was used because of its high sensitivity and detection limit. This enabled the investigation of all oxidation states for Nb throughout the oxide layer of an irradiated low-tin ZIRLO sample. It also enabled a quantifiable deconvolution of the oxidation states to give percentages of the various oxidation states at positions in the oxide. However, due to the beam size in this experiment (approximately 0.7μm x 0.8μm), it was not possible to exactly separate where the Nb signal came from, i.e. SPP or matrix. The second

technique used was STEM-EELS. This technique has very high spatial resolution and areas of a few nanometres in a thin (less than 100nm) TEM foil could be individually probed. This gave the advantage that the speciation of Nb at an exact position could be studied, i.e. at a crack edge or an SPP. The drawback with our EELS dataset due to the acquisition yield is that the devconvolution is not feasible, and thus it is not possible to quantify the amount of different oxide phases as the different oxidation states only show a shift in a Gaussian peak. Hence when a shift from the metallic Nb state is found in the oxide, the combination of Nb oxides existing at that point to create that resultant shift cannot always be determined. Another drawback from EELS for this task is that the signal from Nb in the matrix is very low and cannot be seen in every pixel in the matrix, it can therefore be difficult to always distinguish if such a peak is present. The STEM-EELS work was carried out on an irradiated Zr-2.5%Nb alloy. The two techniques are complementary. By comparing two different Nb-containing alloys which form two different types of Nb-containing SPPs ($\beta - Nb$ for ZIRLO and $\beta - Zr$ for Zr-2.5%Nb), it was possible to identify phenomenons which appear to occur in Nb containing alloys irrespective of other parameters.

In both materials, Nb appeared to remain metallic some distance into the oxide: for the ZIRLO, the majority was metallic approximately until 1.4µm, and in the Zr-2.5%Nb at least the first micron. The EDS data however demonstrated that large $\beta - Zr$ SPPs can remain metallic up to 2µm into the oxide, which has been previously reported for this material [67]. From the XANES data, it is not possible to differentiate the signal from Nb in SPPs and Nb in the matrix, with approximately half the signal coming from matrix and half from SPPs as calculated for a ZIRLO material in [213]. However since 50% of the signal should come from Nb in the matrix if the percentage of metallic Nb is much larger than 50%, it is possible to conclude that Nb is also metallic in the matrix. In contrast, Nb in SPPs and matrix can be differentiated in the EELS data. It is seen that Nb remains metallic even in the matrix up to 0.8µm from the interface. This is a new finding to the best of my knowledge. It should be noted that due to the difficulty in seeing the Nb peak, the positions in the matrix that could be analysed with EELS were often close to SPPs (but at least 200nm away from the SPP to confidently say it was matrix) and hence enriched with Nb due to the depletion of Nb from the SPP. Even so, some points in the matrix were included that appeared not to be near an SPP. From the XANES data, moving further into the oxide, a gradually increasing oxidation state for Nb can be seen until finally being fully oxidised to a 5+ state. An almost continuous gradual shift is also demonstrated in the Nb L3 edge from the EELS data and it may be assumed that this shift comes from the gradual oxidation of Nb in a similar way to the XANES data, but technically the mixture of oxidised Nb cannot be known from this. Finally, in the same campaign as the XANES, XRD data was also acquired across the whole sample. The tetragonal vs monoclinic phase fraction in the oxide was quantified and it was found the highest tetragonal (16%)

to be closest to the interface in the oxide. This finding can be correlated with the delayed oxidation of Nb and will be discussed in more detail in this section.

Three things can be taken from these results to explain the superior corrosion and hydrogen uptake properties of the Nb-containing alloys in reactor. Firstly, since Nb is found in the vicinity of the metal-oxide interface in an oxidation state less than $Nb^{4+}$ this is evidence supporting the C4 model [42]. The model states that Nb in such oxidation states can compensate for space charge build up in the oxide increasing the conductivity of the oxide and thus meaning electrons can transport out towards the oxide-water surface and reduce hydrogen there, decreasing the HPUF. However, this should increase the oxidation and hence that model does not explain the superior corrosion performance of Nb-containing alloys in reactor. The second suggested reason is the presence of $Nb^{5+}$, which was shown to be present by both EELS and XANES measurements. It has been claimed [212] that the presence of $Nb^{5+}$ near the outer oxide creates a higher density of electrons and promotes the reduction of $H^+$ closer to the coolant and thus further reduces the ingress of hydrogen into the metal substrate. The third reason is that metallic Nb, particualrly SPPs, can accommodate stress build up in the oxide since they are more ductile than the surrounding oxide matrix [64]. This was suggested in the case of the Zr-2.5%Nb examined in that study to be responsible for maintaining a region of less cracked protective oxide close to the interface. This phenomenon seems to better explain the superior behaviour of Zr-2.5%Nb  in reactor. Whether this is also valid for ZIRLO alloys (which do not show the same morphology of Nb phases) could be debated but it may still be the case.

### 8.2.2   *Summary and discussion of the study of hydrides at the metal-oxide interface and their impact on newly formed oxide*

The porosity in the oxide has been shown to have a direct correlation with the hydride volume fraction at the metal-oxide interface [64]. Therefore in the current study, these hydrides as well as the newly formed oxide were examined using STEM-EELS and EDS. This allowed for the chemical quantification of different regions on a very small scale as well as the collection of information on the structure of different phases in the vicinity of the interface. One of the limitations of the EELS data set collected as mentioned before is that although a peak shift can be seen and indicate a change in material, it is not possible to exactly determine the nature of the signal acquired. To be more precise, a shift in plasmon energy is seen at the interface between hydride and metal matrix, however it is not clear from these results if that is due to the presence of a separate hydride phase containing less H or if it is due to a combination of other phases.

It was shown in chapter 7 that hydrides were depleted of alloying elements Fe and probably Cr and the matrix was then enriched. This observation is in agreement with previous studies, using other methodologies as well as TEM in other materials [64]. How the oxide front moving inwards from further oxidation would inherit these chemical properties was also shown. From the analysis of low loss EELS spectra in regions of oxidised hydride and oxidised metal, no difference could be seen in the tetragonal to monoclinic phase fraction between the two regions. This means that if both areas of hydride and metal were transforming to similar products, calculations in [64] would be valid and more void space (porosity) would be left in the region which was previously hydride. This is also in agreement with other researchers who have found oxides grown on prehydrided materials to include more porosity [74], [75], [215]

# 8.3 Barrier layer

Finally from the data collected in this thesis, evidence of an inner protective oxide (the so called 'barrier layer') can be seen across the wide range of samples studied. This can be seen by the presence of a more conductive inner region seen for LK3/L material which is thought to be due to the sub-stoichiometric oxide as it is acting as a diffusion layer.

There is further evidence of a 'barrier layer' by the presence of sub-stoichiometric oxide seen in the Zr-2.5%Nb (see EDS 6.1.2) and a region of unoxidised or less oxidised Nb, which would suggest that region of oxide is not totally accessible to oxidising species. Even though the oxygen content of the oxide is not available for this material, evidence for the barrier is also seen in the ZIRLO by the increased tetragonal fraction close to the metal-oxide interface which is indicative of a more dense protective oxide. Futhermore, in the ZIRLO, unoxidised or less oxidised Nb was also seen in the oxide studied.

Furthermore, this barrier layer is evidenced from the micromechanical testing by the increase in strength seen at the metal oxide interface compared to the bulk oxide (although the data for this is only available for 6 cycle LK3/L and 4 cycle low-tin Zircaloy-4).

The results show that this barrier layer is variable and suggest that at later stages of life time, the thickness of this layer reduces for the same alloy. This may mean that time between transitions decreases as is suggested in ref [61]. As the oxide layer increases initially, it seems that this barrier layer increases, and after the first transition, it breaks and a new layer grows with time. However,

under irradiation and long-term residence time, its maximum thickness is expected to decrease. In any case it seems that the smaller the thickness of this layer, and the more porous the layer is, the higher the HUP (or HPUF) of the material would be. For the materials studied in this research, the thickness of the layer was of the order of micron size. This is larger than the values suggested by other authors, reporting tens of nanometers. The reason for this difference is not yet clearly determined and the methodologies used to determine the thickness of layer could influence this value.

# 9 Conclusions

In this chapter, the main conclusions from the thesis will be given in bullet point form attempting to state them in the order in which they appear in the thesis. These conclusions are already given at the end of each chapter but repeated here to have a summary and all the conclusions in one place.

## 9.1 Conductivity results

- The intrinsic resistivity of oxide in the vicinity of the metal-oxide interface varies as a function of distance from the interface.
- An inner more conductive region has been identified in the oxide close the interface.
- Above a given oxide thickness, the value of resistivity plateaus although some scatter is still observed as a function of thickness.
- The resistivity of the 6-cycle and 9-cycle cladding at a given distance from the interface, before the values reach the plateau, is higher than that of 3-cycle cladding.
- The values of maximum resistivity seem to be similar between the 3 and 9-cycle materials, however higher values are reached in the 6-cycle material.
- These findings agree with the hypothesis that the increased hydrogen pickup fraction can be correlated to the increased resistivity of the oxide at a given distance from the interface.
- The comparison of results with previous studies on the same set of materials (by means of electron microscopy, 3-D FIB and EPMA) shows that the cause of this increased resistivity is an increased oxygen stoichiometry and in general chemical compositional changes in the oxide, and also owing to an increased micro-crack and micro-pore in the microstructure.

## 9.2 Micro-compression results

- The metal of a Zircaloy-2 LK3/L is shown to increase in 'strength' due to irradiation hardening at early stages of residence time in reactor. However, after a certain time (between 3 and 6 cycles in this case) this effect saturates and begins to soften again. The same trend of

increased 'strength' could be observed in low-tin Zircaloy-4 between non-irradiated and irradiated, but due to the lack of high burnup samples it cannot be confirmed if the trend would continue to match.

- Generally, a higher strength was seen in the metal at the interface, which was correlated, with the oxygen saturated metal. However since the size of the pillar was larger than the expected size of this zone and could not be directly at the interface due to undulation, only a portion of the pillars would be oxygen saturated metal.

- In the oxide of Zircaloy-2 LK3/L, a decrease in strength could be seen with residence time with the 6-cycle sample being more similar to the 3-cycle than the 9-cycle. This finding was correlated with the increase in porosity found in the oxide.

# 9.3 XANES, XRD and EELS results from Nb containing alloys

- Both sets of results indicated a trend of increasing Nb oxidation state in the oxide with increasing distance from the metal-oxide interface.

- Both sets of results agree that Nb remains predominantly metallic within the first micron of oxide but with an increasing amount of Nb being oxidised to the $Nb^{2+}$ state.

- Both sets of results show that Nb remains metallic even in the oxide matrix in this region. It is expected that the majority of the Nb oxidation occurring is the Nb in solid solution and both sets suggest that approximately half of the Nb in the matrix could be oxidised to a $Nb^{2+}$ state at a distance of approximately 1μm.

- After the first micron, the results appear to diverge slightly with the Nb in the ZIRLO sample appearing to remain metallic for a greater distance into the oxide. This would be in agreement with other work since the two materials have two different types of Nb SPPs. However, it cannot be shown that the metallic Nb at a distance of 1-1.4μm in the ZIRLO sample is found in SPPs (although it is suspected) and the lack of SPPs studied in the Zr-2.5%Nb sample at this distance may mean the overall Nb state could be different. The exact comparison of the two materials with respect to SPP dissolution is not reasonable as ZIRLO contains β-Nb SPPs (80% Nb) and 2.5%Nb contains β-Nr SPPs (20% Nb).

- The XRD results show the ZIRLO sample to have a considerable amount of tetragonal phase in the oxide close to the metal oxide interface. The highest phase fraction of tetragonal was found to be approximately 16% at the closest point to the interface examined. This amount then decreased with distance from the interface to approximately 8% at a distance of 1.5μm.

Due to the size of the sample it cannot be concluded if this trend would continue until the oxide contained no tetragonal or if cyclic behaviour may be present or some other behaviour.

- The tetragonal oxide was also found to vary in concentration even between points at the same perpendicular distance from the interface. Such that 'islands' or regions of higher tetragonal concentration were found rather than a continuous layer at the interface.

## 9.4 Study of hydrides and newly formed oxide results

- Hydrides are seen close to the metal-oxide interface however they are separated from the oxide by the oxygen saturated metal.

- Hydrides are depleted of Fe and Cr and the surrounding metal matrix enriched so that approximately two times the amount is found there.

- The newly formed region of oxide (approximately 300nm) was seen to inherit the chemical properties of the underlying metal/hydride so that an enrichment of Fe could be seen in the oxide adjacent to Zr metal matrix.

- No difference could be seen in the shape and peak positions of the low loss EELS spectra between the area of oxide adjacent to metal and oxide adjacent to hydride, implying that the ratio of tetragonal to monoclinic zirconia is similar in the two areas.

## 9.5 General conclusions

The findings from this thesis further verify that many properties of zirconium based fuel claddings evolve with residence time and could play a role on the HUP of these materials. Findings agree with the theory that a higher oxide resistivity in the vicinity of the metal-oxide interface would result in higher HPUF. However, more generally a thinner or less protective (e.g more porous) 'barrier' layer would increase the HUP of the materials studied.

In the case of Nb containing alloys, shown to have a lower HUP, two explanations are proposed. Firstly, in both alloys studied Nb is found to exist in the inner oxide with an oxidation state below 4+, which has been suggested to compensate for space charge and improve the HPUF. Secondly, metallic Nb

could accommodate stress build up in the oxide and help maintain a less cracked (more protective) inner oxide.

The properties of the oxide layer in the vicinity of the metal-oxide interface of the irradiated claddings studied in this thesis, are evidence of the existence and the extent of a barrier layer. The measurement of electrical, mechanical and chemical properties further complements the previous studies of the porosity of this layer as a function of residence time as well as the evolution of its chemical composition.

# 10 Future work

In this chapter suggestions are given to help improve similar experimental work in the future as well as suggesting areas for further investigation which could be important based on the findings from this thesis.

- Due to the novel and newly developed nature of the conductivity measurements there are possibilities to improve the experimental setup: If Fibbing/Pt deposition was quicker larger areas could be milled meaning larger electrodes could be placed, this would decrease the measured resistance (due to an increased cross-sectional area) and hence larger resistivities could be measured using this technique. It may also have an additional benefit that a more average value would be measured which is less affected by undulation and inhomogeneity. It should be kept in mind though that having small electrodes and hence investigating small areas of oxide is considered one of the advantages of this technique.

- The electronic set up of the conductivity measurements especially outside the SEM may have the possibility to be improved to reduce noise, once again this would allow for higher resistances to be measured.

- Unfortunately, as mentioned it was not possible to accurately measure the resistivity of non-irradiated oxide from autoclaved Zircaloy-2 with this technique due to its high resistivity, if improvements are made such as suggested in the two points above, it would be valuable to measure this oxide to compare the change over similar oxide thicknesses to better understand the effect irradiation is having. If not by this technique even measuring by a bulk measurement such as EIS or normal circuitry could also give useful information. It should be noted though that due to difference in techniques and what they are measuring the results may not be directly comparable.

- Another interesting experiment would be measuring the resistivity of the samples measured in this thesis (Zircaloy-2 LK3 3,6,9 cycle) by EIS to compare the ultimate values given by the two techniques. Even if this is only possible for the points across the whole oxide it could still be useful.

- While there has been some TEM examinations on these samples particularly 3 and 9 cycle, taking lamella directly from underneath an electrode after measurement may help to confirm which parameters are causing the difference in resistivities.

- Another interesting application for this technique could be to compare the resistivity of the metal rather than oxide as this may give an indication of the defect structure within the metal. Larger electrodes and distances would be suggested for this to minimize error.

- In regards to the micropillar work creating smaller pillars in the future would allow for a more accurate subdivision of regions i.e. the pillars made for this study were larger than the expected oxygen saturated region and hence would always include the metal matrix not just oxygen saturated metal. After doing this experiment I believe this would be quite possible. It may also mean the pillars could be compared as single crystal in the metal.

- Improvements in Fibbing would mean the faster and potentially more uniform creation of pillars.

- Investigation into the causes for the increase and subsequent decrease in yield strength seen in the metal with irradiation could be valuable.

- It was attempted also to create pillars only of zirconium hydride in the claddings, due to the precision needed and the time available it was not possible, if this could be performed in the future it may give useful information for the mechanical properties for zirconium hydrides and their relation to radiation.

- Although very difficult it would be interesting to confirm if the Nb, seen to be metallic in the matrix in both the Nb containing alloys, was in solid solution or in nano precipitates. Then to confirm if and to what distance Nb may remain unoxidised/partially oxidised in solid solution into the oxide.

- To compare the Nb speciation in similar Nb alloys after varying residence time in reactor should give an indication of the evolution of the newly formed oxide at different burnups. For example it may be that at higher burnups there is a shorter distance of unoxidised or partially oxidised Nb indicating a smaller barrier layer formed at higher burnups.

- Evidence for a hydride shell between hydride and matrix is given in this thesis, however the question is not fully answered and further work such as the use of diffraction techniques or high resolution TEM is needed to confirm this. This was planned however not possible due to time constraints.

- Further study into the distribution of alloying elements in oxide adjacent to hydride and matrix and its effects over numerous samples and hydrides would confirm the segregation seen in the newly formed oxide. As well as giving a more averaged reliable value to the phenomenon.

- One experiment which was planned but unfortunately not possible due to the Coronavirus pandemic towards the end of my PhD was using an indexing technique such as A-star or TKD to give fuller insight into the distribution of tetragonal grains in the oxide and their placement relative to hydride placement in the metal.

*Table A-1 Resistance results from three measurement campaigns on three different areas of the sample, for the 3-cycle sample. For each electrode minimum oxide thickness under respective electrodes is shown as well as resistivity values calculated as described in chapter 3 section 3.2.5*

| Measurement number | Minimum thickness (nm) | Resistance (Ohms, Ω) | Resistivity low (Ω.m) | Resistivty high (Ω.m) | Resisitivty average (Ω.m) | Log resistvity average (Ω.m) |
|---|---|---|---|---|---|---|
| **Metal-Metal reference** | | | | | | |
| I | ≈100000 | 3.00E+01 | 2.43E-07 | 9.60E-06 | 4.92E-06 | -5.31 |
| II | ≈3000000 | 1.50E+02 | 4.05E-08 | 1.60E-06 | 8.20E-07 | -6.09 |
| III | ≈200000 | 5.00E+01 | 2.03E-07 | 8.00E-06 | 4.10E-06 | -5.39 |
| **Oxide** | | | | | | |
| I | 100 | 7.00E+04 | 0.57 | 22.40 | 11.48 | 1.06 |
| II | 200 | 1.00E+04 | 0.04 | 1.60 | 0.82 | -0.09 |
| II | 240 | 2.00E+04 | 0.07 | 2.67 | 1.37 | 0.14 |
| II | 290 | 1.30E+04 | 0.04 | 1.43 | 0.74 | -0.13 |
| II | 300 | 1.00E+04 | 0.03 | 1.07 | 0.55 | -0.26 |
| II | 320 | 3.00E+05 | 0.76 | 30.00 | 15.38 | 1.19 |
| II | 320 | 1.00E+05 | 0.25 | 10.00 | 5.13 | 0.71 |
| III | 340 | 4.00E+05 | 0.95 | 37.65 | 19.30 | 1.29 |
| II | 350 | 6.50E+05 | 1.50 | 59.43 | 30.47 | 1.48 |
| II | 380 | 2.00E+05 | 0.43 | 16.84 | 8.63 | 0.94 |
| II | 520 | 6.00E+05 | 0.93 | 36.92 | 18.93 | 1.28 |
| II | 640 | 4.00E+06 | 5.06 | 200.00 | 102.53 | 2.01 |
| III | 700 | 3.60E+06 | 4.17 | 164.57 | 84.37 | 1.93 |
| III | 790 | 2.00E+05 | 0.21 | 8.10 | 4.15 | 0.62 |
| I | 810 | 9.50E+06 | 9.50 | 375.31 | 192.40 | 2.28 |

| | | | | | |
|---|---|---|---|---|---|
| III | 980 | 2.20E+07 | 18.18 | 718.37 | 368.28 | 2.57 |
| II | 1030 | 1.00E+05 | 0.08 | 3.11 | 1.59 | 0.20 |
| III | 1030 | 4.00E+07 | 31.46 | 1242.72 | 637.09 | 2.80 |
| III | 1030 | 2.80E+07 | 22.02 | 869.90 | 445.96 | 2.65 |
| II | 1240 | 4.00E+07 | 26.13 | 1032.26 | 529.19 | 2.72 |
| I | 1320 | 7.50E+07 | 46.02 | 1818.18 | 932.10 | 2.97 |
| III | 1330 | 1.00E+08 | 60.90 | 2406.02 | 1233.46 | 3.09 |
| II | 1670 | 6.00E+08 | 291.02 | 11497.01 | 5894.01 | 3.77 |
| I | 1870 | 7.00E+08 | 303.21 | 11978.61 | 6140.91 | 3.79 |
| III | 1900 | 2.20E+07 | 9.38 | 370.53 | 189.95 | 2.28 |
| III | 2100 | 2.20E+07 | 8.49 | 335.24 | 171.86 | 2.24 |
| III | 2300 | 3.50E+08 | 123.26 | 4869.57 | 2496.41 | 3.40 |
| II | 2990 | 1.00E+09 | 270.90 | 10702.34 | 5486.62 | 3.74 |
| II | 3260 | 1.00E+09 | 248.47 | 9815.95 | 5032.21 | 3.70 |

*Table A-2 Resistance results from three measurement campaigns on three different areas of the sample, for the 6-cycle sample. For each electrode minimum oxide thickness under respective electrodes is shown as well as resistivity values calculated as described in chapter 3 section 3.2.5.*

| Measurement number | Minimum thickness (nm) | Resistance (Ohms, Ω) | Resistivity low (Ω.m) | Resistivty high (Ω.m) | Resisitivty average (Ω.m) | Log resistvity average (Ω.m) |
|---|---|---|---|---|---|---|
| **Metal-Metal reference** | | | | | | |
| I | ≈200000 | 1.00E+02 | 4.05E-07 | 1.60E-05 | 8.20E-06 | -5.09 |
| II | ≈400000 | 8.0E+01 | 1.62E-07 | 6.40E-06 | 3.28E-06 | -5.48 |
| **Oxide** | | | | | | |
| ii | 160 | 1.50E+07 | 75.94 | 3000.00 | 1537.97 | 3.19 |
| ii | 210 | 2.00E+04 | 0.08 | 3.05 | 1.56 | 0.19 |

| | | | | | | |
|---|---|---|---|---|---|---|
| i | 244 | 4.00E+05 | 1.33 | 52.46 | 26.89 | 1.43 |
| ii | 540 | 3.30E+09 | 4950.00 | 195555.56 | 100252.78 | 5.00 |
| ii | 640 | 3.90E+09 | 4935.94 | 195000.00 | 99967.97 | 5.00 |
| ii | 750 | 4.60E+09 | 4968.00 | 196266.67 | 100617.33 | 5.00 |
| ii | 800 | 3.00E+09 | 3037.50 | 120000.00 | 61518.75 | 4.79 |
| i | 880 | 3.00E+08 | 276.14 | 10909.09 | 5592.61 | 3.75 |
| ii | 900 | 9.20E+09 | 8280.00 | 327111.11 | 167695.56 | 5.22 |
| i | 960 | 1.10E+09 | 928.13 | 36666.67 | 18797.40 | 4.27 |
| i | 1080 | 4.30E+09 | 3225.00 | 127407.41 | 65316.20 | 4.82 |
| ii | 1080 | 7.80E+09 | 5850.00 | 231111.11 | 118480.56 | 5.07 |
| ii | 1130 | 6.70E+09 | 4802.65 | 189734.51 | 97268.58 | 4.99 |
| ii | 1610 | 4.20E+09 | 2113.04 | 83478.26 | 42795.65 | 4.63 |
| i | 1830 | 2.04E+10 | 9029.51 | 356721.31 | 182875.41 | 5.26 |
| ii | 1880 | 9.00E+09 | 3877.66 | 153191.49 | 78534.57 | 4.90 |
| ii | 1950 | 7.60E+09 | 3156.92 | 124717.95 | 63937.44 | 4.81 |
| ii | 2300 | 6.00E+09 | 2113.04 | 83478.26 | 42795.65 | 4.63 |
| ii | 3800 | 4.90E+09 | 1044.47 | 41263.16 | 21153.82 | 4.33 |
| i | 4510 | 1.00E+06 | 0.18 | 7.10 | 3.64 | 0.56 |
| i | 4700 | 2.00E+09 | 344.68 | 13617.02 | 6980.85 | 3.84 |
| i | 4880 | 5.70E+09 | 946.11 | 37377.05 | 19161.58 | 4.28 |
| i | 5280 | 3.00E+09 | 460.23 | 18181.82 | 9321.02 | 3.97 |

*Table A-3. Resistance results for the 9-cycle sample from three measurement campaigns on three different areas of the sample. For each electrode minimum oxide thickness under respective electrodes is shown as well as resistivity values calculated as described in chapter 3 section 3.2.5.*

| Measurement number | Minimum thickness (nm) | Resistance (Ohms, Ω) | Resistivity low (Ω.m) | Resistivty high (Ω.m) | Resisitivty average (Ω.m) | log resistvity average (Ω.m) |
|---|---|---|---|---|---|---|
| **Metal-Metal reference** | | | | | | |
| I | 100000 | 3.00E+01 | 2.43E-07 | 9.60E-06 | 4.92E-06 | -5.31 |
| II | 150000 | 3.00E+01 | 1.62E-07 | 6.40E-06 | 3.28E-06 | -5.48 |
| III | 200000 | 5.00E+01 | 2.03E-07 | 8.00E-06 | 4.10E-06 | -5.39 |
| **Oxide** | | | | | | |
| I | 300 | 5.00E+04 | 0.14 | 5.33 | 2.73 | 0.44 |
| II | 450 | 7.00E+06 | 12.60 | 497.78 | 255.19 | 2.41 |
| II | 480 | 7.00E+06 | 11.81 | 466.67 | 239.24 | 2.38 |
| III | 590 | 2.10E+07 | 28.83 | 1138.98 | 583.91 | 2.77 |
| III | 670 | 2.60E+07 | 31.43 | 1241.79 | 636.61 | 2.80 |
| II | 770 | 5.50E+07 | 57.86 | 2285.71 | 1171.79 | 3.07 |
| I | 850 | 2.00E+08 | 190.59 | 7529.41 | 3860.00 | 3.59 |
| III | 1200 | 4.30E+08 | 290.25 | 11466.67 | 5878.46 | 3.77 |
| III | 1320 | 4.40E+08 | 270.00 | 10666.67 | 5468.33 | 3.74 |
| III | 1450 | 5.70E+08 | 318.41 | 12579.31 | 6448.86 | 3.81 |
| I | 1480 | 4.30E+08 | 235.34 | 9297.30 | 4766.32 | 3.68 |
| II | 1740 | 7.00E+08 | 325.86 | 12873.56 | 6599.71 | 3.82 |
| II | 2000 | 6.50E+08 | 263.25 | 10400.00 | 5331.63 | 3.73 |
| II | 2300 | 7.00E+08 | 246.52 | 9739.13 | 4992.83 | 3.70 |
| I | 2440 | 5.00E+08 | 165.98 | 6557.38 | 3361.68 | 3.53 |
| I | 2950 | 1.50E+09 | 411.86 | 16271.19 | 8341.53 | 3.92 |

| | | | | | |
|---|---|---|---|---|---|
| I | 3760 | 2.50E+09 | 538.56 | 21276.60 | 10907.58 | 4.04 |
| I | 4300 | 1.00E+09 | 188.37 | 7441.86 | 3815.12 | 3.58 |
| I | 4800 | 2.80E+09 | 472.50 | 18666.67 | 9569.58 | 3.98 |

**APPENDIX B**

In this appendix images of representative micro-pillars are given for four regions in the three materials tested but not given in chapter 5 each figure is laid out in the same way as Figure 5-2 and Figure 5-3. That is a,b,c and d show bulk metal, metal at interface, oxide at interface and bulk oxide respectively both before compression and then the same pillars after compression. The three materials shown here are autoclaved low-tin Zircaloy-4, 6-cycle LK3/L Zircaloy-2 and, autoclaved LK3/L Zircaloy-2. 4-cycle low-tin Zircaloy-4 is given in chapter 5 as Figure 5-2 and Figure 5-3.
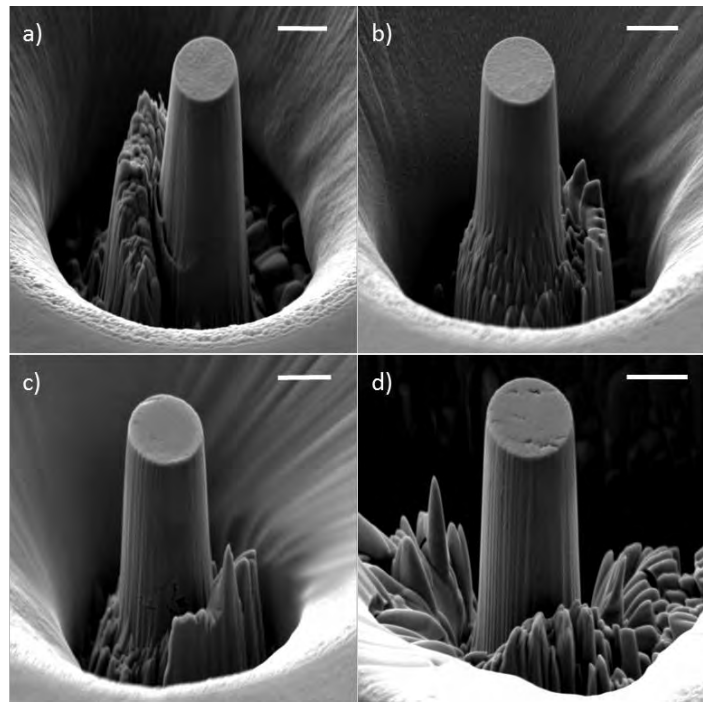
Figure B-1 Examples of completed and polished micropillars in the material low-tin Zircaloy-4 (autoclave). a),b),c) and d) show pillars from different regions; bulk metal, metal at interface, oxide at interface and bulk oxide respectively. The scale bar corresponds to 2µm for all.
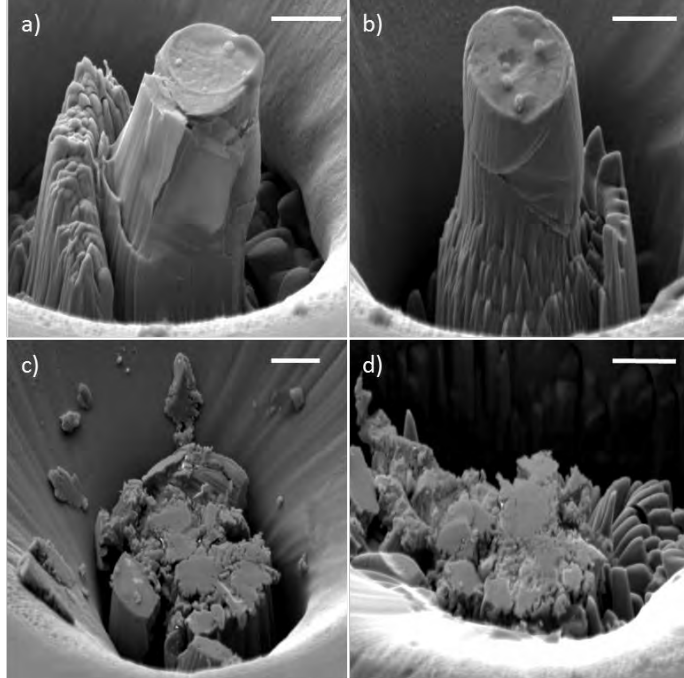


Figure B-2. Pillars after compression in low-tin Zircaloy-4 (autoclave). a),b),c) and d) show compressed pillars from different regions; bulk metal, metal at interface, oxide at interface and bulk oxide respectively. The scale bar corresponds to 2µm for all.
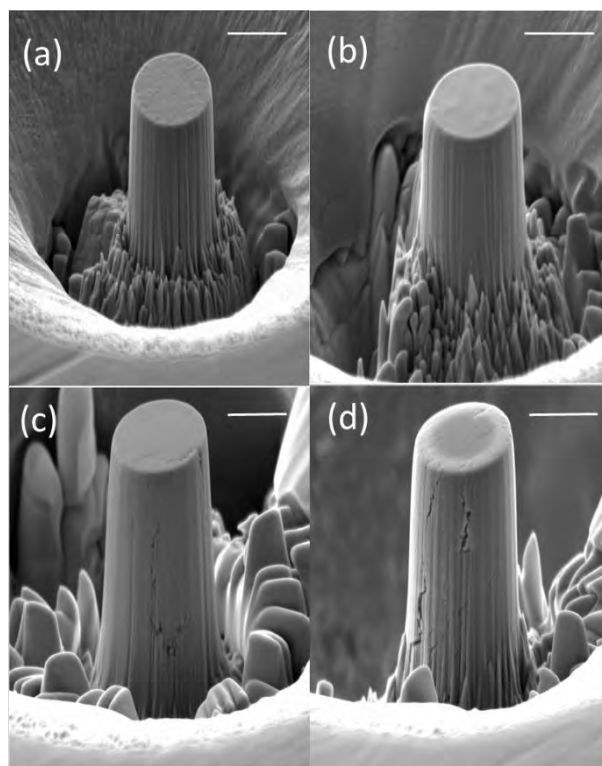
Figure B-3 Examples of completed and polished micropillars in the material Zircaloy-2 LK3/L (autoclave). a),b),c) and d) show pillars from different regions; bulk metal, metal at interface, oxide
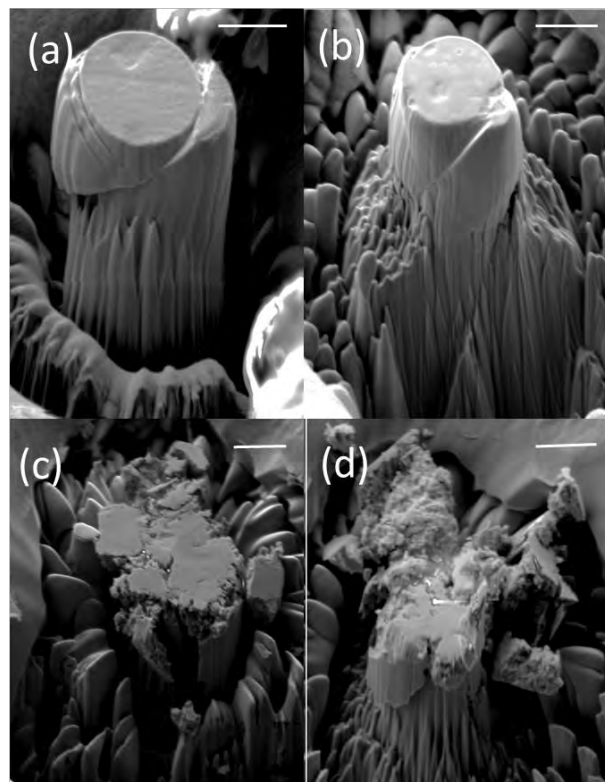
Figure B-4. Pillars after compression in Zircaloy-2 LK3/L (autoclave). a),b),c) and d) show compressed pillars from different regions; bulk metal, metal at interface, oxide at interface and bulk oxide respectively. The scale bar corresponds to 2µm for all.
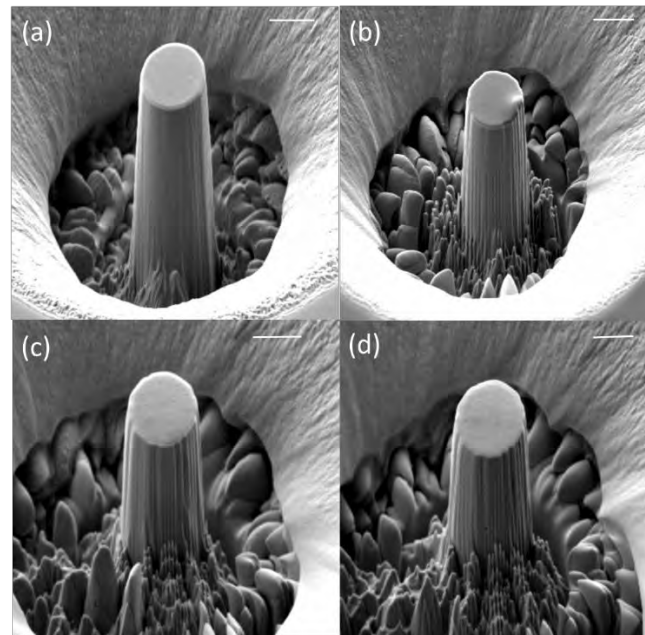


Figure B-5 Examples of completed and polished micropillars in the material Zircaloy-2 LK3/L (6-cycle). a),b),c) and d) show pillars from different regions; bulk metal, metal at interface, oxide
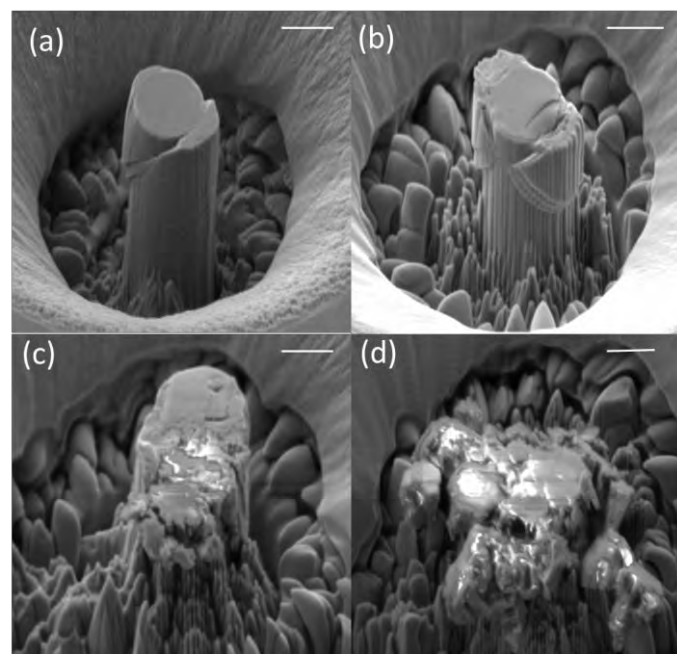


Figure B-6. Pillars after compression in Zircaloy-2 LK3/L (6-cycle). a),b),c) and d) show compressed pillars from different regions; bulk metal, metal at interface, oxide at interface and bulk oxide respectively. The scale bar corresponds to 2µm for all.

To investigate the sensitivity to the choice of energy range used for fitting, the fit was re-calculated iteratively using a progressively wider range of spectral energies. The start of the fitting range was kept constant at 18950 eV (i.e. just before the edge for the metallic $Nb^0$ standard), since the signal before the edge is not considered relevant to the fit, but would only add noise. On the other hand, the signal past the edge contains useful structure for fitting, but this is partly dependent on the local environment (which cannot be accounted for by the standards). Thus, we have considered a fitting range ending between 19000 eV and 19150 eV, with a step size of 2 eV.
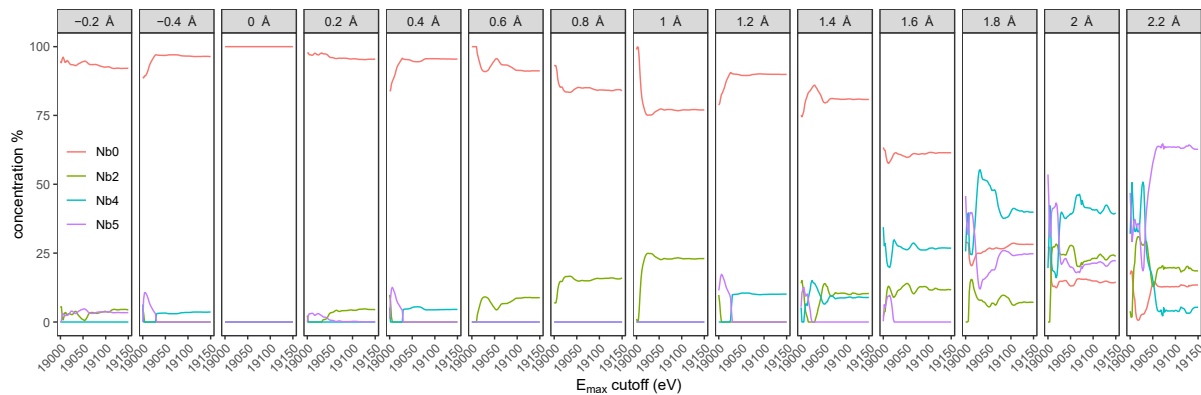


*Figure C-1. Best-fit of four of the Nb standards to the measured XANES spectra as a function of fitting range end-point. The fitting range started at 18950 eV for all points, and ended between 19000 eV and 19150 eV, as per x-axis.*

The result of the sensitivity analysis, presented in figure C-1, shows that curtailing the energy range too soon (< 19050 eV) leads to significant uncertainties on the predicted concentrations of the Nb charge states. However, once the fitting is extended past 19050 eV, the predicted concentrations appear to converge for all points and become insensitive to further changes in the fitting range. For this reason, a fitting range of 18950–19070 eV was used for the analysis presented in this paper.

To characterize the quality-of-fit over the extended edge of the XANES measurements, the fit was repeated across the entire compositional range. That is, the residual error (RMSE) of the fit was calculated for all possible combinations of fitting variables *a*, *b*, *c* and  *d* in the range [0,1] with a step size of 0.01. In all cases a single minimum is observed in the RMSE's five-dimensional parameter space. This provides reassurance that conventional optimisation algorithm should successfully identify the best-fit solution, irrespective of starting concentrations.

The distribution of residual errors for all possible fitting solutions, as shown in figure C-2, provides insight on the uniqueness of the best-fit combination: for most points, the distribution of solution is sharp near the optimum, indicating that the best fit is in fact quite distinguishable from the other solutions. But in some cases, further into the oxide, the optimum becomes quite shallow, meaning that multiple solutions exist with different combinations of Nb standards but with similar residual error. By considering all solutions that yield a residual error that is within 0.1% of the best fit RMSE (shaded areas in Figure 6-9), we can identify those Nb oxidation states that are most sensitive to variations in the quality of fit. It is evident that in the metal and for most of the oxide, the variations in concentrations for solutions within 0.1% of the optimum are small. They become larger for the last three points, deeper in the oxide, but at all points the uncertainty is reasonably small and does not affect the conclusions drawn.
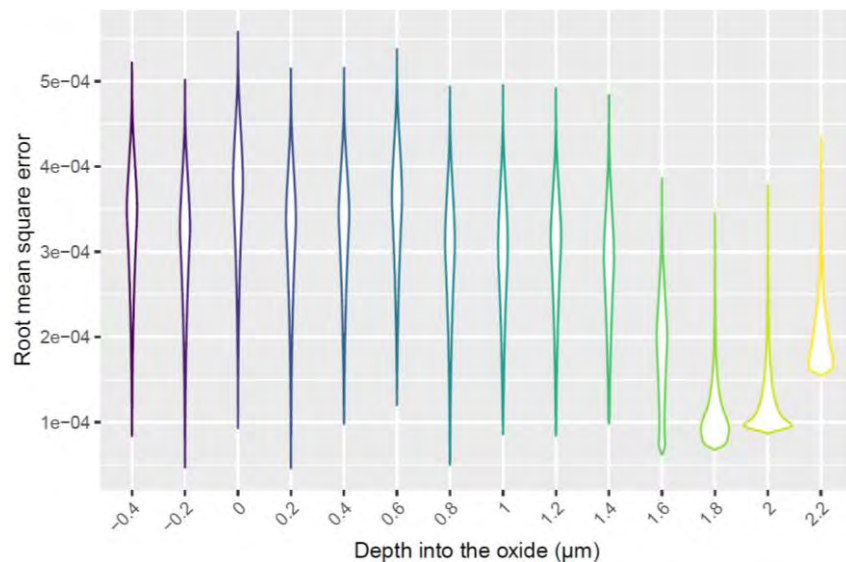


*Figure C-2 Distribution of residual errors between model (linear combination of standard spectra) and measured spectra, when the fit is performed across all parameter space (i.e. for all allowed values of $Nb^0$, $Nb^{2+}$, $Nb^{3+}$, $Nb^{4+}$ and $Nb^{5+}$ between [0,1]).*
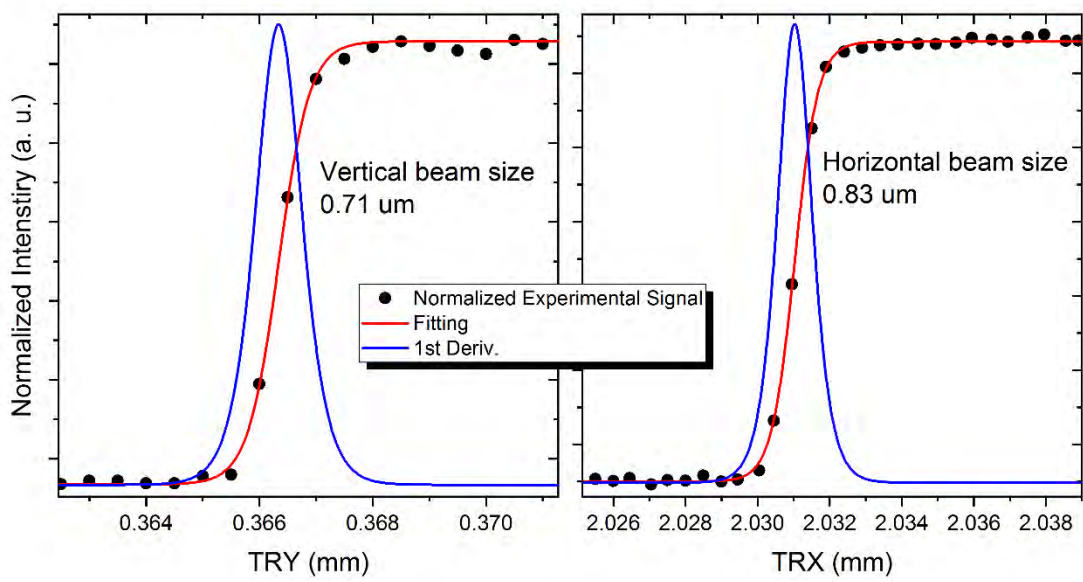
*Figure C-3. Measured beam size for X-ray beam, in the vertical direction a diameter of 0.71 µm and in the horizontal direction 0.83 µm*

Table. D-1: Low-loss spectra of different hydrides and comparison with Zr as well as different zirconium oxides, from different references.

| State of sample | 1st peak | 2nd peak | 3rd peak |
|---|---|---|---|
| Epsilon $\epsilon - ZrH_{1.7-2}$ [218] | 19.6 ($\pm$ 0.2eV) | - | ≈40* |
| Delta $\delta - ZrH_{1.5-1.66}$ [218] | 19.2 ($\pm$ 0.2eV) | - | ≈40* |
| Gamma $\gamma - ZrH$ [218] | 18.3 ($\pm$ 0.2eV) | - | ≈40* |
| Zeta $\zeta - ZrH_{0.25-0.5}$ [220] | 17.4 ($\pm$ 0.2eV) | - | ≈40* |
| $ZrO_2$ monoclinic [217] | 14.4 | 25.8 | 41.2 |
| $ZrO_2$ tetrahedral [217] | 14.4 | 25.4 | 42.3 |
| Zirconium matrix $\alpha - Zr$ [218] | 16.8 ($\pm$ 0.2eV) | - | ≈40* |

Also included in this appendix is two low loss EELS SI from the metal-oxide interface of a 9-cycle Zircaloy-2 LK3/L material (Figure D-1 and Figure D-2). These are included to show the phemonon of hydrides being separated from the interface by the oxygen saturated metal being present also in this material studied.
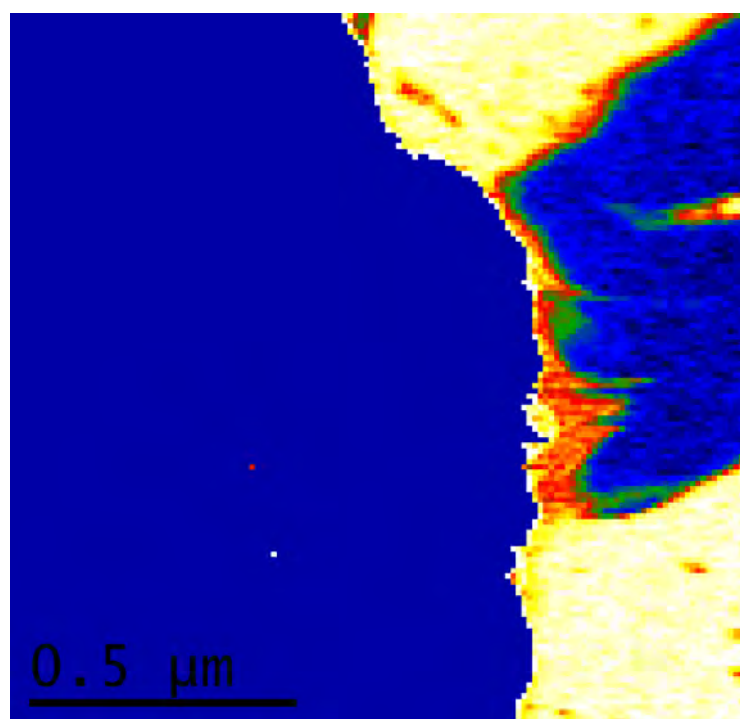
*Figure D-1. Peak shift map of metal-oxide interface of 9-cycle Zircaloy-LK3/L. hydride (blue) is separated from oxide (uniform colour blue) by oxygen saturated metal (red/yellow).*
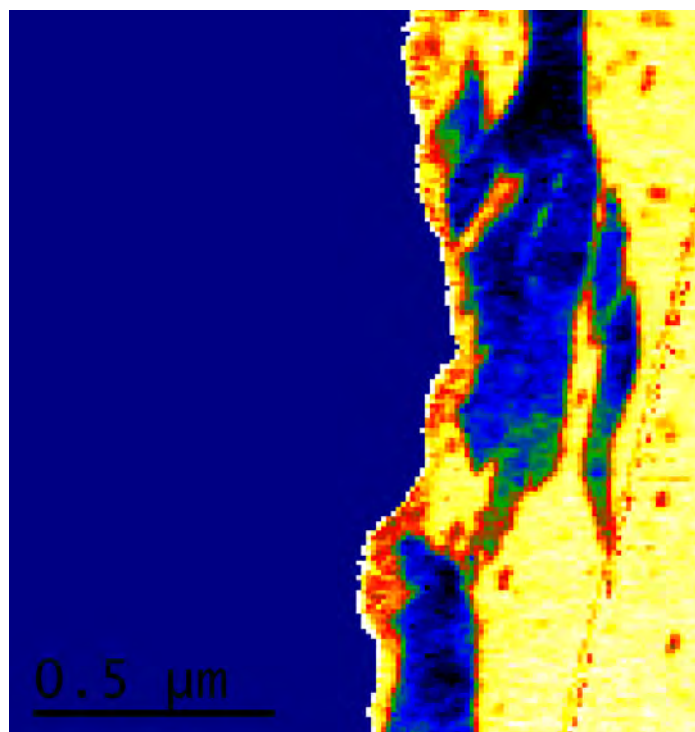


*Figure D-2. Peak shift map of metal-oxide interface of 9-cycle Zircaloy-LK3/L. hydride (blue) is separated from oxide (uniform colour blue) by oxygen saturated metal (red/yellow).*

# 11 References

[1] W. Martin, "Nuclear power," *Encyclopædia Britannica, inc.* https://www.britannica.com/technology/nuclear-power.

[2] W. Wiesenack, *Nuclear fuel assembly design and fabrication*. Woodhead Publishing Limited, 2012.

[3] D. G. Cacuci, *Handbook of Nuclear Engineering*, vol. 1, no. 3. 2010.

[4] D. O. Northwood, "The Development and Applications of Zirconium Alloys," *Mater. Des.*, vol. 6, no. 2, pp. 143–149, 1985, doi: 10.1007/978-1-4615-4257-5_20.

[5] S. Kass, "Hydrogen Pickup in Various Zirconium Alloys during Corrosion Exposure in High-Temperature Water and Steam," *J. Electrochem. Soc.*, vol. 107, no. 7, pp. 594–597, 1960, doi: 10.1149/1.2427781.

[6] B. Cox, K. VG, and L. C, "Waterside corrosion of zirconium alloys in nuclear power plants," *IAEA Tecdoc*, no. January, pp. 1–313, 1998, doi: IAEA-TECDOC-996.

[7] Y. Zhang, L. You, X. Li, J. Zhou, and X. Song, "In-situ investigation of the fatigue crack initiation and propagation behavior of Zircaloy-4 with different hydrogen contents at RT and 300 °C," *J. Nucl. Mater.*, vol. 532, p. 152065, 2020, doi: 10.1016/j.jnucmat.2020.152065.

[8] S. Abolhassani *et al.*, "Corrosion and hydrogen uptake in zirconium claddings irradiated in light water reactors," *Zircon. Nucl. Ind. 17th Int. Symp. ASTM STP 1543*, vol. 1543, pp. 540–573, 2015, doi: 10.1520/STP154320130007.

[9] G. Ledergerber *et al.*, "Fuel performance beyond design - Exploring the limits," *LWR Fuel Perform. Meet. Fuel/WRFPM 2010*, pp. 513–524, 2010.

[10] Z. Duan *et al.*, "Current status of materials development of nuclear fuel cladding tubes for light water reactors," *Nucl. Eng. Des.*, vol. 316, pp. 131–150, 2017, doi: 10.1016/j.nucengdes.2017.02.031.

[11] A. T. Motta, A. Couet, and R. J. Comstock, "Corrosion of Zirconium Alloys Used for Nuclear Fuel Cladding," *Annu. Rev. Mater. Res.*, vol. 45, no. 1, pp. 311–343, 2015, doi: 10.1146/annurev-matsci-070214-020951.

[12] H. AALTONEN, P., HANNINEN, "WATER CHEMISTRY AND BEHAVIOUR OF MATERIALS IN PWRs AND BWRs," *IAEA-TECDOC-667*, 1997.

[13] B. Lustman and F. Kerze, *The metallurgy of zirconium*, no. xviii, 776 p. 1955.

[14] H. Okamoto, "O-Zr (Oxygen-Zirconium)," *J. Phase Equilibria Diffus.*, vol. 28, no. 5, p. 498, 2007, doi: 10.1007/s11669-007-9154-2.

[15] C. Anghel, *Modified oxygen and hydrogen transport in Zr-based oxides*. 2006.

[16] C. Proff, S. Abolhassani, and C. Lemaignan, "Oxidation behaviour of zirconium alloys and their precipitates - A mechanistic study," *J. Nucl. Mater.*, vol. 432, no. 1–3, pp. 222–238, 2013, doi: 10.1016/j.jnucmat.2012.06.026.

[17]    R. Krishnan and M. K. Asundi, "Zirconium alloys in nuclear technology," *proc. Indian Acad. Sci. (Engg. Sci.) v*, vol. 4, pp. 41–56, 1980, doi: 10.1007/BF01118114.

[18]    D. Charquet, R. Hahn, E. Ortlieb, J.-P. Gros, and J.-F. Wadier, "Solubility Limits and Formation of Intermetallic Precipitates in ZrSnFeCr Alloys," *Zircon. Nucl. Ind. Eighth Int. Symp.*, pp. 405-405–18, 2008, doi: 10.1520/stp18878s.

[19]    P. Tejland *et al.*, "Oxidation mechanism in zircaloy-2 - The effect of SPP size distribution," *ASTM Spec. Tech. Publ.*, vol. STP 1543, pp. 373–403, 2015, doi: 10.1520/STP154320130052.

[20]    R. Adamson, F. Garzarolli, B. Cox, A. Strasser, and P. Rudling, "Corrosion Mechanisms in Zirconium Alloys," *ZIRAT12 Spec. Top. Rep.*, no. October, 2007, [Online]. Available: www.antinternational.com.

[21]    W. Yeniscavich, R. A. A. Wolfe, and R. M. M. Lieberman, "Hydrogen Absorption by Nickel Enriched Zircaloy-2," *J. Nucl. Mater.*, vol. 1, no. 3, pp. 271–280, 1959, doi: 10.1016/0022-3115(59)90023-6.

[22]    B. Cox, "Mechanisms of Hydrogen Absorption By Zirconium Alloys.," *At. Energy Canada Limited, AECL*, no. January, 1985.

[23]    Z. G. Zhang, Z. H. Feng, X. J. Jiang, X. Y. Zhang, M. Z. Ma, and R. P. Liu, "Microstructure and tensile properties of novel Zr-Cr binary alloys processed by hot rolling," *Mater. Sci. Eng. A*, vol. 652, pp. 77–83, 2016, doi: 10.1016/j.msea.2015.11.045.

[24]    Y. Il Jung, Y. N. Seol, B. K. Choi, J. Y. Park, and Y. H. Jeong, "Effect of Cr on the creep properties of zirconium alloys," *J. Nucl. Mater.*, vol. 396, no. 2–3, pp. 303–306, 2010, doi: 10.1016/j.jnucmat.2009.10.058.

[25]    C. Lemaignan, *Zirconium alloys: Properties and characteristics*, vol. 2. Elsevier Inc., 2012.

[26]    A. Couet, A. T. Motta, and R. J. Comstock, "Effect of Alloying Elements on Hydrogen Pickup in Zirconium Alloys," *Zircon. Nucl. Ind. 17th Vol.*, pp. 479–514, 2015, doi: 10.1520/STP154320120215.

[27]    P. Kofstad, "Defects and transport properties of metal oxides," *Oxid. Met.*, vol. 44, no. 1–2, pp. 3–27, 1995, doi: 10.1007/BF01046721.

[28]    T. Arima, K. Moriyama, N. Gaja, H. Furuya, K. Idemitsu, and Y. Inagaki, "Oxidation kinetics of Zircaloy-2 between 450°C and 600°C in oxidizing atmosphere," *Journal of Nuclear Materials*, vol. 257, no. 1. pp. 67–77, 1998, doi: 10.1016/S0022-3115(98)00069-5.

[29]    D. Wiemhiifer, "Sensing effects at gas-solid interfaces," *Solid State Commun.*, vol. 2738, no. 94, 1995.

[30]    X. Ma, C. Toffolon-Masclet, T. Guilbert, D. Hamon, and J. C. Brachet, "Oxidation kinetics and oxygen diffusion in low-tin Zircaloy-4 up to 1523 K," *J. Nucl. Mater.*, vol. 377, no. 2, pp. 359–369, 2008, doi: 10.1016/j.jnucmat.2008.03.012.

[31]    H. E. Evans, "Stress effects in high temperature oxidation of metals Stress effects in high temperature of metals," vol. 6608, 2013, doi: 10.1179/imr.1995.40.1.1.

[32]    B. Cox, J. P. Pemsler, and D. Bchantillons, "Diffusion of oxygen in growing zirconia films," *J. Nucl. Mater.*, vol. 28, pp. 73–78, 1968, doi: 10.1016/0022-3115(68)90058-5.

[33]  S. Abolhassani, G. Bart, and A. Jakob, "Examination of the chemical composition of irradiated zirconium based fuel claddings at the metal/oxide interface by TEM," *J. Nucl. Mater.*, vol. 399, no. 1, pp. 1–12, 2010, doi: 10.1016/j.jnucmat.2009.10.060.

[34]  N. Ramasubramanian, "Localised electron transport in corroding zirconium alloys," *J. Nucl. Mater.*, vol. 55, no. 2, pp. 134–154, 1975, doi: 10.1016/0022-3115(75)90148-8.

[35]  M. Lindgren and I. Panas, "Oxygen Vacancy Formation, Mobility, and Hydrogen Pick-up during Oxidation of Zirconium by Water," *Oxid. Met.*, vol. 87, no. 3–4, pp. 355–365, 2017, doi: 10.1007/s11085-016-9695-z.

[36]  R. . Causey, D. . Cowgill, and R. . Nilson, "Review of the Oxidation Rate of Zirconium Alloys," *Sandia Natl. Lab Rep.*, 2005, doi: 10.2172/876346.

[37]  M. Silva, "Influence of oxide microstructure on corrosion behaviour of zirconium-based model alloys," *PhD Thesis, Pennsylvania State Univ.*, 2007.

[38]  A. T. Motta *et al.*, "Microstructure and growth mechanism of oxide layers formed on Zr alloys studied with micro-beam synchrotron radiation," *Zircon. Nucl. Ind. 14th Int. Symp.*, vol. 1467, no. 5, pp. 205–232, 2005, doi: 10.1520/stp37508s.

[39]  G. P. Sabol, S. G. McDonald, and G. P. Airey, "Microstructure of the oxide films formed on zirconium-based alloys," *Astm Stp*, vol. 551, pp. 435–448, 1974.

[40]  K. Hauffe, "Oxidation of Metals," *Plenum Press. New York*, vol. 228, 1965.

[41]  H. A. Porte and J. Electrochem, "Oxidation of Zirconium and Zirconium Alloys," 1960.

[42]  A. Couet, A. T. Motta, and A. Ambard, "The coupled current charge compensation model for zirconium alloy fuel cladding oxidation: I. Parabolic oxidation of zirconium alloys," *Corros. Sci.*, vol. 100, pp. 73–84, 2015, doi: 10.1016/j.corsci.2015.07.003.

[43]  G. P. Sabol, "The Origin of the Cubic Rate Law in Zirconium Alloy Oxidation," *J. Electrochem. Soc.*, vol. 122, no. 2, p. 316, 1975, doi: 10.1149/1.2134204.

[44]  A. Yilmazbayhan, A. T. Motta, R. J. Comstock, G. P. Sabol, B. Lai, and Z. Cai, "Structure of zirconium alloy oxides formed in pure water studied with synchrotron radiation and optical microscopy: Relation to corrosion rate," *J. Nucl. Mater.*, vol. 324, no. 1, pp. 6–22, 2004, doi: 10.1016/j.jnucmat.2003.08.038.

[45]  M. Tupin, "Differences in reactivity of oxide growth during the oxidation of Zircaloy-4 in water vapour before and after the kinetic transition," *J. Nucl. Mater.*, vol. 317, pp. 130–144, 2003, doi: 10.1016/S0022-3115(02)01704-X.

[46]  R. Bossis and R. Iltis, "Multi-Scale Characterization of the Metal- Oxide Interface of Zirconium Alloys," *Zircon. Nucl. Ind. 12th Int. Symp.*, pp. 918–945, 2000.

[47]  C. C. Dollins and M. Jursich, "A MODEL FOR THE OXIDATION OF ZIRCONIUM-BASED," *J. Nucl. Mater.*, vol. 113, pp. 19–24, 1983.

[48]  J. P. G. and P. B. M. TUPIN, C. BATAILLON, "High temperature corrosion of Zircaloy-4 followed by in-situ impedance spectroscopy and chronoamperometry," in *CEA - Saclay, France*, pp. 134–155.

[49]  W. Qin, C. Nam, H. L. Li, and J. A. Szpunar, "Tetragonal phase stability in ZrO2 film formed on

zirconium alloys and its effects on corrosion resistance," *Acta Mater.*, vol. 55, no. 5, pp. 1695–1701, 2007, doi: 10.1016/j.actamat.2006.10.030.

[50]  M. Y. Yao, "A superior corrosion behavior of Zircaloy-4 in lithiated water at 360 ° C / 18 . 6 MPa by b -quenching," vol. 374, pp. 197–203, 2008, doi: 10.1016/j.jnucmat.2007.08.002.

[51]  Y. H. Jeong, J. H. Baek, S. J. Kim, H. G. Kim, and H. Ruhmann, "Corrosion characteristics and oxide microstructures of Zircaloy-4 in aqueous alkali hydroxide solutions," vol. 270, pp. 322–333, 1999.

[52]  M. Oskarsson, E. Ahlberg, U. Andersson, and K. Pettersson, "Characterisation of pre-transition oxides on Zircaloys," vol. 297, pp. 77–88, 2001.

[53]  H. I. Yoo, B. J. Koo, J. O. Hong, I. S. Hwang, and Y. H. Jeong, "A working hypothesis on oxidation kinetics of Zircaloy," *J. Nucl. Mater.*, vol. 299, no. 3, pp. 235–241, 2001, doi: 10.1016/S0022-3115(01)00695-X.

[54]  R. . Pilling, N.B and Bedworth, "No Title," *J. Inst. Met.*, vol. 29, pp. 529–582, 1923.

[55]  N. Pétigny, P. Barberis, C. Lemaignan, C. Valot, and M. Lallemant, "In situ XRD analysis of the oxide layers formed by oxidation at 743 K on Zircaloy 4 and Zr-1NbO," *J. Nucl. Mater.*, vol. 280, no. 3, pp. 318–330, 2000, doi: 10.1016/S0022-3115(00)00051-9.

[56]  A. T. Motta, "Waterside Corrosion in Zirconium Alloys," *JOM*, vol. 63, no. 8, pp. 59–63, 2011.

[57]  P. Platt *et al.*, "A study into the impact of interface roughness development on mechanical degradation of oxides formed on zirconium alloys A study into the impact of interface roughness development on mechanical degradation of oxides formed on zirconium alloys," *J. Nucl. Mater.*, vol. 459, no. April, pp. 166–174, 2015, doi: 10.1016/j.jnucmat.2015.01.028.

[58]  H. Kim, I. Kim, B. Choi, and J. Park, "A study of the breakaway oxidation behavior of zirconium cladding materials," *J. Nucl. Mater.*, vol. 418, no. 1–3, pp. 186–197, 2011, doi: 10.1016/j.jnucmat.2011.06.039.

[59]  N. Ni *et al.*, "Porosity in oxides on zirconium fuel cladding alloys, and its importance in controlling oxidation rates," *Scr. Mater.*, vol. 62, no. 8, pp. 564–567, 2010, doi: 10.1016/j.scriptamat.2009.12.043.

[60]  M. Gass *et al.*, "Corrosion of Zircaloys: Relating the microstructural observations to the corrosion kinetics," *J. Nucl. Mater.*, vol. 509, pp. 343–354, 2018, doi: 10.1016/j.jnucmat.2018.07.017.

[61]  A. Couet, A. T. Motta, A. Ambard, and D. Livigni, "In-situ electrochemical impedance spectroscopy measurements of zirconium alloy oxide conductivity: Relationship to hydrogen pickup," *Corros. Sci.*, vol. 119, pp. 1–13, 2017, doi: 10.1016/j.corsci.2016.12.008.

[62]  P. Bossis *et al.*, "Comparison of the high burn-up corrosion on M5 and low tin zircaloy-4," *J. ASTM Int.*, vol. 3, no. 1, pp. 199–230, 2006, doi: 10.1520/stp37522s.

[63]  M. Blat and D. Noel, "Detrimental role of hydrogen on the corrosion rate of zirconium alloys," *Zircon. Nucl. Ind. 11th Int. Symp.*, pp. 319–337, 1996.

[64]  A. Baris, "INCREASED HYDROGEN UPTAKE OF ZIRCONIUM BASED CLADDINGS AT HIGH BURNUP," *A thesis Submitt. to Univ. Birmingham degree Dr. Philos. Sch. Metall. Mater. Univ. Birmingham*, no. March, 2019.

[65] S. Abolhassani, R. Restani, and L. Hallstadius, "Comparative analysis of the evolution of Zircaloy-2 cladding irradiated in BWR," *Top Fuel React. Perform. 2015. Conf. Proc. Poster*, pp. 272–298, 2015.

[66] M. Chollet *et al.*, "Synchrotron X-ray diffraction investigations on strains in the oxide layer of an irradiated Zircaloy fuel cladding," *J. Nucl. Mater.*, vol. 488, pp. 181–190, 2017, doi: 10.1016/j.jnucmat.2017.03.010.

[67] S. Abolhassani *et al.*, "TEM Examinations of the Metal-Oxide Interface of Zirconium Based Alloys Irradiated in a Pressurized Water Reactor," *J. ASTM Int.*, vol. 2, no. 6, p. 12390, 2005, doi: 10.1520/JAI12390.

[68] B. Cox, "Some thoughts on the mechanisms of in-reactor corrosion of zirconium alloys," *J. Nucl. Mater.*, vol. 336, no. 2–3, pp. 331–368, 2005, doi: 10.1016/j.jnucmat.2004.09.029.

[69] A. Baris, S. Abolhassani, Y. L. Chiu, and H. E. Evans, "Observation of crack microstructure in oxides and its correlation to oxidation and hydrogen-uptake by 3D FIB Tomography – case of Zr-ZrO $_2$ in reactor," *Mater. High Temp.*, vol. 3409, pp. 1–8, 2017, doi: 10.1080/09603409.2017.1392412.

[70] A. Garner, A. Gholinia, P. Frankel, M. Gass, I. Maclaren, and M. Preuss, "The microstructure and microtexture of zirconium oxide films studied by transmission electron backscatter diffraction and automated crystal orientation mapping with transmission electron microscopy," *Acta Mater.*, vol. 80, pp. 159–171, 2014, doi: 10.1016/j.actamat.2014.07.062.

[71] W. Gong, H. Zhang, C. Wu, H. Tian, and X. Wang, "The role of alloying elements in the initiation of nanoscale porosity in oxide films formed on zirconium alloys," *Corros. Sci.*, vol. 77, pp. 391–396, 2013, doi: 10.1016/j.corsci.2013.08.006.

[72] A. Kumar, M. Nasrallah, and D. L. Douglass, "The effect of yttrium and thorium on the oxidation behavior of Ni-Cr-Al alloys," *Oxid. Met.*, vol. 8, no. 4, pp. 227–263, 1974, doi: 10.1007/BF00604042.

[73] A. Baris *et al.*, "Chemical and microstructural characterization of a 9 cycle Zircaloy-2 cladding using EPMA and FIB tomography," *J. Nucl. Mater.*, vol. 504, pp. 144–160, 2018, doi: 10.1016/j.jnucmat.2018.01.065.

[74] M. Tupin, C. Bisor, P. Bossis, J. Chêne, J. L. Bechade, and F. Jomard, "Mechanism of corrosion of zirconium hydride and impact of precipitated hydrides on the Zircaloy-4 corrosion behaviour," *Corros. Sci.*, vol. 98, pp. 478–493, 2015, doi: 10.1016/j.corsci.2015.05.058.

[75] B. Ensor, A. M. Lucente, M. J. Frederick, J. Sutliff, and A. T. Motta, "The role of hydrogen in zirconium alloy corrosion," *J. Nucl. Mater.*, vol. 496, pp. 301–312, 2017, doi: 10.1016/j.jnucmat.2017.08.046.

[76] S. Suman, M. K. Khan, M. Pathak, R. N. Singh, and J. K. Chakravartty, "Hydrogen in Zircaloy: Mechanism and its impacts," *Int. J. Hydrogen Energy*, vol. 40, no. 17, pp. 5976–5994, 2015, doi: 10.1016/j.ijhydene.2015.03.049.

[77] E. Hillner, "Hydrogen absorption in Zircaloy during aqueous corrosion, effect of environment," *Westinghouse Electr. Corp. Bettis At. Power Lab., Pittsburgh*, 1964.

[78] K. Videm, "Properties of zirconium base cladding materials-corrosion and hydrogen pickup," *Nucl. Eng. Des.*, vol. 21, no. 2, pp. 200–211, 1972, doi: 10.1016/0029-5493(72)90073-8.

[79]   A. Couet, A. T. Motta, and R. J. Comstock, "Hydrogen pickup measurements in zirconium alloys: Relation to oxidation kinetics," *J. Nucl. Mater.*, vol. 451, no. 1–3, pp. 1–13, 2014, doi: 10.1016/j.jnucmat.2014.03.001.

[80]   M. Harada and R. Wakamatsu, "The effect of hydrogen on the transition behavior of the corrosion rate of zirconium alloys," *J. ASTM Int.*, vol. 5, no. 3, pp. 1–17, 2008, doi: 10.1520/JAI101117.

[81]   M. Oskarsson, U. Andersson, and K. Pettersson, "Pre-transition oxidation behaviour of pre-hydrided Zircaloy-2," *J. Nucl. Mater.*, vol. 289, 2001.

[82]   T. Smith, "Kinetics and mechanism of hydrogen permeation of oxide films on zirconium," *J. Nucl. Mater.*, vol. 18, no. 3, pp. 323–336, 1966, doi: 10.1016/0022-3115(66)90173-5.

[83]   B. Malki, O. Le Bacq, and A. Pasturel, "Ab initio study of hydrogen related defect in ZrO2: Consequences on dry and aqueous oxidation," *J. Nucl. Mater.*, vol. 416, no. 3, pp. 362–368, 2011, doi: 10.1016/j.jnucmat.2011.06.038.

[84]   M. S. Veshchunov and A. V. Berdyshev, "Modelling of hydrogen absorption by zirconium alloys during high temperature oxidation in steam," *J. Nucl. Mater.*, vol. 255, no. 2–3, pp. 250–262, 1998, doi: 10.1016/S0022-3115(98)00018-X.

[85]   J. Hu *et al.*, "Hydrogen pickup during oxidation in aqueous environments: The role of nano-pores and nano-pipes in zirconium oxide films," *Acta Mater.*, vol. 180, pp. 105–115, 2019, doi: 10.1016/j.actamat.2019.09.005.

[86]   Y. Hatano, M. Sugisaki, K. Kitano, and M. Hayashi, "Role of intermetallic precipitates in hydrogen transport through oxide films on Zircaloy," *ASTM Spec. Tech. Publ.*, no. 1354, pp. 901–917, 2000, doi: 10.1520/stp14333s.

[87]   K. Baur, F. Garzarolli, H. Ruhmann, and H.-J. Sell, "Electrochemical Examinations in 350°C Water with Respect to the Mechanism of Corrosion-Hydrogen Pickup," *Zircon. Nucl. Ind. Twelfth Int. Symp.*, pp. 836-836–17, 2008, doi: 10.1520/stp14330s.

[88]   B. Cox, "Zirconium Intermetallics and Hydrogen Uptake During Corrosion.," *At. Energy Canada Limited, AECL*, no. April, 1987.

[89]   R. Sato, S. Ohkuma, Y. Shibuta, F. Shimojo, and S. Yamaguchi, "Proton Migration on Hydrated Surface of Cubic ZrO2: Ab initio Molecular Dynamics Simulation," *J. Phys. Chem. C*, vol. 119, no. 52, pp. 28925–28933, 2015, doi: 10.1021/acs.jpcc.5b09026.

[90]   N. Ramasubramanian, V. Perovic, and M. Leger, "Hydrogen transport in the oxide and hydrogen pickup by the metal during out- and in-reactor corrosion of Zr-2.5Nb pressure tube material," *ASTM Spec. Tech. Publ.*, no. 1354, pp. 853–876, 2000, doi: 10.1520/stp14331s.

[91]   M. Lindgren, G. Sundell, I. Panas, L. Hallstadius, M. Thuvander, and H.-O. Andrén, "Toward a Comprehensive Mechanistic Understanding of Hydrogen Uptake in Zirconium Alloys by Combining Atom Probe Analysis With Electronic Structure Calculations," *Zircon. Nucl. Ind. 17th Vol.*, pp. 515–539, 2015, doi: 10.1520/STP154320120164.

[92]   G. Sundell, M. Thuvander, and H. O. Andrén, "Barrier oxide chemistry and hydrogen pick-up mechanisms in zirconium alloys," *Corros. Sci.*, vol. 102, pp. 490–502, 2015, doi: 10.1016/j.corsci.2015.11.002.

[93]   N. Ramasubramanian, P. Billot, and S. Yagnik, "Hydrogen Evolution and Pickup During the

Corrosion of Zirconium Alloys: A Critical Evaluation of the Solid State and Porous Oxide Electrochemistry," *Zircon. Nucl. Ind. Thirteen. Int. Symp.*, pp. 222-222–23, 2009, doi: 10.1520/stp11391s.

[94]    N. Ni, S. Lozano-Perez, J. M. Sykes, G. D. W. Smith, and C. R. M. Grovenor, "Focussed ion beam sectioning for the 3D characterisation of cracking in oxide scales formed on commercial ZIRLO$^{TM}$ alloys during corrosion in high temperature pressurised water," *Corros. Sci.*, vol. 53, no. 12, pp. 4073–4083, 2011, doi: 10.1016/j.corsci.2011.08.013.

[95]    L. Kurpaska, I. Jozwik, and J. Jagielski, "Study of sub-oxide phases at the metal-oxide interface in oxidized pure zirconium and Zr-1.0% Nb alloy by using SEM/FIB/EBSD and EDS techniques," *J. Nucl. Mater.*, vol. 476, pp. 56–62, 2016, doi: 10.1016/j.jnucmat.2016.04.038.

[96]    K. J. Annand, I. Maclaren, and M. Gass, "Utilising DualEELS to probe the nanoscale mechanisms of the corrosion of Zircaloy-4 in 350°C pressurised water," *J. Nucl. Mater.*, vol. 465, pp. 390–399, 2015, doi: 10.1016/j.jnucmat.2015.06.022.

[97]    J. Hu *et al.*, "Identifying suboxide grains at the metal-oxide interface of a corroded Zr-1.0%Nb alloy using (S)TEM, transmission-EBSD and EELS," *Micron*, vol. 69, pp. 35–42, 2015, doi: 10.1016/j.micron.2014.10.004.

[98]    B. De Gabory, A. T. Motta, and K. Wang, "Transmission electron microscopy characterization of Zircaloy-4 and ZIRLO$^{TM}$ oxide layers," *J. Nucl. Mater.*, vol. 456, pp. 272–280, 2015, doi: 10.1016/j.jnucmat.2014.09.073.

[99]    N. Ni *et al.*, "How the crystallography and nanoscale chemistry of the metal/oxide interface develops during the aqueous oxidation of zirconium cladding alloys," *Acta Mater.*, vol. 60, no. 20, pp. 7132–7149, 2012, doi: 10.1016/j.actamat.2012.09.021.

[100]   R. J. Nicholls *et al.*, "Crystal structure of the ZrO phase at zirconium/zirconium oxide interfaces," *Adv. Eng. Mater.*, vol. 17, no. 2, pp. 211–215, 2015, doi: 10.1002/adem.201400133.

[101]   J. Hu *et al.*, "Understanding Corrosion and Hydrogen Pickup of Zirconium Fuel Cladding Alloys: The Role of Oxide Microstructure, Porosity, Suboxides, and Second-Phase Particles," *Zircon. Nucl. Ind. 18th Int. Symp.*, pp. 93–126, 2018, doi: 10.1520/stp159720160071.

[102]   K. Li *et al.*, "3D-characterization of deuterium distributions in zirconium oxide scale using high-resolution SIMS," *Appl. Surf. Sci.*, vol. 464, no. September 2018, pp. 311–320, 2019, doi: 10.1016/j.apsusc.2018.09.101.

[103]   A. S. S. Yardley, "Oxidation Mechanisms in Zirconium Alloys for Nuclear Applications," no. January, 2017.

[104]   B. Cox and Y. M. Wong, "Hydrogen uptake micro-mechanism for Zr alloys," *J. Nucl. Mater.*, vol. 270, no. 1, pp. 134–146, 1999, doi: 10.1016/S0022-3115(98)00898-8.

[105]   D. Olander and A. Motta, *Light Water Reactor Materials*. 2011.

[106]   A. Garner, P. Frankel, J. Partezana, and M. Preuss, "The effect of substrate texture and oxidation temperature on oxide texture development in zirconium alloys," *J. Nucl. Mater.*, vol. 484, pp. 347–356, 2017, doi: 10.1016/j.jnucmat.2016.10.037.

[107]   G. David, R. Geschier, and C. Roy, "ETUDE DE LA CROISSANCE DE L'OXYDE SUR LE ZIRCONIUM ET LE ZIRCALOY-2," *J. Nucl. Mater.*, vol. 38, pp. 329–339, 1971.

[108] A. Couet, "HYDROGEN PICKUP MECHANISM OF ZIRCONIUM ALLOYS," The Pennsylvania State University The, 2014.

[109] V. Renčiuková, J. Macák, P. Sajdl, R. Novotný, and A. Krausová, "Corrosion of zirconium alloys demonstrated by using impedance spectroscopy," *J. Nucl. Mater.*, vol. 510, pp. 312–321, 2018, doi: 10.1016/j.jnucmat.2018.08.005.

[110] V. N. Shishov, "The evolution of microstructure and deformation stability in Zr-Nb-(Sn,Fe). alloys under neutron irradiation," *J. ASTM Int.*, vol. 7, no. 7, pp. 37–66, 2010, doi: 10.1520/JAI103005.

[111] D. F. Taylor, "An oxide-semiconductance model of nodular corrosion and its application to Zirconium alloy development," *J. Nucl. Mater.*, vol. 184, no. 1, pp. 65–77, 1991, doi: 10.1016/0022-3115(91)90534-E.

[112] A. Couet, A. T. Motta, B. De Gabory, and Z. Cai, "Microbeam X-ray Absorption Near-Edge Spectroscopy study of the oxidation of Fe and Nb in zirconium alloy oxide layers," *J. Nucl. Mater.*, vol. 452, no. 1–3, pp. 614–627, 2014, doi: 10.1016/j.jnucmat.2014.05.047.

[113] K. Sakamoto, K. Une, M. Aomi, and K. Hashizume, "Depth profile of chemical states of alloying elements in oxide layer of Zr-based alloys," *Prog. Nucl. Energy*, vol. 57, pp. 101–105, 2012, doi: 10.1016/j.pnucene.2011.12.012.

[114] B. D. C. Bell *et al.*, "The influence of alloying elements on the corrosion of Zr alloys," *Corros. Sci.*, vol. 105, pp. 36–43, 2016, doi: 10.1016/j.corsci.2015.12.022.

[115] A. M. Garde, "Enhancement of Aqueous Corrosion of Zircaloy-4 Due to Hydride Precipitation at the Metal-Oxide Interface," *Zircon. Nucl. Ind. Ninth Int. Symp.*, pp. 566–594, 1991, [Online]. Available: https://compass.astm.org/download/STP25527S.19981.pdf.

[116] N. M. TALLAN and R. W. VEST, "Electrical Properties and Defect Structure of Y2O3," *J. Am. Ceram. Soc.*, vol. 49, no. 8, pp. 401–404, 1966, doi: 10.1111/j.1151-2916.1966.tb15404.x.

[117] R. Collongues, "La non-stœchiométrie," *Masson cie, Ed. Paris,* pp. 40-64., 1971.

[118] A. Sinhamahapatra, J. P. Jeon, J. Kang, B. Han, and J. S. Yu, "Oxygen-Deficient Zirconia (ZrO2-x): A New Material for Solar Light Absorption," *Sci. Rep.*, vol. 6, no. May, pp. 1–8, 2016, doi: 10.1038/srep27218.

[119] J. Schefold, D. Lincot, A. Ambard, and O. Kerrec, "The Cyclic Nature of Corrosion of Zr and Zr-Sn in High-Temperature Water „ 633 K … A Long-Term In Situ Impedance Spectroscopic Study," pp. 451–461, 2003, doi: 10.1149/1.1602079.

[120] J. J. Vermoyal, A. Frichet, L. Dessemond, and A. Hammou, "AC impedance study of corrosion films formed on zirconium based alloys," *Electrochim. Acta*, vol. 45, no. 7, pp. 1039–1048, 1999, doi: 10.1016/S0013-4686(99)00307-2.

[121] R. K. Münch, G. Bart, O. Gebhardt, and D. Landolt, "Investigation of Zircaloy-4 Oxidation under Simulated Pressurised Water Reactor Conditions Using Electrochemical Impedance Spectroscopy," *Mater. Sci. Forum*, vol. 289–292, pp. 163–168, 1998, doi: 10.4028/www.scientific.net/MSF.289-292.163.

[122] P. Barberis and A. Frichet, "Characterization of Zircaloy-4 oxide layers by impedance spectroscopy," vol. 273, pp. 182–191, 1999.

[123]  J. K. Stortelder, "Ionic Conductivity in Yttria-Stabilized Zirconia Thin Films grown by Pulsed Laser Deposition," *Inorg. Mater. Sci.*, no. August, 2005, [Online]. Available: http://www.utwente.nl/tnw/ims/people/formerMSc/Jetske Stortelder.pdf.

[124]  X. Guo, "Hydrothermal degradation mechanism of tetragonal zirconia," *J. Mater. Sci.*, vol. 36, no. 15, pp. 3737–3744, 2001, doi: 10.1023/A:1017925800904.

[125]  S. Forsberg, E. Ahlberg, and M. Limbäck, "Studies of corrosion of cladding materials in simulated BWR environment using impedance measurements," *J. ASTM Int.*, vol. 4, no. 9, pp. 1–22, 2007, doi: 10.1520/JAI101123.

[126]  B. D. C. Bell, S. T. Murphy, R. W. Grimes, and M. R. Wenman, "The effect of Nb on the corrosion and hydrogen pick-up of Zr alloys," *Acta Mater.*, vol. 132, pp. 425–431, 2017, doi: 10.1016/j.actamat.2017.04.063.

[127]  Z. Yu, A. Couet, and M. Bachhav, "Irradiation-induced Nb redistribution of ZrNb alloy: An APT study," *J. Nucl. Mater.*, vol. 516, pp. 100–110, 2019, doi: 10.1016/j.jnucmat.2019.01.015.

[128]  M. Moorehead, Z. Yu, L. Borrel, J. Hu, Z. Cai, and A. Couet, "Comprehensive investigation of the role of Nb on the oxidation kinetics of Zr-Nb alloys," *Corros. Sci.*, vol. 155, no. June, pp. 173–181, 2019, doi: 10.1016/j.corsci.2019.04.017.

[129]  E. Polatidis *et al.*, "Residual stresses and tetragonal phase fraction characterisation of corrosion tested Zircaloy-4 using energy dispersive synchrotron X-ray diffraction," *J. Nucl. Mater.*, vol. 432, no. 1–3, pp. 102–112, 2013, doi: 10.1016/j.jnucmat.2012.07.025.

[130]  C. Roy and B. Burgess, "A study of the stresses generated in zirconia films during the oxidation of zirconium alloys," *Oxid. Met.*, vol. 2, no. 3, pp. 235–261, 1970, doi: 10.1007/BF00614620.

[131]  L. Kurpaska, J. Favergeon, J. L. Grosseau-Poussard, L. Lahoche, and G. Moulin, "In-situ stress analysis of the Zr/ZrO 2 system as studied by Raman spectroscopy and deflection test in monofacial oxidation techniques," *Appl. Surf. Sci.*, vol. 385, pp. 106–112, 2016, doi: 10.1016/j.apsusc.2016.05.074.

[132]  R. B. Adamson, "Effects of neutron irradiation on microstructure and properties of Zircaloy," *ASTM Spec. Tech. Publ.*, no. 1354, pp. 15–31, 2000, doi: 10.1520/stp14292s.

[133]  B. V. Cockeram, K. J. Leonard, T. S. Byun, L. L. Snead, and J. L. Hollenbeck, "Development of microstructure and irradiation hardening of Zircaloy during low dose neutron irradiation at nominally 377-440 °c," *J. Nucl. Mater.*, vol. 449, no. 1–3, pp. 69–87, 2014, doi: 10.1016/j.jnucmat.2014.03.004.

[134]  B. F. Kammenzind, J. A. Gruber, R. Bajaj, and J. D. Smee, "Neutron Irradiation Effects on the Corrosion of Zircaloy-4 in a Pressurized Water Reactor Environment," *Zircon. Nucl. Ind. 18th Int. Symp.*, pp. 448–490, 2018, doi: 10.1520/stp159720160085.

[135]  Q. Dong, H. Qin, Z. Yao, and M. R. Daymond, "Irradiation damage and hardening in pure Zr and Zr-Nb alloys at 573 K from self-ion irradiation," *Mater. Des.*, vol. 161, pp. 147–159, 2019, doi: 10.1016/j.matdes.2018.11.017.

[136]  K. N. Jang and K. T. Kim, "The effect of neutron irradiation on hydride reorientation and mechanical property degradation of zirconium alloy cladding," *Nucl. Eng. Technol.*, vol. 49, no. 7, pp. 1472–1482, 2017, doi: 10.1016/j.net.2017.05.006.

[137]  A. W. Colldeweih, A. Baris, P. Spätig, and S. Abolhassani, "Evaluation of mechanical properties

of irradiated zirconium alloys in the vicinity of the metal-oxide interface," *Mater. Sci. Eng. A*, vol. 742, no. April 2018, pp. 842–850, 2019, doi: 10.1016/j.msea.2018.09.107.

[138]   Y. Dong, "CORRELATIONS BETWEEN OXIDE STRUCTURE , IRON DISTRIBUTIONS , AND ZIRCONIUM OXIDE GROWTH by Yan Dong A dissertation submitted in partial fulfillment of the requirements for the degree of Doctor of Philosophy ( Materials Science and Engineering ) in the Univ," 2017.

[139]   J. P. Abriata, J. C. Bolcich, and D. Arias, "The Sn-Zr (Tin-Zirconium) system," *Bull. Alloy Phase Diagrams*, vol. 5, no. 1, p. 21, 1984, doi: 10.1007/BF02868715.

[140]   D. Arias and L. Roberti, "The solubility of tin in α and β zirconium below 1000°C," *J. Nucl. Mater.*, vol. 118, no. 2–3, pp. 143–149, 1983, doi: 10.1016/0022-3115(83)90219-2.

[141]   G. P. Sabol, "ZIRLO$^{TM}$ - An alloy development success," *J. ASTM Int.*, vol. 2, no. 2, pp. 229–250, 2005, doi: 10.1520/stp37500s.

[142]   A. Garner *et al.*, "The effect of Sn concentration on oxide texture and microstructure formation in zirconium alloys," *Acta Mater.*, vol. 99, pp. 259–272, 2015, doi: 10.1016/j.actamat.2015.08.005.

[143]   V. S. Emel'ianov, I. G. Godin, and A. I. Evstiukhin, "Study of the zirconium apex of the Zr-Ta-Nb phase diagram," *Sov. J. At. Energy*, vol. 4, no. 2, pp. 211–220, 1958, doi: 10.1007/BF02207344.

[144]   J. P. Abriata and J. C. Bolcich, "The Nb-Zr (Niobium-Zirconium) system," *Bull. Alloy Phase Diagrams*, vol. 3, no. 1, pp. 34–44, 1982, doi: 10.1007/BF02873409.

[145]   Y. P. Lin and O. T. Woo, "Oxidation of β-Zr and related phases in Zr-Nb alloys: An electron microscopy investigation," *J. Nucl. Mater.*, vol. 277, no. 1, pp. 11–27, 2000, doi: 10.1016/S0022-3115(99)00153-1.

[146]   B. Ensora, Michael Moorehead, J. R. Seidensticker, A. Couet, and  and A. T. Motta, "XANES Study of Fe and Nb Oxidation in Zr-2.5Nb Oxide Layers Brendan Ensor," pp. 3–6.

[147]   A. Froideval, C. Degueldre, C. U. Segre, M. A. Pouchon, and D. Grolimund, "Niobium speciation at the metal / oxide interface of corroded niobium-doped Zircaloys : A X-ray absorption near-edge structure study," vol. 50, pp. 1313–1320, 2008, doi: 10.1016/j.corsci.2008.01.011.

[148]   A. Froideval *et al.*, "Microprobe analysis of neutron irradiated and autoclaved zirconium niobium claddings using synchrotron-based hard X-ray imaging and spectroscopy," *J. Nucl. Mater.*, vol. 385, no. 2, pp. 346–350, 2009, doi: 10.1016/j.jnucmat.2008.12.022.

[149]   K. Sakamoto, K. Une, M. Aomi, T. Otsuka, and K. Hashizume, "Change of chemical states of niobium in the oxide layer of zirconium-niobium alloys with oxide growth," *J. Nucl. Sci. Technol.*, vol. 52, no. 10, pp. 1259–1264, 2015, doi: 10.1080/00223131.2015.1058196.

[150]   D. Bach, R. Schneider, D. Gerthsen, J. Verbeeck, and W. Sigle, "EELS of Niobium and Stoichiometric Niobium-Oxide Phases—Part I: Plasmon and Near-Edges Fine Structure," *Microsc. Microanal.*, vol. 15, no. 6, pp. 505–523, 2009, doi: 10.1017/S143192760999105X.

[151]   E. G. S. A. A. Kiselev, V. A. Myshkin, A. V. Kozhevnikov, S. I. Korolev, "Research on the Corrosion of Zirconium Alloys in Water and Steam at High Temperature and Pressure," *Corros. React. Mater. 2*, p. p67, 1962.

[152]   J. P. Arias, D. Abriata, "The Fe-Zr ( Iron-Zirconium ) System," *Bull. Alloy Phase Diagrams*, vol. 9,

no. 5, pp. 597–604, 1988.

[153] K. Kakiuchi, K. Ohira, N. Itagaki, Y. Otsuka, Y. Ishii, and A. Miyazaki, "Irradiated behavior at high burnup for hifi alloy," *J. Nucl. Sci. Technol.*, vol. 43, no. 9, pp. 1031–1036, 2006, doi: 10.1080/18811248.2006.9711192.

[154] T. B. Massalski, "Binary Alloy Phase Diagrams," in *Second Edition ed.: ASM International. [15]*, .

[155] J. Y. Park, S. J. Yoo, B. K. Choi, and Y. H. Jeong, "Oxide microstructures of advanced Zr alloys corroded in 360 °C water loop," *J. Alloys Compd.*, vol. 437, no. 1–2, pp. 274–279, 2007, doi: 10.1016/j.jallcom.2006.07.101.

[156] C. Proff and D. Z. Autre, "Zirconium To cite this version : HAL Id : tel-00609232 Aspects microstructuraux de l´oxydation d´alliages de zirconium," 2011.

[157] S. Abolhassani, D. Gavillet, F. Groeschel, P. Jourdain, and H. U. Zwicky, "Recent Observations on the Evolution of the Secondary Phase Particles in Zircaloy-2 under Irradiation in a BWR up to a High Burnup," *Proc. Int. Top. Meet. LWR Fuel Perform.*, pp. 63–71, 2000.

[158] E. L. Berry, Warren E. Vaughan, Dale A. White, "Hydrogen Pickup During Aqueous Corrosion Of Zirconium Alloys," *Corros. Sci.*, vol. 17, no. 109, 1961.

[159] G. Sundell, *Atomic scale degradation of zirconium alloys for nuclear applications*. 2015.

[160] B. E. Zuzek, J. R. Abdata, C. A. Barlloche, C. Nacional, and D. E. Atomlca, "Hiltibran, 1960. chemical Control in illinois Farm Ponds..pdf," vol. 11, no. 4, pp. 385–395, 1990.

[161] M. A. Louchez, R. Besson, L. Thuinet, and A. Legris, "Interfacial properties of hydrides in μ-Zr: A theoretical study," *J. Phys. Condens. Matter*, vol. 29, no. 41, 2017, doi: 10.1088/1361-648X/aa7f8a.

[162] Z. Zhao *et al.*, "Characterization of Zirconium Hydrides and Phase Field Approach to a Mesoscopic-Scale Modeling of Their Precipitation," *J. ASTM Int.*, vol. 5, no. 3, p. 101161, 2008, doi: 10.1520/JAI101161.

[163] A. T. Motta and L. Q. Chen, "Hydride formation in zirconium alloys," *Jom*, vol. 64, no. 12, pp. 1403–1408, 2012, doi: 10.1007/s11837-012-0479-x.

[164] S. M. Hanlon, S. Y. Persaud, F. Long, and M. R. Daymond, "Advanced characterization of hydrides in zirconium alloys," *Miner. Met. Mater. Ser.*, vol. Part F11, pp. 577–597, 2018, doi: 10.1007/978-3-319-68454-3_45.

[165] M. Christensen *et al.*, "Effect of Hydrogen on Dimensional Changes of Zirconium and the Influence of Alloying Elements: First-Principles and Classical Simulations of Point Defects, Dislocation Loops, and Hydrides," *Zircon. Nucl. Ind. 17th Vol.*, pp. 55–92, 2015, doi: 10.1520/STP154320120170.

[166] A. J. Breen *et al.*, "Scripta Materialia Atomic scale analysis of grain boundary deuteride growth front in Zircaloy-4," vol. 156, pp. 42–46, 2018, doi: 10.1016/j.scriptamat.2018.06.044.

[167] B. Cox, "Pore structure in oxide films on irradiated and unirradiated zirconium alloys," *J. Nucl. Mater.*, vol. 148, no. 3, pp. 332–343, 1987, doi: 10.1016/0022-3115(87)90027-4.

[168] S. Abolhassani, C. Proff, L. Veleva, T. M. Karlsen, P. Bennett, and B. Oberla, "Transmission Electron Microscopy Examinations of Metal-Oxide Interface of Zirconium-Based Alloys

Irradiated in Halden," *Zircon. Nucl. Ind. 18th Int. Symp.*, pp. 614–644, 2018, doi: 10.1520/STP159720160039.

[169] M. Dahlbäck *et al.*, "The effect of liner component iron content on cladding corrosion, hydriding, and PCI resistance," *J. ASTM Int.*, vol. 2, no. 9, pp. 267–289, 2005, doi: 10.1520/JAI12444.

[170] E. Steinberg, H. G. Weidinger, and A. Schaa, "Analytical Approaches and Experimental Verification To Describe the Influence of Cold Work and Heat Treatment on the Mechanical Properties of Zircaloy Cladding Tubes.," *ASTM Spec. Tech. Publ.*, pp. 106–112, 1984, doi: 10.1520/stp34465s.

[171] J. P. Gros and J. F. Wadier, "Precipitate growth kinetics in Zircaloy-4," *J. Nucl. Mater.*, vol. 172, no. 1, pp. 85–96, 1990, doi: 10.1016/0022-3115(90)90012-C.

[172] A. W. and A. M. W. T. Andersson, T. Thorvaldsson, "Influence of Thermal Processing and Microstructure on the Corrosion Behaviour of Zicaloy-4 Tubing," *IAEA Int. Symp. Improv. Water React. Fuel Technol. Util. Stock.*, pp. 387–408, 1987, [Online]. Available: http://www.iaea.org/inis/collection/NCLCollectionStore/_Public/18/083/18083095.pdf.

[173] A. G. F. de la Peña, T. Ostasevicius, V.T. Fauske, P. Burdet, E. Prestat, P. Jokubauskas, M. Nord, K.E. MacArthur, M. Sarahan, D.N. Johnstone, J. Taillon, A. Eljarrat, V. Migunov, J. Caron, T. Furnival, S. Mazzucco, T. Aarholt, M. Walls, T. Slater, F. Winkler, "HyperSpy v1., 4," *10.5281/ZENODO.1407391*, 2018.

[174] M. Lynch, J. Swan, "THE CHARACTERISTIC LOSS SPECTRA OF THE SECOND AND THIRD SERIS TRANSITION METALS," *Phys. Rev.*, pp. 811–816, 1968.

[175] J. Frandon, B. Brousseau, and F. Pradal, "Electronic Excitations in Some Transition Metals and Their Oxides," *Phys. Status Solidi*, vol. 379, no. 98, pp. 379–385, 1980, doi: 10.1002/pssb.2220980140.

[176] R. Stockbauer, D. E. Ramaker, and E. Madey, "Ph_vsrkalrsche Chemie, Uniuersitiir Innsbruck, A- 6020 Innrhruck, Austriu," vol. 153, pp. 776–783, 1985.

[177] R. K. Zheng, "Electron energy loss spectroscopy," in *Microscopy and Imaging science*, 2001, pp. 545–586.

[178] R. A. Y. Egerton, "Electron energy-loss spectroscopy," *IOP Conf. Ser. Mater. Sci. Eng.*, 1997.

[179] R. F. Egerton, "Electron energy-loss spectroscopy in the TEM," *Reports Prog. Phys.*, vol. 72, no. 1, p. 016502, 2009, doi: 10.1088/0034-4885/72/1/016502.

[180] F. Hofer, F. P. Schmidt, W. Grogger, and G. Kothleitner, "Fundamentals of electron energy-loss spectroscopy," *IOP Conf. Ser. Mater. Sci. Eng.*, vol. 109, no. 111, p. 012007, 2016, doi: 10.1088/1757-899X/109/1/012007.

[181] S. Abolhassani and P. Gasser, "Preparation of TEM samples of metal-oxide interface by the focused ion beam technique," *J. Microsc.*, vol. 223, no. 1, pp. 73–82, 2006, doi: 10.1111/j.1365-2818.2006.01599.x.

[182] F. Baxter, A. Garner, M. Topping, H. Hulme, M. Preuss, and P. Frankel, "Phase stability of zirconium oxide films during focused ion beam milling," *J. Nucl. Mater.*, vol. 504, pp. 176–180, 2018, doi: 10.1016/j.jnucmat.2018.03.037.

[183] C. A. Volkert and E. T. Lilleodden, "Size effects in the deformation of sub-micron Au columns," *Philos. Mag.*, vol. 86, no. 33-35 SPEC. ISSUE, pp. 5567–5579, 2006, doi: 10.1080/14786430600567739.

[184] N. Ilchuk, H. P. Seifert, and P. Spätig, "Analytical determination of the constitutive behavior from micro-pillar testing: Application to a tempered martensitic steel," *AIP Adv.*, vol. 4, no. 4, 2014, doi: 10.1063/1.4873155.

[185] R. Vanta and S. Abolhassani, "Study of the change of semiconducting properties of the oxide at the vicinity of metal-oxide interfaces in fuel rods," *Master Thesis EPFL*, 2015.

[186] R. Vanta, S. Abolhassani, and M. Dadras, "Examination of semiconducting properties of oxides in the vicinity of metal-oxide interfaces for selected alloys," *Eur. Microsc. Congr. 2016 Proc.*, vol. 399, no. 1, pp. 382–383, 2016, doi: 10.1002/9783527808465.emc2016.6954.

[187] M. M. R. Howlader, K. Shiiyama, C. Kinoshita, M. Kutsuwada, and M. Inagaki, "The electrical conductivity of zircaloy oxide films," *J. Nucl. Mater.*, vol. 253, no. 1–3, pp. 149–155, 1998, doi: 10.1016/s0022-3115(97)00309-7.

[188] R. M. Pashley, M. Rzechowicz, L. R. Pashley, and M. J. Francis, "De-gassed water is a better cleaning agent," *J. Phys. Chem. B*, vol. 109, no. 3, pp. 1231–1238, 2005, doi: 10.1021/jp045975a.

[189] A. Atkinson, "Wagner theory and short circuit diffusion," *Mater. Sci. Technol.*, vol. 4, no. 12, pp. 1046–1051, 1988, doi: 10.1186/bcr773.

[190] A. T. Fromhold, "Theory of Metal Oxidation," *North Holl. Publ. Co.*, pp. 1–16, 1976.

[191] J. Shin, J. H. Joo, D. Samuelis, and J. Maier, "Oxygen-Deficient $TiO_{2-\delta}$ Nanoparticles via Hydrogen Reduction for High Rate Capability Lithium Batteries," *Chem. Mater.*, vol. 24, no. 3, pp. 543–551, 2012, doi: 10.1021/cm2031009.

[192] A. M. A. A. H. Al-mowali, "Doping , Vacancy formation and Substitutional Effects on Semiconductor Selectivity of Rutile $TiO_2$ Crystal," vol. 3, no. 2, pp. 22–32, 2013.

[193] B. J. Morgan and G. W. Watson, "Erratum: Intrinsic n-type defect formation in $TiO_2$: A comparison of rutile and anatase from GGA+ U calculations (Journal of Physical Chemistry C (2010) 114:5 (2321-2328) DOI: 10.1021/jp9088047))," *J. Phys. Chem. C*, vol. 116, no. 12, p. 7242, 2012, doi: 10.1021/jp301913c.

[194] L. Liu *et al.*, "Oxygen vacancies: The origin of n-type conductivity in ZnO," *Phys. Rev. B*, vol. 93, no. 23, 2016, doi: 10.1103/PhysRevB.93.235305.

[195] A. Couet, A. T. Motta, A. Ambard, and R. J. Comstock, "Hydrogen pickup mechanism in zirconium alloys," *ASTM Spec. Tech. Publ.*, vol. STP 1597, pp. 312–349, 2018, doi: 10.1520/STP159720160055.

[196] D. S. Rutmal et al, "Relationship between electric resistance of zirconia ceramics and porosity," *UDC 666.764.262.315.592*, no. 6, pp. 36–39, 1970.

[197] J. Romero, J. Partezana, R. J. Comstock, L. Hallstadius, A. T. Motta, and A. Couet, "Evolution of Hydrogen Pickup Fraction with Oxidation Rate on Zirconium Alloys," *Top Fuel React. Fuel Perform.*, pp. 1–7, 2015.

[198] S. K. Yagnik *et al.*, "Ductility of zircaloy-4 fuel cladding and guide tubes at high fluences," *ASTM*

*Spec. Tech. Publ.*, vol. 2, no. 1467, pp. 604–631, 2005, doi: 10.1520/stp37527s.

[199] C. Krautgasser, R. Bermejo, P. Supancic, and R. Danzer, "Influence of the scatter of strength and of measurement uncertainties on the determination of the subcritical crack growth exponent in ceramics and glasses," *J. Eur. Ceram. Soc.*, vol. 37, no. 4, pp. 1873–1878, 2017, doi: 10.1016/j.jeurceramsoc.2016.11.043.

[200] E. Sánchez-González, J. J. Meléndez-Martínez, A. Pajares, P. Miranda, F. Guiberteau, and B. R. Lawn, "Application of hertzian tests to measure stress-strain characteristics of ceramics at elevated temperatures," *J. Am. Ceram. Soc.*, vol. 90, no. 1, pp. 149–153, 2007, doi: 10.1111/j.1551-2916.2006.01339.x.

[201] R. Odette and S. Zinlke, *STRUCTURAL ALLOYS FOR NUCLEAR ENERGY APPLICATIONS*, no. 1. 2019.

[202] H. Hulme *et al.*, "An X-ray absorption near-edge structure (XANES) study of the Sn L3 edge in zirconium alloy oxide films formed during autoclave corrosion," *Corros. Sci.*, vol. 105, pp. 202–208, 2016, doi: 10.1016/j.corsci.2016.01.018.

[203] G. Kuri, C. Degueldre, J. Bertsch, and S. Abolhassani, "Micro-focussed XAFS spectroscopy to study Ni-bearing precipitates in the metal of corroded Zircaloy-2," *Appl. Phys. A Mater. Sci. Process.*, vol. 98, no. 3, pp. 625–633, 2010, doi: 10.1007/s00339-009-5456-z.

[204] A. L. Foster, "Studies of Metal Species in Solid Phases : the Case of Arsenic," *U.S. Geol. Surv.*, pp. 0–4.

[205] T. Aarholt, "Analytical microscopy of corroded zirconium alloys," 2017.

[206] B. De Gabory, Y. Dong, A. T. Motta, and E. A. Marquis, "EELS and atom probe tomography study of the evolution of the metal/oxide interface during zirconium alloy oxidation," *J. Nucl. Mater.*, vol. 462, pp. 304–309, 2015, doi: 10.1016/j.jnucmat.2015.03.043.

[207] N. Upadhyay and D. Gangopadhyay, "Least-squares fit of a linear combination of functions," *J. Interpolat. Approx. Sci. Comput.*, vol. 2013, pp. 1–16, 2013, doi: 10.5899/2013/jiasc-00046.

[208] R. C. GARVIE and P. S. NICHOLSON, "Phase Analysis in Zirconia Systems," *J. Am. Ceram. Soc.*, vol. 55, no. 6, pp. 303–305, 1972, doi: 10.1111/j.1151-2916.1972.tb11290.x.

[209] D. Bach, R. Schneider, and D. Gerthsen, "EELS of Niobium and Stoichiometric Niobium-Oxide Phases — Part II : Quantification," *Microsc. Microanal.*, vol. 15, no. 6, pp. 524–538, 2009, doi: 10.1017/s1431927609991061.

[210] R. Tao *et al.*, "Electron energy-loss spectroscopy study of metallic Nb and Nb oxides," *J. Appl. Phys.*, vol. 110, no. 12, pp. 0–8, 2011, doi: 10.1063/1.3665193.

[211] G. He *et al.*, "Investigating the stability of second phase particles in Zr-Nb alloys under irradiation," *J. Nucl. Mater.*, vol. 526, p. 151738, 2019, doi: 10.1016/j.jnucmat.2019.151738.

[212] H. W. K. UNE, K. SAKAMOTO, J. MATSUNAGA, Y. ETOH, M. AOMI, I. TAKAGc, K. SAWADA, "CONTROLLING FACTORS IN HYDROGEN ABSORPTION OF ZIRCONIUM ALLOYS," *Proc. Topfuel 2012, Manchester, UK*, vol. TopFuel-A0, 2012.

[213] Aylin Yilmazbayhan, "MICROSTRUCTURAL BASIS OF UNIFORM CORROSION IN ZR ALLOYS," Pennsylvania State University, 2004.

[214]    K. Une *et al.*, "Hydrogen absorption mechanism of zirconium alloys based on characterization of oxide layer," *J. ASTM Int.*, vol. 8, no. 5, pp. 401–432, 2011, doi: 10.1520/JAI102950.

[215]    M. Jublot *et al.*, *Influence of hydride precipitation on the corrosion kinetics of zircaloy-4: Effect of the nanostructure and grain boundary properties of the zirconium oxide layer on oxygen diffusion flux*, vol. STP 1597, no. January. 2018.

[216]    M. Tupin, P. Bossis, J. Chene, J. L. Bechade, and A. Motta, "UNDERSTANDING OF HYDRIDING MECHANISMS OF ZIRCALOY-4 ALLOY DURING CORROSION IN PWR SIMULATED CONDITIONS AND INFLUENCE OF ZIRCONIUM HYDRIDES ON ZIRCALOY-4 CORROSION," pp. 1–9.

[217]    L. K. Dash, N. Vast, P. Baranek, M.-C. Cheynet, and L. Reining, "Electronic structure and electron energy-loss spectroscopy of zirconia," *Phys. Rev. B*, vol. 70, no. 24, p. 245116, 2004, doi: 10.1103/PhysRevB.70.245116.

[218]    G. J. C. Woo, O.T., Carpenter, "EELS characterization of zirconium hydrides," *Microsc. Microanal. Microstruct.*, vol. 3, no. February, pp. 35–44, 1992, doi: 10.1051/mmm:019920030103500.

[219]    G. R. Corallo, D. A. Asbury, R. E. Gilbert, and G. B. Hoflund, "Interpretation of EELS spectra from polycrystalline zirconium surfaces after exposure to hydrogen and hydrogen/oxygen," *Langmuir*, vol. 4, no. 1, pp. 158–163, 1988, doi: 10.1021/la00079a029.

[220]    Z. Zhao *et al.*, "Characterization of Zirconium Hydrides and Phase Field Approach to a Mesoscopic-Scale Modeling of Their Precipitation," *J. ASTM Int.*, vol. 5, no. 3, p. 101161, 2008, doi: 10.1520/JAI101161.